

Collective Magnetization Dynamics in Magnetic Nanostructures at Various Length Scales and Time Scales

Thesis submitted for the degree of
Doctor of Philosophy (Science)

in
Nanoscience
by
Susmita Saha

**Centre for Research in Nanoscience
and Nanotechnology
University of Calcutta**

2015

Dedicated to My Dadu and Dida.....

Acknowledgement

At first I would like to express my deepest gratitude to my Ph.D supervisor Prof. Anjan Barman for his excellent guidance and giving me a chance to work in an extremely sophisticated well equipped laboratory. He introduced me to the field of magnonics and spintronics. He taught me how to perform an experiment and also the simulation and analysis of a research problem. Whenever I faced any problem in my research, he was always there to advise me. He always encouraged me to grow myself as an experimentalist and a good researcher. When I joined as a researcher, my English writing skill was very poor. He helped me a lot improve my writing skills and presentation skills. He trained me how to build a world class laboratory and how to maintain a healthy and friendly lab environment. When I joined his group, we could only measure magnetization dynamics in time domain (by using Time resolved magneto optical Kerr microscope). In 5 years, lots of new equipments were installed in our laboratory. Now, we can fabricate samples by using RF/DC sputtering, e-beam lithography and e-beam evaporation techniques. We also have the experimental facilities to measure spin wave dynamics of different magnetic nanostructures by using time domain (TR-MOKE), frequency domain (VNA-FMR) and wavevector domain (BLS) techniques. It was possible only due to his enthusiasm, patience and immense knowledge in field of magnetism. These qualities make him an excellent scientist and great mentor. In addition to this he gave me opportunities to present my research work in many national and international conferences. He also gave me chance to visit Durham University, UK, for collaborative research work. His mentorship is a blessing to me which will help me in my long term career.

I am also very thankful to Dr. Saswati Barman for teaching me Fortran and LLG-micromagnetics. At the beginning of my research work I was working with her to simulate Ising model using Fortran. She helped me to draw the graph in Origin and to prepare a power point presentation. I am really very grateful to her for her valuable advice regarding my professional and personal life.

I would like to express my sincere gratitude to Prof. YoshiChika Otani of Quantum Nano-Scale Magnetics Laboratory, RIKEN, Japan and Prof. Adekunley Adeyeye of National

University of Singapore for providing me very high quality samples for my work. I must also thank Dr. Y. Fukuma and Dr. S. Sugimoto for providing me lithographically patterned permalloy dot array samples of different lattice symmetry. I am also thankful to Dr. J. Ding for providing me samples for my work. I would like to acknowledge Prof. Del Atkinson, Durham University, for giving me an opportunity to work in his laboratory under DST-UKIERI project. I am also thankful to Dr. A. T. Hindmarch, R. M. Rowan-Robinson, Dr. J. A. King and S. Jaiswal for helping me in various ways during my stay in Durham.

I am really very thankful to Dr. Semanti Pal. She helped me a lot to learn different experimental techniques and proper lab attitude. She also helped me a lot to improve my English writing skill. After Semanti, I would like to acknowledge Dr. Bivas Rana, one of my best labmates, for his constant help during experiments and data analysis. I also learnt a lot from him about proper lab attitude and responsibilities. I would like to thank Dheeraj for helping me in numerical analysis especially for the work related to magnetic vortex based transistor. I am also very thankful to Ruma for fabricating lithographically patterned dot array samples arranged in various lattice symmetries. I would like to thank Semanti, Ruma, Bivas, Debanjan, Arnab, Chandrima, and Sucheta for their help in experimental work. I am also very thankful to Dr. Pinaki Laha and Dr. Jaivardhan Sinha for giving me valuable suggestions regarding RF/DC sputtering unit. Thanks to Samiran for helping me during measurement using VNA-FMR technique. Beyond all academic help, Samiran always stood beside me in all ups and downs. I am also very thankful to Dr. Sabareesan Ponraj and Dr. Arabinda Haldar for their valuable discussions over different scientific topics. Thanks to Semanti, Ruma, Debanjan, Arnab, Chandrima, Sucheta, Samiran, Santanu, Kaushik, Avinash, Neeraj, Neha, Saurav, Bipul and Kallol for providing a great work environment, and for their help and chats. Apart from my labmates I really want to thank my sisters, Monalisa and Ishita and my brothers Pranav, Arka, Ayan, Animesh, Subhashish and Nirnay and my friends Dr. D. P. Sinde and Y. Chaoba Devi for all the help they provided.

Last I am really very thankful to my parents for their constant support and love. They sacrificed a lot for me. During Ph.D, it was difficult for me to spend much time with them but they never complained. They always trust me on my decisions and give me the freedom to fulfill all my dreams. I am also thankful to my brother Sreeraj. After my family he is the

only person who always has faith on me. Today I can dream higher because I know my parents and my brother will always be there to support me. Thanks to Uday Mama for showing me the right path whenever I needed. Last but not the least I would like to thank my grandfather and grandmother for their encouragement. Though today they are not with me I know it was their dream that I should be a good researcher.

Finally, I thank S. N. Bose National Centre for Basic Sciences for giving me an opportunity to work here. Thanks to University Grant Commission for providing me with junior and senior research fellowships. The common research facilities under the Technical Cell were very helpful for initial characterization of my samples. I must thank various funding agencies including Department of Science and Technology, Government of India and Department of Information Technology, Govt. of India for their funding towards development of the experimental set ups that I used during my Ph.D. study.

Susmita Saha

S. N. Bose National Centre for Basic Sciences,

Kolkata

List of Publications:

This thesis is based on the following publications and manuscripts

1. Tunable magnonic spectra in two-dimensional magnonic crystals with variable lattice symmetry

S. Saha, R. mandal, S. Barman, D. Kumar, B. Rana, Y. Fukuma, S. Sugimoto, Y. Otani and A. Barman

Adv. Funct. Mater. **23**, 2378 (2013)

2. Time-domain study of spin-wave dynamics in two-dimensional arrays of bi-component magnetic structures

S. Saha, S. Barman, J. Ding, A. O. Adeyeye and A. Barman

Appl. Phys. Lett. **102**, 242409 (2013)

3. Tunable magnetic anisotropy in two-dimensional arrays of Ni₈₀Fe₂₀ elements

S. Saha, S. Barman, J. Ding, A. O. Adeyeye, and A. Barman

Appl Phys. Lett. **103**, 242416 (2013)

4. Tunable picosecond spin dynamics in two dimensional ferromagnetic nanodot arrays with varying lattice symmetry

S. Saha, S. Barman, S. Sugimoto, Y. Otani and A. Barman

RSC Advances **5**, 30748 (2015)

5. All-optical investigation of tunable picosecond magnetization dynamics in ferromagnetic nanostripes with width down to 50 nm

S. Saha, S. Barman, Y. Otani and A. Barman

(Manuscript Submitted)

6. Giant Amplification and Fan-Out in Magnetic Vortex Transistor

S. Barman, **S. Saha**, D. Kumar, S. Mandal and A. Barman

(*Manuscript to be submitted*)

The following publications are not included in the thesis:

1. Magnetization reversal dynamics in Co nanowires with competing magnetic anisotropies

S. Pal, **S. Saha**, D. Polley and A. Barman

Solid state Commun. **151**, 1994 (2011)

2. Optically induced tunable magnetization dynamics in nanoscale Co antidote lattices.

R. Mandal, **S. Saha**, D. Kumar, S. Barman, S. pal, B. Rana, K. Das, A. K.Raychaudhury, Y. Fukuma, Y. Otani, and A. Barman

ACS Nano **6**, 3397(2012).

3. Time-resolved measurement of spin-wave spectra in CoO capped $[Co(t)/Pt(7\text{\AA})]_{n-1}$ $Co(t)$ multilayer systems

S. Pal, B. Rana, **S. Saha**, R. Mandal, O. Hellwig, J. Romero-Vivas, S. Mamica, J. W. Klos, M. Mruczkiewicz, M. L. Sokolovskyy, M. Krawczyk, and A. Barman

J. Appl. Phys. **111**, 07C507 (2012).

4. Effects of antidot shape on the spin wave spectra of two-dimensional $Ni_{80}Fe_{20}$ antidot lattices,

R. Mandal, P. Laha, K. Das, **S. Saha**, S. Barman, A. K. Raychaudhuri and A. Barman

Appl. Phys. Lett. **103**, 262410 (2013).

5. Width dependent transition of quantized spin-wave modes in $Ni_{80}Fe_{20}$ square nanorings,

C. Banerjee, **S. Saha**, S. Barman, O. Rousseau, Y. Otani and A. Barman,
J. Appl. Phys. **116**, 163912 (2014).

6. Fast and facile preparation of CTAB based gels and their applications in Au and Ag nanoparticles synthesis,

R. K. Upadhyay, N. Soin, **S. Saha**, A. Barman and S. S. Roy,

Materials Chemistry and Physics **156**, 105 (2015).

7. Optical, structural, catalytic and electrochemical properties of the Au nanoparticles synthesized using CTAB based gels,

R. K. Upadhyay, S. Deshmukh, **S. Saha**, A. Barman and S. S. Roy,

Journal of Materials Science: Materials in Electronics (Accepted).

8. Dependence of spin wave properties in $[Co/Ni_{80}Fe_{20}]_r$ multilayers on the number of repetitions,

C. Banerjee, A. K. Chaurasiya, **S. Saha**, J. Sinha and A. Barman.

(Submitted)

9. Manipulating spin waves in high aspect ratio single crystalline ferromagnetic nanowires

S. Pal, **S. Saha**, M. V. Kamalakar and A. Barman.

(Submitted)

10. Tunable spin wave spectra in two-dimensional $Ni_{80}Fe_{20}$ antidot lattices with varying lattice symmetry

R. Mandal, S. Barman, **S. Saha**, Y. Otani, and A. Barman

(Submitted)

Abstract

Metamaterials demand the invention of new material properties, which may not always be possible to achieve in a single material in the bulk or thin film form. Instead, structuring of known materials in one-, two-, and three- dimensions at various length scales and exploiting dynamical magnetic properties over various time scales may potentially offer the desirable material properties. An existing example is the patterned magnetic media, which uses ordered arrays of lithographically patterned two dimensional arrays of bits, and the magnetic switching behaviors of such systems including switching field distribution have been thoroughly studied. An essential criterion has been to manipulate magnetostatic interactions (cross-talks) between the individual bits for the application in patterned magnetic media. The similar kind of array may be used to propagate magnetic excitations in the form of collective long wavelength spin waves (SWs), when the individual magnetic elements are strongly magnetostatically coupled. Such magnetostatically coupled and periodically modulated magnetic materials forms a new class of artificial crystals known as magnonic crystals (MCs) where collective excitations of SWs (magnons) can be used to carry and process information. This introduces a new field of research known as magnonics. MCs form magnonic minibands consisting of allowed and forbidden SW frequencies and corresponding magnonic bandgap. The SWs in MCs can be controlled by changing its various physical and geometrical parameters such as material, shape, size, lattice spacing, lattice symmetry, and also strength and orientation of the external bias field.

In this thesis, we have investigated the static and ultrafast magnetization dynamics of magnetic nanostructures at various length scales and time scales. The ultrafast magnetization dynamics is measured using home-built time resolved magneto optical Kerr effect (TR-MOKE) microscope. First we have investigated the magnetization dynamics of magnetostatically coupled 20 nm thick Ni₈₀Fe₂₀ (Permalloy or Py) circular (diameter \sim 100 nm, edge to edge separation \sim 30 nm) nanodot lattices by varying their lattice symmetry namely square, rectangular, hexagonal, honeycomb and octagonal lattice. The spin wave spectra show significant dependence on the lattice symmetry. It has been found that the

symmetry of the lattice plays a major role in determining the magnetic stray field configuration which eventually affects the SW spectra. The dominant precessional mode frequencies showed four-fold, two-fold, six-fold, six-fold and eight-fold anisotropy superposed with a weak four-fold anisotropy for square, rectangular, hexagonal, honeycomb and octagonal lattice, respectively which arises due to the angular variation of the magnetostatic field distribution within the arrays. The magnetization dynamics at a different length scale has been investigated in elongated Py ellipse with length 1 μm and width 450 nm dispersed in three different lattice geometries. The dominant precessional mode shows a two-fold anisotropy. The simulated magnetostatic field distribution confirms the variation of magnetostatic field with different lattice arrangements. The competition between the shape anisotropy of the constituent elements and the magnetostatic field leads towards a variation in the net magnetic anisotropy and the corresponding frequency variation. Next we studied the SW spectra in a bi-component MC which is a periodic composite structure made of two different magnetic materials (Py and Co). The frequency spectra change significantly depending upon the direction of the external bias field with respect to the long axis (LA) of the sample and both optical and acoustic modes are observed. The frequencies and the spatial profiles of the modes of individual elements are modified significantly in the bi-component unit as opposed to the individual constituents and further in the two-dimensional arrays. At even longer length scale, such as Py nanostripes with 5 μm long and width between 50 nm and 200 nm manipulation of SW spectra by changing the bias field orientation is demonstrated both by experiment and simulation. We have observed a significant difference in the spin wave frequencies and nature of modes with the variation of the width of the stripe as well as by varying the bias field orientation. Depending on the bias field orientation quantization of SWs varies from a mixture of DE and BV like mode to a pure DE like mode. Finally, we have studied the gyroscopic motion of magnetic vortex cores in a magnetostatically coupled Py disks. Such system acts as a magnetic vortex based transistor. We have optimized the gain of a two and three vortex system by controlling the separation between the vortices. Giant amplification in magnetic vortex transistor is obtained by introducing asymmetry in the three vortex sequence. For the two vortex system, the gain is maximum for smaller separation ($S = 10$ nm). The three vortex system provides us the maximum gain for a particular combination

of distances between the first two vortices and between the second and third vortex and it can efficiently work as a vortex transistor. The dynamics of strayfield antivortices explains the observed gain and efficiency of the transistor. All the observations are important for future applications of these samples in nanoscale microwave communications.

List of Abbreviations

MC: Magnonic crystal

SW: Spin wave

BMC: Bi-component magnonic crystal

Co: Cobalt

Eqn.: Equation

DE : Damon-Esbach

BV: Backward volume

MVT: Magnetic vortex transistor

AMVT: Asymmetric magnetic vortex transistor

LA: Long axis

SA: Short axis

STNO: Spin torque nano oscillator

SNR: Signal to noise ratio

FFT: Fast Fourier transforms

Fig. : Figure

FM: Ferromagnetic/ Ferromagnet

AFM: Antiferromagnetic/ Antiferromagnet

FMR: Ferromagnetic resonance

VNA: Vector network analyzer

BLS: Brillouin light scattering

LLG : Landau-Lifshitz-Gilbert

MO : Microscope objective

MOKE : Magneto-optical Kerr effect

MRAM : Magnetic random-access memory

N. A. : Numerical aperture

OBD : Optical bridge detector

OOMMF : Object oriented micromagnetic framework

PMA : Perpendicular magnetic anisotropy

Py : Permalloy (Ni₈₀Fe₂₀)

rf : Radio-frequency

SO : Spin-orbit

STT : Spin-transfer torque

TR-MOKE : Time-resolved magneto-optical Kerr effect

List of Symbols

α : Damping constant

γ : Gyromagnetic ratio

λ : Wavelength

τ : Time constant

K : Anisotropy

K_{eff} : Effective anisotropy

M : Magnetization

M_s : Saturation magnetization

m : Unit vector of magnetization

H : Magnetic field

H_{eff} : Effective magnetic field

f : Frequency

A : Exchange stiffness constant

List of Figures:

Fig. 2.1 Coordinate system for (a) uniaxial hexagonal closed packed system and (b) cubic system.....	13
Fig. 2.2 (a) Simulated static magnetization states are shown for a single 200 nm square dot of thickness (t) = 20 nm at a bias field of 1.15 kOe applied at different azimuthal angles (ϕ). (b) The geometry of the applied bias field is shown. (c) Simulated magnetostatic stray field distributions are shown for an array of 200 nm square dot of thickness (t) = 20 nm and interdot separation (s) = 100 nm at a bias field of 1.15 kOe applied at different azimuthal angles (ϕ)	16
Fig. 2.3 Magnetization precession (a) without damping and (b) with damping.....	19
Fig. 2.4 Characteristic time scale of various magnetization dynamics.....	23
Fig. 2.5 Schematic representation of ultrafast magnetization dynamics based upon three temperature model.	24
Fig. 2.6 Anisotropy field pulse in all-optical TR-MOKE microscope.....	28
Fig. 2.7 Co-ordinate systems used for (a) an ellipsoid, (b) a plane and (c) a cylinder.....	29
Fig. 2.8 Geometry of the magnetization and applied magnetic field is shown in an orthogonal coordinate system (a, b, c).	34
Fig. 2.9 A schematic diagram of spin-wave is shown.....	36
Fig. 2.10 A representative plot of frequency as a function of wavelength of spin waves....	38
Fig. 2.11 Schematics of (a) perpendicular standing spin wave mode (PSSW) and magnetostatic surface spin wave mode (MSSW) are shown for a ferromagnetic thin film. (b) The dispersion relations for three different types of magnetostatic SWs modes are shown.	40

Fig. 2.12 A Ni ₈₀ Fe ₂₀ circular disk of diameter 200 nm and thickness 40 nm formed magnetic vortex whose center contains an out-of-plane polarized core with (a) $p = +1$ and (b) $p = -1$	44
Fig. 2.13 A schematic of the incident light linearly polarized along X – direction and propagating along Z – direction.	47
Fig. 2.14 (a) Geometry of the Kerr rotation (θ_K) and Kerr ellipticity (ε_K) are shown. Here r is the Fresnel reflection coefficient, k is the Kerr coefficient and M is the magnetization of the sample. Schematics of (b) polar, (c) longitudinal and (d) transverse MOKE geometries are shown.	51
Fig. 3.1 Schematic diagram of optical beam lithography process is shown.....	54
Fig. 3.2 Schematic diagram of electron beam lithography process is shown.....	56
Fig. 3.3 Schematic diagram of electron beam evaporation technique is shown.....	56
Fig. 3.4 Schematic diagram of magnetron sputtering unit is shown.....	58
Fig. 3.5 Schematic diagram of shadow deposition is shown.....	59
Fig. 3.6 Schematic diagram of scanning electron microscope is shown.....	60
Fig. 3.7 Interaction of accelerated electrons with sample and emission of X-rays are shown schematically.	62
Fig. 3.8 Schematic diagram of longitudinal microfocused static MOKE setup is shown.	64
Fig. 3.9 A photograph of the focused static magneto-optical Kerr effect (MOKE) microscope in our laboratory in the S. N. Bose National Centre for Basic Sciences.	65
Fig. 3.10 A photograph of the all optical time-resolved magneto-optical Kerr effect (TR-MOKE) microscope in our laboratory in the S. N. Bose National Centre for Basic Sciences. 66	66
Fig. 3.11 Schematic diagram of all-optical time-resolved magneto-optical Kerr effect (TR-MOKE) microscope with collinear pump probe geometry is shown.	71

Fig. 3.12 Schematic diagrams of the collinear geometry of pump and probe beams focused by the microscope objective (MO) on the sample surface with (a) in-plane and (b) out of plane bias magnetic field (H).....	72
Fig. 3.13 A photograph of the enlarged view of the detection procedure. The important components in the set up are labeled in the figures.....	73
Fig. 3.14 Schematic diagram of the optical autocorrelator is shown.....	75
Fig. 3.15 Schematic diagram of the optical bridge detector is shown.....	76
Fig. 3.16 A typical mode-locked power spectrum of the output beam from Tsunami.....	78
Fig. 3.17 The reflectivity signal obtained from a Si (100) wafer as a function of the time delay between the pump and the probe beams. The decay of the reflectivity signal after the zero delay can be fitted with a double exponential decay function to obtain the time constant of the longer decay which is about 195 ps in our case.	80
Fig. 3.18 (a) SEM image of an array of $10 \times 10 \mu\text{m}^2$ blanket Ni ₈₀ Fe ₂₀ thin film with 25 nm thickness. The schematic of the experimental geometry of bias magnetic field is shown on the image. (b) The typical time-resolved Kerr rotation data (solid circles) from this film at a bias field (H) of 1.15 kOe, applied along the positive x - axis is shown. The solid line corresponds to the fit with Eqn. (3.8). (c) The corresponding FFT power spectra showing the resonant mode.....	81
Fig. 4.1 The schematic diagrams show the discretization of a rectangular sample into a number of (a) cuboidal cells with equal size for FDM and (b) tetrahedral cells with varying size for FEM based simulation.....	83
Fig. 4.2 Stray field distribution along with the color scale calculated by using OOMMF software is shown for two Ni ₈₀ Fe ₂₀ circular nanodots of diameter 200 nm and thickness 40 nm separated by 100 nm at $H = 1.5$ mT and $\phi = 0^\circ$	87
Fig. 4.3 (a) Contour maps of magnetostatic field distributions (x-component) calculated using LLG micromagnetics simulator are shown for Ni ₈₀ Fe ₂₀ circular nanodots (diameter:	

100 nm, separation: 30 nm, thickness: 20 nm) with square lattice symmetry for $H = 1.3$ kOe applied at $\phi = 0^\circ$. The arrows inside the dots represent the magnetization states of the dots, while the strengths of the stray magnetic fields are represented by the color bar at the bottom of the figure. (b) Linescans of simulated magnetostatic fields from square lattices obtained from the positions indicated by horizontal dashed lines in (a). 88

Fig. 4.4 (a) Simulated spatially averaged magnetization (M_z) vs time is shown for a single Ni₈₀Fe₂₀ circular nanodot (diameter: 100 nm, thickness: 20 nm) for $H = 1.3$ kOe applied at $\phi = 0$. (b) Corresponding fast Fourier transform (FFT) power spectrum of the simulated time-resolved magnetization curve of single circular nanodot. Two well resolved resonant modes are observed in this case. (c) The calculated power and phase distributions corresponding to two resonant modes are shown along with the color scale..... 90

Fig. 6.1 (a) Scanning electron micrographs of the Py dot lattices with different lattice symmetry, namely square, rectangular, hexagonal, honeycomb and octagonal symmetry. The dot diameter and separation are shown in the micrograph for the octagonal lattice along with the length scale bar. The geometry of the applied magnetic field for all lattices is shown in the micrograph of the hexagonal lattice..... 104

Fig. 6.2 Experimental MOKE loops of square, hexagonal, honeycomb and octagonal lattices for bias field applied at $\phi = 0^\circ$ 107

Fig. 6.3 Typical time resolved (a) reflectivity and (b) Kerr rotation data are shown for the Py dot lattice with hexagonal lattice symmetry for $H = 1.3$ kOe applied at $\phi = 0^\circ$. (c) The time-resolved Kerr rotation data showing ultrafast demagnetization and fast remagnetization for square, rectangular, honeycomb and octagonal lattices are shown for $H = 1.3$ kOe applied at $\phi = 0^\circ$ 109

Fig. 6.4 Experimental (a) time resolved Kerr rotation data and (b) the corresponding FFT spectra are shown for permalloy dot lattices with five different lattice symmetry at $H = 1.3$ kOe at $\phi = 0^\circ$. (c) FFT spectra of the simulated time-domain magnetization for five different lattice symmetry. The mode numbers are shown in the simulated FFT spectra, while the

dashed vertical lines show the positions of the centre and edge modes of the simulated single dot with width = 100 nm and thickness = 20 nm.....	111
Fig. 6.5 The power spectra of the simulated magnetization dynamics of a single circular permalloy dot with 100 nm diameter and 20 nm thickness at $H = 1.3$ kOe. The power and phase maps of the two observed modes are shown in the inset. Mode 2 is identified as the centre mode while mode 1 as the edge mode of the permalloy dot.....	112
Fig. 6.6 The power and phase maps for different precessional modes of permalloy dot lattices with square, rectangular and hexagonal symmetry. The colormaps for the power and phase distributions are shown at the top of the images.....	114
Fig. 6.7 The power and phase maps for different precessional modes of permalloy dot lattices with honeycomb and octagonal symmetry. The colormaps for power and phase distributions are as shown in Fig. 6.6.	115
Fig. 6.8 Contour maps of simulated magnetostatic field distributions (x-component) are shown for permalloy dots lattices with variable lattice symmetry at $H = 1.3$ kOe at $\phi = 0^\circ$. The arrows inside the dots represent the magnetization states of the dots, while the strengths of the stray magnetic fields are represented by the color bar at the lower right corner of the figure.....	116
Fig. 6.9 Linescans of simulated magnetostatic fields from various lattices as obtained from the positions indicated by horizontal dashed lines in Fig. 6.8. Linescans of simulated magnetostatic field from a single dot is superposed on each panel for comparison.....	118
Fig. 7.1 (a) A schematic of the experimental geometry is shown on the scanning electron micrograph of an array of circular nanodots with rectangular lattice symmetry. (b) Typical experimental time-resolved Kerr rotation data from the octagonal lattice at $H = 1.3$ kOe revealing ultrafast demagnetization, fast and slow relaxations, and precession of magnetization (left panel). Background subtracted time-resolved Kerr rotation data is shown in the right panel. (c) The spin wave spectra obtained by FFT of the time-resolved data from square, rectangular, hexagonal, honeycomb and octagonal lattices are shown for	

different values of ϕ at $H = 1.3$ kOe. The corresponding scanning electron micrographs are shown in the insets.....	122
Fig. 7.2 (a) Experimental and (b) simulated spin wave frequencies (symbols) as a function of the azimuthal angle ϕ of the in-plane bias magnetic field at $H = 1.3$ kOe. The solid curves show the theoretical fits.....	124
Fig. 7.3 The power ((a), (c) and (e)) and phase ((b), (d) and (f)) maps of the asterisk (*) marked modes for the square ((a), (b)), rectangular ((c), (d)) and hexagonal ((e), (f)) lattices for selected values of ϕ at $H = 1.3$ kOe. The color maps for power and phase distributions are shown at the bottom of the left panel of figure.....	125
Fig. 7.4 The power ((a) and (c)) and phase ((b) and (d)) maps of the asterisk (*) marked modes for the honeycomb ((a), (b)) and octagonal ((c), (d)) lattices for selected values of ϕ at $H = 1.3$ kOe. The color maps for power and phase distributions are shown at the top of the figure.....	128
Fig. 7.5 Contour maps of simulated magnetostatic field distributions (x -component) are shown for (a) rectangular, (b) honeycomb and (c) octagonal lattice for selected values of ϕ at $H = 1.3$ kOe. The schematics of the applied bias field directions are also shown for all values of ϕ . The color map for the magnetostatic field is shown at the right panel of the figure.....	130
Fig. 7.6 Variation of the simulated average magnetostatic field as a function of ϕ at $H = 1.3$ kOe from samples with different lattice symmetry. The symbols show simulated data, while the solid curves show the theoretical fits.....	131
Fig. 8.1 (a) The scanning electron micrographs of two-dimensional arrays of Py elements (S1, S2 and S3). The schematic of the experimental geometry is shown on the SEM image of S1. (b) Typical experimental time-resolved Kerr rotation data for S1 at $H = 1.5$ kOe at $\phi = 0^\circ$ revealing ultrafast demagnetization, fast and slow relaxations and precession of magnetization is shown in the top panel. Background subtracted time-resolved Kerr rotation for S1 is shown in the bottom panel. (c) The Kerr rotation data showing ultrafast	

demagnetization and fast remagnetization are shown for S2 and S3 at $H = 1.5$ kOe at $\phi = 0^\circ$.	
.....	135
Fig. 8.2 The spin wave spectra obtained by FFT of the time-resolved Kerr rotation are shown for (a) $\phi = 0^\circ$ and (b) $\phi = 90^\circ$ at $H = 1.5$ kOe.....	136
Fig. 8.3 (a) Experimental precessional frequencies (symbols) are plotted as a function of azimuthal angle of the bias field (ϕ) for S1, S2, and S3 at $H = 1.5$ kOe. (b) Simulated spin wave spectra from the central element of 3×3 arrays used in S2 ($\phi = 45^\circ$) and S3 ($\phi = 90^\circ$). (c) Simulated precessional frequencies (symbols) are plotted as a function of azimuthal angle of the bias field (ϕ) for a single permalloy element and the central element from three different arrays (S1, S2 and S3) at $H = 1.5$ kOe. The solid lines in (a) and (c) represent fits to Eqn. (8.1). (d) The power (P) and phase (Ph) maps of the corresponding mode (*) from the central element of S1, S2, and S3 at $\phi = 0^\circ, 45^\circ$, and 90° at $H = 1.5$ kOe.	138
.....	138
Fig. 8.4 (a) Contour maps of the simulated magnetostatic stray field distributions (X-component) for S1, S2 and S3 at $H = 1.5$ kOe at $\phi = 0^\circ$ are shown with the colour map. (b) The linescans of the simulated magnetostatic fields along X direction from S1, S2 and S3 at $H = 1.5$ kOe at $\phi = 0^\circ$. (c) The linescan of simulated magnetostatic fields along X direction from S1, S2 and S3 at $H = 1.5$ kOe at $\phi \approx 90^\circ$	140
Fig. 9.1 (a) Scanning electron micrographs of two-dimensional lattices of bi-component structures (S1 and S2). The insets show magnified images of single bi-component units. (b) Typical experimental data of time-resolved Kerr rotation for S1 and S2 at $H = 1.65$ kOe applied along the long-axis (LA) of the bi-component unit. The time-resolved data reveal the ultrafast demagnetization, fast remagnetization and a slow remagnetization superposed with precession of magnetization. (c) The same data for S1 and S2 are shown after elimination of the demagnetization part and subtraction of a bi-exponential decay.	144
Fig. 9.2 Experimentally obtained SW spectra for S1 and S2 after a bias field $H = 1.65$ kOe is applied along (a) the short axis (SA) and (b) the long axis (LA) of the bi-component unit.	

The schematic of experimental geometry is shown on the SEM image of a single bi-component unit.....	145
Fig. 9.3 (a) Variation of experimentally obtained mode frequencies (symbols) with bias magnetic field for S1. The bias field is applied along the LA and SA of the bi-component unit. The solid lines are fit to Eqn. 9.1. (b) Schematics of the external (H), and internal field (H_{int}) acting on the bi-component unit in LA and SA configurations are shown.	146
Fig. 9.4 Simulated spin-wave spectra from a single Py ellipse, single Co ellipse, single Py/Co bi-component unit and two-dimensional lattices of bi-component structures (S1 and S2) after application of a bias field along the long-axis (LA) and the short-axis (SA) of the ellipse. The mode numbers are assigned to each spectrum. The mode profiles (power) are shown for the single Py and Co ellipses at the inset of the corresponding spectrum. The colormap for power profile is shown at the top of the figure.....	149
Fig. 9.5 Simulated mode profiles (power and phase) for a single bi-component unit and the central bi-component unit from 3×3 lattices of S1 and S2. The colormaps for power and phase are shown at the top of the image.	150
Fig. 10.1 (a) Scanning electron micrographs of Py nanostripes with different stripe widths (S1, S2 and S3) are shown. (b) The schematic of the experimental configuration. Here, $\phi = 0^\circ$ corresponds to backward volume (BV) geometry and $\phi = 90^\circ$ corresponds to Damon-Eshbach (DE) geometry. (c) Typical experimental time-resolved Kerr rotation data from S3 ($w = 50$ nm) for $H = 1$ kOe applied at $\phi = 0^\circ$. The data reveals three different temporal regimes namely, the ultrafast demagnetization, fast and slow relaxations, and precession of magnetization.....	155
Fig. 10.2 Experimental SW spectra at (a) $\phi = 0^\circ$, (b) $\phi = 90^\circ$ and simulated SW spectra at (c) $\phi = 0^\circ$, (d) $\phi = 90^\circ$ are shown for S1, S2 and S3 at $H = 1.0$ kOe.....	157
Fig. 10.3 (a) Experimental (filled symbols) and (b) simulated SW frequencies (open symbols) as a function of the azimuthal angle ϕ of the in-plane bias magnetic field at $H = 1$ kOe for S1, S2 and S3. (c) Simulated SW frequencies (symbols) as a function of the	

azimuthal angle ϕ of the in-plane bias magnetic field at $H = 1$ kOe for single nanostripes of widths $w = 200$ nm, 100 nm and 50 nm. The solid lines are only guide to the eyes.....158

Fig. 10.4 Simulated static magnetic configurations for S1, S2 and S3 are shown for $H = 1$ kOe applied at (a) $\phi = 0^\circ$, (b) $\phi = 60^\circ$ and (c) $\phi = 90^\circ$. The region close to right edge of the stripe is shown in (a) and (b) whereas the center of the stripe is shown in (c). The y-component of magnetization vector is represented by blue-white-red color map.160

Fig. 10.5 (a) The phase profiles of all SW modes for single stripes of three different widths for $H = 1$ kOe applied at $\phi = 0^\circ$. The (b) power and (c) phase profiles of all simulated SW modes for S1, S2 and S3 for $H = 1$ kOe applied at $\phi = 0^\circ$. The color maps for power and phase distributions are shown at the top of the figure. The direction of external bias magnetic field (H) is shown at the bottom of the figure.161

Fig. 10.6 (a) The phase profile of all SW modes for single stripes of different widths for $H = 1$ kOe applied at $\phi = 90^\circ$ are shown. The (b) power and (c) phase profiles of all SW modes for S1, S2 and S3 for $H = 1$ kOe applied at $\phi = 90^\circ$ are shown. The color maps for power and phase distributions are shown in (a). The direction of external bias magnetic field (H) is shown at the right of the figure.163

Fig. 10.7 (a) The schematic of the linescan of the simulated magentostatic field and the geometry of the applied magnetic field for the array of stripes are shown. (b) The linescans of the simulated magnetostatic fields along Y (red dotted line) direction from S1, S2 and S3 for $H = 1$ kOe applied at $\phi \approx 90^\circ$ are shown. The linescans of the simulated magnetostatic fields along X direction (green dotted line) from S1, S2 and S3 for $H = 1$ kOe applied at (c) $\phi = 0^\circ$ and (d) $\phi \approx 90^\circ$ are shown.165

Fig. 11.1 The ground state spin configurations of Py disks of diameter (d) 200 nm and thickness (t) 40 nm arranged in coupled (a) two vortex system with inter disk separation (S) 10 nm and (b) three vortex system with the separation between left and centre vortex ($S1$) of 10 nm and the separation between centre and right vortex ($S2$) of 100 nm.....173

Fig. 11.2 Energy spectral densities (ESDs) for coupled two vortex systems with varying inter-disk separation (S) for a signal amplitude of 1.5 mT rotating CCW at $f_0 = 1.27$ GHz. 174

Fig. 11.3 Variation of gain (B) with inter-disk separation (S) is plotted for coupled two vortex systems	175
Fig. 11.4 Strayfield distributions for coupled two vortex systems with four different interdisk separations (S) are shown. The green arrows represent the paths of the antivortex solitons. The dimensions of the disk shown in different panels are not in scale.	176
Fig. 11.5 Energy spectral densities (ESDs) for asymmetric magnetic vortex transistor (AMVT) with varying S_2 . A 1.5 mT signal rotating CCW at $f_0 = 1.27$ GHz is applied to the left vortex.....	178
Fig. 11.6(a) Variation of gain (B) with S_2 is plotted for AMVT. (b) Gain B , versus logarithm of signal amplitude h_0 is plotted for AMVT with $S_1 = 10$ nm and $S_2 = 100$ nm.....	179
Fig. 11.7 Strayfield distributions for three vortex sequences with varying inter-disk separations S_1 and S_2 are shown. The green dotted lines represent the paths of the antivortex solitons. The dimensions of the disk shown in different panels are not in scale.	180
Fig. 11.8 Variation of the length of the major axis of the ellipse with S_2 for AMVT are plotted.	181
Fig. 11.9 (a) - (c) ESDs for fan-out operation are plotted. (d) - (f) Strayfield distributions in an AMVT network are shown. Signal is given only to the left vortex ('I') in the middle row and gain is measured at upper and lower right vortices which are marked as '01' and '02' respectively. The green lines represent the paths of the antivortex solitons.	182

Content

1. Introduction.....	1
2. Theoretical Background.....	10
2.1 Introduction:.....	10
2.2 Magnetic Anisotropy:	11
2.3 Magnetization Dynamics:.....	18
2.4 Ferromagnetic Resonance (FMR):.....	29
2.5 Spin Waves:.....	36
2.6 Magnetic Vortices:	43
2.7 Magneto-Optical Kerr Effect (MOKE):.....	46
3. Sample Fabrication, Characterization and Measurement Techniques for Magnetization Dynamics	53
3.1 Introduction:.....	53
3.2 Sample Fabrication:	54
3.3 Sample Characterization:.....	60
3.4 Measurement Techniques for Magnetization Dynamics:.....	63
A. Description of Lasers:.....	66
B. Description of the Set up:.....	69
F. Alignment of the Set Up:.....	77
G. Optimization of the Setup Using Standard Silicon (Si) Wafer:	79
H. Optimization of the Setup Using a Standard Ni ₈₀ Fe ₂₀ Film:.....	80

4.	Micromagnetic Simulations.....	82
4.1	Introduction:.....	82
4.2	Micromagnetic Numerical Simulations:.....	82
4.3	Object Oriented Micromagnetic Framework (OOMMF):	85
4.4	LLG Micromagnetics Simulator:	87
4.5	Calculation of Power and Phase profile of the Resonating Mode:	89
5.	Literature Review.....	91
5.1	Introduction:.....	91
5.2	Magnonic Crystal:	91
6.	Tunable Magnonic Spectra in Two Dimensional Magnonic Crystals with Variable Lattice Symmetry:.....	102
6.1	Introduction:.....	102
6.2	Experimental Details:.....	104
6.3	Results and Discussions:	106
6.3	Conclusions:	118
7.	Extrinsic Configurational Anisotropy of Spin Waves in Two-Dimensional Ferromagnetic Nanodot Lattices with Varying Lattice Symmetry	120
7.1	Introduction:.....	120
7.2	Experimental Details:	121
7.3	Measurement Techniques:	123
7.4	Results and Discussions:	123
7.5	Conclusions:	131

8.	Tunable Magnetic Anisotropy in Two-Dimensional Arrays of Ni ₈₀ Fe ₂₀ Elements.....	133
8.1	Introduction:.....	133
8.2	Experimental Details:.....	134
8.3	Results and Discussions:.....	135
8.4	Conclusions:.....	141
9.	Time-Domain Study of Spin-Wave Dynamics in Two-Dimensional Arrays of Bi-Component Magnetic Structures	142
9.1	Introduction:.....	142
9.2	Experimental Details:.....	143
9.2	Results and Discussions:	146
9.3	Conclusions:.....	152
10.	All-Optical Investigation of Tunable Magnetization Dynamics in Ni ₈₀ Fe ₂₀ Nanostripes.....	153
10.1	Introduction:.....	153
10.2	Experimental Details:	155
10.3	Conclusions:.....	166
11.	Giant Amplification and Fan-Out Operation in Asymmetric Magnetic Vortex Transistor.....	167
11.1	Introduction:	167
11.2	Methods:	171
11.3	Results:	173
11.4	Discussions:	184

12. Summary and Future Perspectives.....	186
12.1 Summary:	186
12.2 Future Perspectives:	189
References	192

1. Introduction

On 29th December 1959, Richard Feynman, gave a lecture entitled “There’s plenty of room at the bottom” at American Physical Society meeting in California Institute of technology where he emphasized the scope of possible technological developments at the nano scale. From that day the scientific community is paying considerable attention to manipulate the matter on an atomic, molecular and supermolecular scale and in 1981 Norio Taniguchi introduced a new research field named nanoscience and nanotechnology. One of the most interesting and emerging branches of research in the field of nanoscience and nanotechnology is nanomagnetism where magnetic phenomena of submicron sized magnetic structures are studied. The magnetic properties of submicron sized magnetic structures (nanomagnets) are modified due to the size reduction effects. As a result nanomagnets have tremendous fundamental scientific interest. In addition to this nanomagnets also have huge amount of applications in modern technology such as magnetic data storage devices [1-2], nonvolatile magnetic memory [3-4], magnetic logic devices [5-8], sensors, and magnetic resonance imaging [9], biomedicine and biotechnology [10], spin torque nano oscillators (STNOs) [11] and magnonic crystal [12-13].

In modern hard disks, magnetic thin films are used as the recording media. Magnetic thin films are polycrystalline alloys of Co, Cr and Pt with additional elements such as B or Ta. In such longitudinal magnetic media each grain acts as a single domain with easy axis of magnetization parallel to the plane of the film[14]. However, the magnetization of the grain is randomly distributed and as a result the signal to noise ratio (SNR) is low. To overcome this problem, sometime the easy axis of magnetization is set along the track direction. This is known as oriented longitudinal magnetic media [15]. The storage capacity of such media increases with the decrease of the grain size. But due to superparamagnetic effect [16-17], the magnetization direction of these tiny grains randomly flips at room temperature. Therefore, to increase thermal stability the concept of perpendicular magnetic recording (PMR) [18-19] was introduced by Shun-Ichi Iwasaki in 1976. In PMR, the magnetic thin

Chapter1

films of materials with high magnetocrystalline anisotropy like Co, CoCr, CoPt, CoCrPt are used as the recording media. As a result the recording density of hard disk drive increases from 15 GB/cm² (longitudinal recording) to 150 GB/cm² (PMR) [20]. However, the main problem with PMR is that the value of magnetic anisotropy is limited by the magnetic field required to switch the magnetization (write field). To avoid this problem heat assisted magnetic recording (HAMR) method is used where the switching field of the material is reduced by heating the material with a laser [15]. Another very promising approach to new storage architecture is the use of patterned recording media [20-22] where the recording layer is fabricated as an ordered array of nanomagnets, each one storing a single bit of information depending on its magnetization states. For patterned magnetic media the volume of individual nanomagnet is much larger when compared to a single grain. Therefore, it has the potential to increase the longitudinal recording density from 15 GB/cm² to 30 GB/cm² without the need for high write field [20]. The recording density of patterned magnetic media could also be increased by decreasing the size of the individual element. The only essential criterion for patterned magnetic media is to eliminate the magnetostatic interaction (crosstalk) between the individual bits.

Similar kinds of ordered arrays having strong magnetostatic interaction may show long wavelength collective dynamics where the dynamics of constituent nanomagnets maintain constant amplitude and phase relationship. This type of magnetostatically coupled array of nanomagnets forms two dimensional magnonic crystals (MCs) [23-25] where spin waves (SWs), the fundamental magnetic excitation in a metallic ferromagnetic material having frequency in microwave regime, are the transmission wave similar to electromagnetic (photonic crystal) or acoustic (phononic crystal) wave. The quasi-particles associated with the quantization of SWs are known as magnons. Magnons are spin-1 particles and obey Bose-Einstein statistics similar to photons and phonons. The dispersion relation of magnon is quadratic in nature ($\omega \propto k^2$) for long wavelength limit and they form magnonic minibands. Magnonic minibands consist of allowed magnonic states with alternating forbidden band gaps. The magnonic band structure can be tuned by varying various physical and geometrical parameters as well as external magnetic field [26]. This is the most significant advantage of SW based systems over electronic, photonic and phononic

crystals. In addition to this the wavelengths of magnons are orders of magnitude shorter than the light wave operating in the same frequency, which makes MCs a suitable candidate for nanoscale on chip signal processing and data communication. They can also offer better prospects for miniaturization as compared to the conventional photonic and electronic devices. Magnetostatically coupled ordered array of nanodots, nanostripes, nanoparticles which are made of single component, bi-component (element) and multilayered structures are the most popular examples of MCs. Another example of MCs is magnetic antidots which are basically arrays of holes on a continuous magnetic thin film. Magnetic antidots are exchange coupled magnetic system and hence offer larger SW propagation velocity than magnetostatically coupled magnetic dot lattices. In addition to this magnetic antidots [26-27] have also been considered as a candidate for ultrahigh density data storage devices, so that the memory bit could be trapped between consecutive holes along the intrinsic hard axis of the antidot nanostructure.

In micro- and nanoscale ferromagnetic disks when the aspect ratio defined by thickness/diameter is much less than one, and both thickness and diameter exceed the exchange length of that material, an in-plane flux closed non-uniform ground state of magnetization is formed which is known as magnetic vortex [28-29]. At the centre of the ferromagnetic circular disk, due to exchange interaction the direction of the magnetization is out of plane creating the vortex core with a distinct polarity [30], either ‘up’ or ‘down’ and the sense of flux closed magnetization structure represents the chirality of the vortex. Magnetic vortices can be used in magnetic data storage [31], magnetic random access memory [32-33], magnetic logic circuitry [34] and information processing devices [34] among many other applications.

Present electronic systems suffer from problem of huge power loss due to Joule heating as it is associated with the translational motion of the electron. Therefore, it is important to develop particle-less technologies for data transport and processing. This leads us to magnonics [35-37], a rapidly evolving sub-field of magnetism which mainly deals with magnon based data operation and related aspects of SW dynamics. The aim of this field is to control and manipulate SWs in ferromagnetic material by changing various physical and geometrical parameters such as material [38-39], shape [40-41], size, lattice constant [42],

lattice symmetry [43] as well as magnitude and orientation of external bias magnetic field [44-45]. Depending upon the wavelength of SWs ($k = 2\pi/\lambda$) mainly two types of SWs namely exchange dominated SWs and dipolar dominated SWs are observed. The exchange dominated SWs are observed if the wavelength of the SWs are much shorter than the exchange length ($l_{ex} = (2A/(\mu_0 M^2))^{1/2}$) whereas the wavelength of dipolar dominated SWs are much greater than l_{ex} . SWs with intermediate wavelength are known as dipole-exchange SWs. The frequency and the damping of exchange dominated SWs are very high as compared to dipolar dominated SWs. Also, propagation velocities of dipolar dominated and dipole-exchange SWs are higher. As a result, dipolar dominated SWs are mainly used to carry the information in the form of energy and momentum. In addition to this, the dipolar dominated magnetostatic surface SW shows non-reciprocal behavior. Depending upon this SW nonreciprocity, spin based logic devices operating in GHz range with low power dissipation is proposed [46]. In SW logic devices [47-50] information or data is coded into magnon phase or density and processed using the wave effects such as interference. In SW logic gates, the magnon phase is manipulated by the application of direct current electric pulse whereas the output is carried by the magnon themselves. For combining two gates additional magnon to voltage converter is required. To overcome this problem all magnon based logic operations are proposed [51] which is based on magnon transistor where the information will be carried and processed by the magnons rather than electrons. The main advantage of this type of magnon based logic gate is that the output signal of one gate can be directly sent as an input signal to the next logic gate for designing complicated logic gates such as XOR and NAND gate. In addition to magnon transistor, the other important components of an integrated magnonic circuit [52] are a SW source, a channel for longer propagation of SW and a SW detector. Nano-contact spin torque nano oscillator (STNO) [52-55] act as a nanoscale source of localized and propagating SWs and magnonic waveguide is used to transmit the SWs and SWs can be detected by probing optically [56], electrically [57] or by inductive [58] method. But the main challenge in the development of this type of SW based magnonic devices is the anisotropic dispersion [59-60] relation of SWs. This means that the energy of SWs significantly depends upon the angle between the propagation direction and orientation of magnetization. As a result, in a homogeneous isotropic magnetic medium exposed to uniform external magnetic field, the SWs will travel

along a preferred direction with respect to the magnetization orientation. This problem can be avoided by exciting the SWs using local Oersted field instead of external bias field. Microstructured SW multiplexer [61] which is a building block of magnon based logic is demonstrated where locally generated Oersted field is used to manipulate the path of SW propagation. In addition to this, to propagate the SWs over significantly larger distance, loss-less propagation of SWs in a magnetic medium are required. The possible way to minimize the loss of SWs is by choosing suitable material with very low Gilbert damping like Yttrium iron garnet [62] or Heusler [63-64] alloys. The damping of SWs in a material can be modulated by introducing different capping layers like Au, Cr, Pd and Pt or by introducing different dopants like Cr [65-66], Au [66] and Tb [67]. SWs can also be generated by injecting spin polarized current generated by spin Hall effect (SHE) [68-72], spin pumping effect [73-74], spin-Seebeck effect (SSE) [75-76], lateral spin valve [77]. This spin polarized current has many advantages over the conventional charge current like no stray Oersted fields as there is no net flow of charge, minimum power dissipation and tunable damping of SWs by which one can achieve loss-less propagation of SWs in magnetic media. Hence the existing technology of electronic data storage devices which are currently driven by charge current can be replaced by a new technology named spintronics which solely deals with the spin degrees of freedom of an electron. The most challenging spintronic device is spin field effect transistor (SFET) proposed by Datta-Das [78] but the major drawback of this transistor is lack of current gain. To remove this problem there is also a proposal of spin torque transistor (STT) [79-80] which is based on the current induced spin transfer torque. But the main disadvantage of this transistor is that there is a stand by current similar to the leakage current in a bipolar junction transistor (BJT) which depends on the quality of the magnetic film used in the system and the demands on the response time. There is also a proposal that a sequence of three vortex chain act as a magnetic vortex based transistor [81] which has a potential to work as a stable BJT. Other key magnonic components currently demonstrated are magnonic waveguides [82], filters [83], splitters, phase shifters [84], SW emitters [11], SW amplifier and SW interferometer.

In addition to this, SWs in MCs exhibits both classical and quantum mechanical properties like reflection [85-87], refraction [85, 87], interference [88-90], quantization [91],

Chapter1

diffraction [90], self-focusing [92], Doppler effect [93] and tunneling [94-95]. As a result, both quasistatic and ultrafast magnetization dynamics of 1D or 2D MCs have attracted much attention. Among many of the interesting magnetic properties, magnetic anisotropy receives particular attention for technological importance. Magnetic anisotropy primarily originates due to the violation of spin-orbit angular momentum with respect to the rotation of magnetization direction. The finite dimensions of elements in MCs further modify the effective anisotropy by introducing additional complications. The magnetization at the edges of a confined magnetic element deviates from the external field direction to minimize the magnetic energies. These regions are known as the demagnetized regions. Consequently, the average magnetization and the internal magnetic field changes with the rotation of the azimuthal angle of the external bias field. This is known as intrinsic configurational anisotropy [15, 96-97]. The effective magnetic field inside an element within an array is also modified due to the stray magnetic fields from the neighboring elements. Tailoring of this field by rotating the bias field angle with respect to the symmetry axes of the array leads to the concepts of extrinsic configurational anisotropy [98]. For various applications of magnetic nanostructures of different length scales, it is important to study this configurational magnetic anisotropy corresponding to the magnetization dynamics over a broad time scale. This includes slower processes such as magnetization reversal, domain wall dynamics and magnetic vortex dynamics to faster processes such as magnetization precession, and Gilbert damping.

The goal of this thesis is to investigate magnetization processes over various time scales starting from quasistatic processes such as magnetic hysteresis to domain dynamics occurring in micro and nanoseconds and finally the ultrafast processes such as magnetization precession occurring at the picoseconds and ultrafast demagnetization occurring at femtosecond time scales. We will investigate the magnetization dynamics of magnetostatically coupled Ni₈₀Fe₂₀ (Permalloy or Py) nanodot lattices by varying the lattice symmetry, which will in turn affect the magnetic stray field distributions as well as the configurational magnetic anisotropy of the systems. Moving to a micrometer length scale, we will also investigate the tunability of magnetization dynamics in Py elliptical dots, Py/Co bi-component MCs, and Py nanostirpes using time-resolved magneto-optical Kerr

Chapter1

effect microscopy (TR-MOKE) and micromagnetic simulation. In addition to this we will also study the vortex core gyration of a magnetostatically coupled Py disks which shows transistor like operations using micromagnetic simulations.

The quasistatic and ultrafast magnetization dynamics of magnetic nanostructures are different from their bulk counterparts and continuous thin films. The magnetization dynamics of magnetic nanostructures strongly depends upon their intrinsic material properties such as exchange stiffness constant (A), saturation magnetization (M), Gilbert damping (α) and magnetocrystalline anisotropy (K). As a result invention of new material properties is important. This may not always be possible to achieve in a single material in the bulk or thin film form. Instead, structuring of known materials in one-, two-, and three-dimensions at various length scales and exploiting dynamical magnetic properties over various time scales may potentially offer the desirable material properties. But the key challenge is to fabricate high quality ordered arrays of patterned nanomagnets with narrow size dispersion and in an ordered array over a macroscopic length scale. The patterning of the structures can be done by using different kinds of lithography techniques such as photolithography [99], electron beam lithography (EBL) [100], X-ray lithography [101], interference or holographic lithography (IL) [102], deep ultraviolet lithography (DUV) [103], nanoimprint lithography (NIL) [104] and ion beam lithography (IBL) [38]. The deposition of the material (magnetic or non-magnetic) is mainly done by using magnetron sputtering and electron beam evaporation techniques. Self aligned shadow deposition [105], laser irradiation [106], ion implantation, molecular beam epitaxy (MBE), pulsed laser deposition (PLD) are also very popular techniques for fabricating nanostructures and thin films. On the other hand, many chemical methods like reduction, nonhydrolytic sol-gel and thermal decomposition process are used to synthesize nanoparticles. Electrodeposition [107] through nanoporous anodized alumina template [108] or poly carbonate track etched template [109] is also a very efficient and cost effective method to produce large scale magnetic nanowires with very high aspect ratio.

The crystal structure, surface morphology and the chemical purity of the nanostructures can be characterized by using X-ray diffraction (XRD), scanning electron microscopy (SEM), atomic force microscopy (AFM) and energy dispersive x-ray spectroscopy (EDX). To study

the static and quasistatic magnetic properties of the nanomagnets various techniques like magnetic force microscopy (MFM) [110-111], magneto-optical Kerr effect magnetometry (MOKE) [112] and vibrating sample magnetometry (VSM) etc. have been introduced. To investigate the magnetization dynamics different kinds of techniques are developed. Ferromagnetic resonance (FMR) [113] with a vector network analyzer (VNA) [114] is very efficient frequency domain technique to measure the high frequency magnetic response from MHz to GHz regime but the spatial resolution of FMR technique is very poor. To overcome this problem the spatially resolved FMR technique is developed. Spin-torque induced FMR (ST-FMR) [115] is another special type of FMR technique which is mainly used to measure the SHE or SW non-reciprocity effect. Another very useful technique to study SWs in wave-vector domain is Brillouin light scattering (BLS) technique [116]. This technique is used to measure dispersion relation (frequency vs. wavevector) of SWs in MCs. Recently space-resolved and time-resolved BLS techniques have been developed which can also be used to probe magnetization dynamics with sub- μm spatial resolution and few ns temporal resolution [117]. Pulse inductive microwave magnetometry (PIMM) [118] is one type of time domain technique with a temporal resolution of tens of picoseconds. The best spatio-temporal resolution is obtained from time-resolved magneto optical Kerr effect microscope (TR-MOKE) [119]. This technique offers time resolution of sub hundred of femtosecond and it is used to probe the femtosecond magnetization dynamics of a ferromagnetic material very efficiently. The time-resolved scanning Kerr microscope (TRSkm) [96] is also developed to image the time evolution of propagation of magnetostatic SWs in magnetic nanostructure. All-optical TR-MOKE [120] and field pumped TR-MOKE [121] are two special types of TR-MOKE techniques. In case of all optical TR-MOKE, all optical excitation and detection technique is used whereas in field pumped TR-MOKE, excitation is usually done by using picoseconds pulse generator and detection is done by using picoseconds/femtosecond laser pulse. The ultrafast demagnetization occurring within sub-ps, relaxations occurring within few ps to hundreds of ps and precession of magnetization and damping occurring within few ns can be measured using the former technique. In contrary the latter technique can only excite and probe magnetization precession, damping and other slower dynamics such as gyration of magnetic vortex core and domain wall dynamics upto time delays of about 40 ns. In this

Chapter1

thesis, the first technique *i.e.*, all optical TR-MOKE technique is used to measure the collective magnetization dynamics of magnetic nanostructures.

2. Theoretical Background

2.1 Introduction:

Any material if placed in a magnetic field H , acquires some magnetic moment. The principal sources of this magnetic moment are the spin and orbital angular momentum and the change in the orbital angular moment induced by the applied magnetic field. Depending upon these origins of magnetic moment mainly three types of magnetism are possible namely, diamagnetism, paramagnetism and ferromagnetism. In case of diamagnetism the third source is mainly responsible whereas the first two sources are responsible for other types of magnetism.

The magnetic moment per unit volume is defined as magnetization (M). The magnetization M is proportional to H and it can be written as [122-123]

$$M = \chi H \quad (2.1)$$

here, χ is known as magnetic susceptibility of the material.

In case of diamagnetic material, the diamagnetic susceptibility, χ_d is negative and it is independent of temperature whereas for paramagnetic material, χ_p is independent of the magnetic field but it inversely varies with temperature as shown below

$$\chi_p = \frac{C}{T} \quad (2.2)$$

here,

$$C = \frac{Ng^2 J(J+1)\mu_B^2}{3k_B} \quad (2.3).$$

In case of ferromagnetism spontaneous magnetic moment is observed even at zero applied magnetic field. The existence of spontaneous moments suggests that the electron spin and

magnetic moments are arranged in a regular manner. The ferromagnetic susceptibility can be expressed as

$$\chi_f = \frac{C}{T - T_c} \quad (2.4)$$

where, T_c is the Curie temperature below which all ferromagnetic material exhibits spontaneous magnetization.

Ferromagnets possess many interesting properties like ultrafast demagnetization occurring in femtosecond range, remagnetization in low picoseconds range, precessional dynamics varying over a broad range of time scale. This includes slower processes such as magnetization reversal, domain wall dynamics and magnetic vortex dynamics to faster processes such as magnetization precession, and Gilbert damping. It is very challenging to explore different quasistatic and dynamic magnetic properties of ferromagnets using ultrafast optical microscopy.

2.2 Magnetic Anisotropy:

According to non-relativistic quantum mechanics, the free energy of a ferromagnetic system is independent of magnetization direction *i.e.*, the magnetization should be isotropic in nature but experimentally it is observed that magnetization can be easily aligned along some preferential direction with respect to the crystallographic axis or to the shape of the body. This property is known as magnetic anisotropy. The directions along which magnetization lie easily are known as easy axes of magnetization and the axes along which it is most difficult to produce saturation are called the hard axes of magnetization. There are mainly two microscopic sources for magnetic anisotropy [123-125]. They are

- a) the dipole-dipole interaction.

$$H_{dd} = \frac{1}{4\pi\epsilon_0} \frac{1}{R_{ij}^3} \left[S_i \cdot S_j - \frac{3}{R_{ij}^3} (S_i \cdot R_{ij})(S_j \cdot R_{ij}) \right] \quad (2.5)$$

- b) the spin-orbit coupling.

$$H_{LS} = -\lambda(L_i \cdot S_i) \quad (2.6)$$

Let us consider, for a ferromagnetic material the magnetization (M) can be expressed as:

$$M = m\Omega_M \quad (2.7)$$

where, m is the magnitude of magnetization and Ω_M is the unit vector of magnetization. Ω_M can be expressed by its components $(\alpha_1, \alpha_2, \alpha_3)$ where $\alpha_1^2 + \alpha_2^2 + \alpha_3^2 = 1$.

At below Curie temperature, the free energy density (F) can be expressed as

$$F = F(T, M, \Omega_M, \varepsilon) \quad (2.8)$$

where, T and ε are the temperature and the strain tensor, respectively. Under some approximation the thermodynamic potential or the anisotropy energy can be expressed only as a function of Ω_M .

I. Magnetocrystalline Anisotropy:

Due to the spin-orbit interaction, the spins prefer to align along some well defined crystallographic axes. This is known as magnetocrystalline anisotropy. This is the intrinsic property of the material.

The magnetocrystalline anisotropy energy (G_{cryst}) can be expanded in successive powers of components $(\alpha_1, \alpha_2, \alpha_3)$ of Ω_M

$$G_{cryst}(\Omega_M) = b_0(H_M) + \sum_{ij} b_{ij}(H_M) \alpha_i \alpha_j + \sum_{ijkl} b_{ijkl}(H_M) \alpha_i \alpha_j \alpha_k \alpha_l + \dots \quad (2.9)$$

here, H_M is the projection of external field along the direction of Ω_M .

a. Uniaxial Anisotropy:

For hexagonal crystal, the magnetocrystalline anisotropy energy is a function of angle between c -axis and the direction of magnetization (θ). The anisotropy energy is symmetric with respect to the ab -plane. The expression for anisotropy energy for *hcp* structure is

$$G_{crys}(\Omega_M) = K_0 + K_1 \sin^2 \theta + K_2 \sin^4 \theta + (K_3 + K'_3 \cos 6\phi) \sin_6 \theta + \dots \quad (2.10)$$

where, θ and ϕ are the angle between magnetization and c -axis or a -axis, respectively as shown in Fig. 2.1(a) and K_1, K_2 etc. are the constants which depends on temperature.

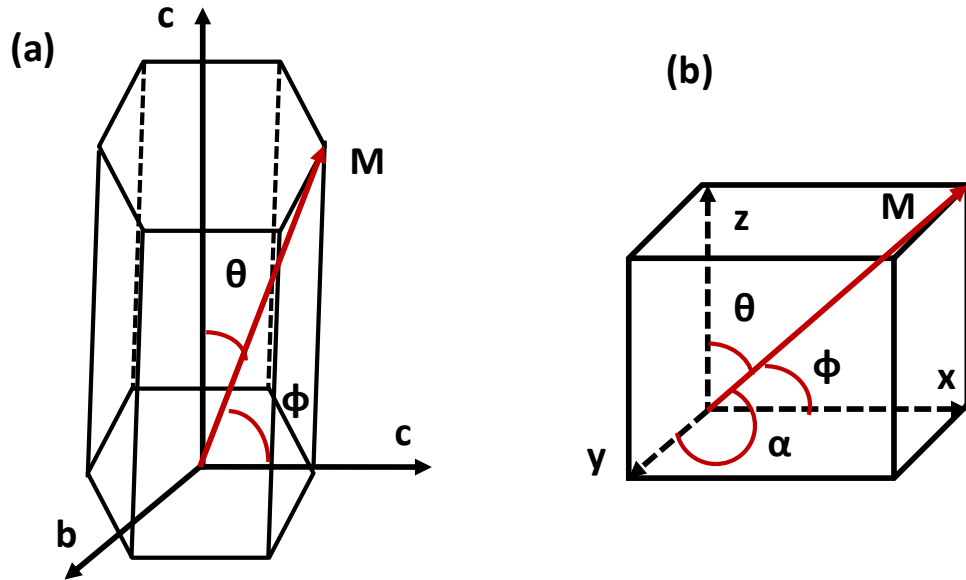


Fig. 2.1 Coordinate system for (a) uniaxial hexagonal closed packed system and (b) cubic system.

b. Cubic Anisotropy:

For cubic crystals, x -, y - and z -axis are the crystallographic axes and the expression for cubic anisotropy energy will be

$$\begin{aligned} G_{crys}(\Omega_M) &= K_0 + K_1(\alpha_1^2 \alpha_2^2 + \alpha_3^2 \alpha_2^2 + \alpha_1^2 \alpha_3^2) + K_2 \alpha_1^2 \alpha_2^2 \alpha_3^2 \\ &+ K_1(\alpha_1^2 \alpha_2^2 + \alpha_3^2 \alpha_2^2 + \alpha_1^2 \alpha_3^2)^2 + \dots \end{aligned} \quad (2.11)$$

here, the magnetization vector (M) made angle ϕ , α and θ with x -, y - and z -axis, respectively as shown in Fig. 2.1(b) and α_1, α_2 and α_3 are the direction cosines along x, y and z direction. For $K_1 > 0$, the easy axes are along (100) plane and for $K_1 < 0$, the easy axes are along (111) plane.

II. Shape Anisotropy:

When the anisotropy energy depends upon the orientation of Ω_M of magnetization with respect to the external shape of the sample, then it is known as the shape anisotropy. Shape anisotropy is an extrinsic contribution which completely depends upon the geometry of the sample. The origin of shape anisotropy is the long range dipole-dipole interaction or the magnetostatic interaction which senses the outer shape of the sample.

The magentostatic energy of a uniformly magnetized (M) ferromagnetic material can be expressed as

$$E_d = -\frac{1}{2} \mu_0 \int_{sample} M \cdot H_d d^3 r \quad (2.12)$$

here H_d is the interaction field on one dipole created by the other dipoles.

The field inside (H_{in}) a uniformly magnetized ellipsoid can be written as

$$H_{in} = -N \cdot M \quad (2.13)$$

here, M is parallel to one of the principal axes of the ellipsoid and N is the demagnetizing factor with components (N_x, N_y, N_z) along x, y , and z axes of the ellipsoid such that

$$N_x + N_y + N_z = 1 \quad (2.14)$$

If there is an external applied field (H_{ex}), the resultant field (H) will be the vector sum of H_{ex} and H_{in} .

$$H = H_{ex} + H_{in} \quad (2.15)$$

Substituting Eqn. (2.13) in (2.12), the magnetostatic energy of a uniformly magnetized ellipsoid of volume V can be written as

$$E_d = \frac{1}{2} \mu_0 V (N_x M_x^2 + N_y M_y^2 + N_z M_z^2) \quad (2.16)$$

This is the expression for shape anisotropy energy.

III. Configurational Anisotropy:

According to Brown's fundamental theorem as the length scale of a magnetic particle is reduced, there comes a point at which the competition between exchange energy and the magnetostatic energy requires that a uniform magnetization should be adopted. But for non ellipsoidal element this theorem is not valid. The term 'uniform magnetization' can be replaced by 'nearly-uniform magnetization' for non ellipsoidal element. This small deviation of static magnetization from the uniformly magnetized state results in a strong anisotropy with symmetry corresponds to the shape of the nanoelement. In 1988, Schabes and Bertram identified this as configurational magnetic anisotropy [98].

a. Intrinsic Configurational Anisotropy:

In 1998, Cowburn *et al.* showed [126] that mainly two types of single domain magnetization states namely "flower" and "leaf" states are possible for square planer sample. For a single domain square element there is no in-plane shape anisotropy. But as shown in Fig. 2.2 (a) as the in-plane angle (ϕ) of the external bias field (H) changes leaf state and flower state is observed for a single domain square element. There is an energy difference between leaf and flower states due to the non-uniformity of the magnetization distribution within the near single domain state. This energy difference of an isolated element is referred to as intrinsic configurational anisotropy.

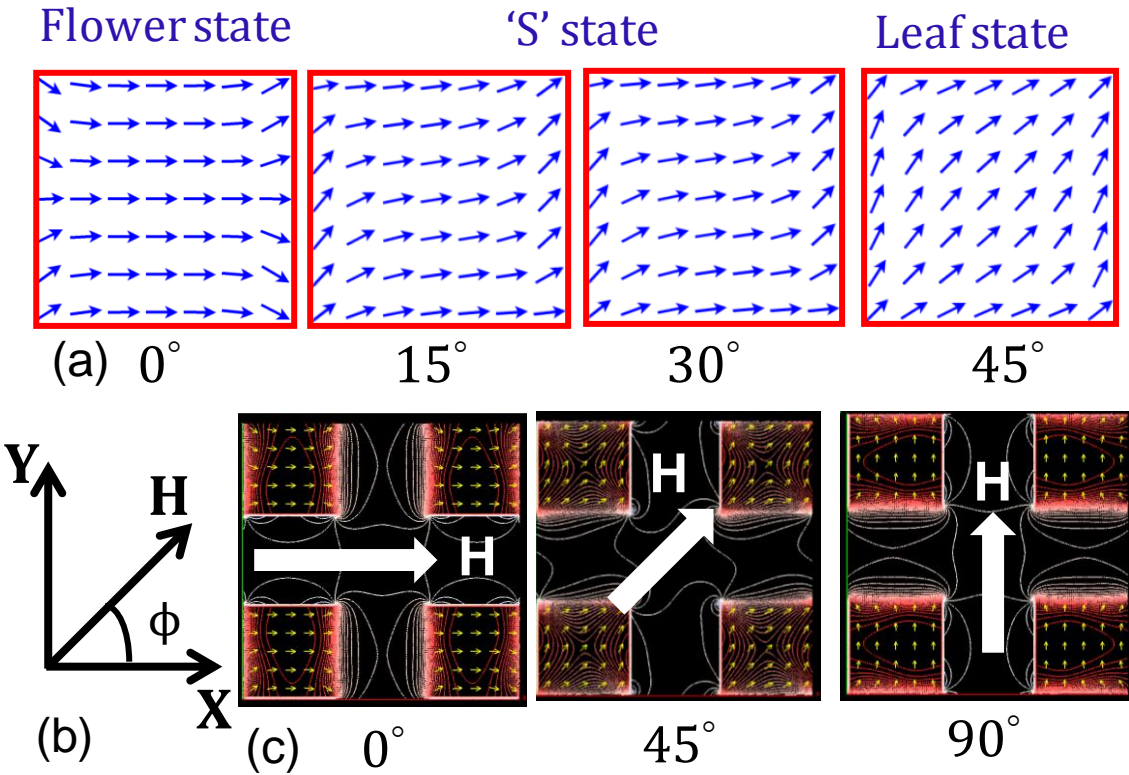


Fig. 2.2 (a) Simulated static magnetization states are shown for a single 200 nm square dot of thickness (t) = 20 nm at a bias field of 1.15 kOe applied at different azimuthal angles (ϕ). (b) The geometry of the applied bias field is shown. (c) Simulated magnetostatic stray field distributions are shown for an array of 200 nm square dot of thickness (t) = 20 nm and interdot separation (s) = 100 nm at a bias field of 1.15 kOe applied at different azimuthal angles (ϕ).

b. Extrinsic Configurational Anisotropy:

Magnetostatically unsaturated regions situated near the edges of an element vary with the in plane angle (ϕ) of the external bias magnetic field (H). The schematic of the geometry of applied magnetic field is shown in Fig 2.2(b). As a result, the magnetostatic interaction between the elements also changes which will in turn affect the magnetic stray field distributions as well as the configurational magnetic anisotropy of the array as shown in Fig. 2.2(c). This can be referred to as extrinsic configurational anisotropy.

IV. Surface Anisotropy:

In 1954, Neel pointed out that the spins at the surface has a nearest neighbor on one side and none on the other side and as a result the exchange energy will not be the same as the bulk. Surface anisotropy arises due to this reduced symmetry of a ferromagnetic surface. The surface anisotropy is a geometrical feature that depends upon the shape of the sample. The expression for surface anisotropy is

$$E_s = \frac{1}{2} K_s \int (n \cdot \Omega(M))^2 ds \quad (2.17)$$

here, n is the unit vector parallel to the normal pointing out of the surface and K_s is a coefficient which should be taken from experiment. It can also be assumed that surface anisotropy caused by the reduced symmetry of the spin orbit interaction at the surface. The surface anisotropy energy depends upon the angle between the magnetization at the surface and the crystallographic axes of the material.

V. Exchange Anisotropy:

Exchange anisotropy [127-128] or exchange bias is the result of an interfacial exchange interaction between a ferromagnetic (FM) and antiferromagnetic (AFM) material. In a FM/AFM bilayer system, at $T_N < T < T_C$ all spins in FM layer is aligned along the applied magnetic field (H) direction, whereas all the spins in AFM layer is randomly oriented. As $T < T_N$, in the presence of H the spins in AFM at the FM/ AFM interface aligned along the direction of the spins in FM layer due to exchange interaction. The rest of the spins in AFM layer arrange themselves according to AFM ordering. Now if we reverse the H , the spins in FM layer start to rotate but the spins in AFM layer do not rotate due to strong exchange anisotropy. But the spins in FM layer tries to align along the direction of the spins in AFM at the interface due to the interfacial exchange interaction. Thus the FM layer only has one stable configuration *i.e.*, the anisotropy is unidirectional. To fully rotate the spins in FM layer in a FM/AFM bilayer system larger H is required as compared to bare FM system with same thickness. The hysteresis loop also shifted in the field axis due to the presence of an extra internal biasing field.

2.3 Magnetization Dynamics:

2.3.1 Magnetization Precession:

According to quantum mechanics the equation of motion of a spin (S) is given by [129-130]

$$i\hbar \frac{d}{dt} \langle S \rangle = [S, H] \quad (2.18)$$

The Hamiltonian operator H which can be described as the interaction between the spin (S) and external field (B) is

$$H = -\frac{g\mu_B}{\hbar} (S \cdot B) \quad (2.19)$$

where μ_B is the Bohr magneton and g is the gyromagnetic factor for a free electron. The Z-component of the commutator relation in Eqn. (2.18) can be expressed as

$$[S_z, H] = ig\mu_B (S \times B)_z \quad (2.20)$$

Substituting Eqn. (2.20) in Eqn. (2.18) we can write

$$i\hbar \frac{d}{dt} \langle S \rangle = ig\mu_B (S \times B) \quad (2.21)$$

This is the spin equation of motion for a single spin. For homogeneous magnetization (M) we can write

$$M = \frac{g\mu_B}{\hbar} \langle S \rangle \quad (2.22)$$

and,

$$B = \mu_0 H_{\text{Eff}} \quad (2.23)$$

Substituting Eqn. (2.22) and (2.23) in Eqn. (2.21) we will get

$$\frac{d}{dt} M = -\gamma\mu_0 (M \times H_{\text{Eff}}) \quad (2.24)$$

where gyromagnetic ratio, $\gamma = g\mu_B/\hbar$. This is the Landau-Lifshitz (LL) equation of motion of magnetization in presence of an external magnetic field H . This equation states that at equilibrium the magnetization presses around the effective magnetic field (H_{Eff}) for infinitely long time.

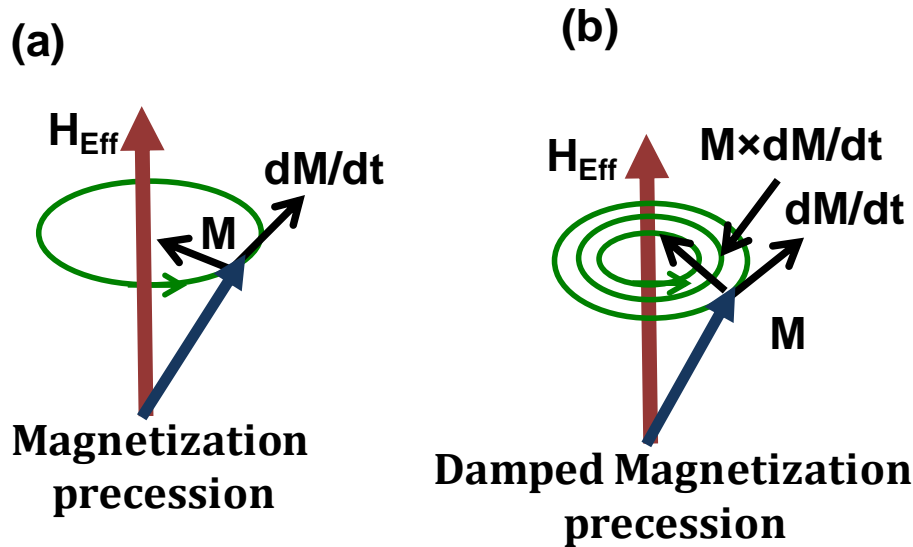


Fig. 2.3 Magnetization precession (a) without damping and (b) with damping.

2.3.2 Magnetic Damping:

Experimentally it is observed that the amplitude of magnetization is gradually reduced until the magnetization is aligned along the direction of external magnetic bias field (H). Gilbert first introduces the damping term in LL equation to match the experimental observation.

The equation of motion of magnetization in presence of damping is

$$\frac{d}{dt}M = -\gamma\mu_0(M \times H_{Eff}) + \frac{\alpha}{M}(M \times \frac{dM}{dt}) \quad (2.25)$$

This is known as the famous Landau-Lifshitz-Gilbert (LLG) Equation. Here α is the Gilbert damping parameter. The values of α for Nickel (Ni), Cobalt (Co), Iron (Fe) Heusler alloy, and Ni₈₀Fe₂₀ (Permalloy) are about 0.064, 0.0019, 0.01, 0.003 and 0.008 respectively.

2.3.3 Energies of a Ferromagnet:

The total free energy (E_{total}) of a ferromagnetic material in presence of an external magnetic field can be expressed as

$$E_{total} = E_e + E_d + E_Z + E_K \quad (2.26)$$

here E_e is the exchange energy, E_d is the magnetostatic self energy, E_Z is the Zeeman energy and E_K is the magnetocrystalline anisotropy energy.

I. Exchange energy:

The tendency of spins is to align themselves in parallel or antiparallel to each other is known as exchange interaction. The expression for Heisenberg Hamiltonian for exchange energy can be evaluated as

$$E_e = -\sum_{i,j} J_{ij} S_i \cdot S_j \quad (2.27)$$

where J_{ij} is the exchange integral and S_i and S_j is the spin operator of i^{th} and j^{th} spin. Exchange energy depends upon the nearest neighbour interaction *i.e.*, it is a short range interaction.

$J_{ij} = +1$ for parallel arrangement of the spin *i.e.*, for ferromagnetic arrangement.

$J_{ij} = -1$ for antiparallel arrangement of the spin *i.e.*, for antiferromagnet arrangement.

Considering continuum model, the exchange energy can be expressed as

$$E_e = A \int_V (\nabla m)^2 d^3 r \quad (2.28)$$

where, $m = M/M_s$ is the ratio of magnetization to the saturation magnetization. The summation in Eqn. (2.27) is replaced by the integral over the ferromagnetic material considering m as a continuously defined vector quantity and A is the exchange stiffness coefficient given by

$$A = \frac{2JS^2}{a} \quad (2.29)$$

here, a is the lattice constant. The value of A for Ni, Co, Fe and Py are 9×10^{-12} J/m, 30×10^{-12} J/m, 21×10^{-12} J/m, and 13×10^{-12} J/m respectively.

II. Magnetostatic Self Energy:

Magnetostatic self energy in a ferromagnetic material originates due to the classical interaction between the magnetic dipoles. This energy is also known as demagnetization field energy or shape anisotropy energy. The demagnetizing energy can be expressed as

$$E_d = -\frac{1}{2} H_d \cdot M \quad (2.30)$$

Where, H_d is the demagnetizing field which can be expressed as

$$H_d = -N_d \cdot M \quad (2.31)$$

here, N_d is the demagnetizing factor.

In continuum limit, the demagnetizing field can be expressed as

$$E_d = -\frac{1}{2} \mu_0 \int_{sample} M \cdot H_d d^3 r \quad (2.32)$$

Magnetostatic self energy depends upon the entire sample *i.e.*, it is a long range interaction. The magnetostatic self energy is proportional to the saturation magnetization M but in case of exchange energy scales with the exchange stiffness constant A .

III. Zeeman Energy:

Zeeman energy (E_z) is the interaction between the magnetization (M) and external field (H). The expression for Zeeman energy is

$$E_z = - \int_v M \cdot H d^3 r \quad (2.33)$$

IV. Magnetocrystalline Anisotropy Energy:

Experimentally it is observed that though the Heisenberg exchange energy is isotropic, but the magnetization of ferromagnetic material tends to lie along some crystallographic axes due to spin orbit coupling which is known as magnetocrystalline anisotropy as we discussed in section 2.2.1

For hexagonal closed packed (*hcp*) crystal, the expression for uniaxial magnetocrystalline anisotropy energy is

$$E_K = K_1 \sin^2 \theta + K_2 \sin^4 \theta \quad (2.34)$$

here θ is the angle made by the magnetization with c-axis for *hcp* crystal.

For cubic crystal, the expression for cubic anisotropy energy is

$$E_K = K'_1 (\alpha_1^2 \alpha_2^2 + \alpha_3^2 \alpha_2^2 + \alpha_1^2 \alpha_3^2) + K'_2 \alpha_1^2 \alpha_2^2 \alpha_3^2 \quad (2.35)$$

here, α_1, α_2 and α_3 are the direction cosines.

2.3.4 Time Scales of Magnetization:

Magnetization dynamics can occur over a broad range of time scale. Figure 2.4 shows several magnetization dynamic phenomena at the relevant time scales ranging from 1 fs to a few hundred nanoseconds (μs).

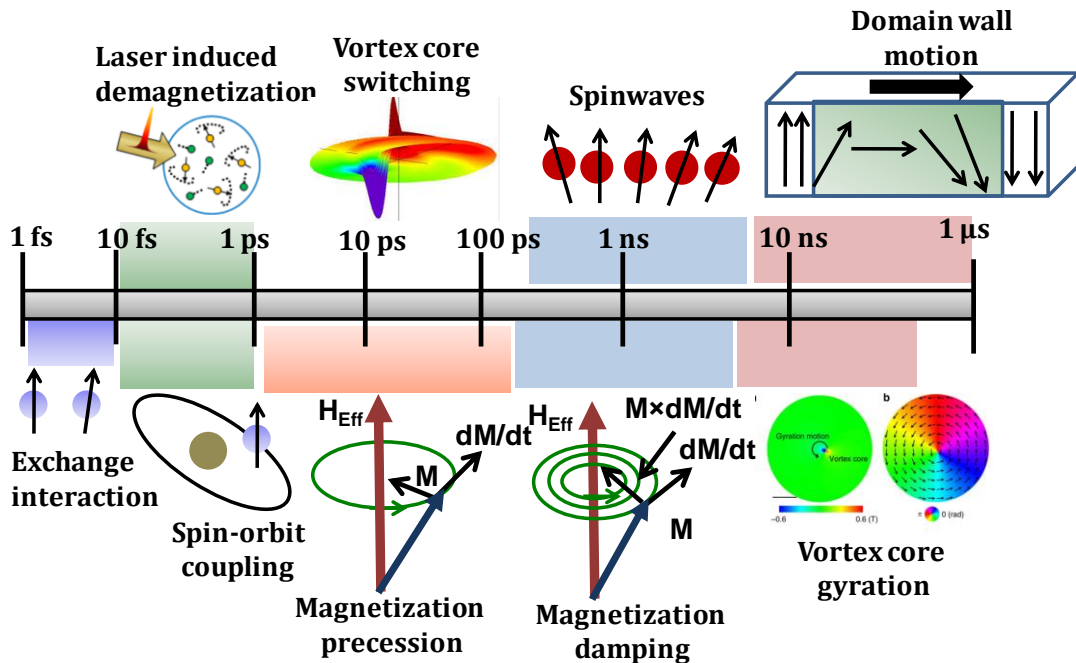


Fig. 2.4 Characteristic time scale of various magnetization dynamics.

The fastest process is the exchange interaction which occurs from 1 to 10 fs. The spin orbit coupling occurs from 10 fs to 1 ps. The ultrafast demagnetization occurs within hundreds of fs. Following the ultrafast demagnetization, a fast remagnetization occurs within 1ps to 10 ps. Magnetization precession is observed in few ps to few hundred of ps time scale and Gilbert damping associated with it occurs within 1 ns to few tens of ns time scale. The slowest magnetization processes are the vortex core gyration and domain wall dynamics which occur within 10 to 100 ns.

2.3.5 Laser Induced Ultrafast Demagnetization:

When a femtosecond laser pulse is incident on an ordered ferromagnetic material, the photon field of the laser beams interacts with the spin degrees of freedom. The angular momentum of the light gets nonlinearly modified and during the thermalization of charges and spins, the electronic wavefunction loses its phase memory (incoherent process) with respect to the excitation, which leads to the demagnetization of the ferromagnet. The exact physical mechanism for the demagnetization process is still a topic of debate. However, some proposed [131-134] mechanisms are the excitation of Stoner pair, spin – orbit

coupling, the coupling with the electromagnetic field via a terahertz emission [135], spin flip scattering including Elliott-Yafet type of scattering [134] , super diffusive spin transport [136-137], electron-magnon spin-flip scattering and Coulomb exchange spin-flip scattering [138]. After demagnetization the electronic charges and spins start to relax, which can be described by a three temperature model [131, 139]. The hot electrons and spins exchange energy with the lattice and this is mediated by the electron - phonon interaction. By exchanging energy, spin system comes to an equilibrium temperature with the charge and lattice systems. Therefore, the lattice temperature also changes. The magnetocrystalline anisotropy and magnetization (M), which are functions of lattice temperature, also change rapidly. This rapid change in magnetocrystalline anisotropy or the shape anisotropy ($4\pi M$) acts as an internal pulsed field and triggers the precession of magnetization.

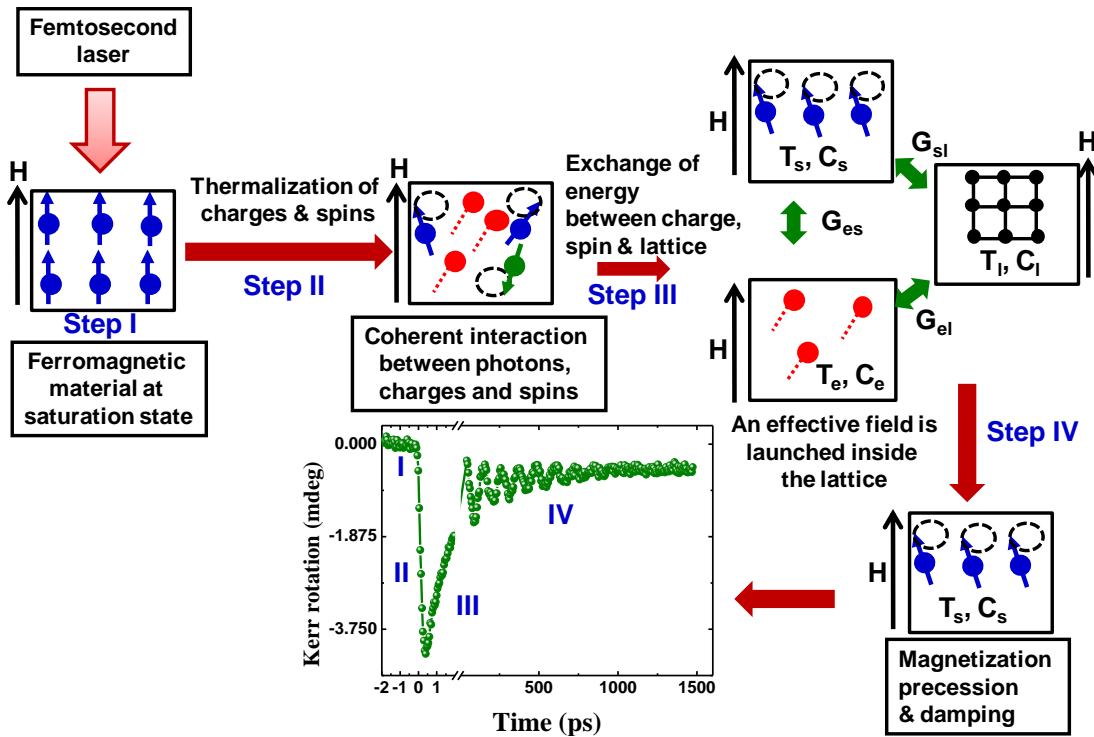


Fig. 2.5 Schematic representation of ultrafast magnetization dynamics based upon three temperature model.

I. Three Temperature Model (3TM):

In 1996, Beaurepaire *et al.* first observed [131] the ultrafast demagnetization in a Nickel (Ni) film after excitation with a 60 fs laser pulse. They explain their observations phenomenologically by three temperature model (3TM). According to this theory, there exist three thermalized reservoirs that exchange energy, namely, the electron system at temperature T_e , the spin system at temperature T_s and the lattice system at temperature T_l . The initial hot electrons induce the spin dynamics associated with spin temperature T_s which leads to the ultrafast demagnetization. The temporal evolution of the system can be described by three coupled differential equations. They are

$$C_e(T_e) \frac{dT_e}{dt} = -g_{el}(T_e - T_l) - g_{es}(T_e - T_s) + p(t) \quad (2.36)$$

$$C_s(T_s) \frac{dT_s}{dt} = -g_{es}(T_s - T_e) - g_{sl}(T_s - T_l) \quad (2.37)$$

$$C_l(T_l) \frac{dT_l}{dt} = -g_{el}(T_l - T_e) - g_{sl}(T_l - T_s) \quad (2.38)$$

here, C_e , C_s and C_l are electronic, magnetic (spin) and lattice contribution to specific heat, respectively and g_{el} , g_{es} and g_{sl} are the electron-lattice, electron-spin and spin-lattice interaction constants. $P(t)$ is the laser source term. This model described that there are heat transfers between three coupled baths namely electron, spin and lattice and in sub picoseconds temporal regime the main interactions are electron-spin and electron-lattice type.

II. Spin Orbit Coupling (SOC):

In 2000, Zhang *et al.* proposed [140] that the ultrafast demagnetization is a cooperative effect of the external laser field and internal spin orbit coupling (SOC). The external laser field cannot change the magnetic spin moment in fs time scale if there is no spin orbit coupling. On the other hand without laser field spin orbit coupling cannot change the magnetic moment. It is concluded that the laser induced demagnetization is occurred via spin orbit coupling.

III. Elliot-Yafet Type Spin Flip Scattering:

In 2005, Koopmans *et al.* proposed [134] that phonon mediated spin flip scattering is responsible for ultrafast demagnetization. They introduced a Hamiltonian inspired by Elliot-Yafet (EY) type of (quasi) elastic spin flip scattering by electron interacting with impurities, mainly phonons. The scattering process is associated with the spin orbit interaction that transfers the angular momentum between the electron and lattice.

The Hamiltonian can be written as

$$H = H_e + H_s + H_{ee} + H_{si} \quad (2.39)$$

here, H_e , H_s , H_{ee} and H_{si} represent electron Hamiltonian, spin Hamiltonian, screened Coulomb interaction Hamiltonian and spin flip interaction Hamiltonian, respectively.

When a laser beam incidents on a ferromagnetic material laser excitation enhanced the electron temperature but the temperature of the spin system initially remains unaffected. The imbalance of spin up and spin down scattering occurs due to this nonequilibrium situation which leads towards the ultrafast demagnetization.

IV. Relativistic Quantum Electrodynamics Processes:

In 2009, Bigot *et al.* proposed [133] that ultrafast demagnetization can be explained by using relativistic quantum electrodynamics. When a femtosecond laser pulse incident on a ferromagnetic material, the magnetic induction (B) results both from an external static magnetic field (H) and from the time dependent magnetic component of the laser field. As a result within the material the value of B can be as large as 1 Tesla. The electric potential is also dynamically modified due to the laser field which affects both spin orbit interaction and the spin dynamics. As a result the angular momentum of the light is nonlinearly modified in first 50 fs due to this coherent interaction of the photon field with the electronic charges and spins. Next, the relaxations of electrons and spins to the thermalized population take place. During this temporal regime the electronic wave function lost its phase memory by incoherent interaction which leads to the ultrafast demagnetization.

Finally, for longer time delay, the energy exchange between charges and spins to lattice play an important role.

V. Spin Flip Coulomb Scattering:

In 2009, Krauß *et al.* proposed [141] that EY-like mechanism based on electron-electron Coulomb scattering in presence of spin orbit interaction has the potential to explain the ultrafast magnetization dynamics. This type of scattering mechanism is not (quasi) elastic type. In case of electron-electron scattering the available phase space for minority to majority transition is much larger compared to electron-phonon scattering. As a result, the transition for energetically close bands *i.e.*, the bands present near Brillouin zone is also possible to explain using this mechanism. In case of electron-electron scattering, when femtosecond laser is incident on a ferromagnetic material, nonequilibrium electronic distribution within the accessible bands is created. The electrons undergo an intraband or interband Coulomb scattering process. The ultrafast demagnetization mainly occurred due to the interband scattering between the optically excited electrons. As a result there is a redistribution of electrons from majority to minority bands and the overall magnetization value reduces. They assumed that optical excitation will not change the magnetization.

VI. Super Diffusive Spin Transport:

In 2010, Battiato *et al.* proposed [136] a semi classical model for ultrafast demagnetization due to diffusion of spin polarized electrons in a super diffusive regime. In their theory they considered the multiple spin conserving electron scattering events and electron cascades created by inelastic scattering are responsible for ultrafast demagnetization. According to this theory, after the absorption of photon electrons are excited from *d* band to *s-p* like band. The mobility of *s-p* band electron is much larger compare to *d* band electron. The velocity of a laser induced *s-p* band electron is around 1nm/fs. The excited spin majority and minority electrons have different lifetime. The mean free path for a majority carrier is higher compared to the mean free path of a minority carrier. This may lead to a depletion of majority carriers from the magnetic films and a transfer of magnetization away from the surface which leads towards the ultrafast demagnetization. In addition to this, the excited

electrons will undergo inelastic scattering and generate an electron cascade. These newly excited electrons will also contribute to the demagnetization.

2.3.6 Induced Magnetization Precession:

After the absorption of intensive laser pulse, the lattice temperature changes its value. The magnetocrystalline anisotropy and magnetization (M), which are functions of lattice temperature, also change rapidly. The easy axis of magnetization also changes and the magnetization starts to precess around the new easy axis of magnetization to align along the new effective field as shown in Fig. 2.6. The change in easy axis of magnetization due to thermally induced anisotropy is present only for few ps. After that, the easy axis returns to its original position. This rapid change in magnetocrystalline anisotropy or the shape anisotropy ($4\pi M$) acts as an internal pulse field and triggers the precession of magnetization. As a result, the magnetization precession is observed on top of a bi-exponential recovery of magnetization. The faster relaxation time (τ_1) of the hot electrons and spins occurs, because they exchange energy with the lattice and this is mediated by the electron - phonon interaction [142-143]. By exchanging energy, spin system comes to an equilibrium temperature with the charge and lattice systems. The second or longer relaxation time (τ_2) corresponds to the diffusion of electron and lattice heat to the surroundings (such as substrate)[142]. The magnetic damping determines the time scale on which the magnetization aligns with the effective field.

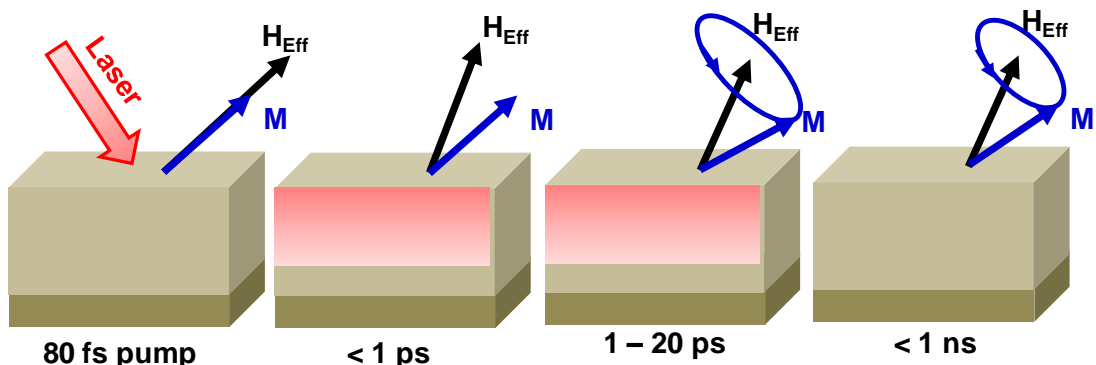


Fig. 2.6 Anisotropy field pulse in all-optical TR-MOKE microscope.

2.4 Ferromagnetic Resonance (FMR):

The collective excitation of an ensemble of electron spin magnetic moment in a magnetic solid is known as ferromagnetic resonance or FMR. If a ferromagnetic material (plane surface) is placed in a static magnetic field H , the magnetization will start to precess with an angular frequency ω_0 and according to Larmor condition $\omega_0 = \gamma H$. If an alternating (rf) magnetic field is applied perpendicular to this steady magnetic field, then the resonance will occur. The magnetization will precess with a resonance frequency absorbing power from the rf magnetic field. The expression for resonance frequency for ferromagnetic material is

$$\omega_0 = \gamma(BH)^{\frac{1}{2}} \quad (2.40)$$

here γ is the gyromagnetic ratio and B is the magnetic induction.

2.4.1 Derivation of the Kittel Formula Using Macrospin Model:

In 1947, Charles Kittel first derived the expression for ferromagnetic resonance considering the shape of the specimen. The theory was developed on macrospin model. According to this model, the magnetization in a ferromagnetic material is uniform throughout the element and as a result the magnetic moment of the whole element can be replaced by a giant magnetic moment.

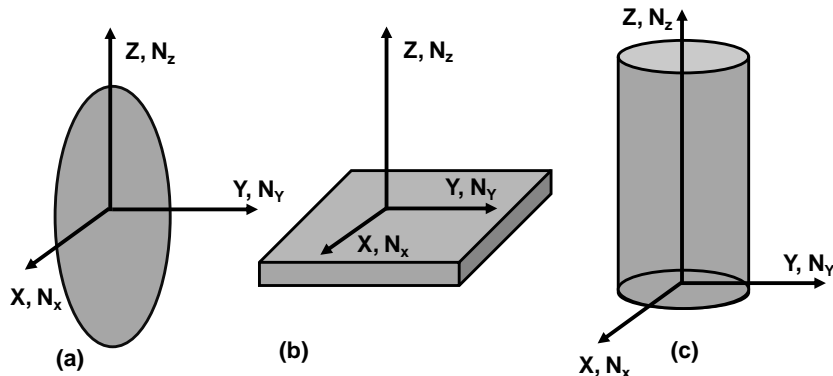


Fig. 2.7 Co-ordinate systems used for (a) an ellipsoid, (b) a plane and (c) a cylinder.

The equation of motion of a ferromagnetic material can be written as

$$\frac{d}{dt} \mathbf{M} = -\gamma(\mathbf{M} \times \mathbf{H}_{\text{Eff}}) + \frac{\alpha}{M} (\mathbf{M} \times \frac{d\mathbf{M}}{dt}) \quad (2.41)$$

For uniform precession (considering $\alpha = 0$) the Eqn. (2.41) reduces to

$$\frac{d}{dt} \mathbf{M} = -\gamma(\mathbf{M} \times \mathbf{H}_{\text{Eff}}) \quad (2.42)$$

The Eqn. (2.42) will take the following form

$$\frac{dM_x}{dt} = \gamma(M_y H_z^{\text{eff}} - H_y^{\text{eff}} M_z) \quad (2.43)$$

$$\frac{dM_y}{dt} = \gamma(M_z H_x^{\text{eff}} - H_z^{\text{eff}} M_x) \quad (2.44)$$

$$\frac{dM_z}{dt} = \gamma(M_x H_y^{\text{eff}} - H_x^{\text{eff}} M_y) \quad (2.45)$$

For a general ellipsoid, the demagnetizing factors along x, y and z directions are N_x, N_y and N_z respectively. H_z is the static magnetic field which is applied along the z axis and H_x is the rf field applied along the x axis. The value of the effective magnetic field along x, y and z directions are [144]

$$H_x^{\text{Eff}} = H_x - N_x M_x \quad (2.46)$$

$$H_y^{\text{Eff}} = -N_y M_y \quad (2.47)$$

$$H_z^{\text{Eff}} = H_z - N_z M_z \quad (2.48)$$

Substituting Eqn. (2.46), (2.47) and (2.48) in Eqns. (2.43), (2.44) and (2.45), we can write

$$\frac{dM_x}{dt} = \gamma[H_z + (N_y - N_z)M_z]M_y \quad (2.49)$$

$$\frac{dM_y}{dt} = \gamma[M_z H_x - (N_x - N_z)M_z M_x - M_x H_z] \quad (2.50)$$

$$\frac{dM_z}{dt} \equiv 0 \quad (2.51)$$

These three equations can be solved considering

$$M = me^{j\omega t} \quad (2.52)$$

Finally the expression susceptibility (χ_x) can be obtained as

$$\chi_x = \frac{M_x}{H_x} = \frac{\chi_0}{[1 - (\frac{\omega}{\omega_0})^2]} \quad (2.53)$$

where,

$$\chi_0 = \frac{M_z}{[H_z + (N_x - N_z)M_z]} \quad (2.54)$$

$$\omega_0 = \gamma [H_z + (N_y - N_z)M_z] \{H_z + (N_x - N_z)M_z\}^{\frac{1}{2}} \quad (2.55)$$

here, ω_0 is the resonance frequency for a ferromagnetic material.

The expressions for some special cases are shown below.

a. Infinite Thin Film:

For $H_z \perp$ film plane,

The demagnetizing factors are

$$N_x = N_y = 0, N_z = 4\pi \quad (2.56)$$

The expression for FMR frequency is

$$\omega_0 = \gamma [H_z - 4\pi M_z] \quad (2.57)$$

For $H_z \parallel$ film plane,

The demagnetizing factors are

$$N_x = N_z = 0, N_y = 4\pi \quad (2.58)$$

The expression for FMR frequency is

$$\omega_0 = \gamma [H_z (H_z + 4\pi M_z)]^{\frac{1}{2}} \quad (2.59)$$

Sphere:

The demagnetizing factors are

$$N_x = N_y = N_z = \frac{4\pi}{3} \quad (2.60)$$

The expression for FMR frequency is

$$\omega_0 = \gamma H_z \quad (2.61)$$

b. Infinite Circular Cylinder:

The demagnetizing factors are

$$N_x = N_y = 2\pi, N_z = 0 \quad (2.62)$$

The expression for FMR frequency is

$$\omega_0 = \gamma (H_z + 2\pi M_z) \quad (2.63)$$

Let us consider the anisotropy energy in f . Then the expression for anisotropy field H^e will be

$$\frac{df}{d\theta} = (M_z \times H^e) \quad (2.64)$$

The expression for anisotropy field in terms of effective demagnetizing factor N^e is

$$H_x^e = -N_x^e M_x \quad (2.65)$$

$$H_y^e = -N_y^e M_y \quad (2.66)$$

The expression for the Kittel formula considering demagnetizing factor and anisotropy field is

$$\omega_0 = \gamma [H_z + (N_y + N_y^e - N_z) M_z] \{ H_z + (N_x + N_x^e - N_z) M_z \}^{1/2} \quad (2.67)$$

For uniaxial anisotropy,

$$f = K_1' \sin^2 \theta \quad (2.68)$$

$$\text{Or, } \frac{df}{d\theta} = 2K_1' \sin \theta \cos \theta \quad (2.69)$$

From Eqn. (2.68) and (2.69)

$$\frac{df}{d\theta} = 2K_1' \sin \theta \cos \theta = M_z H_x^e \sin \theta \cong N_x^e M_z^2 \sin \theta \quad (2.70)$$

Under small angle approximation (For, $\theta \cong 0$ and $\cos \theta \cong 1$)

$$N_x^e = N_y^e = \frac{2K_1'}{M_z^2} \quad (2.71)$$

Finally, the expression of resonance frequency for an infinite thin film considering uniaxial magnetocrystalline anisotropy can be written as

$$\omega_0 = \gamma \left[\left\{ H_z + \frac{2K_1'}{M_z} \right\} \left\{ H_z + \frac{2K_1'}{M_z} + 4\pi M_z \right\} \right]^{1/2} \quad (2.72)$$

2.4.2 Resonance Equation for Two-fold Anisotropy:

The general expressions for effective demagnetizing factor are [145]

$$N_x^e M_s^2 \sin \varepsilon = \left[\left(\frac{\partial G}{\partial \theta} \right)_{\theta+\varepsilon} - \left(\frac{\partial G}{\partial \theta} \right)_\theta \right]_\phi \quad (2.73)$$

$$N_y^e M_s^2 \sin \delta = \frac{\left[\left(\frac{\partial G}{\partial \phi} \right)_{\phi+\delta} - \left(\frac{\partial G}{\partial \phi} \right)_\phi \right]_\theta}{\sin^2 \theta} + \frac{\sin \delta \cos \theta}{\sin \theta} \frac{\partial G}{\partial \theta} \quad (2.74)$$

G is the magnetocrystalline anisotropy energy and θ and ϕ are the angles made by the external magnetic field H with z and x axis respectively as shown in Fig. 2.8.

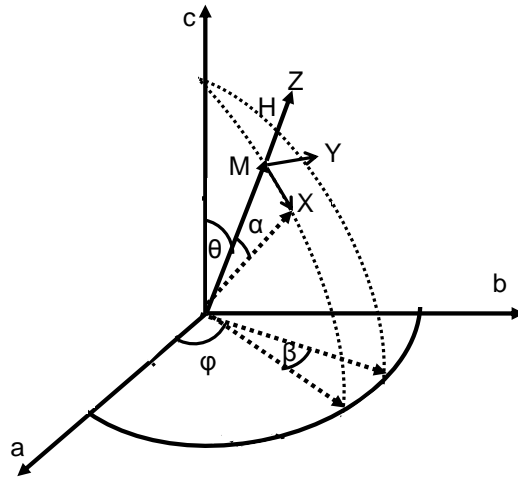


Fig. 2.8 Geometry of the magnetization and applied magnetic field is shown in an orthogonal coordinate system (a, b, c).

The expression for uniaxial magnetocrystalline anisotropy energy is

$$G = K_1 \sin^2 \theta \quad (2.75)$$

$$\text{or, } \frac{\partial G}{\partial \theta} = K_1 \sin 2\theta \quad (2.76)$$

$$\text{and, } \frac{\partial G}{\partial \phi} = 0 \quad (2.77)$$

Substituting Eqn. (2.76) and (2.77) in Eqn. (2.73) and (2.74) at $\phi = \theta$ under small angle approximation we get

$$N_x^e = \frac{2K_1'}{M_s^2} \cos 2\theta \quad (2.78)$$

$$N_y^e = \frac{2K_1'}{M_s^2} \cos^2 \theta \quad (2.79)$$

Substituting Eqn. (2.78) and 2.79 in Eqn. (2.67), we get the expression for resonance frequency for systems with two-fold magnetic anisotropy as

$$\omega_0 = \gamma \left[\left\{ H_z + (N_y - N_z + \frac{2K_1'}{M_s} \cos 2\theta) M_z \right\} \left\{ H_z + (N_x - N_z + \frac{2K_1'}{M_s} \cos^2 \theta) M_z \right\} \right]^{\frac{1}{2}} \quad (2.80)$$

For an infinite thin film, the demagnetizing factors are $N_y = 4\pi$, $N_x = N_z = 0$.

The expression for resonance frequency for two-fold magnetic anisotropy can be written as

$$\omega_0 = \gamma \left[\left\{ H_z + \frac{2K_1'}{M_s} \cos 2\theta \right\} \left\{ H_z + \frac{2K_1'}{M_s} \cos^2 \theta + 4\pi M_s \right\} \right]^{\frac{1}{2}} \quad (2.81)$$

Free energy for four-fold anisotropy can be written as

$$G = K_4 (\sin^4 \theta \cos^4 \theta + \sin^4 \theta) \quad (2.82)$$

$$\text{Or, } G = \frac{K_4}{4} \sin^4 \theta (\cos 4\theta + 3) \quad (2.83)$$

Following the similar process, the expression for resonance frequency in systems with four-fold anisotropy can be written as

$$\omega_0 = \gamma \left[\left\{ H_z + (N_y - N_z - \frac{4K_4}{M_s^2} \cos 4\theta) M_z \right\} \left\{ H_z + (N_x - N_z + \frac{K_4}{M_s^2} (3 + 4 \cos 4\theta)) M_z \right\} \right]^{\frac{1}{2}} \quad (2.84)$$

2.5 Spin Waves:

2.5.1 Introduction:

In 1930, Bloch first introduced the concept of spin-waves (SWs). The low-lying collective excitations occur in magnetic lattices with continuous symmetry propagates as a wave (SW) generated by collective phase coherent precession of spins in ferromagnetic materials. The magnetization orientation of individual spins in a ferromagnetic material can be disturbed from its ground state by various perturbing methods like temperature, pressure, magnetic field, spin-polarized current or electromagnetic waves. This disturbance propagates through the system in the form of spin-wave (SW). The quanta of SWs are known as magnons which are spin-1 quasiparticles and follow the Bose –Einstein statistics.

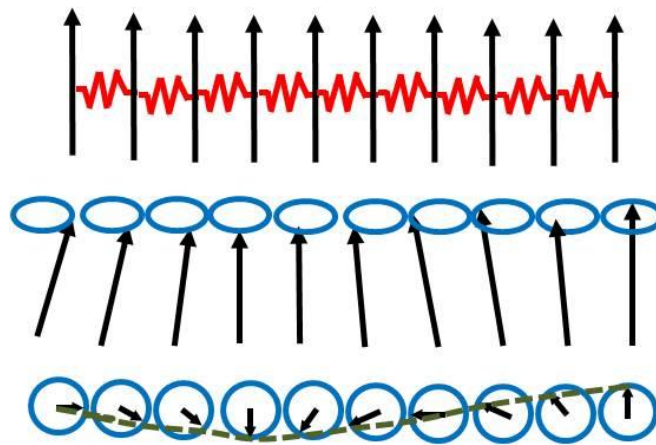


Fig. 2.9 A schematic diagram of spin-wave is shown.

2.5.2 Dispersion Relation of Magnon:

In case of ferromagnetic material at ground state all spins are parallel to each other. Let us consider a chain of N spins and the magnitude of each spin is S . The Heisenberg exchange interaction can be expressed as

$$E_{ex} = -2J \sum_{p=1}^N \mathbf{S}_p \cdot \mathbf{S}_{p+1} \quad (2.85)$$

here, J is the exchange integral and $\hbar S_p$ is the angular momentum of the spin at site p .

The energy term involving p^{th} spin is [122]

$$E_{ex} = -2J \cdot S_p \cdot (S_{p-1} + S_{p+1}) \quad (2.86)$$

The magnetic moment at site p is

$$\mu_p = -g\mu_B S_p \quad (2.87)$$

$$\text{or, } S_p = -\frac{\mu_p}{g\mu_B} \quad (2.88)$$

Substituting Eqn. (2.88) to Eqn. (2.86), we get

$$E_{ex} = -\mu_p \cdot \left[\frac{-2J}{g\mu_B} (S_{p-1} + S_{p+1}) \right] \quad (2.89)$$

Eqn. (2.89) can be writes as

$$-\mu_p \cdot B_p = -\mu_p \cdot \left[\frac{-2J}{g\mu_B} (S_{p-1} + S_{p+1}) \right] \quad (2.90)$$

where the effective magnetic field or exchange field that acts on the p^{th} spin is

$$B_p = \left[\frac{-2J}{g\mu_B} (S_{p-1} + S_{p+1}) \right] \quad (2.91)$$

The torque $\mu_p \times B_p$ which acts on the spin is equal to the rate of change of angular momentum $\hbar S_p$.

$$\frac{dS_p}{dt} = (-g\mu_B/\hbar) S_p \times B_p = (2J/\hbar)(S_p \times S_{p-1} + S_p \times S_{p+1}) \quad (2.92)$$

In Cartesian coordinates:

$$\frac{dS_p^x}{dt} = \frac{2J}{\hbar} [S_p^y (S_{p-1}^z + S_{p+1}^z) - S_p^z (S_{p-1}^y + S_{p+1}^y)] \quad (2.93)$$

considering $S_p^x, S_p^y \ll S$ and $S_p^z = S$, we can linearize Eqn. (2.93). The solution of the linearized equations will be of sinusoidal form as mentioned below

$$S_p^x = m \exp[i(pka - \omega t)]; \quad S_p^y = n \exp[i(pka - \omega t)]; \quad (2.94)$$

The magnon dispersion relation can be obtained as

$$\hbar\omega = 4JS(1 - \cos ka) \quad (2.95)$$

where k is the wave vector and a is the lattice constant. At long wavelength limit, $ka \ll 1$, Eqn. (2.95) can be written as

$$\hbar\omega = (2JSa^2)k^2 \quad (2.96)$$

The dispersion relation of magnon is quadratic in nature for long wavelength limit *i.e.*, in small k limit as opposed to the phonon dispersion relation, which is linear in nature for long wavelength limit.

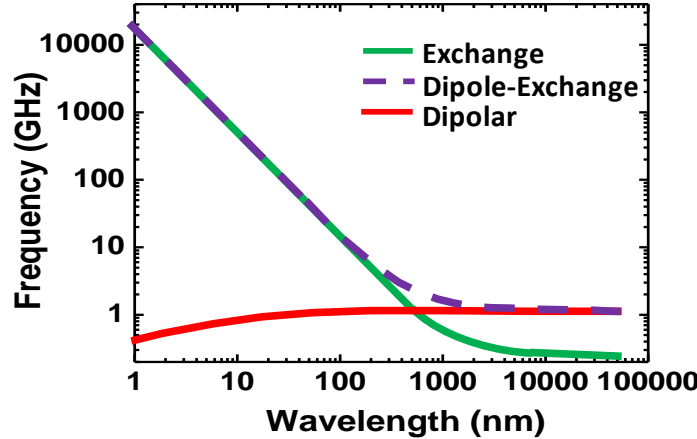


Fig. 2.10 A representative plot of frequency as a function of wavelength of spin waves.

2.5.3 Exchange Dominated Spin-waves in Thin Films:

SWs are called exchange dominated if their wavevector $k \gg 1/\lambda_{ex}$. The dispersion relation for exchange dominated SW is [146]

$$\omega(k) = \gamma(H + Dk^2) \quad (2.97)$$

where $D = 2A/M_s$, A is the exchange stiffness constant and M_s is the saturated magnetization.

The exchange dominated SWs are isotropic in nature. The pure exchange dominated SW modes are often observed in thin films, where they propagate perpendicular to the film surface and form standing wave pattern. They are termed as perpendicular standing SW (PSSW) modes. The wave vector perpendicular to the film, k_\perp is quantized. In case of both pinned ($\sigma_{inter} = \infty$) and unpinned ($\sigma_{inter} = 0$) boundary conditions, the perpendicular wave vector reads $k_{\perp l} = l(\pi/d)$ with d the film thickness and l is a positive integer.

2.5.4 Magnetostatic Modes in Thin Films:

Modes travelling in the film plane usually have a wave vector in the range between the hundreds of nanometers and several micrometers, which is much larger than interatomic distances. Thus exchange interaction is weak in this case and often these modes are governed by dipolar interactions. For $k \ll 1/\lambda_{ex}$ the SWs are almost entirely determined by magnetic dipole interactions - such waves are called as magnetostatic SWs. But for higher values of k , the exchange interaction cannot be neglected; such SWs are known as dipole-exchange SWs. The dispersion relations for dipolar modes can be calculated by solving the Landau-Lifshitz torque equation. The total magnetization can be written as

$$\mathbf{M} = \mathbf{M}_s + \mathbf{m}(R, t) \quad (2.98)$$

here, \mathbf{M}_s and $\mathbf{m}(R, t)$ are the vectors of saturation and variable magnetization respectively.

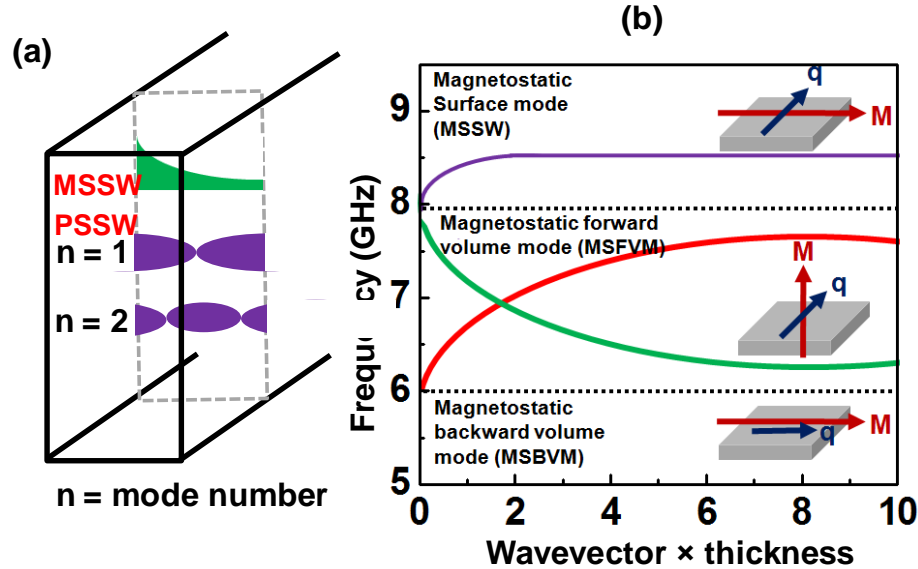


Fig. 2.11. Schematics of (a) perpendicular standing spin wave mode (PSSW) and magnetostatic surface spin wave mode (MSSW) are shown for a ferromagnetic thin film. (b) The dispersion relations for three different types of magnetostatic SWs modes are shown.

Maxwell's equation in magnetostatic limit

$$\nabla \times H_{\text{eff}} = 0 \quad (2.99)$$

$$\nabla \cdot (H_{\text{eff}} + 4\pi M_s) = 0 \quad (2.100)$$

For small angle approximation ($< 10^\circ$) and $m(R, t) \ll M_s$, $m(R, t)$ can be expanded in a series of plane waves of magnetization

$$m(R, t) = \sum_k m_k e^{i(\omega t - k \cdot r)} \quad (2.101)$$

The nonlinear Landau-Lifshitz Eqn. can be linearized and solved under this condition.

Ultimately, the dispersion relation for dipole-exchange SWs in an unlimited ferromagnetic medium is given by the Herring-Kittel formula [147]

$$\omega = \gamma \left[\left(H + \frac{2A}{M_s} k^2 \right) \left(H + \frac{2A}{M_s} k^2 + 4\pi M_s \sin^2 \theta_k \right) \right]^{1/2} \quad (2.102)$$

where θ_k is the angle between k and M_s .

The SW dispersion depends on the relative dispersion of the direction of the wavevector, k , and the direction of the magnetization vector, M , with respect to the film orientation.

Let us consider a ferromagnetic thin film of thickness d film (Y-Z plane) and the external field is applied along the Z direction and X-axis is normal to the film plane. Damon and Eshbach calculated the dispersion relation for dipolar mode in a thin magnetic film and they found two types of modes namely, the surface or Damon-Eshbach (DE) mode[60] and volume mode. The surface or DE mode has largest amplitude at the surfaces but decays exponentially away from the surface as shown in Fig. 2.11(a). The mode exists only for propagation along the surface at an angle $\theta < \theta_c$ around the direction normal to the magnetization. Here, θ is the angle between direction of propagation and sample magnetization and θ_c is the critical angle given by:

$$\theta_c = \tan^{-1} \sqrt{\frac{4\pi M_s}{H}} \quad (2.103)$$

The penetration depth (δ) for surface mode decreases with the increase in θ and vanishes at $\theta = \theta_c$ and it is proportional to k_y^{-1} . Hence, at critical angle the surface mode is completely localized at the surface of the sample. The DE mode is unidirectional (non-reciprocal). This means that for one propagation direction inside the range of angles θ where it exists, it travels only on one surface but not the opposite. The DE mode with the opposite propagation direction is located at the other surface of the slab. Since DE mode is independent of the slab thickness d , the unidirectional propagation characteristic is relaxed upon decreasing d and is lifted when d is small compared to the penetration depth. The finite frequency at $k_y = 0$ represents the uniform Kittel mode. The surface mode is converted to bulk mode when the film thickness is comparable to the penetration depth. In general the propagation vector and the magnetization are in plane but perpendicular to each other for magnetostatic surface spin wave (MSSW) mode. The dispersion relation as shown in Fig. 2.11(b) for MSSW mode considering negligible anisotropy is

$$\omega_{DE} = \gamma[H(H + 4\pi M_s) + (2\pi M_s)^2(1 - e^{-2kd})]^{1/2} \quad (2.104)$$

At $k = 0$, the DE mode converts to uniform Kittel mode as shown below

$$(\omega_{DE})_{k=0} = \gamma[H(H + 4\pi M_s)]^{1/2} \quad (2.105)$$

At $k = \infty$, the frequency of MSSW mode becomes

$$(\omega_{DE})_{k=\infty} = \gamma(H + 2\pi M_s) \quad (2.106)$$

If the propagation wave vector and the magnetization are collinear and lie both in the film plane, we find the so-called backward volume magnetostatic mode (BWVMS) (Fig. 2.11(b)). The slope and thus the group velocity for these modes are negative, *i.e.*, the group and the phase velocity point in opposite directions. The dispersion relation for BWVMS considering negligible anisotropy can be written as

$$\omega_D = \gamma[H\{H + 4\pi M_s(\frac{1 - e^{-2kd}}{kd})\}]^{1/2} \quad (2.107)$$

As $k \rightarrow 0$, the frequency of BWVMS becomes same as the Kittel mode.

If the magnetization is perpendicular to the film plane and the propagation direction is in the film plane, forward volume magnetostatic modes (FWVMS) are observed (Fig. 2.11(b)). Without anisotropy and in the long wavelength limit the dispersion relation for FWVMS mode is

$$\omega_F = \gamma[(H - 4\pi M_s)\{H - 4\pi M_s(\frac{1 - e^{-2kd}}{kd})\}]^{1/2} \quad (2.108)$$

The frequency of the dipole dominated mode is minimum as shown in Fig. 2.10. But for transition metal and alloys as the exchange value A is much higher the frequency of dipole exchange mode is larger than the frequency of purely dipolar mode. Whereas the exchange interaction can be neglected for system with weak exchange stiffness (A) constant like Yttrium Iron Garnet or YIG.

2.5.5 Quantized Lateral Spin Wave Mode:

The SWs can also be laterally quantized in the film plane due to the finite size of the structures such as nanostripes, squares, rectangular and circles *etc.* The quantization condition is [146]

$$w = \frac{n\lambda}{2}; \quad k = \frac{2\pi}{\lambda} = \frac{n\pi}{w}; \quad (2.109)$$

where w is the width of the magnetic structure, n is a positive integer and λ is the spin-wave wavelength.

2.6 Magnetic Vortices:

In confined magnetic elements, various types of domain structure are formed due to the competition between exchange, dipolar and anisotropic energies. It is observed experimentally and theoretically that for a particular range diameter and thickness of magnetic elements, a magnetic vortex state with curling in-plane spin configuration and out-of-plane core is energetically favored. The radius of the core (R_{core}) can be expressed as

$$R_{core} = 0.68\lambda_{ex}^3 \sqrt{\frac{u}{\lambda_{ex}}} \quad (2.110)$$

here, λ_{ex} is the exchange length and u is the thickness of the magnetic element. The value of core radius is about 10 nm. The out of plane component of magnetization *i.e.*, the polarity (p) of the core can point either 'up' ($p = +1$) or 'down' ($p = -1$) at the centre as shown in Fig. 2.12(a, b). The sense of the inplane flux closure configuration *i.e.*, chirality (c) can be clockwise ($c = +1$) or counterclockwise ($c = -1$).

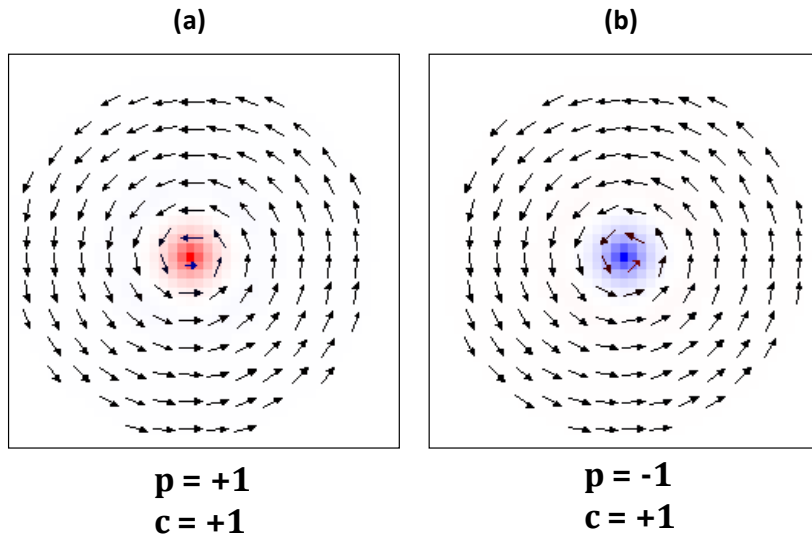


Fig. 2.12 A Ni₈₀Fe₂₀ circular disk of diameter 200 nm and thickness 40 nm formed magnetic vortex whose center contains an out-of-plane polarized core with (a) $p = +1$ and (b) $p = -1$.

Another important parameter is winding number (w_n) which can be defined as

$$w_n = \frac{1}{2\pi} \oint_S \frac{d\varphi}{ds} \quad (2.111)$$

here, $\varphi = \tan^{-1}(m_y/m_x)$ and, S is the boundary of the vortex. The winding number is +1 for a vortex and for an antivortex the winding number is -1.

2.6.1 The Thiele Equation:

When a magnetic fields and spin polarized currents is applied to a magnetic vortex, the core is displaced from its equilibrium position. The restoring force from the demagnetizing field and the gyrotropic force result in a spiral motion of the vortex core with a frequency in the sub-gigahertz range. This is referred as magnetic vortex core gyration. At steady state this gyration can be expressed by Thiele's equation

$$\mathbf{F}_{ext} + \mathbf{G} \times \mathbf{v} + \alpha \mathbf{D} \cdot \mathbf{v} = 0 \quad (2.112)$$

The criterions to follow this equation are

- a. The velocity (v) will be constant.
- b. The shape of the magnetic nanostructure will remain unchanged during motion.

here, G is the gyrotropic vector, D is the net dissipation tensor and F_{ext} is the total external field. In spherical polar coordinate, G and D can be expressed as

$$G = -\frac{\mu_0 M_s}{\gamma} \int (\sin \theta \nabla \theta \times \nabla \phi) dV \quad (2.113)$$

$$D = -\frac{\mu_0 M_s}{\gamma} \int (\sin^2 \theta \nabla \phi \nabla \phi \times \nabla \theta \nabla \theta) dV \quad (2.114)$$

$$F_{ext} = f_{ext} + f_{int} \quad (2.115)$$

here, the total external force (f_{ext}) acting on the vortex is mainly a combination of a force induced by the external magnetic (or spin-polarized current) and the interaction of a vortex with other vortices or anti vortices. However, the total internal force (f_{int}) is a combination of force induced by the gyrotropic vector, restoring force and dissipative force.

2.6.2 Gyrotropic Frequency:

When a vortex core is displaced from its equilibrium position, the circular arrangement of the magnetization will be disturbed. As a result an internal demagnetizing field will be created which will oppose the displacement of the vortex core. Thus the vortex core will be bound within a magnetostatic potential well. The resulting force which tends to restore the vortex core to its equilibrium position can be expressed as

$$F_{ms} = -kr \quad (2.116)$$

Here, r is the core's position and k is a positive constant which can be written as

$$k = \pi \frac{\mu_0 M_s^2 u}{\chi_0} \quad (2.117)$$

The initial susceptibility (χ_0) can be written as

$$\frac{1}{\chi_0} = \frac{2u}{r} \left[\ln\left(\frac{8R}{u}\right) - \frac{1}{2} \right] : \frac{u}{R} \ll 1 \quad (2.118)$$

For low damping value ($D \sim 0$) the Thiele equation can be written as

$$-kr + G \times v = 0 \quad (2.119)$$

From this equation the gyration frequency (f_0) can be expressed as

$$f_0 = \frac{\gamma M_s}{2\chi_0} \quad (2.120)$$

The frequency value obtained from this equation is not exactly same as the frequency value obtained from micromagnetic simulation because this analytical expression is calculated considering rigid vortex model. According to this model, the vortex core displacement leads towards the formation of surface charge as the edges of the boundary. These surface charges are responsible for this discrepancy. But the discrepancy can be removed by considering the boundary condition. The expression for the gyrotropic frequency considering boundary condition is

$$f_0 = \frac{2\gamma M_s}{9\chi_0} \quad (2.121)$$

The gyrotropic frequency of a magnetic vortex is only depends upon the aspect ratio of the elements and the saturation magnetization of the material used.

2.7 Magneto-Optical Kerr Effect (MOKE):

In 1845, Michael Faraday first discovered the magneto-optic effect. He observed that the plane of polarization of a linearly polarized light is rotated when the light transmitted through a magnetized material. This phenomenon is known as Faraday's effect. In 1877 John Kerr observed the same phenomena in reflection geometry also [148]. The linearly polarized light converted to an elliptically polarized light when the light is reflected from a magnetic material. This phenomenon is known as Kerr effect and the corresponding

rotation in plane of polarization is called the Kerr rotation. The magneto-optic rotation is proportional to the first order of magnetization. It is very sensitive but simple technique to image the magnetic domain and to probe the magnetization dynamics at various length scales.

2.7.1 Origin of Magneto-Optic Effect:

There are several theories which can explain the origin of magneto-optic effect in ferromagnetic materials which includes mainly the microscopic theory and macroscopic dielectric theory.

In 1856 William Thomson first offered the classical microscopic explanation of the magneto-optic effect. According to him, the particles in the medium under an external magnetic field follow different circular paths, depending on their direction relative to the magnetic field. This explanation is correct if we identify the “particle” as “electron”.

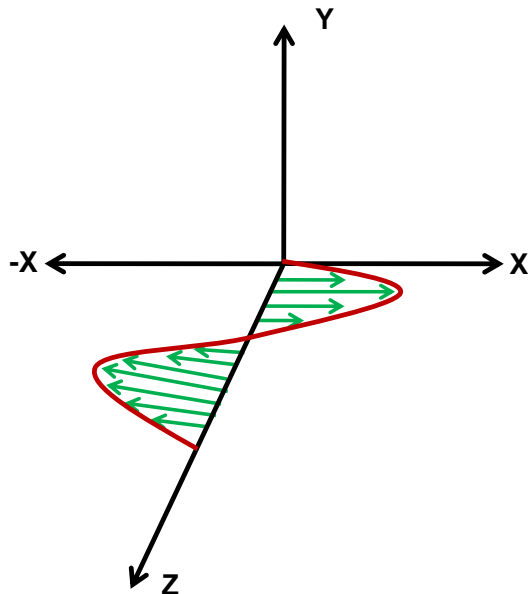


Fig. 2.13 A schematic of the incident light linearly polarized along X – direction and propagating along Z – direction.

A linearly polarized light can be expressed as a superposition of left circularly polarized light (LCP) and right circularly polarized light (RCP). In absence of magnetic field the expression for linearly polarized light will be

$$E = \frac{E_{LCP}}{2} (\hat{e}_x + i\hat{e}_y) e^{i(\omega t - kz)} + \frac{E_{RCP}}{2} (\hat{e}_x - i\hat{e}_y) e^{i(\omega t - kz)} \quad (2.110)$$

where the plane of polarization is along X direction and the propagation is along Z direction as shown in Fig. 2.13. When the light propagates through a medium, the electrons present in the medium are in a motion due to the presence of the electric field. The LCP drive the electrons into left circular motion whereas the RCP drive the electrons into right circular motion. In absence of magnetic field the radius of electron orbit for left and right circular motion is same. As a result no rotation is observed. But in presence of magnetic field the picture is completely different. The radius of electron orbit for left and right circular motion will either expand or reduce depending upon the direction of additional Lorentz force acting on each electron. The difference in the radii of left and right circularly polarized light will give a finite difference in dielectric constants which leads towards the magneto-optical Kerr effect (MOKE).

The quantum description of magneto-optic effect was explained by Hulme in 1932. According to him, the spin-orbit interaction couples the electron spins to its motion which give rise to Kerr rotation. If an electron with momentum p moves through an electric field ΔV , the spin orbit coupling due to the interaction of electron spin s with the magnetic field will be

$$(\Delta V \times p).s = p.(s \times \Delta V) = p.A \quad (2.111)$$

where A = effective field vector potential $= s \times \Delta V$.

The effect of magnetic field on electron motion is

$$E_{Int} = \frac{e}{mc} (p.A) \quad (2.112)$$

The spin-orbit coupling can be considered as an effective field vector potential acting on the motion of the electron. For non magnetic material the number of up-spin and down-spin electrons is same therefore the net effect is zero but for ferromagnetic materials the effect is present because of the unbalanced population in electron spin. But unfortunately this theory is unsatisfying because the quenching of the orbital angular momentum in transition-metal ferromagnets removes the energy splitting.

Macroscopically, magneto-optic effects arise from the antisymmetric, off-diagonal elements in the dielectric tensor. When a plane polarized light propagates through a magnetic medium two circularly polarized light gain different phase shifts due to their different propagation velocities. As a result the plane of polarization rotates and different absorption rate for two different circularly polarized modes affects the ellipticity.

Consider ε_{mn} , a 3×3 dielectric tensor of a medium, which can be decomposed into a symmetric and an antisymmetric part

$$\varepsilon_{mn} = \frac{(\varepsilon_{mn} + \varepsilon_{nm})}{2} + \frac{(\varepsilon_{mn} - \varepsilon_{nm})}{2} \quad (2.113)$$

ε , the dielectric tensor can be generalized using Euler's formulae

$$\tilde{\varepsilon} = \varepsilon_{xx} \begin{pmatrix} 1 & -iQM_z & iQM_y \\ iQM_z & 1 & -iQM_x \\ -iQM_y & iQM_x & 1 \end{pmatrix} \quad (2.114)$$

where the magneto-optical constant $Q = i \varepsilon_{xy}/\varepsilon_{xx}$ and M_x , M_y and M_z are the direction cosines of the magnetization M_s .

The two normal modes for left (η_L) and right (η_R) circularly polarized lights are

$$\eta_L = \eta \left(1 - \frac{1}{2} Q \cdot \hat{k} \right) \quad (2.115)$$

$$\eta_R = \eta \left(1 + \frac{1}{2} Q \cdot \hat{k} \right) \quad (2.116)$$

where average refractive index, $\eta = \sqrt{\epsilon_{xx}}$ and k is the unit vector along the direction of propagation.

The Kerr rotation is given by

$$\theta = \frac{\pi L}{\lambda} (\eta_L - \eta_R) = -\frac{\pi L \eta}{\lambda} Q \cdot \hat{k} \quad (2.117)$$

The real part of this equation will give the Kerr rotation whereas the imaginary part will give the Kerr ellipticity.

Fresnel reflection matrix obtained by solving the Maxwell's equation for Eqn. (2.114) is

$$R = \begin{pmatrix} r_{pp} & r_{ps} \\ r_{sp} & r_{ss} \end{pmatrix} \quad (2.118)$$

The Kerr rotation θ_K and Kerr ellipticity ε_K for s - and p - polarized light can be expressed as

$$\Theta_K^s = \theta_K^s + i\varepsilon_K^s = \frac{r_{ps}}{r_{ss}} \quad (2.119)$$

$$\Theta_K^p = \theta_K^p + i\varepsilon_K^p = \frac{r_{sp}}{r_{pp}} \quad (2.120)$$

If a p - polarized light reflects from a nonmagnetic surface, then the reflected light will be purely p -polarized but if the light reflects from a ferromagnetic sample, then the reflected light will consist of s - (k) and p - (r) polarized light. The linearly polarized light will be converted to elliptically polarized light. The major axis of the ellipse will slightly rotate with respect to the principal plane which is known as Kerr rotation (θ_K) and the flatness of the ellipse is known as Kerr ellipticity (ε_K). k/r will be denoted as the Kerr angle (θ_K) where $k \ll r$ as shown in Fig. 2.14(a).

2.7.2 MOKE Geometries:

Three kinds of MOKE geometries are possible based upon the orientation of magnetization vector with respect to the sample surface and plane of incidence. They are polar, longitudinal and transverse MOKE [121, 149].

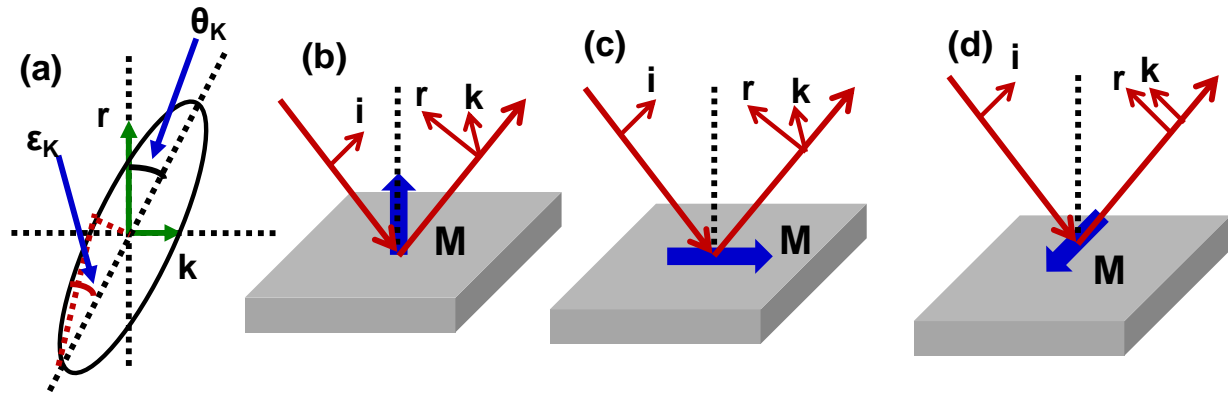


Fig. 2.14 (a) Geometry of the Kerr rotation (θ_K) and Kerr ellipticity (ε_K) are shown. Here r is the Fresnel reflection coefficient, k is the Kerr coefficient and M is the magnetization of the sample. Schematics of (b) polar, (c) longitudinal and (d) transverse MOKE geometries are shown.

In polar geometry the magnetization (M) is perpendicular to the reflection surface and parallel to the plane of incidence as shown in Fig. 2.14(b). In polar configuration, $M_Z = 1$, and $M_X = M_Y = 0$. The expression for polar Kerr angle will be

$$(\Theta_K^s)^{Pol} = \left(\frac{r_{ps}}{r_{ss}} \right)^{Pol} = \frac{-\cos\theta_0}{\cos(\theta_0 - \theta_1)} \cdot \frac{in_0 n_1 Q}{(n_1^2 - n_0^2)} \quad (2.121)$$

$$(\Theta_K^p)^{Pol} = \left(\frac{r_{sp}}{r_{pp}} \right)^{Pol} = \frac{\cos\theta_0}{\cos(\theta_0 + \theta_1)} \cdot \frac{in_0 n_1 Q}{(n_1^2 - n_0^2)} \quad (2.122)$$

here, n_0 , n_1 , θ_0 and θ_1 are the complex refractive index and refractive angle of the non magnetic medium 0, magnetic medium 1. First factor is a function of incident and refractive angle which determined the refractive index of the medium and the second factor is the polar Kerr effect for normal incidence.

In longitudinal MOKE geometry, the magnetization (M) is parallel to the plane of reflection as well as the plane of incidence (Fig. 2.14(c)). In case of longitudinal geometry the light reflected from the surface of reflection at an angle not normal to it. In longitudinal configuration, $M_Y = 1$, and $M_X = M_Z = 0$. The expression for longitudinal Kerr angle will be:

$$(\Theta_K^s)^{Long} = \left(\frac{r_{ps}}{r_{ss}} \right)^{Long} = \frac{\cos\theta_0 \tan\theta_1}{\cos(\theta_0 - \theta_1)} \cdot \frac{in_0 n_1 Q}{(n_1^2 - n_0^2)} \quad (2.123)$$

$$(\Theta_K^p)^{Long} = \left(\frac{r_{sp}}{r_{pp}} \right)^{Long} = \frac{\cos\theta_0 \tan\theta_1}{\cos(\theta_0 + \theta_1)} \cdot \frac{in_0 n_1 Q}{(n_1^2 - n_0^2)} \quad (2.124)$$

The general expressions for Kerr angle with arbitrary magnetization and in oblique incidence are

$$\Theta_K^s = \frac{r_{ps}}{r_{ss}} = \frac{\cos\theta_0 (M_Y \tan\theta_1 - M_Z)}{\cos(\theta_0 - \theta_1)} \cdot \frac{in_0 n_1 Q}{(n_1^2 - n_0^2)} \quad (2.125)$$

$$\Theta_K^p = \frac{r_{sp}}{r_{pp}} = \frac{\cos\theta_0 (M_Y \tan\theta_1 + M_Z)}{\cos(\theta_0 - \theta_1)} \cdot \frac{in_0 n_1 Q}{(n_1^2 - n_0^2)} \quad (2.126)$$

In transverse MOKE geometry, magnetization (M) is perpendicular to the plane of incidence but it is parallel to the reflection surface (Fig. 2.14(d)). Only p -polarized light shows the transverse Kerr effect. In case of transverse geometry the light is not normal to the reflected surface. In this case, the linearly polarized light remains linearly polarized without any Kerr rotation but the reflectivity changes after reflection which is proportional to the component of magnetization which is perpendicular to the plane of incidence and parallel to the surface of reflection. So instead of measuring change in polarity the change in reflectivity is measured.

3. Sample Fabrication, Characterization and Measurement Techniques for Magnetization Dynamics

3.1 Introduction:

Nanomagnets with a very narrow distribution of shapes, sizes and separations over a macroscopic length scale are important for future technology. It is important to fabricate a good quality ordered arrays of nanomagnets using advanced nanofabrication techniques and characterized them properly before any possible applications. The intrinsic magnetic properties of a nanomaterial strongly depend upon the surface quality along with the crystallinity, chemical purity and physical and chemical uniformity of the nanostructures. First challenge is to fabricate chemically pure samples with uniform chemical composition and physically less defective with good surface quality. The next challenge is to develop cost effective fabrication techniques with a high yield. As we discussed in chapter 1 various nanofabrication methods have been developed over the years but very few of them are able to produce good quality ordered nanostructures. Lithographic methods are found to be one of the best options for precise fabrication of high quality sample with sub-micrometre precision and with a very narrow distribution of shapes, sizes and distances. But it is a slow and expensive method. In addition to this, for multilevel lithographic approach there are limitations in alignment of the two contrasting ferromagnetic materials. A new technique is developed for synthesizing magnetic nanostructures over a large area consisting of one or two contrasting ferromagnetic materials which is named as self aligned shadow deposition technique. In this chapter we will discuss different sample fabrication and characterization techniques that were used in the work presented in this thesis. We will also describe static and time-resolved magneto optical Kerr effect microscope (TR-MOKE) setup which was

used to measure the static and dynamic magnetic properties of nanostructures presented in this thesis.

3.2 Sample Fabrication:

3.2.1 Optical Lithography:

The name optical lithography [150-151] comes from the early application where the exposing energy was visible light. Now a days to reduce feature sizes Ultraviolet (UV) and deep ultraviolet (DUV) sources of much shorter wavelengths are used to increase resolution. However, the main drawback of this process is that the resolution is limited by the diffraction of light. Therefore, it is very difficult to fabricate high quality sub-micron structures by optical lithography. The schematic of optical lithography is shown in Fig. 3.1.

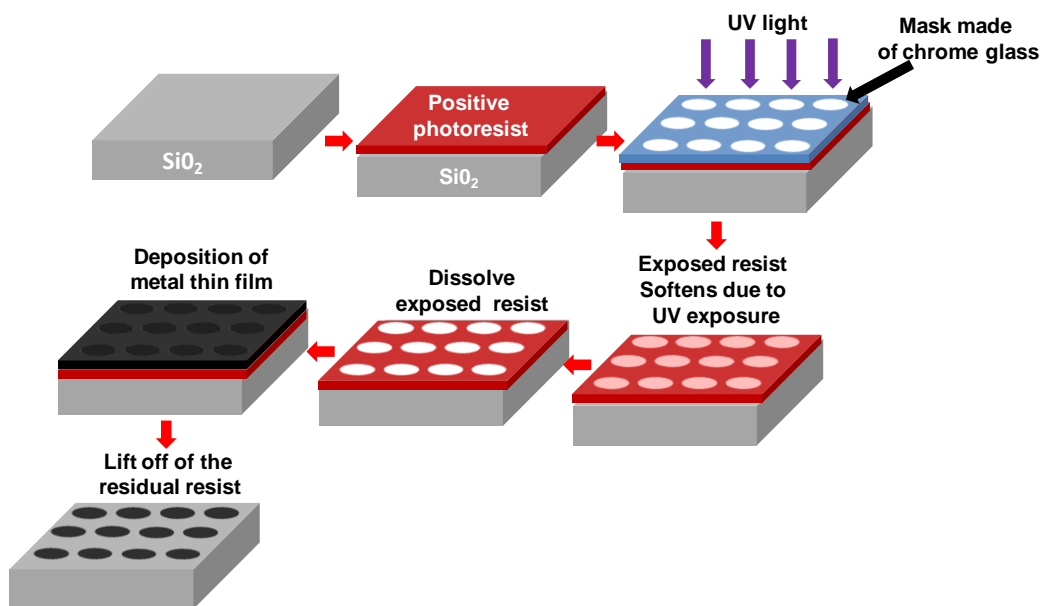


Fig. 3.1 Schematic diagram of optical beam lithography process is shown.

The first step in optical lithography is to apply a resist coating to the substrate. The Si (100) substrate was ultrasonicated in water and acetone for 20 minutes each to remove the inorganic and organic materials from the top surface of the substrate. The substrate was dried after cleaning by a dry nitrogen gas flow. A uniform layer of positive photoresist dissolved in an organic solvent was then coated on the substrate. This is done using a

spinner which spins the substrate as a small amount of liquid resist is applied at the center of the substrate. These results in a uniform coating of the liquid resist on the substrate. To mechanically "fix" the resist, a prescribed baking operation is followed.

Next a photo mask (chrome on glass) containing the patterns to be fabricated was placed on top of the substrate. A convex lens was used in between the UV source and the mask for uniform illumination of the source on the mask. The polymer chains in the resist were broken at the exposed area after a sufficient amount of exposure. The resist in the exposed area softens. The exposed area was etched out by wet chemical process. The substrate was first put into distilled water at room temperature, rinsed for 60 s and dried using dry nitrogen gas flow. The substrate was then put into MIBK: IPA (1:3) (methyl isobutyl ketone : isopropyl alcohol) solution and rinsed for 30 s. Finally, the substrate was put into acetone, rinsed for 60 s and dried with dry nitrogen gas flow. Subsequently, the two dimensional pattern of the photo mask was copied onto the resist as a three dimensional structure.

3.2.2 Electron Beam Lithography:

As electron beams have very short wavelength at large enough accelerating voltage, they are widely used for fabrication of arrays of submicron elements [152]. In our case, the 20 nm thick circular Py dots of diameter 100 nm and separations of 30 nm arranged in square, rectangular, hexagonal. Honeycomb and octagonal lattices were fabricated by electron beam lithography technique. The schematic of the technique is shown in Fig. 3.2.

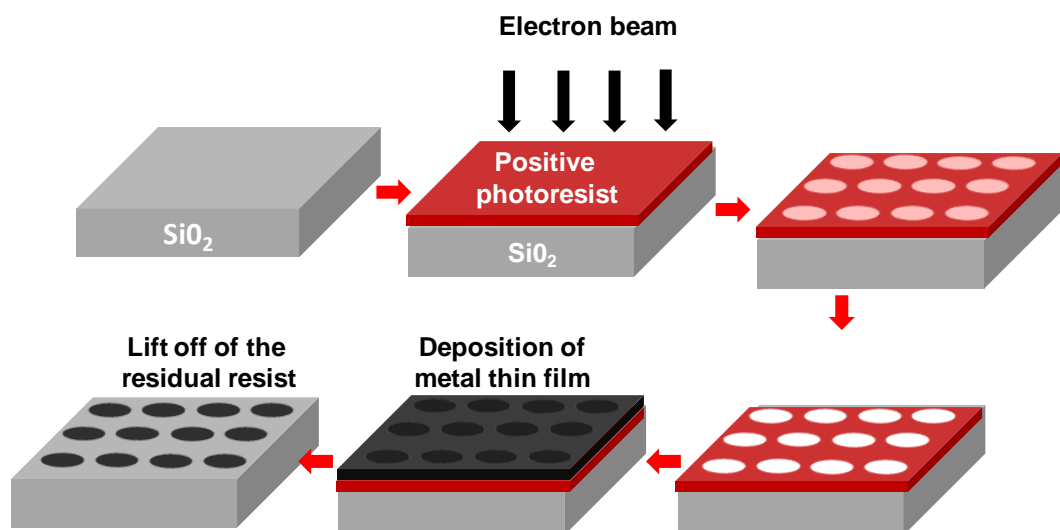


Fig. 3.2 Schematic diagram of electron beam lithography process is shown.

First, the Si (100) substrate is cleaned following the process as mentioned section 3.2.2. Then Polymethyl methacrylate (PMMA) resist was spin coated onto the cleaned Si (100) substrate for 40 s at a speed of 5000 rpm to prepare a 1.5 μm thick layer of it. Another layer of 1 μm thick methyl methacrylate (MMA) was prepared on the PMMA layer at a rotation speed of 1500 rpm for 90 s. In this way the Si substrate was coated with the bilayer (PMMA/MMA) resist. This is because the PMMA layer is developed faster than the MMA layer forming an overhang (undercut) structure. A scanning electron microscope (Elionix ELS-7700H) was used to expose the resist with focused electrons. At first, the desired structures were designed in a computer using commercially available design software (Auto CAD). The design patterns were written onto the resist layers by accelerated electron beam controlled by the attached PC. The beam current and dose time were optimized at 100 pA and 0.9 – 1.0 μs . The substrate with the exposed resist was then dipped into the developer solutions, which helped to develop the required 3-D structure onto the resist after etching out the exposed material from the substrate.

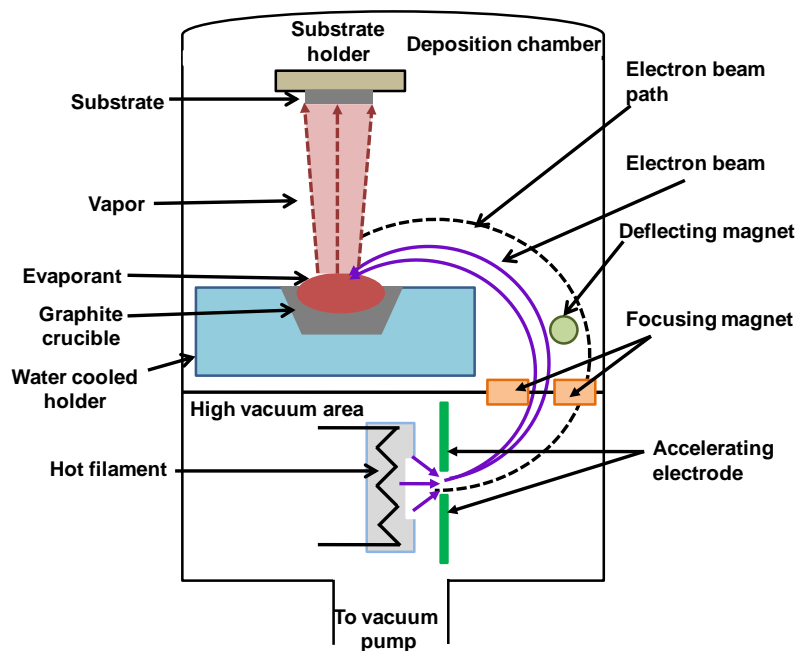


Fig. 3.3 Schematic diagram of electron beam evaporation technique is shown.

3.2.3 Electron Beam Evaporation:

Electron beam evaporation technique is one form of physical vapor deposition technique used to deposit thin film and multylayers. The schematic of the technique is shown in Fig. 3.3. First as shown in the schematic the evaporant or the material to be deposited is kept in water cooled graphite crucible. Then hot tungsten filament produces a beam of electron by thermoionic emission. The excited electron beam is guided toward the evaporant with the help of focusing and deflecting magnets. The focused electron beam is incident on the material to be deposited and the material is heated up to a boiling point and evaporated. The material evaporant move towards the substrate and condensed over the entire surface of the substrate and ultimately the material is deposited.

The patterning of the magnetic samples used for our study is done using optical or electron beam lithography technique and the deposition of the magnetic material is done by using electron beam evaporation technique. A 20 nm thick Py film was post deposited by this technique with an optimized deposition rate of 0.3 nm/s at a base pressure of 2.0×10^{-8} Torr. A 10 nm thick protective layer of silicon dioxide (SiO_2) was also deposited on top of the patterned dots and resist to protect the sample from further oxidization or degradation during the exposure of the laser beam during measurements. The lift-off technique was used to remove the unexposed resist along with the film deposited on it. A clean break-off of the film at the patterned edges of the resist was achieved because of the undercut structure of the edges. Ultimately, the substrate was dipped into acetone for 12 hrs to remove the residual resists.

3.2.4 Sputtering:

Sputtering is another type of thin film deposition technique. In sputtering the target material (to be deposited) and the substrate are kept in an ultra high vacuum chamber (Pressure $\sim 10^{-8}$ Torr) and a high voltage is applied between them so that the target material acts as cathode and the substrate acts as anode. Plasma is created within the ultrahigh vacuum chamber due to ionization of chemically inert heavy gas like Argon. Ionized sputtered gas (say Ar^+) bombards the target and sputters off the target material (say m^+) and ultimately the material is deposited on the substrate.

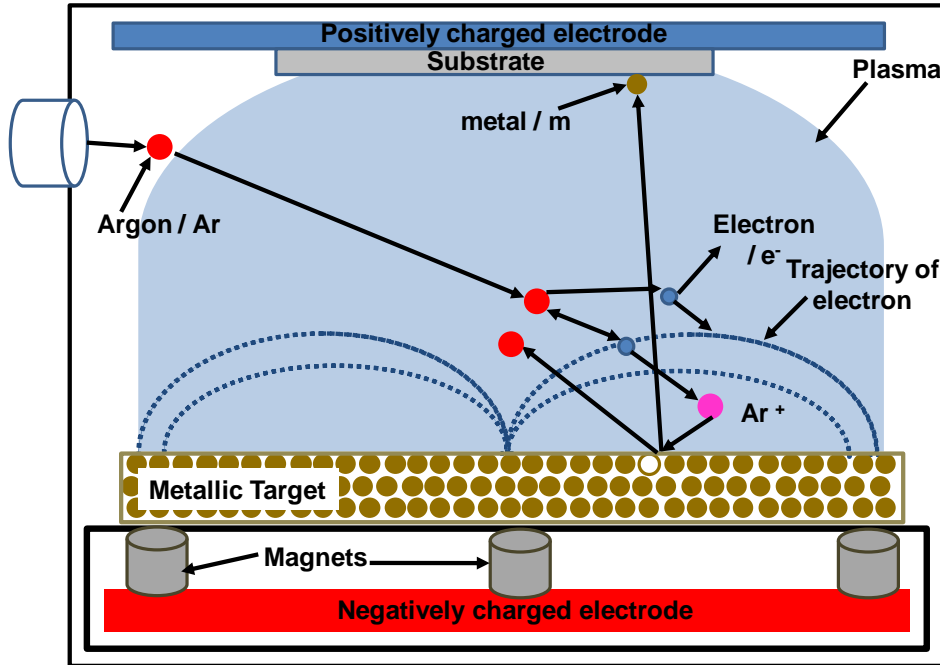


Fig. 3.4 Schematic diagram of magnetron sputtering unit is shown.

There are two major problems in above mentioned diode sputtering technique. First one is the slow deposition rate and the second one is overheating of the substrate and structural damage of the material due to the extensive bombardment of the electron to the substrate. The above mentioned problems are possible to overcome in magnetron sputtering unit. In this case array of strong permanent magnets are used behind the cathode to trap the free electrons in magnetic field directly above the target surface as shown in Fig. 3.4 which increases the probability of ionization of neutral gas (Ar) molecule by several orders of magnitude. As a result the availability of Ar^+ increases which directly increases the rate at which target material is eroded and deposited on the substrate.

3.2.5 Shadow Deposition Technique:

In shadow deposition technique, a pattern is created when a shadow mask or stencil is placed between the source of evaporated material and the substrate [16]. Previously, the shadow deposition method combined with angle deposition process was used to fabricate sub-micrometer-scale thin film structures and simple multilevel structures by single-mask lift-off processing [17]. In present case, the thick resist sidewalls of the patterns play the role as the stencil in conventional shadow deposition. Schematic illustrations of the

fabrication steps of Py/Co binary structures are shown in Fig. 3.5. First Periodic arrays of ellipsoidal patterns were defined on a 240 nm thick positive resists (UV210 from Shipley and M221Y from JSR) on top of a 60 nm bottom antireflection coating (BARC) layer on a Si substrate. A shadow area is formed on the left hand side of the pattern when the material

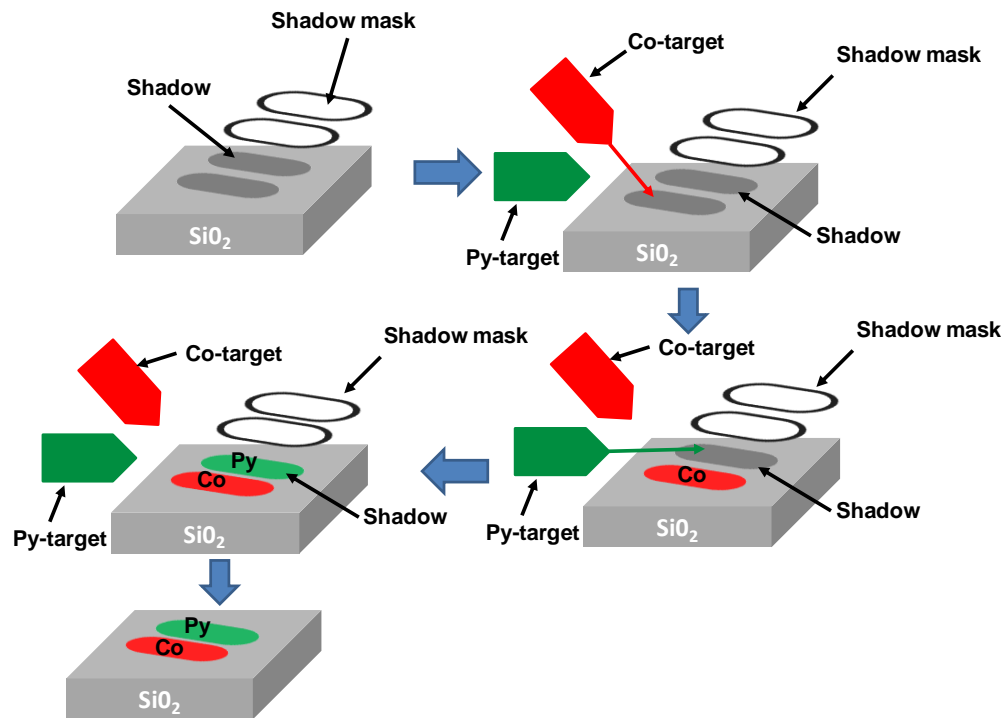


Fig. 3.5 Schematic diagram of shadow deposition is shown.

is deposited from right of the sample, while the shadow area appears on the right hand side of the patterns when the deposition is performed from the left of the sample. The shadow patterns from the two deposition processes are self-aligned by the uniform resist and precise control of deposition angle. To create Py /Co binary structures a tilt-table sample holder was specially designed and used in the shadow deposition process using the electron beam deposition chamber. The size of the shadow area can be controlled conveniently by adjusting the deposition angle. In order to ensure that the two shadow deposition processes result in geometrically identical patterns, we performed our depositions with the substrate tilted at $\pm 35^\circ$ away from the normal direction of the sample. A shadow area is formed on the left hand side of the pattern when the Py is deposited from the left of the sample due to the thick resist sidewalls, while the shadow area appears on

the right hand side of the patterns when Co is deposited from the right of the sample. A lift - off process followed the deposition of the bi-component structure.

3.3 Sample Characterization:

3.3.1 Scanning Electron Microscopy (SEM):

A scanning electron microscope (SEM) is used to investigate the surface topography and morphology of the samples. It is mainly an electron microscope that produces images of the sample by scanning it with a focused beam of electrons. The electrons interact with atoms in the sample, producing various signals that can be detected and that contain information about the sample's surface topography and composition. The schematic diagram of SEM is shown in Fig. 3.6.

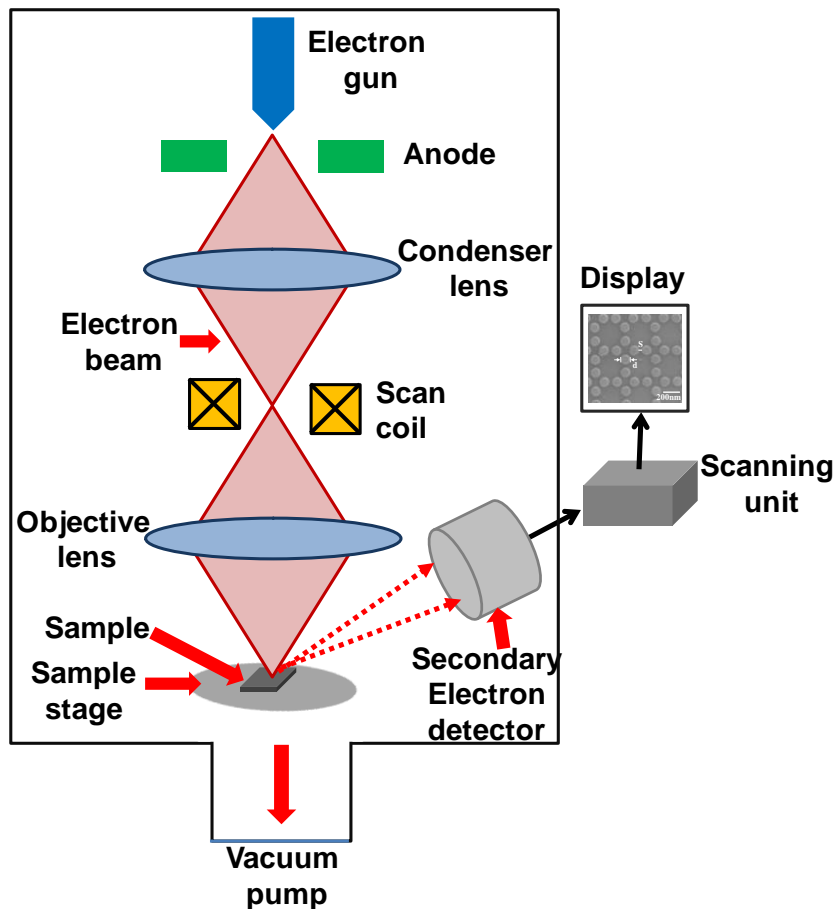


Fig. 3.6 Schematic diagram of scanning electron microscope is shown.

Chapter3

The types of signals produced by a SEM include secondary electrons (SE), backscattered electrons (BSE), characteristic X-rays and visible light (cathodoluminescence). In standard detection mode, secondary electron imaging or SEI is used which can produce very high resolution images of a sample surface, revealing details of few nm in size. Backscattered electrons (BSE) are beam electrons that are reflected from the sample by elastic scattering. BSE are often used in analytical SEM along with the spectra made from the characteristic X-rays, because the intensity of the BSE signal is strongly related to the atomic number (Z) of the specimen. BSE images can provide information about the distribution of different elements in the sample. Characteristic X-rays are emitted when the electron beam removes an inner shell electron from the sample, causing a higher energy electron to fill the shell and release energy. These characteristic X-rays are used to identify the composition and measure the abundance of elements in the sample.

In a typical SEM (Fig. 3.6), an electron beam is thermionically emitted from an electron gun fitted with a tungsten filament cathode. The electron beam, which typically has an energy ranging from 0.2 keV to 40 keV, is focused by one or two condenser lenses to a spot about 0.4 nm to 5 nm in diameter. The beam passes through pairs of scanning coils or pairs of deflector plates in the electron column, typically in the final lens, which deflects the beam in the x and y axes so that it scans in a raster fashion over a rectangular area of the sample surface. When the primary electron beam interacts with the sample, the electrons lose energy by repeated random scattering and absorption. The energy exchange between the electron beam and the sample results in the reflection of high energy electrons by elastic scattering, emission of secondary electrons by inelastic scattering and emission of electromagnetic radiation. An image of the sample surface is constructed by comparing the intensity of these electrons to the scanning primary electron beam. Finally, the image is displayed on a monitor.

SEM images have large depth of field due to a very narrow electron beam. Therefore, SEM is capable of producing three-dimensional images, which are very useful for understanding the surface structure of a sample. The samples are generally mounted rigidly on a specimen stub with carbon tape. The specimens should be electrically conductive at the surface and electrically grounded to prevent the accumulation of electrostatic charge at the surface. We

have used “FEI QUANTA 200” and “FEI Helios NanoLab 600” SEM systems to characterize our samples.

3.3.2 Energy Dispersive X-ray (EDX) Analysis:

Energy dispersive X-ray analysis is an analytical technique used to investigate elemental analysis or chemical purity of a sample. The schematic of the operation principle of EDX spectrometer is shown in Fig. 3.7.

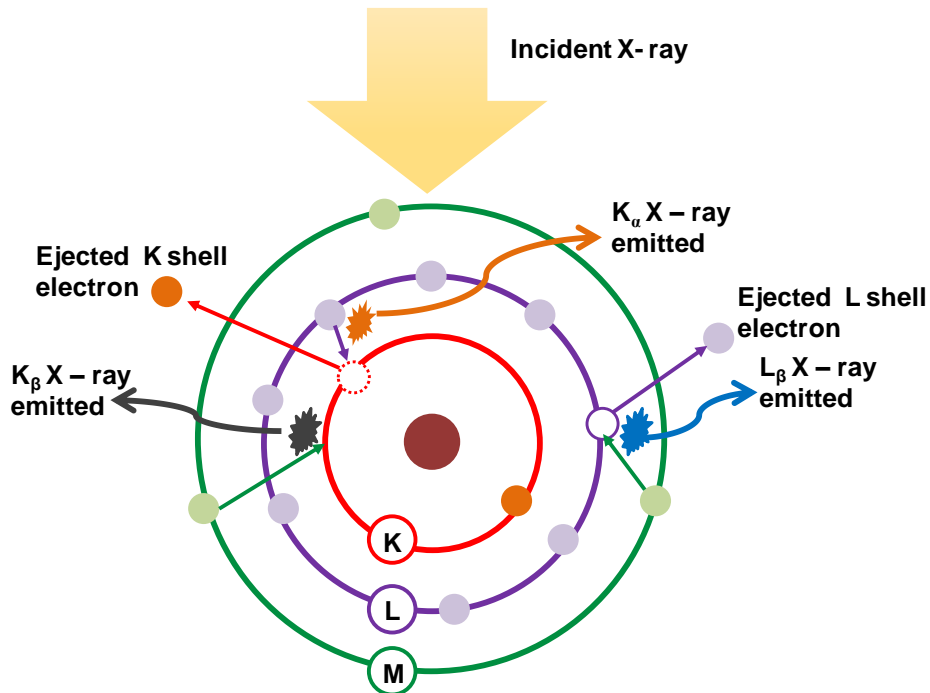


Fig. 3.7 Interaction of accelerated electrons with sample and emission of X-rays are shown schematically.

A high energy beam of charged particles such as electrons or protons, or a beam of X-rays, is focused onto the sample. At rest, an atom within the sample contains ground state (or unexcited) electrons in discrete energy levels or electron shells bound to the nucleus. The incident beam may excite an electron in an inner shell, ejecting it from the shell while creating an electron hole where the electron was. An electron from an outer, higher energy shell then fills the hole, and the difference in energy between the higher energy shell and the lower energy shell may be released in the form of an X-ray. Each element has a unique atomic structure allowing unique set of peaks in its X-ray emission

spectrum. The number and energy of the X-rays emitted from a specimen can be measured by an energy dispersive spectrometer. As the energy of the X-rays is characteristic of the difference in energy between the two shells, and of the atomic structure of the element from which they were emitted, this allows the elemental composition of the specimen to be measured. In general the EDX spectrometer is attached to SEM. We have used an EDX spectrometer from EDAX attached with “FEI QUANTA 200” SEM.

3.4 Measurement Techniques for Magnetization Dynamics:

In section 2.7 we have discussed about the basic theory of magneto-optical Kerr effect (MOKE) and different types of MOKE geometry. MOKE microscopy is a very powerful technique to measure the magnetization dynamics over a wide range of time scale. It can be used to measure the magnetic hysteresis loop and to image the magnetic domains with a sub- μm spatial resolution. Later, in 1991, Freeman *et al.* [153] first measured the picosecond magnetization dynamics of a magnetic thin film using the time resolved magneto optical Kerr effect (TR-MOKE) measurement. After that, lot of works [154] had been reported on time-resolved MOKE measurements. In 1997, Hiebert *et al.* [155] first measured the nonuniform precessional dynamics of a Ni₈₀Fe₂₀ (Py) microelement using time-resolved scanning Kerr microscopy. In 2003, Fassbender first measured [65] the time-domain propagation of magnetostatic SWs in iron garnet thin film by exciting the SWs using a short field pulse and detecting the SWs by time- and space- resolved magneto-optic Kerr magnetometry. In 2006, Barman *et al.* first measured [156] the picosecond precessioanl dynamics of a single nanomagnet using an all-optical time resolved magneto optical Kerr effect microscopy based upon two color collinear pump-probe geometry. The main advantage of all-optical TR-MOKE microscopy is that it can probe the ultrafast demagnetization as the temporal resolution is limited only by the pulse width of the laser and there is no need for complicated sample fabrication including transmission lines and photoconductive switches as was required in the earlier measurements. As we discussed in chapter 1 using this technique we can measure the ultrafast demagnetization, different relaxation processes and coherent precession of magnetization in a single measurement and in this thesis, the magnetization dynamics of different magnetic nanostructures at various time scales are measured using all-optical TR-MOKE microscopy.

3.4.1 Static Magneto-Optical Kerr Effect (Static-MOKE) Magnetometer:

Before getting into TR-MOKE microscope, we will discuss the static MOKE technique. The magnetic hysteresis loops from continuous and patterned thin film are measured by using the static MOKE Magnetometer. The schematic of this set up in shown in Fig. 3.8.

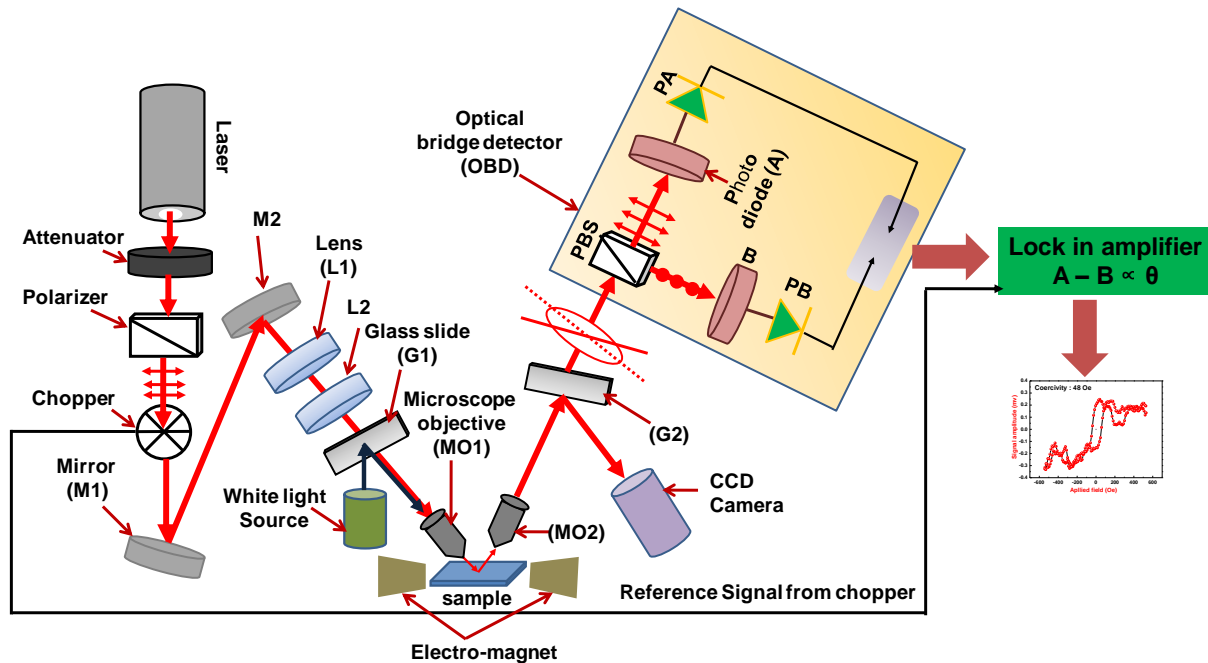


Fig. 3.8 Schematic diagram of longitudinal microfocused static MOKE setup is shown.

A continuous wavelength (CW) He – Ne laser of wavelength (λ) of 632.8 nm is used for static MOKE measurement. First the laser passes through a variable attenuator to control the intensity of the laser. Then the beam is linearly polarized with s -polarization by passing through a Glan-Thompson polarizer. The plane polarized light is mechanically chopped at 2 kHz frequency by using a chopper. The chopped beam passes through two mirrors (M1, M2) and one pair of lenses L1 ($f = 25$ mm) and L2 ($f = 150$ mm) arranged in telescopic arrangement. The telescopic arrangement is used to expand the beam waist so that it can fill the back aperture of the microscope objective (MO1). This beam is obliquely focused on the sample using a microscope objective (MO1, *magnification M* \sim 50-X, *numerical aperture N.A.* \sim 0.55) to a spot size of about 1.5 μm . The sample is placed in between two poles of an electromagnet. The reflected beam is collected by another microscope objective (MO2) and divided into two parts using a glass slide (G2). One part is sent to the CCD camera to locate

the laser spot onto the sample and another part is sent to the optical bridge detector (OBD) which measures the Kerr rotation under a balanced condition. In absence of magnetic field the balanced condition ($A = B$) of OBD is obtained by rotating the axis of the polarized beam splitter (PBS) slightly away from the 45° . But in presence of magnetic field the detector is no longer in balanced condition ($A \neq B$). The difference signal ($A - B$) is measured in a phase sensitive manner by using a lock in amplifier. The reference frequency of the lock-in amplifier is supplied by the chopper. The output signal is converted to Kerr rotation by multiplying it with a calibration factor. The calibration factor is measured by rotating the PBS by 1° on both sides of the balanced condition and the dc output of the detector is the required calibration factor. Finally the Kerr rotation which is proportional to magnetization (M) is measured as a function of the external bias field (H) to obtain the hysteresis loop of the magnetic sample. The photograph of the Static-MOKE microscope, in our lab in the S. N. Bose National Centre of Basic Sciences, Kolkata, India, are presented in Fig. 3.9.

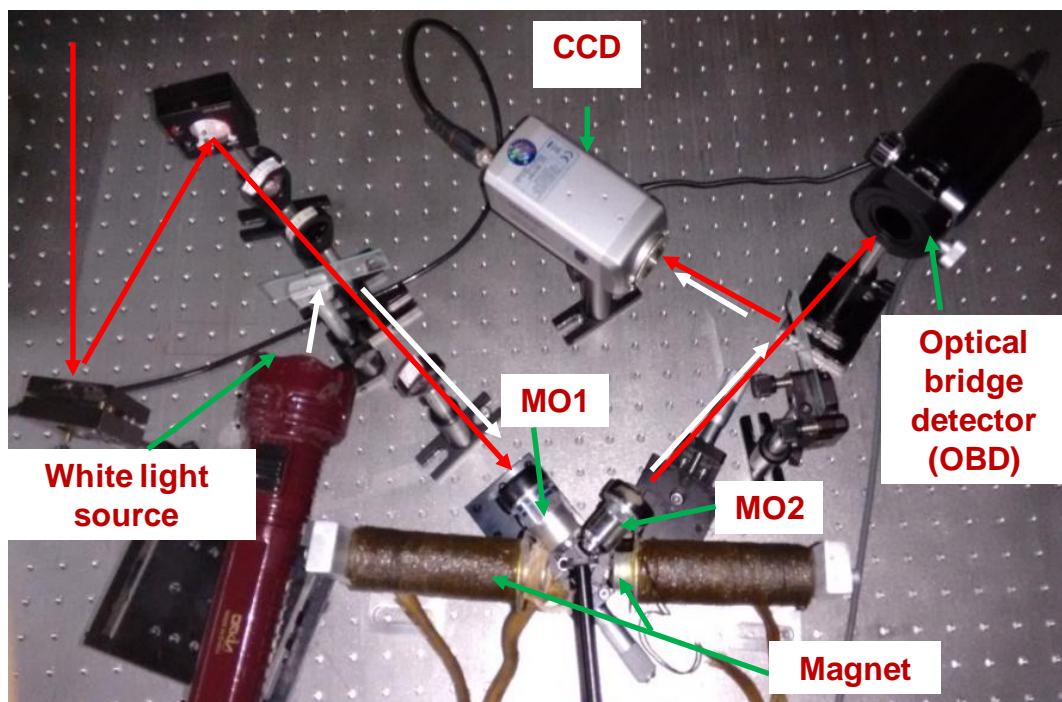


Fig. 3.9 A photograph of the focused static magneto-optical Kerr effect (MOKE) microscope in our laboratory in the S. N. Bose National Centre for Basic Sciences.

3.4.2 Time-Resolved Magneto-Optical Kerr Effect (TR-MOKE) Microscope:

As discussed earlier that all-optical TR-MOKE microscopy is very efficient tool to measure the magnetization dynamics of magnetic nanostructures over a broad range of time scale. All the TR-MOKE results presented in this thesis is measured using an all-optical TR-MOKE microscope based upon two color collinear pump-probe geometry present in our laboratory. A brief overview of the setup is given below. The photograph of the all optical TR-MOKE microscope, in our lab in the S. N. Bose National Centre of Basic Sciences, Kolkata, India, are presented in Fig. 3.10.

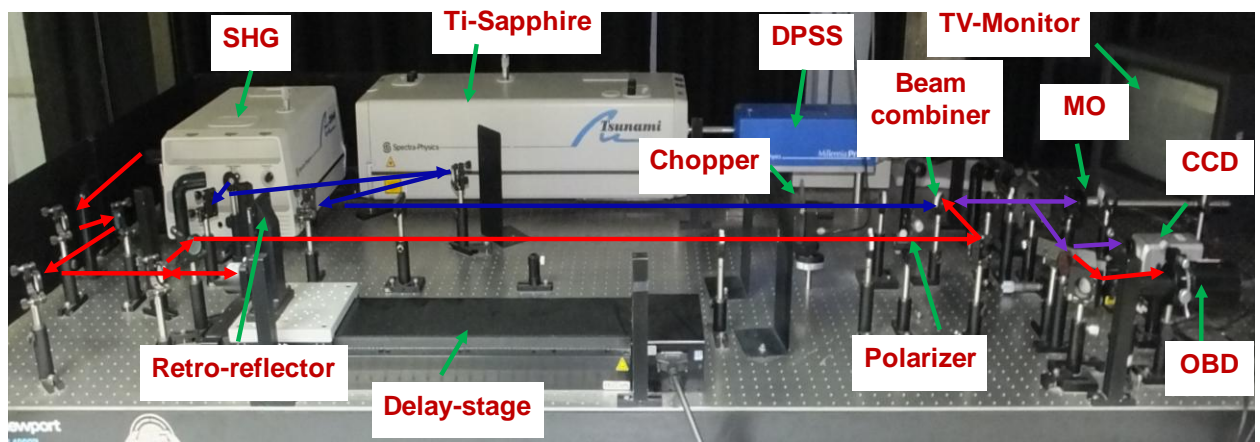


Fig. 3.10 A photograph of the all optical time-resolved magneto-optical Kerr effect (TR-MOKE) microscope in our laboratory in the S. N. Bose National Centre for Basic Sciences.

A. Description of Lasers:

Three lasers and one second harmonic generator (SHG) are used in our TR-MOKE set up. Regenerative acousto-optic mode locked Ti-Sapphire laser or Tsunami is pumped by an adjustable 10 W solid state laser (Millennia) which is again pumped by an array of diode lasers. Here we will discuss the working principles of these lasers.

a. Diode Lasers:

The diode laser bar consisting of twenty diode lasers with high brightness, high efficiency, monochromaticity and high power are used to pump the solid state laser. The output of the

laser bar is collimated with a cylindrical microlens of high numerical aperture. The asymmetric light is coupled into a multimode optical fiber bundle. The high efficiency coupling between the fiber and the diode laser bar is done using FCbar technology. Using this technology 85-90% of the laser light is transmitted by the bundle. This fiber bundle is directly connected to Millennia.

b. Diode Pumped Solid State (DPSS) Laser:

In Millennia, the high output power of the diode laser is used to pump the Nd³⁺ ions doped in a Yttrium Vanadate crystalline matrix (Nd : YVO₄) which acts as a lasing medium. The absorption transition is in red and near infrared regime. One photon of wavelength 1064 nm is emitted when there is a transition of excited electrons from ⁴F_{3/2} state to ⁴I_{1/2} state. There are also transitions at 1319 nm, 1338 nm and 946 nm but at room temperature they have lower gain with high threshold value than the 1064 nm transition. The efficiency of the solid state laser can be improved by maximizing the overlap of the regions of the active medium excited by the pumping source with the region in the laser gain medium. As a result the output of the diode laser will be focused on the active region in such a way that the radius of TEM₀₀ mode will exactly match with it (mode matching). In general, the radius of TEM₀₀ mode is made very small to minimize the solid state laser threshold.

A noncritically, phase-matched, temperature tuned lithium triborate (LBO) nonlinear crystal is used to convert the infrared output with $\lambda = 1064$ nm to visible light with $\lambda = 532$ nm. The nonlinear coefficient of LBO crystal is low but it offers a large acceptance angle which makes it insensitive with slight misalignment of the cavity. It also has a property to keep the fundamental and second harmonic beams collinear (critically phase-matched) and that can be optimized for maximum conversion by changing its temperature (temperature tuned). As a result it is used for frequency doubling in Millennia.

c. Mode Locked Ti-Sapphire Laser:

In Tsunami, Ti³⁺ ion doped sapphire (Al₂O₃) crystal is used as a lasing medium. The absorption transition occurs over a broad range of wavelength from 400 nm to 600 nm. The fluorescence band extends from 600 nm to 1100 nm. As a result the lasing action is

possible at wavelength greater than 670 nm because the long wavelength side of the absorption spectra overlaps with the short wavelength side of the fluorescence spectra.

The Main Features of Ti-Sapphire Laser:

- ✓ Ten mirror folded cavity is used to make a longer cavity than that in a CW laser so that Tsunami can act as a mode locked laser with a repetition frequency ~ 80 MHz.
- ✓ The astigmatism is virtually eliminated by selecting the angles of the cavity focus mirror and the rod length.
- ✓ The acousto-optic modulator (AOM) driven by regenerative rf signal allows the laser to operate for longer time without any dropouts.
- ✓ The wavelength tuning range in Tsunami laser is 690 nm to 1080 nm. The wavelength can be tuned using a four prism sequence and a tuning slit. The prism sequence provides region in the cavity where the wavelengths are spatially spread and by changing the horizontal and vertical positions of the slit the output wavelength can be tuned.
- ✓ The pulse width in Tsunami laser can be tuned from about 70 fs to 150 fs. The pulse width can be tuned by changing the net group velocity dispersion (GVD) of the cavity. The optical components within the cavity introduce positive GVD which causes a pulse spreading. In Tsunami, the four prism sequence is used to provide a negative GVD which compensate the pulse spreading. The net interactive GVD can be changed by translating the prisms perpendicular to their bases using a single micrometer screw.

d. Second Harmonic Generator (SHG):

Frequency doubler or second harmonic generator (SHG) is used to double the frequency of the fundamental beam from the Ti-Sapphire laser. Thin type-I angle tuned Barium Beta Borate (BBO) crystal is used for that purpose. The advantage of thin BBO crystal is:

- ✓ The conversion efficiency is high compare to any other SHG (LBO) crystal.

- ✓ It does not require any heater like LBO crystal.
- ✓ It minimizes the pulse broadening problem due to group velocity dispersion (GVD).
- ✓ No compensating crystal is required.
- ✓ Only a single SHG crystal is enough to phase-match over the entire wavelength tuning range (690 nm to 1080 nm).

The second harmonic output power ($P_{2\omega}$) is given by:

$$P_{2\omega} \propto \frac{d_{eff}^2 P_\omega^2 l^2 [\phi]}{A} \quad (3.3)$$

Here, d_{eff} is the effective nonlinear coefficient, P_ω is the fundamental input power, l is the crystal length, $[\phi]$ is the phase matching factor and A is the cross sectional area of the beam in the crystal.

The second harmonic output power can be optimized by controlling $[\phi]$ which is done by rotating the SHG crystal horizontally about its vertical axis and by decreasing A which is done by minimizing the beam waist.

B. Description of the Set up:

- ✓ The TR_MOKE set up is developed on an L-shaped vibration isolation optical table (Newport RS4000 series). The core of the table is filled up by broadband and tuned hydraulic damper to damp out the acoustic vibration. The mechanical vibration originating from the ground can be eliminated by placing the table on top of vibration isolation in floating condition. The flatness of the table surface is ± 0.1 mm over 600×600 mm² areas. There are square array of holes of 25 mm grid to mount the optics and lasers. The schematic diagram of the TR-MOKE microscope is shown in Fig. 3.11.
- ✓ A solid state laser (Millennia) is pumped by an array diode lasers to produce a maximum output power of 10 W at $\lambda = 532$ nm which is used to pump the Ti-sapphire laser (Tsunami). Regenerative mode locking mechanism in Tsunami

produces a train of laser with maximum average power of 1.64 W at a repetition rate of 80 MHz (25 nJ/pulse). The output wavelength can be tuned from 690 nm to 1080 nm. But for stable operation and for better spectral response of the Si based detectors the output is kept fixed at around 800 nm in our experiments.

- ✓ A very small part of the vertically polarized output laser beam from Ti-sapphire oscillator of spot size 2 mm is sent to an autocorrelator (pulseCheck, A.P.E.) to check the pulse width of the laser beam. The pulse width of the laser beam is found to be around 80 fs.
- ✓ The major part of the 800 nm laser beam is split into two further parts by a 70:30 beam splitter (B2). The intense part is frequency doubled ($\lambda = 400$ nm) by passing into a second harmonic generator (type-I BBO crystal) with pulse width ~ 100 fs. This beam is used to pump the sample.
- ✓ A broad band mirror MB1 (wavelength range ~ 500 nm to 750 nm) and spectral filter FB1 is placed in pump path to filter out the residual fundamental beam. The pump beam is reflected by two highly reflecting mirrors MB2, MB3 and passes through a fixed optical delay. The intensity of the pump beam is controlled by placing a variable attenuator (A2) in the pump path which can be translated across the pump beam with the help of a linear stage. The pump beam is modulated by a mechanical chopper at a frequency of 2 kHz which is used as a reference signal in the lock-in amplifier.
- ✓ The fundamental beam is guided by using a set of highly reflecting mirrors (MR1, MR2, MR3 and MR4) and reflected back from a broadband hollow retro-reflector (Newport, UBBR1-2S) placed on a motorized delay stage (Newport, (M-) IMS series). The retro-reflector is constructed of three front-surface flat mirrors assembled into a corner cube, which can reflect the beam in such a way that the reflected beam is parallel to the incident one independent of the angle of incidence. By moving the retro-reflector back and forth on the delay stage by using a motion controller (Newport, EPS301) we can vary the optical path of the fundamental beam. This

beam is used to probe the magnetization dynamics. The fluence of the probe beam is controlled by using a variable attenuator (A1).

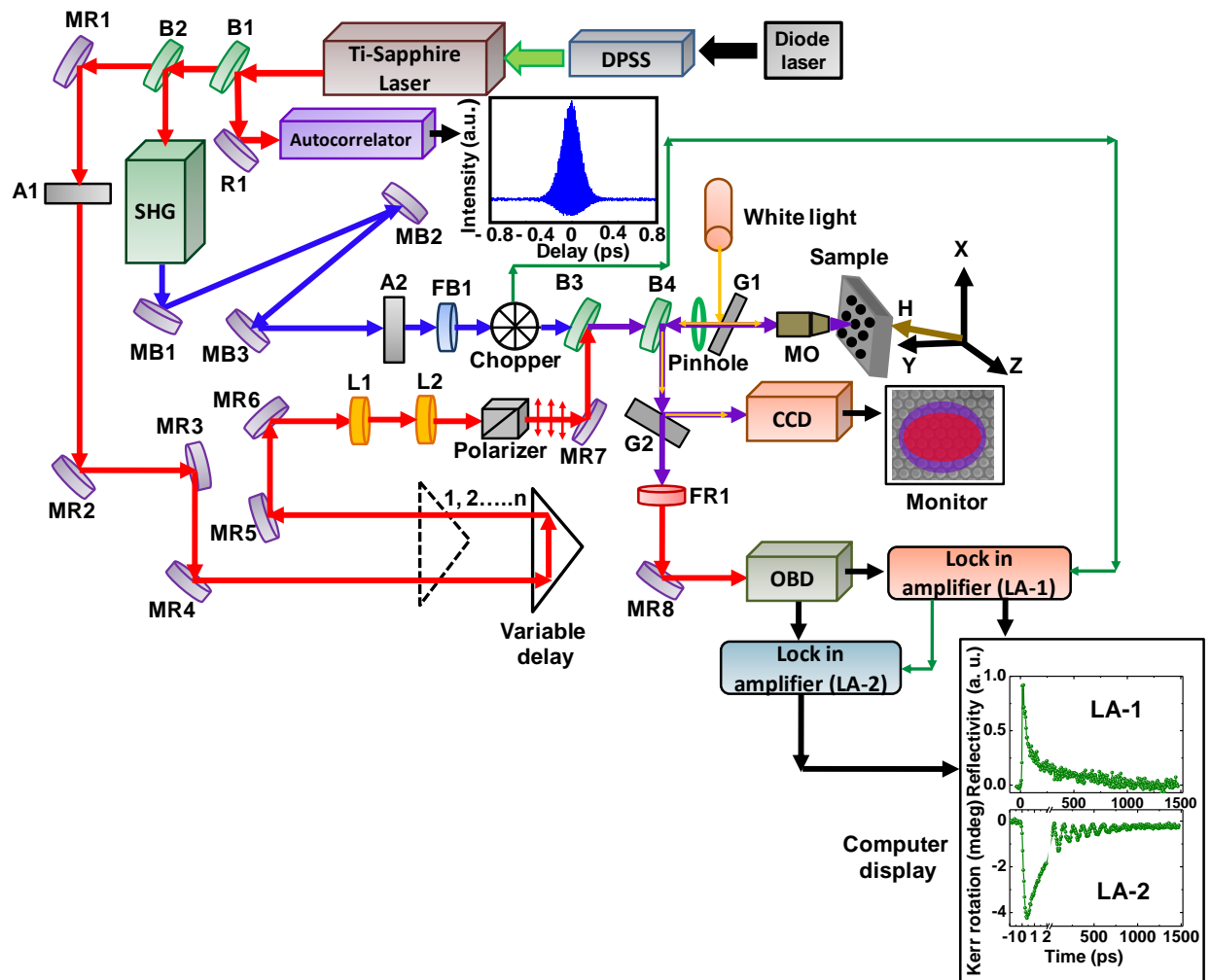


Fig. 3.11 Schematic diagram of all-optical time-resolved magneto-optical Kerr effect (TR-MOKE) microscope with collinear pump probe geometry is shown.

- ✓ A pair of lenses L1 ($f = 75 \text{ mm}$) and L2 ($f = 200 \text{ mm}$) are arranged in a telescopic arrangement and is placed in the probe path to collimate the beam and to increase the beam diameter so that it can fill the back aperture of the microscope objective. The probe beam is passed through a Glan-Thompson polarizer to refine the polarization state of the probe beam.

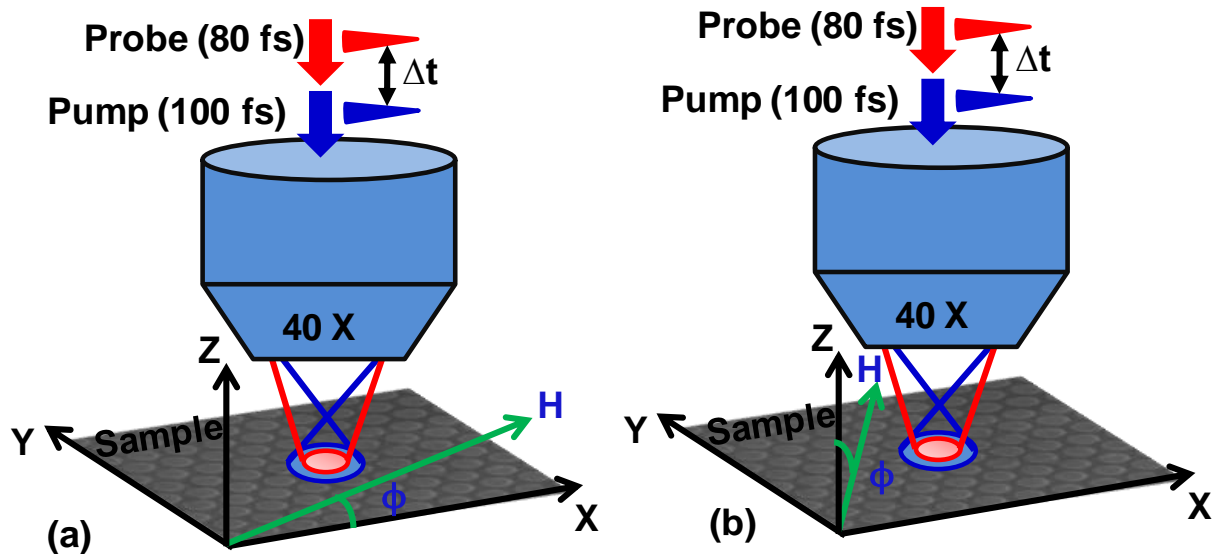


Fig. 3.12 Schematic diagrams of the collinear geometry of pump and probe beams focused by the microscope objective (MO) on the sample surface with (a) in-plane and (b) out of plane bias magnetic field (H).

- ✓ Both pump and probe beams are combined with the help of a 50:50 non polarized beam splitter (B3) placed at 45° to the probe beam path. Both the beams are collinearly focused on the sample by using a microscope objective (Newport, M-40X) of N. A. = 0.65. At the focal plane of the probe (diameter ≈ 800 nm), i.e., on the sample surface, the pump beam is slightly defocused, and has a larger diameter ($\approx 1\mu\text{m}$) than the probe beam, which makes it easier to overlap the pump and probe beams on the sample surface as shown in Fig. 3.12. The sample is mounted on a computer controlled piezo-electronic scanning X-Y-Z stage with a feedback loop.

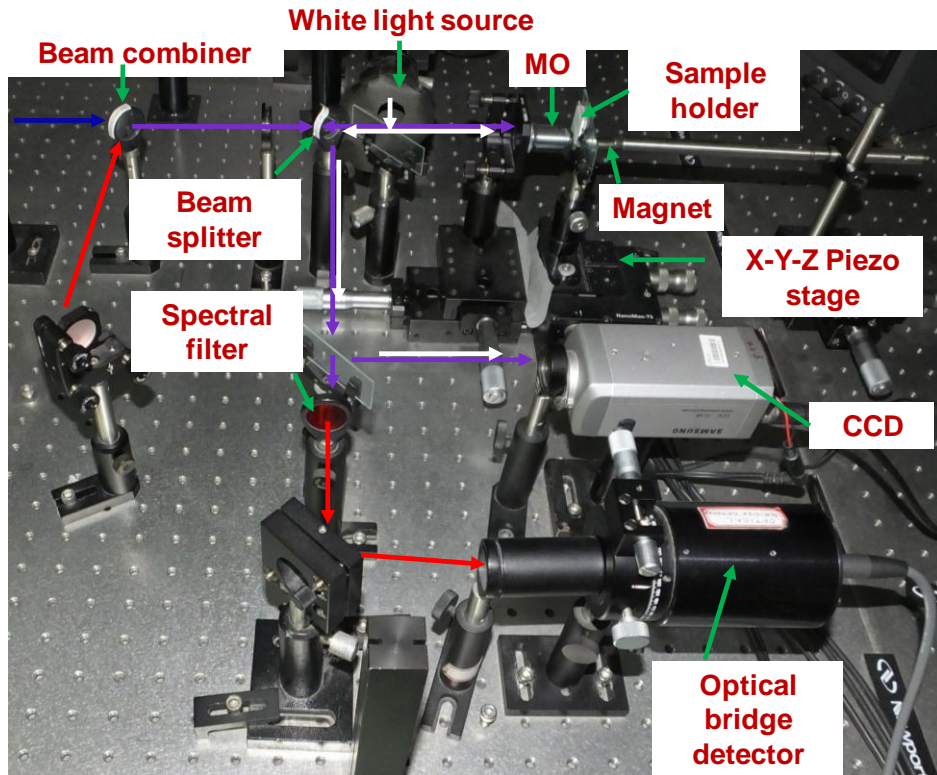


Fig. 3.13 A photograph of the enlarged view of the detection procedure. The important components in the set up are labeled in the figures.

- ✓ Both the back reflected pump and probe beams are collected by the same microscope objective and reflected by the beam splitter B4 which is placed at 90° w.r.t., the incident beam. One small part of the reflected beam is sent to CCD camera for viewing the overlap of pump and probe beams on the sample surface. The remaining part is sent to the optical bridge detector (OBD) after filtering the pump beam by using a spectral filter (FR). The optical bridge detector measures the Kerr rotation under balanced condition and separates it from the total reflectivity signal. Two separate lock-in amplifiers are used to measure the Kerr rotation and reflectivity in a phase sensitive manner. The enlarged view of the detection procedure used in our experiment is shown in Fig. 3.13.

- ✓ The white light is use to view the sample and to locate the exact position of the pump and probe beams on the sample. The white light is reflected by a glass slide (G1) placed in between B4 and MO and is focused onto the sample surface through

the MO. The back-reflected white light from the sample enters into the CCD camera after reflection from B3 and the glass slide (G2).

- ✓ An external magnetic field (H) is applied at a small angle (10°) to the sample plane to create an out-of-plane component of the bias magnetic field which creates a finite demagnetizing field within the sample along the direction of the pump pulse. This is eventually modified by the pump pulse to induce a precessional motion of magnetization within the samples.

C. Working Principle of Optical Autocorrelators:

Optical autocorrelator is mainly used to measure the duration of ultrashort laser pulses with picoseconds or femtosecond duration. As shown in Fig. 3.14, it contains a beam splitter, Michelson interferometer and a non-linear crystal. First the beam splitter (BS) splits the incoming pulse into two equal orthogonal pulses. These two pulses are sent to two arms of Michelson interferometer (MI). The relative timing of the pulses can be adjusted by varying the arm length difference of MI. The superimposed copies of the pulse collinearly propagate and incident on a nonlinear crystal and sum frequency generation is occurred. The two pulses can superimpose constructively or destructively depending upon the difference of the arm length of MI. For small arm length difference, perfect constructive interference occurs and the amplitude of the superimposed pulse is twice as compared to the amplitude of a single pulse. As a result the intensity of the combined pulse increases four times of the background. After frequency doubling, the intensity becomes sixteen times more than the background. In contrary, for a large arm length difference, the pulses do not overlap in the nonlinear crystal and the intensity is only twice of that of a single pulse. Hence, the peak signal is eight times higher than the background. The autocorrelation signal is plotted as a function time delay which is nothing but the arm length difference of MI. The pulse width can be calculated by fitting the plotted data with the theoretical autocorrelation curve considering the shape of the pulse (Gaussian or hyperbolic secant).

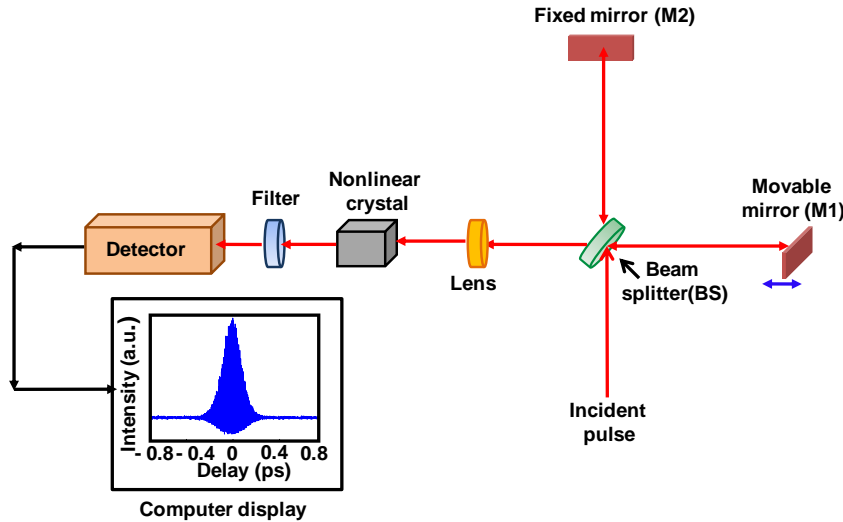


Fig. 3.14 Schematic diagram of the optical autocorrelator is shown.

D. Working Principle of Optical Bridge Detector:

The polar Kerr rotation is measured by using an optical bridge detector (OBD). The schematic diagram of the optical bridge detector is shown in Fig. 3.15. The OBD splits the incident polarized beam into two orthogonally polarized components by a polarized beam splitter (PBS). The intensities of two beams are then measured by two Si-photodiodes PA and PB. The outputs of these two photodiodes are then amplified by using pre-amplifiers PAs and used as inputs for two operational amplifiers (Op-Amps) to measure the total signal ($A+B$) and the difference signal ($A-B$). Initially the PBS is placed at 45° to the light incident on the OBD so that when a linearly polarized probe beam (in absence of pump beam) passes through the PBS, the intensities of lights in two orthogonal components of polarization are identical, giving rise to a "balance" in the bridge ($A - B = 0$). When the pump beam excites the sample, the plane of polarization of the probe beam rotates due to magneto-optical Kerr effect. This Kerr rotation modifies the intensities in the two orthogonal components of polarization and gives rise to a finite electronic signal at the output of the optical bridge detector ($A - B \neq 0$). Therefore, measurement of $(A - B)$ as a function of time delay gives information about the magnetization dynamics including ultrafast demagnetization, relaxations, magnetization precession and damping. On the

other hand, the sum of output of two photodiode ($A + B$) gives the total reflectivity signal which gives information about the carrier and phonon dynamics of the sample.

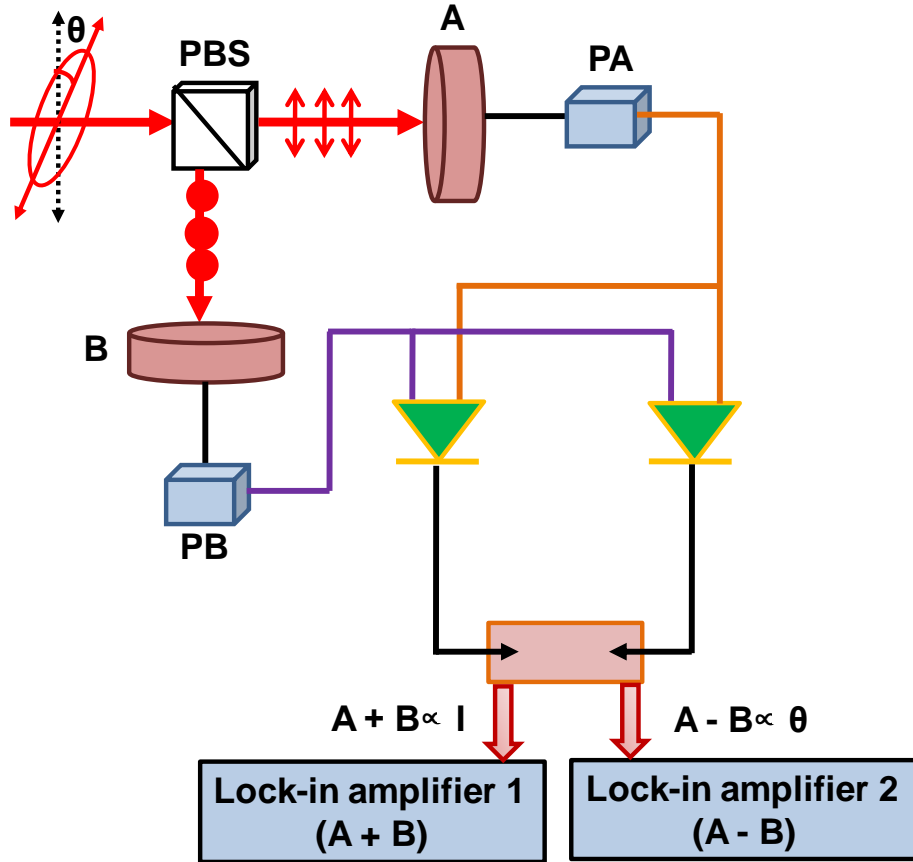


Fig. 3.15 Schematic diagram of the optical bridge detector is shown.

E. Working Principle of Lock-in Amplifier:

The outputs of these two Op-Amps ($A + B$ and $A - B$) are measured by the lock-in-amplifiers (SR830) using a phase sensitive detection which means that it detects the response at reference frequency and rejects the other frequencies. In our experiment the reference frequency of the lock-in amplifier is the chopper frequency.

The lock-in reference is

$$V_{ref} = V_L \sin(\omega_L t + \theta_{ref}) \quad (3.4)$$

The input signal is

$$V_{sig} = V_s \sin(\omega_R t + \theta_{sig}) \quad (3.5)$$

here, ω_L and ω_R are the reference frequency and input frequency, respectively.

The output of the phase sensitive detection (PSD) (V_{psd}) is the product of Eqns. (3.4) and (3.5)

$$V_{psd} = V_s V_L \sin(\omega_R t + \theta_{sig}) \sin(\omega_L t + \theta_{ref})$$

$$V_{psd} = \frac{1}{2} V_s V_L [\cos\{(\omega_R - \omega_L)t + (\theta_{sig} - \theta_{ref})\} - \cos\{(\omega_R + \omega_L)t + (\theta_{sig} + \theta_{ref})\}] \quad (3.6)$$

If the PSD output is passed through a low pass filter, then at $\omega_R = \omega_L$, the filtered PSD output will be a DC signal and the expression will be

$$v_{psd} = \frac{1}{2} V_s V_L \cos(\theta_{sig} - \theta_{ref}) \quad (3.7)$$

Thus we will be able to detect the signal whose frequency is very close to the reference frequency. The signals with frequencies other than reference frequency will be rejected.

F. Alignment of the Set Up:

- ✓ First we monitor the power spectrum of the output beam from Tsunami by a fiber optic spectrometer (Ocean Optics, Model no. USB4000). The power and spectrum of the output of Tsunami is optimized with the help of the external micrometer controllers of the Tsunami. The wavelength of the Tsunami is fixed at around 800 nm, the FWHM is kept ~ 12 nm and power of the fundamental laser beam (800 nm) is ~ 1.64 Watt with a pump power of 8 Watt from the DPSS at 532 nm.

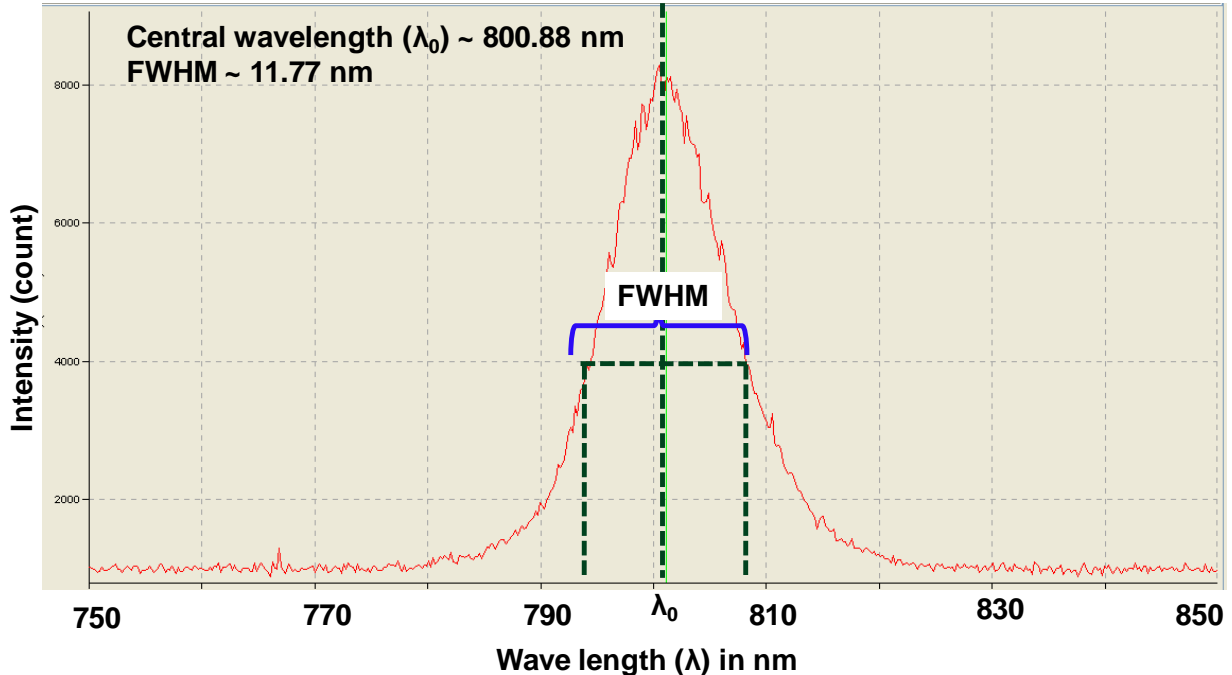


Fig. 3.16 A typical mode-locked power spectrum of the output beam from Tsunami

- ✓ The alignment of the retro-reflector is checked by placing the 'beam height' after B3 and by moving the retro-reflector from extreme left side to extreme right side of the delay stage. If there is a shift of the probe beam with the movement of the retro-reflector, then we have to align the retro reflector. To align the retro reflector the 'beam height' is placed after the mirror MR6. When the retro-reflector is at the left side, the beam is adjusted by mirror MR3 with the help of its screws. The beam should go through the middle of the hole in the 'beam height'. The retro-reflector is then moved to the extreme right side of the delay stage. The position of the beam in 'beam height' will be shifted which brings back to its previous position (middle of the hole in the 'beam height') with the help of mirror MR4. This procedure is continued iteratively till the beam position remains unchanged when the retro-reflector is placed at two extreme ends of the delay stage.
- ✓ To check the collinearity of the pump and probe beams first the 'beam height' is placed after the beam combiner (B3). Both the beams should go through the middle of the hole in the 'beam height' if both the beams are collinear. Any misalignment can be fixed with the help of mirrors MB1, MB3 and MR6 and MR7. The overlap of

the pump and probe beams are also checked by observing their images on the monitor attached to the CCD camera.

- ✓ To check whether the pump and probe beams are co-axial with MO, the MO is moved back and forth by using a micrometer screw. The pump and probe beams will be focused and defocused with this movement of the MO, which can be monitored in the TV screen. If there is a movement of the centre of pump/probe beam along horizontal or vertical direction, we can conclude that beams are not co-axial with MO. To fix this misalignment the beams are need to move to opposite direction with the help of the mirrors MB1, MB3 and MR6 and MR7.
- ✓ Finally, we need to align the OBD. The beam is incident on the centre of the front aperture of the OBD with the help of mirror MR8. The back reflected beams are made collinear to the incident beam by placing an aperture in the incident beam path little before the OBD and rotating the OBD around its horizontal and vertical axes to bring the back-reflected beams back to the aperture. This ensures that the incident beam and the axis of the detector are collinear.

G. Optimization of the Setup Using Standard Silicon (Si) Wafer:

After this alignment to optimize the set up by measuring the reflectivity signal we use Si (100) wafer as a standard sample. For our set up at a reasonably good alignment the maximum reflectivity signal from this standard sample should be above $600 \mu\text{V}$ if the pump and probe fluence are $\sim 10 \text{ mJ/cm}^2$ and 2 mJ/cm^2 , respectively. To achieve the required reflectivity signal, we need to improve the overlap of pump and probe beams with the help of the mirrors MB1, MB3, MR6 and MR7. After achieving the desired alignment we measure the time-resolved reflectivity signal from the Si wafer for about $\sim 2000 \text{ ps}$. The reflectivity increases to a maximum value right after the zero delay and then decays exponentially as the time delay increases. For a good alignment the decay constant is 200 ps . A faster decay indicates a loss of spatial overlap of pump and probe beams for longer time delays. The reflectivity signal is optimized for 3-4 different time delays to achieve the desired decay constant. This process is repeated unless the desired decay constant is obtained. Once the whole alignment is done, the set up is ready for measurement.

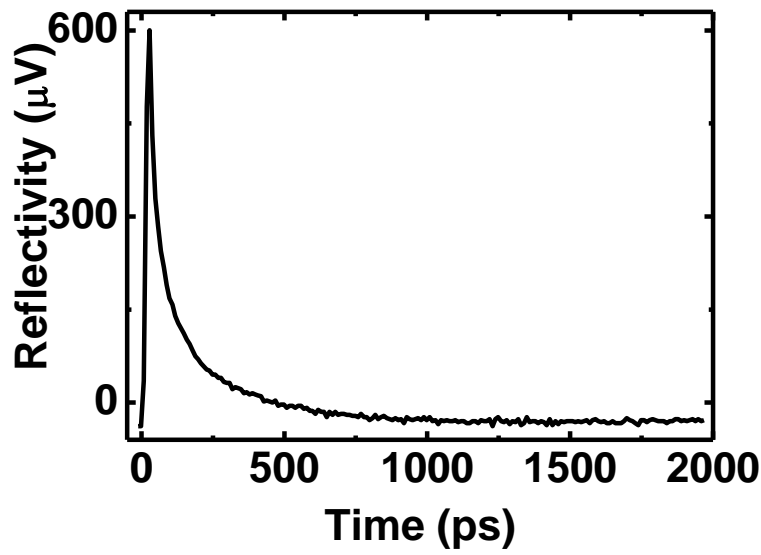


Fig. 3.17 The reflectivity signal obtained from a Si (100) wafer as a function of the time delay between the pump and the probe beams. The decay of the reflectivity signal after the zero delay can be fitted with a double exponential decay function to obtain the time constant of the longer decay which is about 195 ps in our case.

H. Optimization of the Setup Using a Standard Ni₈₀Fe₂₀ Film:

Before measuring the in-plane magnetization dynamics of any unknown magnetic samples, we measure the ultrafast magnetization dynamics and damping of standard $10 \times 10 \mu\text{m}^2$ blanket Ni₈₀Fe₂₀ film to check the overlap of pump and probe beam at a longer time delay for magnetic samples. In plane bias magnetic field (H) of 1.15 kOe (well above the saturation field) is applied parallel to the edge of the film along x -axis as shown in the Fig. 3.18(a).

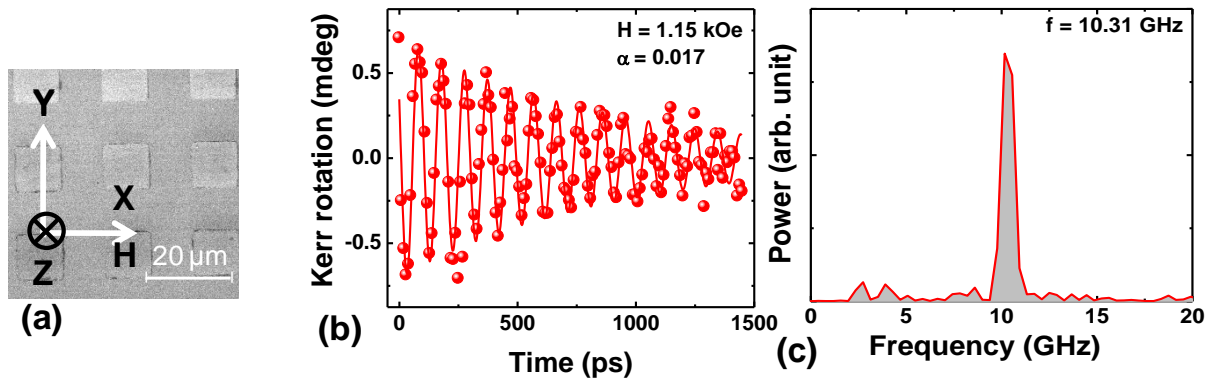


Fig. 3.18 (a) SEM image of an array of $10 \times 10 \mu\text{m}^2$ blanket $\text{Ni}_{80}\text{Fe}_{20}$ thin film with 25 nm thickness. The schematic of the experimental geometry of bias magnetic field is shown on the image. (b) The typical time-resolved Kerr rotation data (solid circles) from this film at a bias field (H) of 1.15 kOe, applied along the positive x - axis is shown. The solid line corresponds to the fit with Eqn. (3.8). (c) The corresponding FFT power spectra showing the resonant mode.

The time-resolved Kerr rotation data is fitted as shown in Fig. 3.18(b) with a damped sine curve given by

$$M(t) = M(0)e^{\frac{-t}{\tau}} \sin(2\pi f t - \phi) \quad (3.8)$$

The relaxation time τ is related to the damping coefficient α by the relation

$$\tau = \frac{1}{2\pi f \alpha} \quad (3.9)$$

where f is the frequency of the uniform mode and ϕ is the initial phase of oscillation. For standard $\text{Ni}_{80}\text{Fe}_{20}$ film the damping value (α) should be around 0.017. In our case the extracted damping value (α) is 0.017 which ensure us that the alignment is good for measuring the magnetization dynamics of any in-plane magnetized unknown sample.

4. Micromagnetic Simulations

4.1 Introduction:

The magnetization dynamics can be calculated by solving the nonlinear Landau-Lifshitz-Gilbert (LLG) equation by linearizing it under small angle approximation. For uniform magnetized samples the magnetization dynamics can be calculated considering macrospin model. But for finite magnetic structures, the magnetization is not uniform due to non uniform nature of the demagnetizing field. Magnetization dynamics of nonuniform magnetized samples can be solved by considering discrete spin model. But it is difficult to calculate the internal spin configuration of micron or submicron sized magnetic structures using discrete spin system due to limitations of computational resources. To overcome these problems scientists proposed the micromagnetic continuum theory which acts as a bridge between the macrospin formalism and discrete spin model. According to this theory, the magnetization is a continuous function of position and the sample is divided into large number of cells and the dynamic motion of each cell is considered as a macrospin interacting with the neighbouring cells by short-range exchange and long-range dipolar interactions as well as magnetocrystalline anisotropy and external magnetic fields. The LLG equation of motion is solved for each cell.

4.2 Micromagnetic Numerical Simulations:

The LLG equation is

$$\frac{d}{dt} M = -\gamma(M \times H_{\text{eff}}) + \frac{\alpha}{M_s}(M \times \frac{dM}{dt}) \quad (4.1)$$

where, M is the instantaneous magnetization, M_s is the saturation magnetization and H_{eff} is the effective magnetization. The LLG equation is an ordinary differential equation (ODE) in time which includes the exchange interaction, dipolar interaction, magnetocrystalline anisotropy and the Zeeman field. This equation can be solved by using standard ODE

solvers like Runge Kutta method or Euler method. The LLG equation can be solved numerically with the help of the finite difference method (FDM) or finite element method (FEM) [157-158].

In finite difference method (FDM) the continuous solution domain is replaced by a discrete set of lattice points. Each lattice points are replaced by the FD operators and the conditions on the boundary of the domain is replaced by their discrete counterparts. The space is discretized by regular cubic lattice. As a result for complicated geometry like curved boundary or irregular microstructures FDM creates some artificial edge roughness unless used with care.

The finite element method (FEM) can solve the above mentioned problem. For FEM the solution domain is discretized into finite elements. Depending upon the dimension of the problem, these can be triangles, squares, or rectangles in two dimensions or tetrahedrons, cubes, or hexahedra for three-dimensional problems. As a result it is easier to construct complex geometries using this method. However, this method is much slower as compared to the FDM and for larger problems it is easier and reasonable to use FDM as opposed to FEM.

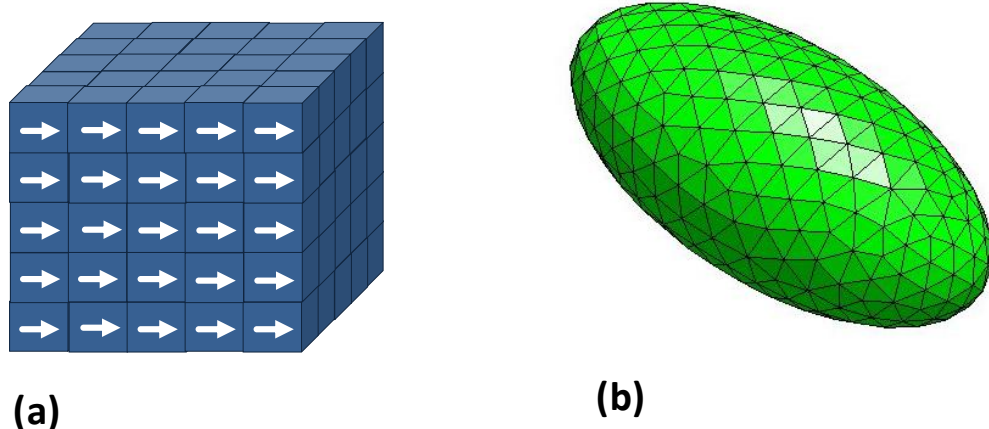


Fig. 4.1 The schematic diagrams show the discretization of a rectangular sample into a number of (a) cuboidal cells with equal size for FDM and (b) tetrahedral cells with varying size for FEM based simulation.

Different types of micromagnetic simulators [159]:

Name of the software	Developer	Open source	Method	Source website
Object Oriented Micromagnetic Frameworks (OOMMF)	M. Donahue and D. Porter	Free	FDM	http://math.nist.gov/oommf/
NMAG	H. Fangohr and F. Fischbacher	Free	FEM	http://nmag.soton.ac.uk
MAGPAR	Werner Scholtz	Free	FEM	http://magnet.atp.tuwien.ac.at/sc_holz/magpar
LLG Simulator	M. R. Scheinfein	Paid	FDM	http://llgmicro.home.mindspring.com/
MicroMagus	D. V. Berkov and N. L. Gorn	Paid	FDM	http://www.micromagus.de/

One can obtain reliable numerical solutions of a system by using any one of the above mentioned codes. All numerical calculations results using the above mentioned codes are valid for time scales longer than 1ps and dimensions greater than 1 nm. The phenomena associated with sub-picosecond timescales like ultrafast demagnetization and heat-induced magnetic switching can be simulated by using a free open source software package named Vampire (source website: <http://vampire.york.ac.uk/>). It also has a provision to run atomistic simulation which bridges the gap between micromagnetic approaches and electronic structure calculations by treating the magnetic material at the natural atomic length scale ($\sim \text{\AA}$).

NMAG is another software which solved the LLG equation by using FEM. In NMAG the sample or space is discretized into small tetrahedral cells as shown in Fig. 4.1(b) [160]. The advantage of this method over OOMMF's approach is that curved and spherical geometries can be spatially resolved much more accurately. However, this method is less efficient in calculating the demagnetizing field of a thin film than OOMMF's approach.

In this thesis, the precessional magnetization dynamics has been simulated by using OOMMF and the magnetostatic stray field profiles has been calculated by using LLG micromagnetic simulator. In addition a MATLAB based code named Dotmag developed within our group has been used for simulation of power and phase profiles of the spin wave modes.

4.3 Object Oriented Micromagnetic Framework (OOMMF):

OOMMF [161] is developed by M. Donahue and D. Porter in the Information Technology Laboratory (ITL) at the National Institute of Standards and Technology (NIST) in 1999. The software is written in C++ and Tcl. In OOMMF, the LLG equation is solved by using FDM. The input parameters and the initial conditions of any problem are specified in OOMMF micromagnetic input format (MIF). The micromagnetic simulation is performed considering $T = 0$ K. Most of the free softwares available for micromagnetic simulations are simulate at $T = 0$ K. Some commercial softwares offer finite temperature option. However, temperature does not significantly affect the SWs in the magnetostatic regime as studied here. The solution domain is divided into rectangular prism-like cells having same dimensions. The linear dimensions of the cells are less or equal to the exchange length, which is defined as $(A/2\pi M^2)^{1/2}$ where A is the exchange constant and M is the magnetization, respectively. It calculates the total energy within individual cells by considering exchange energy, self magnetostatic energy, magnetocrystalline anisotropy energy and Zeeman energy. The magnetization configuration is updated by two types of evolvers from one step to another step. First one is a time evolver which tracks the LLG dynamics and another one is an energy minimization evolver which calculates the local minima in energy by using energy minimization techniques. A 4th order Runge Kutta evolver is used as a time evolver to solve LLG equation as on ODE in time. There are two

drivers, namely time driver and minimization driver, which control the time and minimization evolver, respectively. Depending upon the stopping criteria described in the MIF the driver will determine whether the simulation stage will be stopped or continued. In the MIF, users provide either the stopping time or the stopping value of dm/dt . The stopping value in the MIF is set in such a way that the value of maximum torque ($m \times H$) should be less than 10^{-6} A/m. When the stopping criteria will match, the simulation will terminate.

The advantage of OOMMF software is that it is a collection of programs and each program can be modified or redesigned without changing the entire system. It has a good magnetization file display program (mmDisp) which can display the initial magnetization profile, demag field profile, etc. It can easily calculate the magnetization dynamics for any arbitrarily shaped elements consisting of one or more than one different magnetic materials.

First, the static magnetic state is obtained by applying a large enough bias field to fully magnetize the sample and allowing the magnetization to relax for a longer time. The applied field was then reduced to the bias field values and the magnetization was further allowed to relax again for a longer time. During this process a high damping value (α) was set (say 0.9 for Ni₈₀Fe₂₀) so that the precession dies down quickly and the magnetization fully relaxes within the time. After that magnetization dynamics is calculated where the optical excitation used in the experiment is simulated as a pulsed magnetic field of rise time of 50 ps and peak amplitude of 30 Oe applied perpendicular to the sample plane. During the dynamic simulation the dynamic magnetization averaged over the entire sample volume and configurations of the same were saved for a total duration of 4 ns at intervals of 10 ps. A unique damping parameter (say 0.008 for Ni₈₀Fe₂₀) for the magnetic material was assumed in the dynamic simulations.

During the dynamic simulation the profile of demagnetizing field is also saved in .ohf extension files. The magnetostatic stray field profile is obtained plotting these .ohf files in Matlab. The contour colouring is based on the sum of squares of x- and y-components of the stray field.

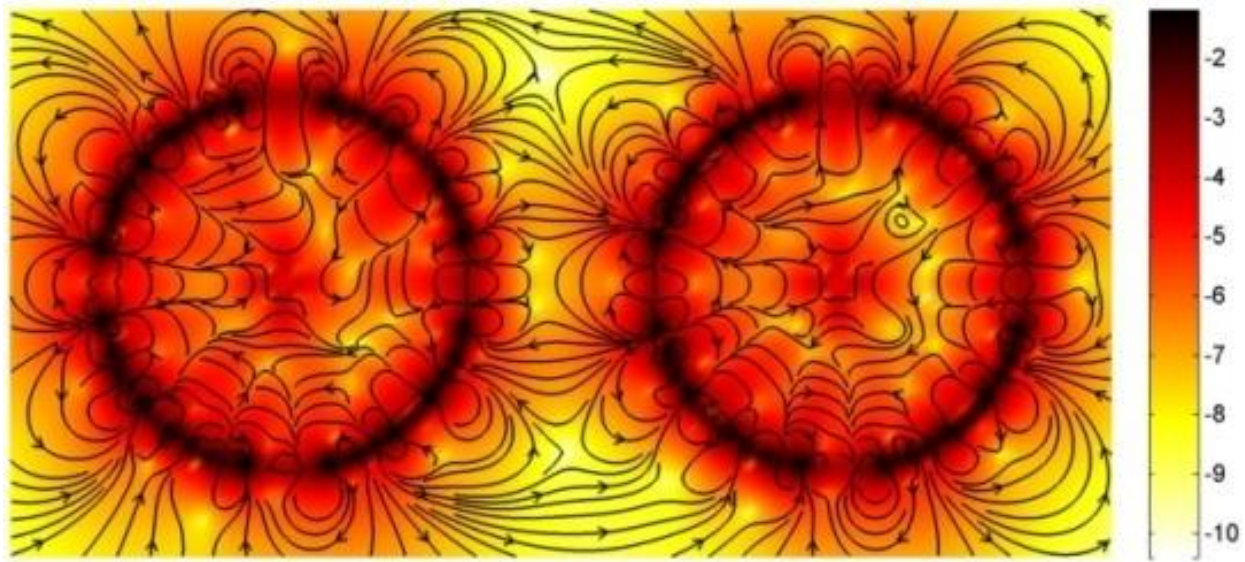


Fig. 4.2 Stray field distribution along with the color scale calculated by using OOMMF software is shown for two $\text{Ni}_{80}\text{Fe}_{20}$ circular nanodots of diameter 200 nm and thickness 40 nm separated by 100 nm at $H = 1.5$ mT and $\phi = 0^\circ$.

4.4 LLG Micromagnetics Simulator:

LLG micromagnetic software [162] is solves the LLG equation using FDM. The main advantage of LLG micromagnetic simulator is that it provides a graphically animated movie of the domain or magnetostatic field profile after finishing the simulation. It also provides the two and three dimensional views of domain or magnetostatic field profile in the form of bitmap images, contour maps and vector field. As shown in Fig. 4.3(a) the magnetostatic field distribution for $\text{Ni}_{80}\text{Fe}_{20}$ circular nanodots (diameter: 100 nm, separation: 30 nm, thickness: 20 nm) arranged in square lattice symmetry was calculated using this software. It also can perform the simulation at various temperatures. Therefore the temperature effect can be introduced during the study of magnetization dynamics, if necessary. This software also can calculate the magnetization dynamics of magnetic multilayers and it is easy to control the input parameters for each layer for such multilayer system using this software. It can also calculate the domain wall dynamics of magnetic nanowire triggering it by spin polarized current which is essential for spin valve like structures.

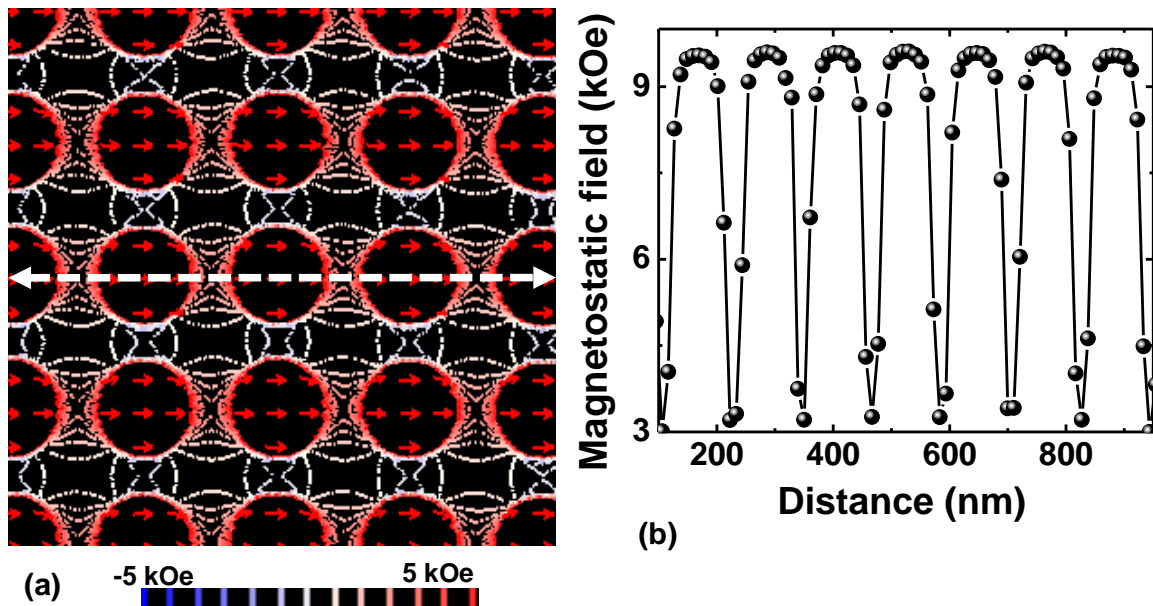


Fig. 4.3 (a) Contour maps of magnetostatic field distributions (x-component) calculated using LLG micromagnetics simulator are shown for $\text{Ni}_{80}\text{Fe}_{20}$ circular nanodots (diameter: 100 nm, separation: 30 nm, thickness: 20 nm) with square lattice symmetry for $H = 1.3$ kOe applied at $\phi = 0^\circ$. The arrows inside the dots represent the magnetization states of the dots, while the strengths of the stray magnetic fields are represented by the color bar at the bottom of the figure. (b) Linescans of simulated magnetostatic fields from square lattices obtained from the positions indicated by horizontal dashed lines in (a).

In this software there is a provision to calculate the total field (B and H) inside or outside of the simulation volume. In the B -probe page, one can evaluate a linescan along any direction of the simulation volume by entering the starting and ending coordinates and number of points. As shown in the Fig. 4.3(b) the linescan will store the field value along the particular line. Thus one can compare the field value at different region as well as on different direction of the simulation volume. It also has a provision to view the B -field (magnetic induction), demag field and effective field, etc. The contour maps of B -field provide us a better understanding regarding the nature of the interaction.

4.5 Calculation of Power and Phase profile of the Resonating Mode:

The power and phase profiles of the resonant modes showed in this thesis is calculated using a code developed in Dotmag software developed by our group[162] as mentioned before. The magnetization dynamics is calculated using OOMMF software. The process is following:

OOMMF produces a number of .omf files containing the information about the magnetization distribution ($M(r, t)$) over the entire simulation volume at a particular instance of simulation time. These files are used as input files for calculating the power and phase profiles of resonant mode.

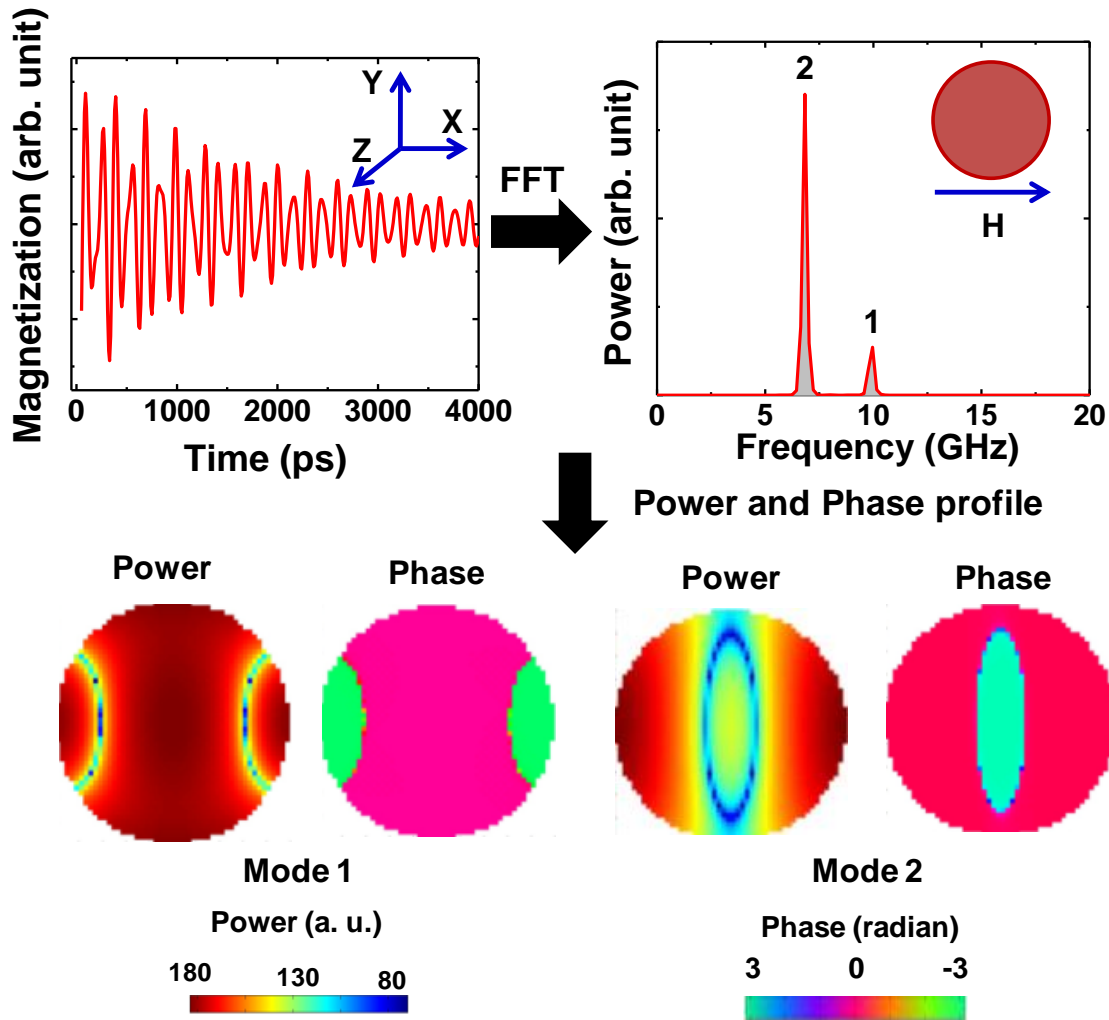


Fig. 4.4 (a) Simulated spatially averaged magnetization (M_z) vs time is shown for a single Ni₈₀Fe₂₀ circular nanodot (diameter: 100 nm, thickness: 20 nm) for $H = 1.3$ kOe applied at $\phi = 0$. (b) Corresponding fast Fourier transform (FFT) power spectrum of the simulated time-resolved magnetization curve of single circular nanodot. Two well resolved resonant modes are observed in this case. (c) The calculated power and phase distributions corresponding to two resonant modes are shown along with the color scale.

The $M(r, t)$ is divided into three four dimensional (4-D) matrices namely $m^i(x, y, z, t)$, $m^j(x, y, z, t)$, $m^k(x, y, z, t)$ where each matrix corresponds to each component of magnetization.

The 4-D matrix of any of magnetization component say m^k is reduced to 3-D matrix of magnetization component m^k at $z = z_m$.

$$m_{z_m}^k(z, t) = m^k(x, y, z_m, t) \quad (4.1)$$

A discrete Fourier transform (DFT) with respect to time is performed on the above mentioned matrix keeping $z (= z_m)$ coordinate fixed. The output will be:

$$m_{z_m}^k(x, y, t) = FFT\{m_{z_m}^k(x, y, t)\} \quad (4.2)$$

If we plot this output, we will get the in-plane space dependent power and phase profiles at a particular resonance frequency. The power and phase profiles at particular frequency f_r can be expresses as:

$$\text{Power: } P^{z_1, f_r}(x, y) = 20 \log_{10} |M_{z_m}^k(x, y, f_r)| \quad (4.3)$$

$$\text{Phase: } \Phi^{z_1, f_r}(x, y) = \tan^{-1} \left[\frac{\text{Im}\{M_{z_m}^k(x, y, f_r)\}}{\text{Re al}\{M_{z_m}^k(x, y, f_r)\}} \right] \quad (4.4)$$

The frequency resolution will depend upon the time window and the spatial resolution will depend upon the spatial discretization.

5. Literature Review

5.1 Introduction:

During last decades, the scientific community has paid a considerable attention for controlling and engineering the optical properties of the materials. They have arranged materials with periodic modulation of the dielectric properties in one, two or three dimensions (1D, 2D or 3D), respectively whose periodicity is comparable to the wavelength of light to control the propagation of light. These types of materials are known as photonic crystals [163]. However, there is another class of crystals known as phononic crystals where acoustic waves (phonons) are used instead of light and the elastic properties of the medium are periodically modulated to form the artificial crystal. The photonic and phononic crystals, and semiconductor superlattices are typical and widely known examples of exploitation of the spatial periodicity for controlling propagation and scattering of light, phonons and electrons in electronic, optoelectronic and acousto-electronic devices.

5.2 Magnonic Crystal:

It is possible to create similar types of artificial crystals where instead of light (or electromagnetic waves) spin waves (SWs) are used for information transmission and processing. Drawing an analogy from photonic and phononic crystals they may be called magnonic crystals (MCs) [35-37] because magnons are the quasiparticles of SWs. The translational symmetry of MCs determines their band structures analogous to crystals in solid [36]. The spectrum of magnons splits into so called minibands, *i.e.*, energy regions in which magnon propagation is allowed. There also exist band gaps *i.e.*, energy regions in which magnon propagation is forbidden. The band structure of the MCs can be modified by modifying of magnetic properties such as anisotropy, exchange stiffness and saturation magnetization by introducing defects and impurities. A broad range of frequency (1-100 GHz) can be covered by changing various physical and geometrical parameters such as material, shape [41], size, lattice spacing [42], lattice symmetry [43], and strength and

orientation of the external bias field [98]. On the other hand magnetic vortex core gyration covers 100 MHz-2 GHz frequency range. Together, they cover essentially the UHF-RF and the whole microwave range from *S* (2 to 4 GHz) to *W* (75 to 110 GHz) bands. In addition to this, magnons with frequencies in the GHz regime have wavelengths in the nanometer scales, which make them potentially interesting for on-chip communication devices, including magnonic waveguides [164], filters [83], splitters, phase shifters [84], spin-wave emitters [11], as well as for magnonic logic devices [7, 48] and nanomagnonic devices [52]. There can be different kinds of MCs, such as 1D, 2D and 3D crystals.

5.2.1 One-Dimensional Magnonic Crystal:

In case of one-dimensional (1D) MCs, the collective behaviour is mediated primarily by a dynamical dipolar interaction[165]. The examples of 1D MCs are the multilayered magnetic structures consisting of alternating ferromagnetic layers [105, 166], an array of closely spaced parallel magnetic stripes [167] or an array of stripes of different magnetic materials in direct physical contact with each other [105]. In this case inter-stripe exchange interaction plays an important role. Lots of studied have been made on magnetization dynamics of magnetic stripes. The enlarged surface-to-volume ratio, inhomogeneous demagnetizing fields due to confined geometries and surface morphology significantly influence their static and dynamic magnetic properties and hence, give rise to rich and complicated SW spectra in ferromagnetic stripes. They also have interesting SW physics such as SW quantization [91], interference [168-169], filtering [170] and self-focusing of SWs [82]. Mathieu *et al.* reported [91] the lateral quantized surface SWs in periodic arrays of Ni₈₁Fe₁₉ stripes of length 500 μm and width 1.8 μm by means of Brillouin light scattering (BLS) spectroscopy. The dipole-dominated dispersionless surface SW modes are observed due to the lateral quantization of surface SW. A collective mode with pronounced dispersive character is observed for magnetic stripes with low (\sim 35 nm) edge to edge separation whereas dispersionless modes are observed if the edge to edge separation between the stripes increases (\sim 175 nm) because the dipolar interaction increases as the separation between the stripe decreases. Demidov *et al.* demonstrated [82] an interference of SW modes in transversely magnetized microstripes. The co-propagation of simultaneously excited SW modes quantized perpendicular to the stripe axis leads to a

spatial interference pattern. This demonstrates the periodic focusing and defocusing of the SWs, which is important for transmission of SWs in magnetic circuits for microelectronics. Lee *et al.* have performed micromagnetic simulations on a perfect 1D waveguide consisting of a Permalloy nanostripe with periodic modulation of its width [16]. They observed allowed and forbidden bands of propagating dipole-exchange spin waves with a wide band gap on the order of 10 GHz that can be manipulated by periodic modulation of different width. This may act as a SW filter operating in GHz range. Chumak *et al.* performed spatially resolved Brillouin light scattering (BLS) experiments in microsized modulating stripes [17] and also observed a rejection frequency band which can be controlled by varying the applied bias field. It is also reported that the propagation of discrete SWs at any angle with respect to the major axis of the stripes is possible for a dipole coupled magnetic stripes. They also observed the partial band gap *i.e.*, the stop bands for propagation along the major axis of the stripe overlap with the frequency pass bands for propagation perpendicular to the major axis of the stripe. It is also important to study how the SW dynamics are influenced by both geometric confinement and magnetic microstructure. The localized SW modes in individual thin ferromagnetic stripes are observed by using time-resolved scanning Kerr microscope [171]. The demagnetizing field originates due to the lateral confinement and the application of the external field parallel or perpendicular to the major axis of the stripe is responsible for the effective confinement of SWs. They imaged the SW modes in both backward volume (BV) and Damon-Eshbach (DE) geometries by using a time-resolved scanning Kerr microscope. They observed that in DE geometry (magnetic field applied parallel to the major axis of the stripe) single uniform precessional mode is present whereas in BV geometry (field is applied perpendicular to the major axis of the stripe) at high field value both center and edge modes are present. As the magnetic field decreases, the frequencies of both the center and edge modes decrease, and the spatial extent of the edge modes grows while that of the center mode shrinks. As a result after a certain field value single mode is observed. However, this investigation was made on ferromagnetic microstripes with micrometer sized width. In contrary, the SW dynamics of nanometer sized stripes by applying bias magnetic field in various directions is still an open problem and a potentially interesting topic to study because the demagnetizing field and ground state spin structure are more complicated in the nanometer regime. In this

thesis we will investigate the width dependent quantization of SW modes by varying the orientation of external bias field using an all-optical time resolved magneto optical Kerr effect microscopy.

5.2.2 Two-Dimensional Magnonic Crystals:

a. Dot Array:

Two dimensional lithographically patterned arrays of ferromagnetic nanodots may act as patterned magnetic media [1] if the magnetostatic interaction (cross-talk) between the dots is eliminated. Similar arrays of nanomagnets having strong magnetostatic interactions shows a collective dynamics, where all elements maintain a constant amplitude and phase relationships. This type of magnetostatically coupled arrays of nanomagnets is used to propagate high frequency magnetic excitations in the form of collective long wavelength SWs as information carries in magnonic crystals. This introduces us with a new field of research known as magnonics.

Ordered arrays of either closely packed magnetic dots or antidots can be considered as two-dimensional (2D) MCs. The collective dynamics [172-176] of 2D magnetic dots have been studied in the frequency [177], time [178-180] and wave-vector domains [181]. In 2002, Jung *et al.* reported [182] magnetization dynamics of square arrays of circular permalloy dots with varying sizes and separations in submicron range by using ferromagnetic resonance (FMR). They observed non-uniform SW modes in addition to the uniform precessional mode where the positions of the resonant peaks depend upon the orientation of external magnetic field and the interdot magnetostatic interactions. The SW dynamics of a tangentially magnetized submicron sized Py cylindrical dot of different radii is measured by using Brillouin Light Scattering (BLS) technique and dispersionless quantized dipole exchange Damon-Esbach (DE) modes and backward volume (BV) magnetostatic modes are observed. The magnetization dynamics of a magnetostatically coupled square array of Py circular dots of different interdot separation is also measured by using BLS technique [175] and a mode splitting of the normal mode is observed as the separation decreases. The precessional dynamics of a Ni₈₈Fe₁₂/Co₈₀Fe₂₀ bilayer square

shaped micro and nanoelements of different sizes was measured by using time resolved scanning Kerr microscope [183]. A crossover between centre mode and edge mode is observed as the diameter of the dot decreases and at a particular dot diameter of 220 nm (crossover region), both center and edge modes are present. Magnetization dynamics of 10 μm Ni₈₀Fe₂₀ square element is measured by using TRSKEM [96] and four-fold anisotropy is observed due to the internal field generated by nonuniform static magnetization. The intrinsic magnetization dynamics of single Ni dots of varying dot diameters down to 125 nm were measured by using a cavity enhanced all-optical TRMOKE setup [156]. In that measurement a transition from a multidomain state with in-plane magnetization to a single domain state with out-of-plane magnetization is observed with the variation of the diameter of the single nanomagnet. Kruglyak *et al.* measured the collective magnetization dynamics of an array of $80 \times 40 \text{ nm}^2$ Co₅₀Fe₅₀ (0.7 nm)/Ni₉₂Fe₈(4.5 nm) stadium shaped elements with edge to edge separation 20 nm by using TRSKEM and they also imaged the collective magnonic modes using the same technique. They observed a broad single mode at higher bias field value which splits into three modes at lower bias field value. Micromagnetic simulation confirms the present of collective non-uniform precessional modes such as quasiuniform, backwad volume like and Damon-Esbach like modes.

More recently using an all-optical time resolve Kerr microscope [42] a transition from a uniform collective mode dynamics to noncollective (isolated) mode dynamics via a weakly collective dynamical regime is observed in arrays of coupled Py square nanoelements having dot width of 200 nm, thickness of 25 nm and varying edge to edge separation of 50 nm to 500 nm. Later, precessional magnetization dynamics of arrays of 50 nm Py dots down to single nanodot regime was reported using the same detection technique [184]. Here, with the increase in the areal density of the array the precession frequency and damping were found to increase significantly due to the increase in the magnetostatic interactions between the nanodots. Finally a mode splitting is observed at an edge to edge separation of 50 nm, where the array enters into a weakly collective regime. A backward volume-like collective mode of the arrays is observed in addition to a uniform collective mode in this regime. A tunable SW spectrum is also observed in strongly magnetostatically coupled array of Py dots with different dot shapes [40] using the same detection technique.

On the other hand, a four-fold configurational anisotropy [185-186] is observed by several groups in square array of circular or square ferromagnetic nanodots. The angular dependence of ultrafast magnetization dynamics of square shaped nanoelement of dimension $220 \times 220 \times 2.5 \text{ nm}^3$ with edge to edge separation 95 nm is measured by using TRSKEM technique. It is observed that the frequency and the number of resonant modes changes with the orientation of in-plane external bias magnetic field due to the dynamic intrinsic configurational anisotropy.

Adeyeye and Singh studied [150] ferromagnetic dot arrays arranged in different lattice symmetry and from the measurement of magnetic hysteresis loops using static magneto-optical Kerr effect configurational anisotropy of various orders were observed commensurate with the lattice symmetry. Weekes *et al.* also observed six-fold configurational anisotropy from static magneto-optical kerr effect measurements in circular dot arrays arranged in hexagonal lattice symmetry [187]. This configurational anisotropy originates from the interactions between unsaturated regions of the elements, which depend on the specific magnetic configurations of the adjacent dots. The magnetodynamical properties of closely packed circular dots arranged in hexagonal lattice symmetry is measured using all-electrical spin-wave spectroscopy (AESWS) and BLS techniques [188]. It is observed that SW excitation spectra for closed packed array ($s = 65 \text{ nm}$) are also isotropic with respect to the in-plane external field direction whereas, excitation spectra for ultraclose packed arrays ($s = 20 \text{ nm}$) shows significant in-plane anisotropy when the direction of the applied field is changed. This is because for ultraclose packed array there is a complete cancellation of the self-demagnetizing field of individual nanodisks by the stray field of its nearest neighbors and the bulk mode strongly depends on the external field orientation due to the anisotropy of the magnetodipolar interaction. However, there is no systematic report on the dependence of the magnetization dynamics on lattice symmetry in ferromagnetic nanodot lattices in the literature. In this thesis we will investigate the magnetization dynamics of magnetostatically coupled Py nanodot lattices by varying the lattice symmetry, which will in turn affect the magnetic stray field distributions as well as the configurational magnetic anisotropy of the systems.

b. Antidot Array:

Ferromagnetic antidot lattices are a periodic array of holes fabricated into a continuous magnetic film. They are promising candidate for magneto-photonic crystal due to the influence of magnetic field on the light coupling to surface plasmons in such systems. In addition to this the antidots do not suffer from the superparamagnetic bottleneck at the deep nanoscale dimensions due to the absence of any small magnetic entity. The holes introduce locally distributed shape anisotropy and act as pinning centres for the wall displacements and spin waves. As a result they have attracted an increasing interest from both technological and fundamental points of view. In a nanohole array the holes introduce locally distributed shape anisotropy and act as pinning centres for the wall displacements and spin waves. As a result static and dynamic magnetic properties of magnetic nanohole arrays are strongly depend on the shape and size of the magnetic materials between the nanoholes. A significant variation in the magnetization dynamics of cobalt antidot lattice of diameter 100 nm is measured by using time-resolved magneto optical Kerr effect microscopy with the variation in the lattice constant between 200 nm to 500 nm [38]. It is observed that two prominent magnonic bands with a clear band gap are present for sparsely packed antidot lattices. The band gap increases with the decrease in the lattice constant, and at the lowest value of the lattice constant, four distinct magnonic bands appear. It is also observed using the same technique that the SW spectra can be tuned in a two-dimensional antidot lattice with varying antidot shapes [189], namely, square, circular, triangular, and diamond shapes. The magnetization dynamics of antidot arrays also changes significantly with the variation of lattice symmetry. In addition to this antidots array attracted the attention due to field-controlled and anisotropic propagation of SW propagation, SW localization and magnonic miniband formation with large SW velocities. The observed tunability of the SW spectrum is important for potential applications of the antidot lattices in nanoscale magnonic crystals.

c. Magnetic Vortex:

As we discussed chapter 2, section 2.6, magnetic platelets of micron or submicron size characterized by an in-plane closed flux magnetization minimizing the dipolar energy are known as magnetic vortices. When magnetic thin films are artificially patterned in such a way that the magnetization of four domains meet radially on one point and form cross-tie walls, then it is known as magnetic antivortices. In both cases, at the center, the magnetization is forced out-of-plane to avoid large angles between magnetic moments as this would drastically increase the exchange energy. The region with a strong out-of plane magnetization component, called the vortex or antivortex core having diameter only few exchange length [190-193] with a distinct polarization(p), either up ($p = +1$) or down ($p = -1$). Apart from polarity, another attribute of a magnetic vortex is known as chirality (c). Depending upon the direction of the in-plane rotating magnetization chirality can be either $+1$ (CCW) or -1 (CW). It is already been discussed in few papers [194-195] that these two binary properties *i.e.*, polarity (p) and chirality (c) may act as an independent bit of information in future high-density nonvolatile recording media. It is been observed that magnetic vortex core starts to rotate around its equilibrium position at a characteristic eigenfrequency (ω) typically ranging from several hundreds of MHz to ~ 1 GHz if an external magnetic field [196-197], alternating magnetic field [32, 198] or spin polarized current [32, 199-201] is applied to an isolated magnetic vortex due to the presence of translational mode [202-203]. This is known as oscillatory gyrotropic motion. The magnetic vortex core reversal can also be done by SW excitation [204]. In addition to the external forces, the moving vortex core experiences another internal force arising from the demagnetizing field of the nonequilibrium magnetization pattern and this force acts along the perpendicular direction to the vortex core velocity. It is observed [205-206] that for large amplitude excitation, the internal force increases nonlinearly and this results into a nonlinear vortex core gyration. Vortex core switching occurs along with the creation and annihilation of new vortex and antivortex. For small amplitude excitation, the internal force increases linearly and the vortex core motion remains in the linear regime [207] and the vortex core equation of motion can be derived from Thiele equation [207] which is given by

$$F_{ext} + G \times v + \alpha D \cdot v = 0 \quad (5.1)$$

where F_{ext} is the applied external force, G is the gyrotropic vector, D is the dissipation vector and v is the velocity of the core. During the dynamical motion of the vortex core, the demagnetization field at the vortex core points antiparallel to the enlarged domain generated due to the displaced vortex and the time derivative of magnetization vector at the vortex core points either into the disk centre or the opposite direction. A variation in chirality inherently changes the direction of the demagnetization field and therefore does not affect the vortex core motion. Therefore, the vortex core gyration direction is solely controlled by the core polarization. In the linear regime, the vortex core can be described in a harmonic oscillator model [208-209].

During the gyration, the vortex core shifted from its center position leads to non-zero side-surface charges, thus producing stray fields around the dot itself. When another neighboring dot is placed sufficiently close to the first dot, the stray field is strong enough to affect it as well. The rotating stray field has the same frequency as the eigenfrequency (ω) of the gyration. It is reported that such dynamic dipolar interaction causes mutual energy transfer between two coupled vortex oscillators, as between two coupled spring-mass oscillators or pendulums [210-212]. One expects mutual energy transfer and a consistent phase relation between the gyrating vortices [213]. The mutual transfer of energy between magnetostatically coupled vortices due to the gyrotropic motion is extremely important for devices for microwave communication and logic operations [214-215]. Many studies of quasistatic and dynamics processes have been performed on pairs [212], chains, and 2D arrays of magnetostatically coupled vortices [216]. Vortex gyration transfer rate and energy attenuation coefficients have been calculated by analytical methods [215] and micromagnetic numerical calculations [215]. Stimulated vortex gyration based energy transfer between spatially separated dipolar coupled magnetic disks has been observed experimentally by time resolved soft X-ray microscopy [212]. It is also observed that the rate of energy transfer is determined by the frequency splitting caused by the dipolar interaction between the vortices [214]. However, the energy transfer efficiency may dependent on several factors such as the frequency of the exciting field

pulse as compared to the resonance frequency of the vortex, which is determined by the dimension and aspect ratio of the structure, the amplitude and nature of the exciting pulse, the distance between the two vortices and relative polarization of the two vortices. It has been previously observed that the propagated signal amplitude in the second vortex, is smaller in amplitude if one excites the first vortex in its resonant frequency [27]. It has also been reported that the interaction strength between coupled vortices is maximum when their core polarities are opposite [212], although, higher interaction strength is not the sufficient condition for higher transfer efficiency. Mutual energy transfer between three vortices, where only one vortex at one end is excited, is even more interesting from the application point of view. Very recently, this system has been proposed to work as a vortex transistor [81], where vortex at one end is excited and the gyration amplitude at the vortex situated at the other end is higher than the gyration amplitude at the vortex which has been excited directly. This has been obtained for a particular combination of polarization of three vortices, where the energy loss is minimum.

d. Bi-Component Magnonic Crystal (BMC):

In MCs, if two different magnetic materials either in direct contact or placed very close with each other form the basis structure, the dynamical dipole coupling is maximized due to the dipolar/exchange coupling at the boundary. As a result, SWs are subject to scattering at the interfaces between the two materials and can transmit through the boundary. Therefore SWs can propagate across its entire structure with considerable group velocities. Such system is popularly known as bi-component magnonic crystals (BMCs) [217-219].

The broad spectrum of scattering and mode-coupling processes makes 2D BMCs an intriguing topic for scientific studies, for controlling the SW propagation and also for other kinds of applications. Microfocused BLS experiments on 2D arrays of Co nanodisks embedded in Py matrix showed spatial shifts in magnonic excitations within the given lattice, which can control the propagation of SWs at nearly the same eigenfrequency in periodically patterned magnetic devices and magnonic crystals [218]. In the similar sample forbidden frequency gaps were measured [24] at the boundaries of both the first and the second Brillouin zones whose widths depend on the magnetic contrast between the

constituent materials. The magnetization dynamics and the reversal mechanism of Fe filled Py antidot structures were measured using VNA-FMR technique [220]. It was observed that the mutual magnetostatic coupling between the two ferromagnetic nanostructures led to a significant modification to the magnetization reversal mechanism and ferromagnetic resonance mode profiles when compared with reference Fe dots and Py antidot array. Propagating SWs in 2D arrays of alternated Py and Co nanodots measured by BLS showed that the Brillouin active modes are based upon the standing wave modes in uncoupled Py dots, whereas the Co dots act as mediators for dipolar coupling between the Py dots [221]. Micromagnetic simulations of Fe embedded in YIG films showed wide bandgap of about 10 GHz [222]. Recently, magnetization switching and ferromagnetic resonance studies of binary Ni/Py nanostructures have been reported [105]. However, there is no report on the study of magnetization dynamics of purely magnetostatically coupled BMCs using all-optical TR-MOKE microscopy. In this thesis, we investigated the SW dynamics of purely magnetostatically coupled BMCs by applying bias field parallel to the long-axis (LA) and short-axis (SA) of the BMC.

5.2.3 Three-Dimensional Magnonic Crystal:

3D magnonic crystals are the least studied objects in magnonics, due to both increased difficulty of their theoretical treatment and currently limited outlook for their fabrication and experimental investigation. Ion implantation with lithographic mask or directed ion beam allows fabrication of magnonic crystals with either 2D or 3D periodicity. Optical fabrication [223] can also be used to fabricate 3D MCs. SW spectra of 3D magnonic crystals composed of two different ferromagnetic materials is calculated using plane wave method [12]. It is found that the contrast of magnetic parameters is essential to generate [67] magnon bands and forbidden-frequency gaps of significant width.

6. Tunable Magnonic Spectra in Two Dimensional Magnonic Crystals with Variable Lattice Symmetry:

6.1 Introduction:

Magnetic nanostructures form the basis of many present and future technologies including patterned magnetic media [1], magnetic random access memory [4], magnetic logic devices [5, 8] and magnetic resonance imaging [9]. The patterned magnetic media uses two-dimensional arrays of lithographically patterned magnetic islands (bits) and the magnetic switching behaviors of such systems including switching field distribution have been thoroughly studied. An essential criterion has been to eliminate the magnetostatic interaction (cross-talks) between the individual bits for the application in patterned magnetic media. Similar arrays of nanomagnets may be used to propagate high frequency magnetic excitations in the form of collective long wavelength spin waves as information carries in magnonic crystals, when the magnetic elements are strongly magnetostatically coupled. Such coupled arrays of nanomagnets undergo a collective dynamics [42, 173-175, 185, 224-225], where the individual nanomagnets maintain constant amplitude and phase relationships, and show rich magnonic band structures with tunable bandgap properties. Thereby a new field of research known as magnonics [36-37, 226] has been introduced, which has potential to use spin waves to carry and process information and also in building nanoscale microwave components such as filters, attenuators and phase shifters [84]. Emerging new field such as coherent oscillation of an array of spin torque nano-oscillators [11, 227] also promises to act as on-chip microwave sources for electronic and magnetoelectronic applications.

Two dimensional ferromagnonic dot lattices have been extensively fabricated and studied in recent years. Various physical parameters of the lattices such as lattice constants, and

shape, size and material of the magnetic dots have been varied to tailor the magnonic properties in those lattices. The high frequency magnetization dynamics of such lattices have been studied experimentally by time domain [111, 228], frequency domain [185], wave vector domain [176] techniques and by analytical methods [229-230] and micromagnetic simulations [180]. The frequency, damping and spatial profiles of collective modes and the dispersion of their frequency with wavevector have been studied with the variation of above parameters. In addition to the periodicity of the lattice, the interdot magnetostatic interactions in the lattices play a very important role in determining the collective magnonic modes in these lattices and further tailoring of this interaction field offers exciting prospects in magnonics. The variation of lattice symmetry is an attractive option, by which the magnetostatic fields of highly complex nature can potentially be introduced but it has hitherto not been tried in the context of the spin wave dynamics of magnonic crystals. The quasistatic magnetization processes of nanomagnets arrays with different symmetry have been reported by static magneto optical Kerr effect measurements [187, 224, 231]. A configurational anisotropy has been observed from the dependence of the hysteresis loops with the angle of the in-plane magnetic field *w.r.t.*, the symmetry of the array. On the other hand, magnetization dynamics of magnetic antidot lattices with varying lattice symmetry has been reported by a combination of Brillouin light scattering and ferromagnetic resonance measurements [225]. In all lattices the eigenfrequencies show angular dependence consistent with the symmetry of the lattice. However, no report on the dependence of the magnetization dynamics in ferromagnetic dot lattices on the lattice symmetry could be found in the literature. Here, we present an all-optical excitation and detection of magnetization dynamics in closely packed circular Ni₈₀Fe₂₀ (Permalloy/ Py) dot lattices arranged in different lattice symmetry. The spin wave spectra show a significant variation as the symmetry is reduced from square lattice to octagonal lattice through the rectangular, hexagonal and honeycomb lattices. We also investigate the anisotropy of the collective modes in the hexagonal lattice as a function of the azimuthal angle (ϕ) of the in-plane bias magnetic field.

6.2 Experimental Details:

$10 \times 10 \mu\text{m}^2$ lattices of 20 nm thick Py dots with circular shapes arranged in different lattice symmetry were fabricated by a combination of electron beam lithography and electron beam evaporation. The diameter of the dots is about 100 nm with about $\pm 10\%$ deviation within different lattices. The edge to edge separation between the dots is about 30 nm with about $\pm 10\%$ deviation within different lattices. The sizes of the dots are chosen in such a way that the individual dots can support both the centre and edge modes of precession of magnetization. The edge to edge separation is chosen in such a way that the dots are strongly magnetostatically coupled and show collective modes of precession. The dots are chosen to be of circular shapes so that the individual dots do not posses any configurational anisotropy [126] due to their shapes.

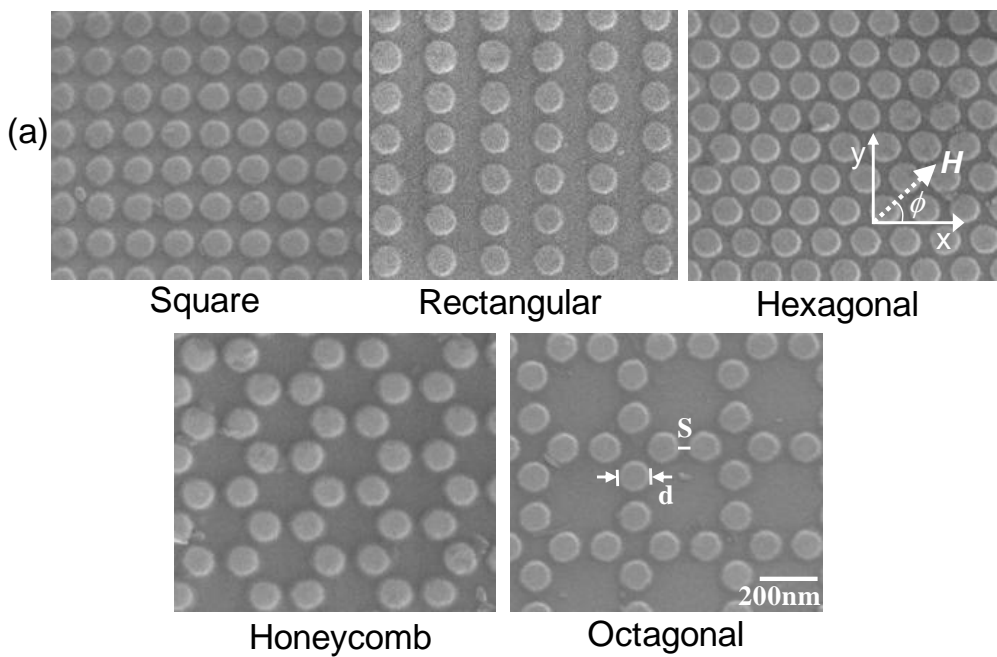


Fig. 6.1 (a) Scanning electron micrographs of the Py dot lattices with different lattice symmetry, namely square, rectangular, hexagonal, honeycomb and octagonal symmetry. The dot diameter and separation are shown in the micrograph for the octagonal lattice along with the length scale bar. The geometry of the applied magnetic field for all lattices is shown in the micrograph of the hexagonal lattice.

6.2.1 Sample Fabrication:

Permalloy dot lattices with varying lattice symmetry were prepared by a combination of electron-beam lithography and electron beam evaporation technique. The details about the sample fabrication are discussed in Chapter 3. The beam current used during electron beam lithography is 100 pA for a dose time of 1.0 μ s. A bilayer MMA/PMMA (methyl methacrylate/poly methyl methacrylate) resist pattern was first prepared on self oxidized Si(100) substrate by using electron-beam lithography and Py was deposited on the resist pattern by electron-beam evaporation at a base pressure of about 1.3×10^{-7} Torr. A 5 nm thick Al₂O₃ capping layer was deposited on top of the Py layer to protect the dots from general degradation with time as well as when exposed to the optical pump-probe experiments in air. This is followed by the lifting off of the sacrificial material and oxygen plasma cleaning of the residual resists that remained even after the lift-off process.

Both two-dimensional Bravais (square, rectangular, hexagonal) and non-Bravais (honeycomb, octagonal) lattices are chosen here to investigate the effects of variation of translational symmetry of the lattice and finally symmetry breaking on the magnonic spectra. Fig. 6.1 shows the scanning electron micrographs of all types of lattices. The small deviation in size and separation from the nominal dimensions as obtained from the micrographs will eventually be included in the micromagnetic simulations. The chemical compositions of the dots measured by the energy dispersive X-ray spectroscopy agree well with the nominal composition of the target material. Atomic force microscope (AFM) images were taken for different lattice symmetry samples and the height profiles of the nanodots were measured from those images. The average height was found to vary between 20 and 22 nm in different lattices from the AFM measurements, which agrees well with the nominal thickness of the samples.

6.2.2 Measurement Details:

The ultrafast magnetization dynamics was measured by a two-color optical pump-probe setup [151] with simultaneous spatial and temporal resolutions of sub- μ m and 100 fs, respectively as described in details in section 3.4.2. of chapter 3. The second harmonic ($\lambda = 400$ nm, 10 mW, pulselwidth ~ 100 fs) of a mode locked Ti-sapphire pulsed laser (Tsunami,

Spectra physics, pulsed width ~ 80 fs) is used to excite the sample. The fundamental laser beam ($\lambda = 800$ nm, 2 mW) is used to probe the dynamics after passing through a variable time delay by measuring the polar Kerr rotation using a balanced photo diode detector, which completely isolates the Kerr rotation and reflectivity signals. The pump and probe beams are made collinear and are focused at the centre of each lattice through the same microscope objective with N.A. = 0.65. At the focal plane of the probe (diameter ~ 800 nm), *i.e.*, on the sample surface, the pump beam is slightly defocused, and has a larger diameter (~ 1 μm) than the probe beam, which makes it easier to overlap the pump and probe beams on the sample surface. The probe beam is centred on the pump beam so that slight misalignment during the course of the experiment does not affect the pump-probe signals. A large enough magnetic field is first applied at a small angle ($10^\circ - 15^\circ$) to the planes of the lattices to saturate their magnetization. The magnetic field strength is then reduced to the bias field value (H = component of bias field in the sample plane), which ensures that the magnetization still remains saturated along the bias field direction. The pump beam was chopped at 2 kHz frequency and a phase sensitive detection of total reflectivity and Kerr rotations were made using lock-in amplifiers. The sample is scanned under the focused laser spots by using a piezoelectric scanning stage (x-y-z) with feedback loop for better stability.

6.3 Results and Discussions:

6.3.1 Quasistatic Magnetization Dynamics of Nanodot Lattices of Different Lattice Symmetry:

The magnetostatic interaction changes when we arrange the nanodots in lattices with varying symmetries. The interdot interaction becomes more complicated with reduced symmetry of the lattice, which may affect the magnetization reversal of these arrays.

Magnetic hysteresis loop (Fig. 6.2)

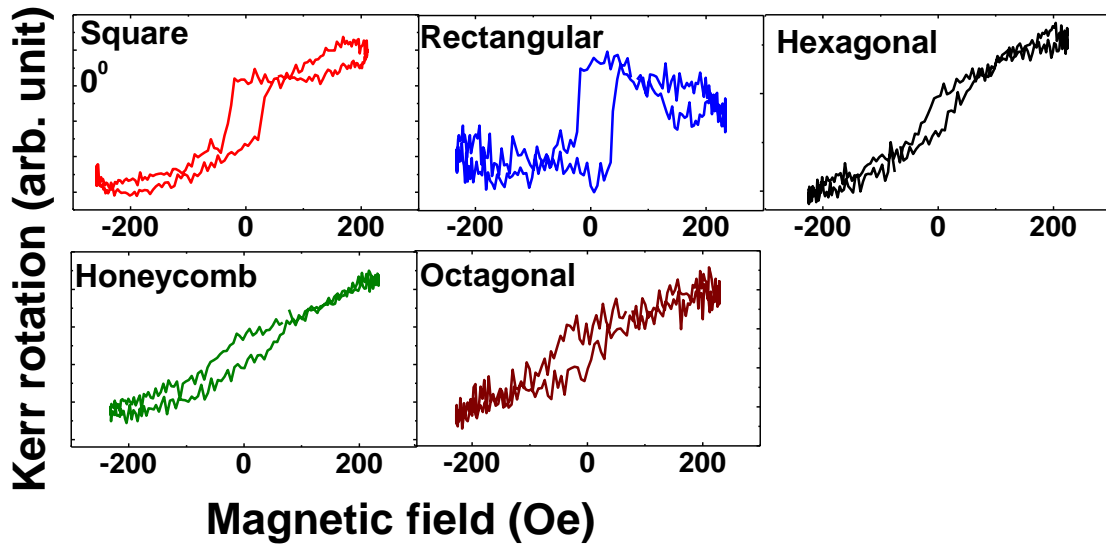


Fig. 6.2 Experimental MOKE loops of square, hexagonal, honeycomb and octagonal lattices for bias field applied at $\phi = 0^\circ$

(Kerr rotation as a function of external bias field H) for nanodot lattices arranged in different lattice symmetry is measured by using a high-sensitivity magneto-optical Kerr effect microscopy. The samples were viewed under an optical microscope and the focused laser spot ($5 \mu\text{m}$) is focused at the center of each $10 \times 10 \mu\text{m}^2$ array. The polarization of reflected beam is analyzed to measure the longitudinal Kerr effect. An electromagnet is used to apply the magnetic field in the plane of the sample. The longitudinal Kerr effect is measured by rotating the sample plane for two different angles like 0° and 30° . The experimental results show that the coercivity changes as the lattice symmetry changes. Coercive field (H_c) also changes with the direction of the external bias field.

Table 6.1 Variation of coercive field (H_c) for different lattice symmetries:

Type of the lattice	H_c in Oe
Square	27.00
Rectangular	30.5

Hexagonal	20.00
Honeycomb	37.00
Octagonal	33.00

In table 6.1 at $\phi = 0^\circ$ the H_c value is minimum for hexagonal lattice and maximum for honeycomb lattice. Hexagonal lattice is mostly closed packed structure and the interaction is very strong as a result magnetization reversal occurs due to coherent interaction which gives rise to a low coercive field. As the symmetry reduces the interaction becomes complicated and weaker and magnetization reversal is no longer coherent. As a result the coercive field is higher for non Bravais lattices.

6.3.2 Variation of Precessional Dynamics with the Symmetry of the Nanodot Lattices:

Figures 6.3 (a) and (b) shows the typical time-resolved reflectivity and Kerr rotation data from a Py dot lattice arranged in hexagonal lattice symmetry for a bias field $H = 1.3$ kOe applied at $\phi = 0^\circ$. The reflectivity shows sharp rise followed by a bi-exponential decay, whereas the time resolved Kerr rotation shows a fast demagnetization within 500 fs with a bi-exponential decay with decay constants of about 2 ps and 500 ps. In Fig. 6.3(c) the ultrafast demagnetization and fast relaxation dynamics are shown for rectangular, hexagonal, honeycomb and octagonal lattices.

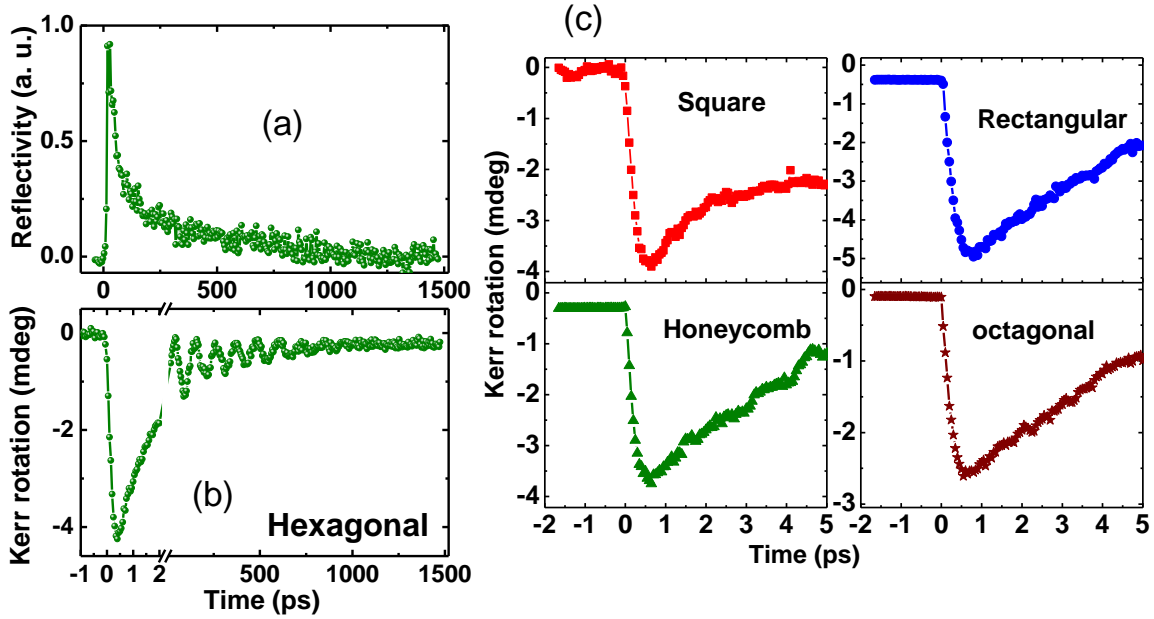


Fig. 6.3 Typical time resolved (a) reflectivity and (b) Kerr rotation data are shown for the Py dot lattice with hexagonal lattice symmetry for $H = 1.3$ kOe applied at $\phi = 0^\circ$. (c) The time-resolved Kerr rotation data showing ultrafast demagnetization and fast remagnetization for square, rectangular, honeycomb and octagonal lattices are shown for $H = 1.3$ kOe applied at $\phi = 0^\circ$.

Table 6.2: Variation of demagnetization, fast relaxation and slow relaxation times for different lattices:

Type of the lattice	Demagnetization time (fs)	Fast relaxation time (ps)	Slow relaxation time (ps)
Square	500	1.07	507
Rectangular	500	1.90	445
Hexagonal	500	2.00	500
Honeycomb	500	1.40	518

Octagonal	550	1.24	445
-----------	-----	------	-----

The demagnetization and fast and slow relaxation times are shown in table 6.2. From table 6.2, we observe that the demagnetization time remains nearly constant with varying lattice symmetry as this is a material property and in this case the material is Py for all samples. The fast and slow relaxation times are found to be different for different lattices but no clear trend is observed for their variations. This variation can therefore be attributed to the difference in roughness, defects and deformation of the samples. All of those could cause a variation of the spin-orbit coupling and different transfer rate of energy to the lattice and the surroundings these samples.

The precessional dynamics appears as an oscillatory signal on the slowly decaying part of the time-resolved Kerr rotation data. A first Fourier transform (FFT) is performed after subtracting the bi-exponential background to find out the corresponding power spectra. The measurement time window of 1.5 ns used in this experiment is a compromise between the total measurement time, which is determined by the number of scan points and the integration time of the lock-in amplifier for each scan point, and the time taken to cause a slow drift of the piezoelectric sample scanning stage. Nevertheless, this 1.5 ns time window is found to be sufficient to resolve the spin wave spectra for different lattices. Fig. 6.4(a) – (b) show the background subtracted experimental time resolved Kerr rotations for lattices with different lattice symmetry and the corresponding power spectra. From the experimental data a clear variation in the spin wave dynamics is observed with the lattice symmetry. For the square lattice the time-domain data shows a damped single frequency oscillation, which transforms into a single sharp peak in the frequency domain. But as the symmetry reduces in the rectangular lattice a mode splitting appears. The high intensity peak shifts slightly towards the lower frequency while a low intensity peak appears at a slightly higher frequency. In the case of hexagonal lattice a dramatic change occurs and three clear peaks are observed in the FFT spectrum as a consequence of the highly non-uniform oscillations in the time-resolved Kerr signal. The peak at the centre has the highest intensity, while the peak at the higher frequency is also significantly intense as compared

to the main peak. The third peak is of very low intensity, which appears at a much lower frequency with about 3.5 GHz shift from the main peak. The time-resolved Kerr rotation and the corresponding FFT spectrum for the honeycomb lattice are even more complicated.

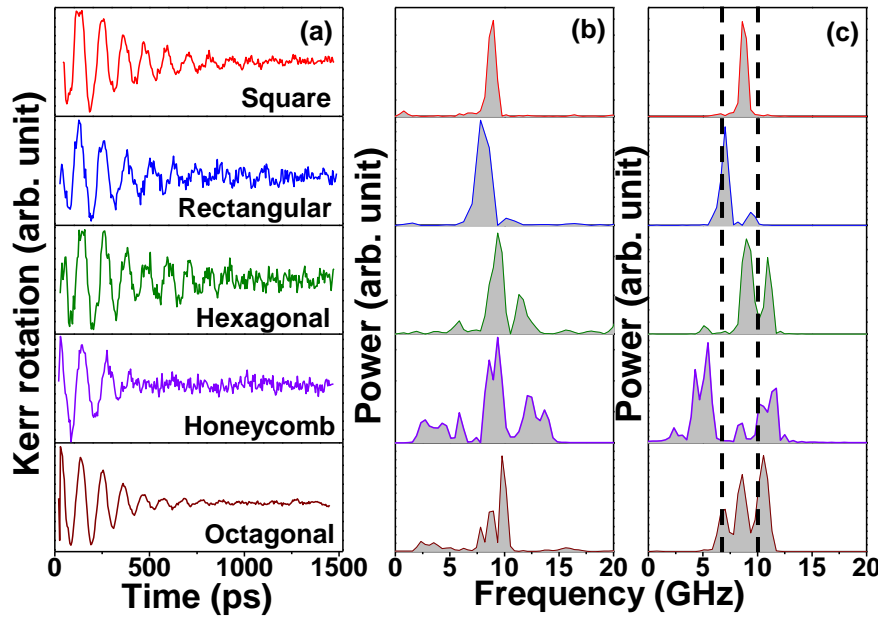


Fig. 6.4 Experimental (a) time resolved Kerr rotation data and (b) the corresponding FFT spectra are shown for permalloy dot lattices with five different lattice symmetry at $H = 1.3$ kOe at $\phi = 0^\circ$. (c) FFT spectra of the simulated time-domain magnetization for five different lattice symmetry. The mode numbers are shown in the simulated FFT spectra, while the dashed vertical lines show the positions of the centre and edge modes of the simulated single dot with width = 100 nm and thickness = 20 nm.

The time-resolved data dephases rapidly after about 3 cycles of oscillation leaving a small amplitude non-uniform oscillation, while a broad band of modes are observed between 1 and 14 GHz in the FFT spectrum. Seven peaks are observed, where the central peak is very broad with a partial splitting. In the octagonal lattice three closely spaced peaks are observed between 7 and 11 GHz, while a low intensity band is observed below 5 GHz.

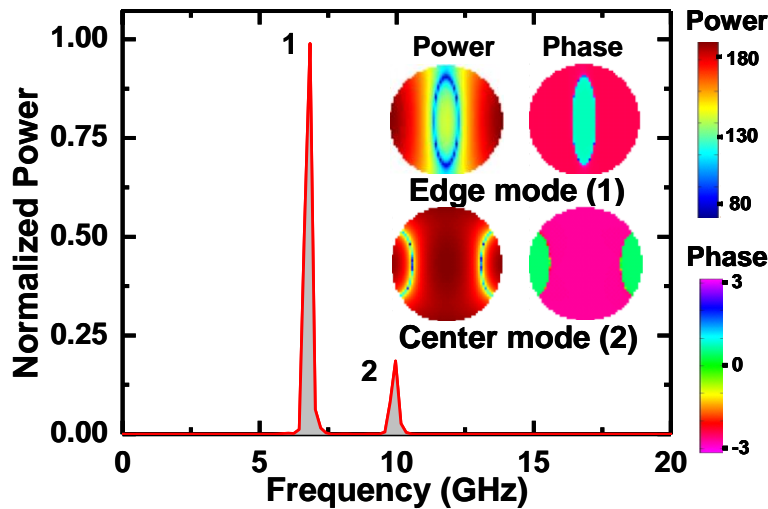


Fig. 6.5 The power spectra of the simulated magnetization dynamics of a single circular permalloy dot with 100 nm diameter and 20 nm thickness at $H = 1.3$ kOe. The power and phase maps of the two observed modes are shown in the inset. Mode 2 is identified as the centre mode while mode 1 as the edge mode of the permalloy dot.

We have performed micromagnetic simulations using the OOMMF software [161] by considering finite lattices of about $1100 \times 1100 \times 20$ nm³ volumes consisting of circular dots arranged in different lattice symmetry. The samples were discretized into $2 \times 2 \times 20$ nm³ cells and materials parameters for Py were used as gyromagnetic ratio $\gamma = 18.5$ MHz/Oe, anisotropy field $H_k = 0$, saturation magnetization $M_s = 860$ emu/cc, and exchange stiffness constant $A = 1.3 \times 10^{-6}$ erg/cm. The material parameters were extracted by experimentally measuring the precession frequency (f) as a function of bias magnetic field (H) of a Py thin film of 20 nm thickness and by fitting the data with Kittel's formula for the uniform precession mode.

$$f = \frac{\gamma}{2\pi} \sqrt{(H + H_K)(H + H_K + 4\pi M_s)} \quad (6.1)$$

The lateral cell size is well below the exchange length of Py (5.3 nm). In general the widths and inter-element separations as observed in the SEM images are included in the simulation. The dynamic simulations were obtained for 1.5 ns at the time steps of 5 ps. Fig. 6.4(c) shows the FFT spectra of the simulated time-domain magnetization, which

qualitatively reproduce the experimental results. The relative intensities and the precise positions of the peaks in the frequency domains are not always quantitatively reproduced due to the limitations in the simulation. The agreement is better for square, rectangular and hexagonal lattices, while for the honeycomb and octagonal lattices the precise quantitative agreements are not obtained. The splitting of the central peak for the honeycomb lattice and the low intensity band for the octagonal lattice below 5 GHz are not reproduced in the simulation. The deviation is primarily because of the smaller size of the simulated lattices as opposed to the experimental lattices and lack of inclusion of the precise edge roughness and other defects in the simulated samples as observed experimentally. In addition, the optical excitation used experimentally is replaced by an estimated pulsed magnetic field in the simulation. Nevertheless, the important features of the experimental spectra are reproduced by the simulation.

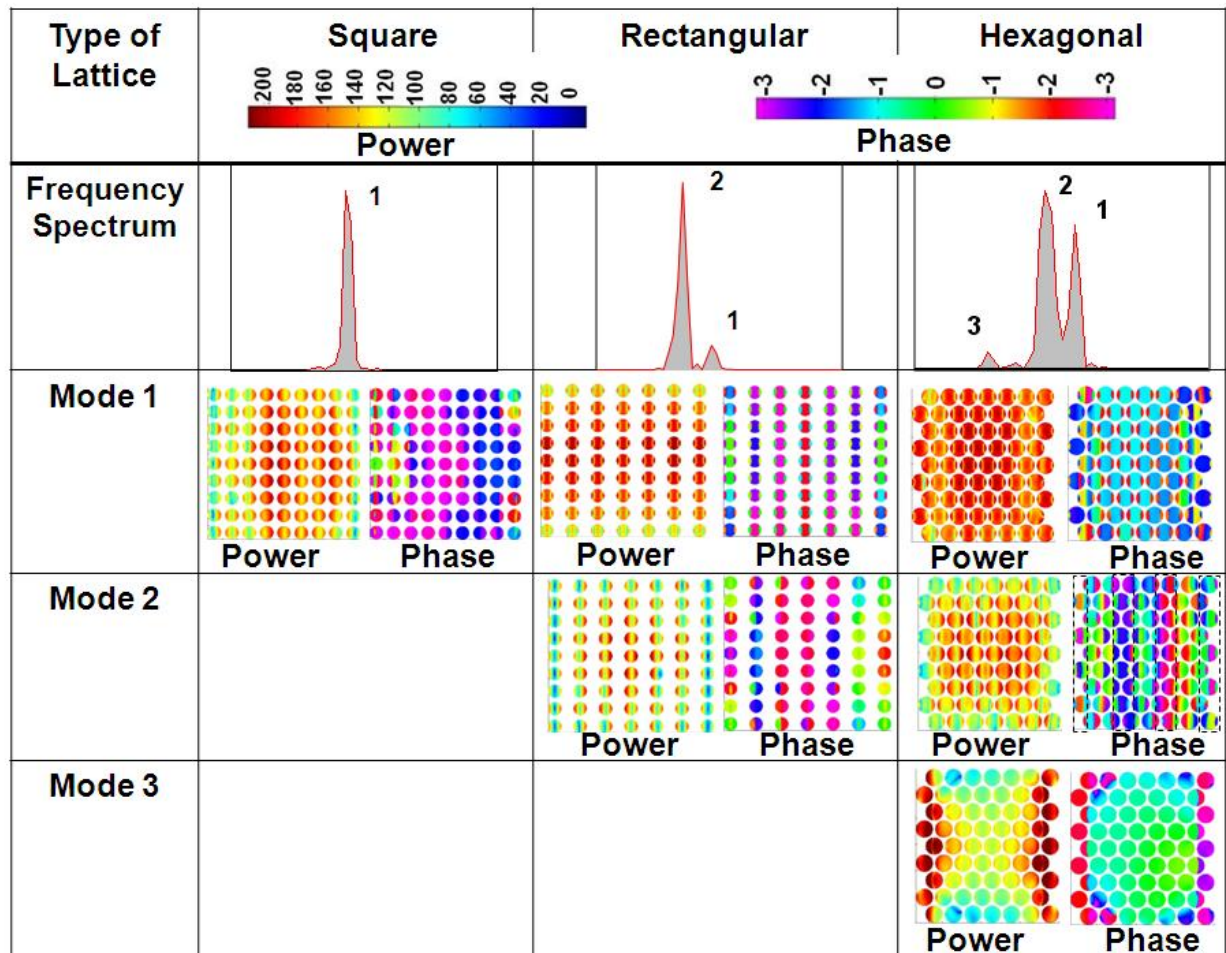


Fig. 6.6 The power and phase maps for different precessional modes of permalloy dot lattices with square, rectangular and hexagonal symmetry. The colormaps for the power and phase distributions are shown at the top of the images.

6.3.3 Micromagnetic Analysis of the Collective Modes in the Lattices:

We have further simulated the power and phase maps of various collective modes as observed both experimentally and in the simulation by using a home built code [162]. However, before that we have calculated the dynamics of a single Py nanodot of 100 nm diameter and 20 nm thickness. Two distinct peaks are observed, out of which the higher frequency peak is identified as the centre mode and the lower frequency peak as the edge mode of the dot as shown in Fig. 6.5. We have further simulated the power and phase maps for all resonant modes in different lattices as shown in Fig. 6.5 and 6.6. The profile of the single mode in the square lattice is found to be the edge mode of the individual nanodots precessing coherently over the central part of the lattice, while the amplitude of precession dies out substantially near the vertical edges of the lattice. Due to the strong magnetostatic interaction the modes in the two central columns become completely uniform over the entire volumes of the nanodots. This is the uniform collective mode of the strongly coupled lattice as opposed to the weakly coupled arrays, where the centre and edge modes of the individual elements are generally observed [181, 232]. For the rectangular lattice, mode 1 corresponds to the centre mode of the individual elements precessing coherently over the entire lattice except for the horizontal edges of the lattice. On the otherhand, mode 2 is the coherent precession of the edge modes of the individual nanodots over the lattice except for the vertical edges of the lattice. For the hexagonal lattice, mode 1 corresponds to the coherent precession of the centre mode of the nanodots over the entire lattice with a slight dephasing near the vertical edges. Mode 2 corresponds to edge modes of the nanodots, which are precessing out of phase within consecutive stripe like regions marked by the vertical dotted lines. This mode is similar to the backward volume magnetostatic mode (BV) of the lattice. In mode 3, the dots are in phase, while the power on the dots reduces gradually from the vertical edges towards the centre of the lattice forming a bowtie like pattern. The honeycomb and octagonal lattices show very rich spectra and the corresponding mode profiles are shown in Fig. 6.7. For the honeycomb lattice, mode 1

corresponds to the magnetostatic surface wave (SW) mode of the lattice, where consecutive rows are out of phase and alternative rows are in phase. Mode 2 is a mixed mode. Mode 3 corresponds to vertical stripe-like regions, where the half circles (full circle) are alternatively precessing in-phase and out-of-phase with each other. Mode 4 is localized within the centre of the lattice, which shows the BV mode of the individual dots. Mode 5 has its power reduced from the vertical edges towards the centre of the lattice and is out of phase with mode 4. Mode 6 is edge mode of the individual nanodots, which are primarily distributed in the even rows of the simulated lattice. This is because the edge to edge separations between the neighbouring dots in the even rows are much larger than those in the odd rows. The strong magnetostatic interactions between the dots in the odd rows

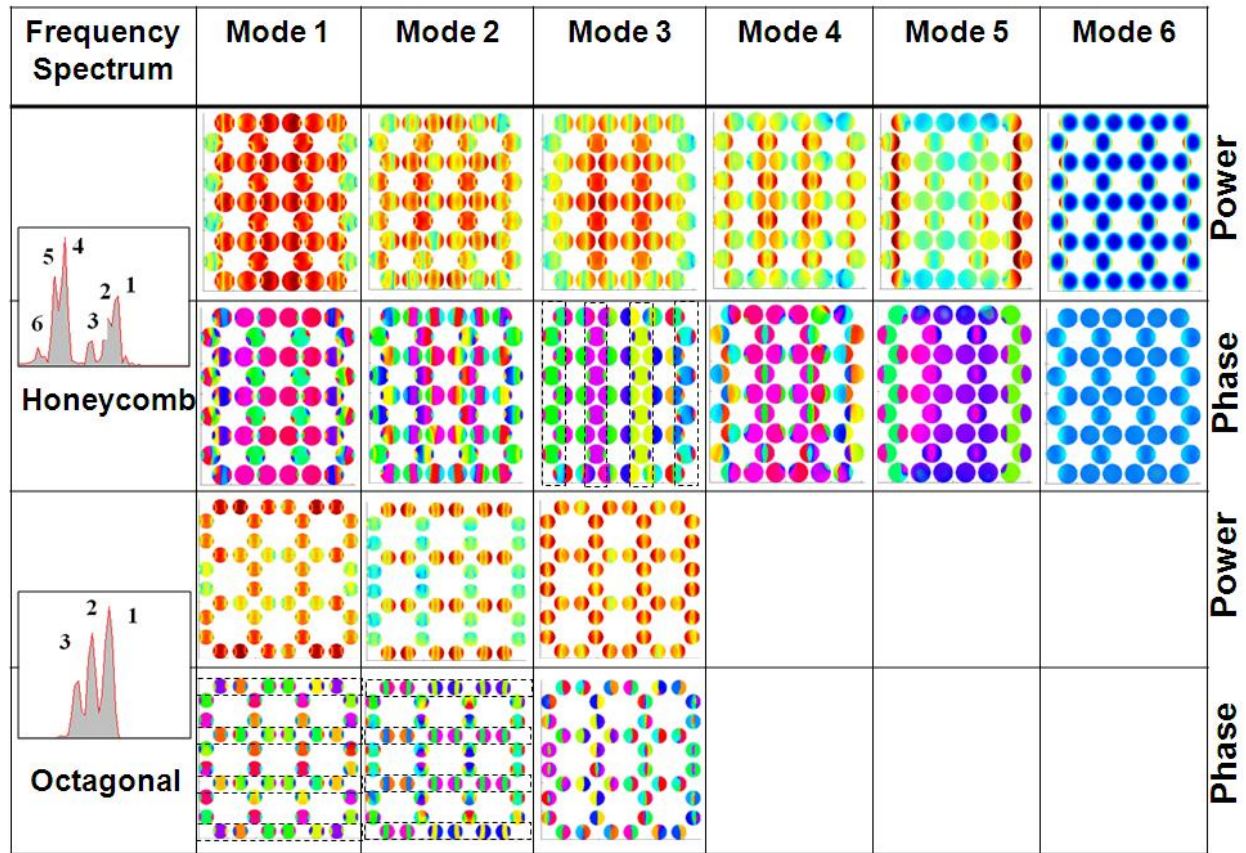


Fig. 6.7 The power and phase maps for different precessional modes of permalloy dot lattices with honeycomb and octagonal symmetry. The colormaps for power and phase distributions are as shown in Fig. 6.6.

result in the disappearance of the edge modes in those rows. Mode 1 of the octagonal lattice is the centre mode of the nanodots, where they are collectively precessing in phase within the regions shown by the dotted boxes. Mode 2 is the BV mode of the nanodots localized within the same regions as mode 1. Mode 3 is the edge mode of the individual nanodots uniformly distributed over the entire lattice.

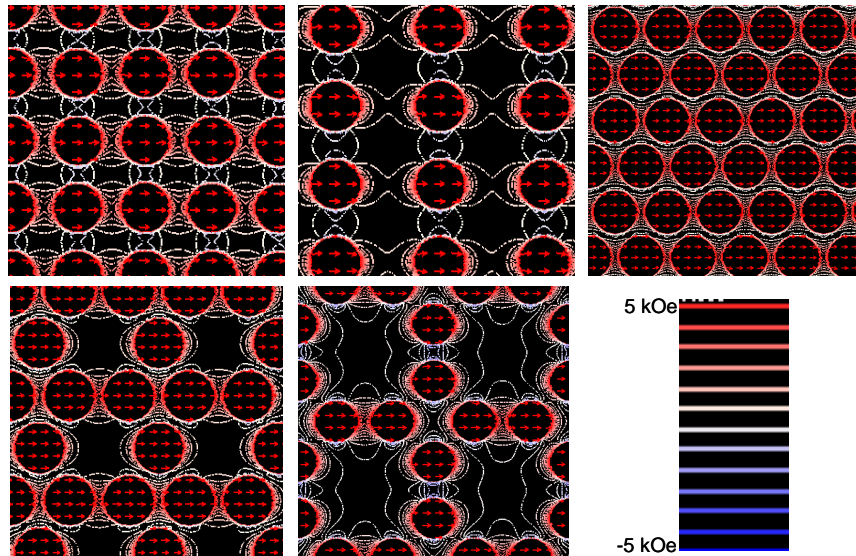


Fig. 6.8 Contour maps of simulated magnetostatic field distributions (x-component) are shown for permalloy dots lattices with variable lattice symmetry at $H = 1.3$ kOe at $\phi = 0^\circ$. The arrows inside the dots represent the magnetization states of the dots, while the strengths of the stray magnetic fields are represented by the color bar at the lower right corner of the figure.

To understand the origin of the differences in the spin wave spectra in different lattices, we have calculated the magnetostatic field distributions for lattices with different lattice symmetry as shown in Fig. 6.8. Linescans of the simulated magnetostatic fields from various positions of the lattices as indicated by horizontal dashed lines in Fig. 6.8 are shown in Fig. 6.9 along with the linescan of simulated magnetostatic field from a single 100-nm Py dot as a way of comparison. It is clear that both the internal fields on different dots as well as the stray fields are influenced by the lattice symmetry as well as the arrangement of the dots on a given lattice such as honeycomb and octagonal lattices. The overall internal fields inside the dots are increased significantly as compared to the single

dot for all dots in the square and hexagonal lattices, while they increase only marginally in the rectangular lattice. For the honeycomb and octagonal lattices the internal fields inside the dots increase significantly as compared to the single dot for dots lying on the denser rows and do not increase significantly for the dots lying on the sparser rows. The above variation of the internal fields of the dots in various lattices along with the stray fields are responsible for the variation in the frequencies of the collective modes as compared to the centre and edge mode frequencies of the single dot as shown in Fig. 6.4 . The stray field varies significantly with lattice symmetry primarily due to the arrangement of neighbouring dots in the lattice, as the boundary for every dot is almost identical in the simulation and the dots themselves are symmetric. Experimentally, there is some effect from the edge roughness and small differences in sizes and shapes from one dot to another. However, these effects are either introduced in the simulation (differences in size) or affect the dynamics only quantitatively, while the qualitative features of the spectra stems primarily from the lattice symmetry. For Bravais lattices (square, rectangular and hexagonal) dipolar contribution to the stray field is dominant but there are distinct differences due to the reasons stated as below. If we consider the columns standing perpendicular to the bias field, we see that for the square lattice the stray field is equally distributed on both sides of the columns as well as all elements on the columns are experiencing equivalent fields except for the edge elements. For the rectangular lattice the columns are separated by twice the distance of that of the square lattice causing a reduction of the stray fields between the columns but have similar amount of stray fields as the square lattice between the row elements. This caused two collective modes in the rectangular lattice. The hexagonal lattice is most closely packed and has the largest stray field and consequently shows a highly collective mode (mode 1). However, if we consider any column perpendicular to the bias field, it has alternative regions of interdot stray field or a full dot, which causes mode 2 in this lattice. However, for the honeycomb and octagonal lattices the stray field is even more complicated primarily because in the honeycomb lattice the unit cell has two nanodots, while there is a broken translational symmetry in the octagonal lattice. This causes unequal distributions of stray fields within the lattices and the occurrence of higher order multipolar contributions to the stray fields. Consequently, a larger number of modes with complicated profiles are

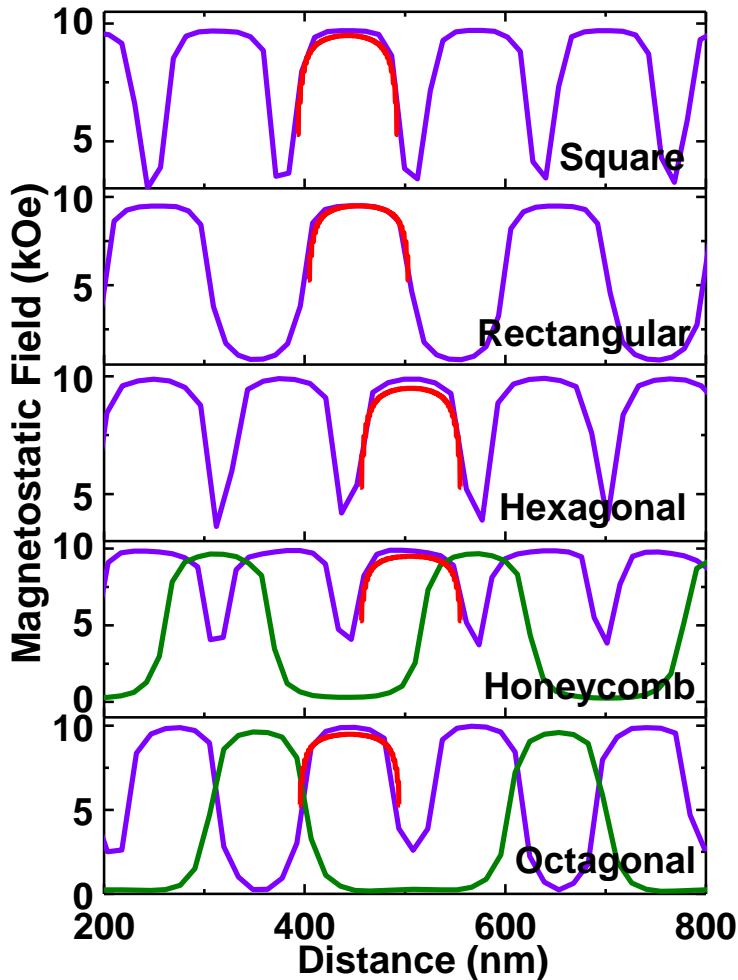


Fig. 6.9 Linescans of simulated magnetostatic fields from various lattices as obtained from the positions indicated by horizontal dashed lines in Fig. 6.8. Linescans of simulated magnetostatic field from a single dot is superposed on each panel for comparison.

observed in the honeycomb lattice. In the octagonal lattice also a band of modes are observed below 5 GHz experimentally but are not reproduced in the simulation possibly because the simulations are done on a much smaller lattice.

6.3 Conclusions:

We have fabricated closely packed permalloy nanodot lattices with 100 nm dot diameter and edge to edge inter-dot spacing of about 30 nm having variable lattice symmetry. We have chosen three two-dimensional Bravais lattices, namely the square, rectangular and hexagonal lattices and two non-Bravais lattices namely the honeycomb and octagonal

lattices for this study. We have investigated the influence of lattice symmetry on the ultrafast magnetization dynamics of these lattices. The precessional dynamics have been induced and probed in an all-optical manner following an ultrafast demagnetization and a fast remagnetization. The dynamics has also been simulated by a time-dependent micromagnetic simulation method and the time-domain magnetization, power spectra, and the power and phase profiles of the resonant modes have been numerically calculated to get an extensive picture of the dynamics. The precessional modes of magnetization show significant variation with the variation of lattice symmetry. The square lattice shows a single uniform precessional mode, which is the coherent precession of the edge mode of all the dots in the lattice. The rectangular lattice shows two modes, which are coherent precession of the edge and centre modes of the dots over the entire lattice. The hexagonal lattice shows three clear modes, which correspond to the uniform collective mode, a BV like mode and a bowtie like mode of the whole lattice. The honeycomb lattice shows broad and rich spin wave spectrum, which includes various localized and extended modes including the SW mode of the lattice. For octagonal lattice three modes are observed, which are uniform, SW like, and localized modes of the lattice. The magnetostatic stray fields within the lattices have been calculated, which helps in the interpretation of different observed modes of the lattices. The anisotropy of the collective modes in the hexagonal lattice has been investigated and mode 2, which is the edge mode of the dots forming a BV like mode of the lattice, shows a clear six-fold anisotropy, while other modes do not show any clear anisotropy with the variation of the azimuthal angle of the bias magnetic field. Analysis of the power profile of the anisotropic mode clearly shows the six-fold variation of the net dynamic component of magnetization with the azimuthal angle as a result of a similar variation of the stray magnetic field. The time-resolved MOKE experiment generally probes the zero and low wave-vector modes of spin-wave dispersion in a lattice and the effect of stray magnetic field is very prominent for these modes. Further study of the full magnonic band structure may reveal more rich physics leading towards the application of these artificial lattices in nanoscale microwave communication devices and components.

7. Extrinsic Configurational Anisotropy of Spin Waves in Two-Dimensional Ferromagnetic Nanodot Lattices with Varying Lattice Symmetry

7.1 Introduction:

Magnonic crystals (MCs) [13, 23, 35-37, 159] are artificial crystals with periodic modulation of magnetic properties where spin-waves (SWs) are the transmission waves. MCs form magnonic minibands consisting of allowed and forbidden SW frequencies and corresponding magnonic bandgap. The SWs in MCs can be controlled by changing its various physical and geometrical parameters such as material [218], shape [40, 233], size, lattice spacing [42], lattice symmetry [43, 225], as well as strength and orientation of the external bias field [98]. This tunability of MCs makes them a potential candidate for on-chip microwave communication devices and components, including magnonic waveguides [234], filters [83], splitters, phase shifters [84], spin-wave emitters [11], as well as for magnonic logic devices [7, 48]. In case of photonic crystals it is reported [235] that the anisotropy of photonic bandgap is dependent on the symmetry of the photonic crystal lattices. As the symmetry increases the Brillouin zone becomes more circular, resulting in a complete band gap. The highest order symmetry observed in a periodic lattice is six-fold, however, higher levels of symmetry can be potentially achieved by using complex geometries of quasicrystals [236]. It is well known that the spin and orbital angular momentum are responsible for the magnetic properties of solid. The violation of spin orbit angular momentum with respect to the rotation of magnetization direction leads to the concept of basic magnetic anisotropy. The magnetization at the edges of a confined magnetic element deviates from the external field direction to minimize the magnetic energies. These regions are known as the demagnetized regions. Consequently, the average

magnetization and the internal magnetic field changes with the rotation of the azimuthal angle of the external bias field. This is known as intrinsic configurational anisotropy [96, 126]. The effective magnetic field inside an element within an array is modified due to the stray field from the neighbouring elements. The tailoring of this field by rotating the bias field angle with respect to the symmetry axes of the array leads to the occurrence of extrinsic configurational anisotropy [98].

In chapter 6 we showed that lattice symmetry of two-dimensional nanodot arrays plays a significant role in their spin wave spectra. The single uniform collective mode in a square lattice splits into two modes in the rectangular lattice and into three modes in both the hexagonal and octagonal lattices. However, in the honeycomb lattice a broad band of modes is observed. This is due to a large variation of the stray field causing the inter-dot interaction. For such systems rotation of the azimuthal angle of the external bias field may lead to interesting extrinsic configurational anisotropy in the collective magnetization dynamics according to the lattice arrangements. Here, we investigate the above possible configurational anisotropy in circular nanodot arrays arranged in square, rectangular, hexagonal, honeycomb and octagonal lattices. We will show that the square lattices exhibit a four-fold configuration anisotropy [151] whereas for the rectangular, hexagonal, honeycomb and octagonal lattices the most intense peak shows primarily two-fold, six-fold, six-fold and eight-fold anisotropies superposed with a relatively weak four-fold anisotropy due to the shape of the boundary of the arrays respectively.

7.2 Experimental Details:

$10 \times 10 \mu\text{m}^2$ arrays of 20 nm thick Ni₈₀Fe₂₀ dots with negligible magnetocrystalline anisotropy and with circular shapes arranged in square, rectangular, hexagonal, honeycomb and octagonal lattices are fabricated by a combination of electron beam lithography and electron beam evaporation. The diameters of individual dots are about 100 nm and the edge-to-edge separations between the dots are about 30 nm. The dot shape, size and the inter-dot separation are chosen to ensure negligible shape anisotropy, accommodation of two intrinsic modes [24, 232] (edge and centre modes) inside the dots and a strongly collective magnetization dynamics of the array.

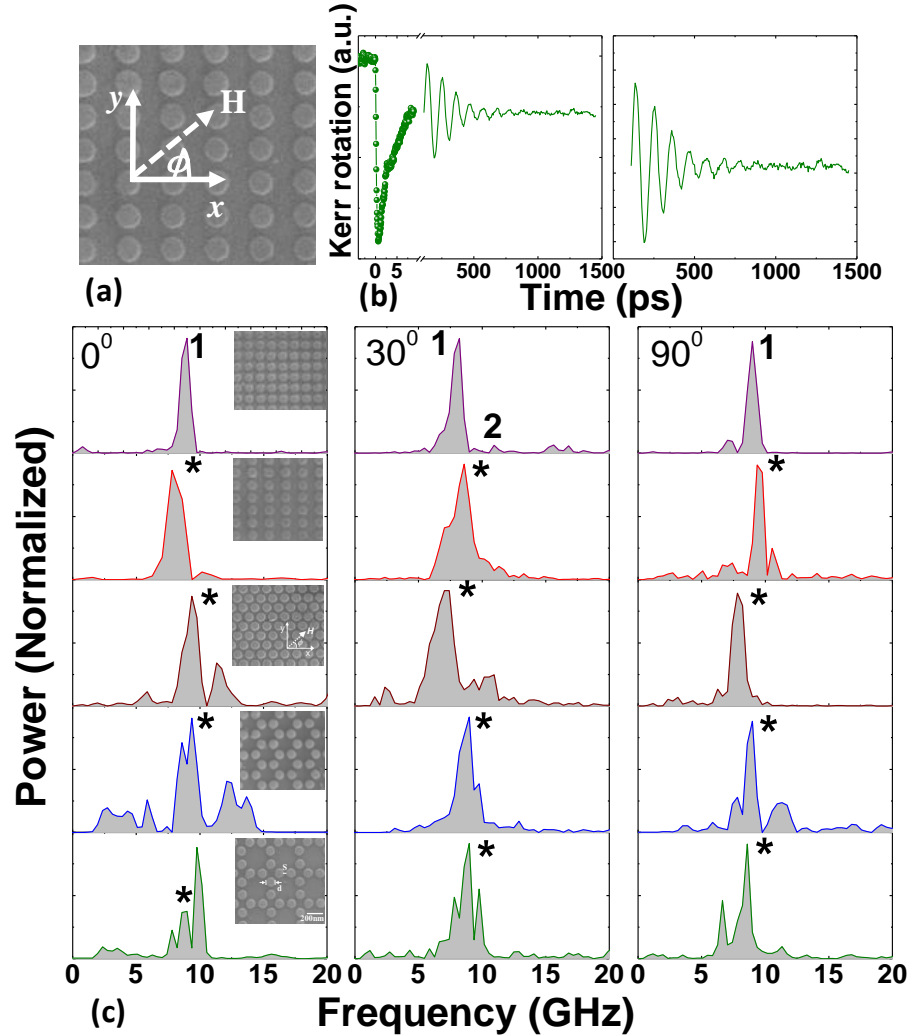


Fig. 7.1 (a) A schematic of the experimental geometry is shown on the scanning electron micrograph of an array of circular nanodots with rectangular lattice symmetry. (b) Typical experimental time-resolved Kerr rotation data from the octagonal lattice at $H = 1.3$ kOe revealing ultrafast demagnetization, fast and slow relaxations, and precession of magnetization (left panel). Background subtracted time-resolved Kerr rotation data is shown in the right panel. (c) The spin wave spectra obtained by FFT of the time-resolved data from square, rectangular, hexagonal, honeycomb and octagonal lattices are shown for different values of ϕ at $H = 1.3$ kOe. The corresponding scanning electron micrographs are shown in the insets.

7.3 Measurement Techniques:

The ultrafast magnetization dynamics of the samples is measured by an all-optical time-resolved magneto-optical Kerr effect microscope based upon a two-color collinear pump-probe geometry [29] as described in details in section 3.4.2 of chapter 3. The second harmonic ($\lambda = 400$ nm, pulse width ~ 100 fs) of a mode-locked Ti- Sapphire laser (Tsunami, Spectra Physics) is used to excite the magnetization dynamics in the sample whereas the time-delayed fundamental ($\lambda = 800$ nm, pulse width ~ 80 fs) is used to probe the dynamics by measuring the Kerr rotation as a function of the time-delay between the pump and probe beams. The pump and probe beams are made collinear and are focused onto the centre of the whole array by using a microscope objective (N.A. = 0.65) to spot sizes of 1 μm and 800 nm, respectively to measure the local magnetization dynamics under the focused laser spot. An external magnetic field (H) is applied at a small angle (10°) to the sample plane. In the experimental set up, we effectively vary the azimuthal angle (ϕ) (Fig. 7.1 (a)) of H between 0° and 180° at intervals of 5° , 10° , 10° , 15° and 15° for octagonal, honeycomb, hexagonal, rectangular and square lattice, respectively. This is done by rotating the samples using a high precession rotary stage while keeping the microscope objective and H constant. The pump and the probe beams are made to incident on the same region of the array for each value of ϕ .

7.4 Results and Discussions:

Figure 7.1(b) represents a typical time-resolved Kerr rotation data for octagonal lattice at a bias field $H = 1.3$ kOe at $\phi = 0^\circ$. The data in the left panel shows an ultrafast demagnetization within 500 fs with a bi-exponential decay with decay constants of 3 ps and 400 ps. The precessional dynamics appears as an oscillatory signal on the slowly decaying part of the time-resolved Kerr rotation data. The background subtracted Kerr rotation data is shown in the right panel. The fast Fourier transformations (FFTs) of the time resolved data reveal the SW spectra as shown in Fig. 7.1(c) for the square, rectangular, hexagonal, honeycomb and octagonal lattices at $\phi = 0^\circ$, 30° and 90° . The corresponding SEM images of the lattices are shown in the inset. The experimental geometry is shown on the

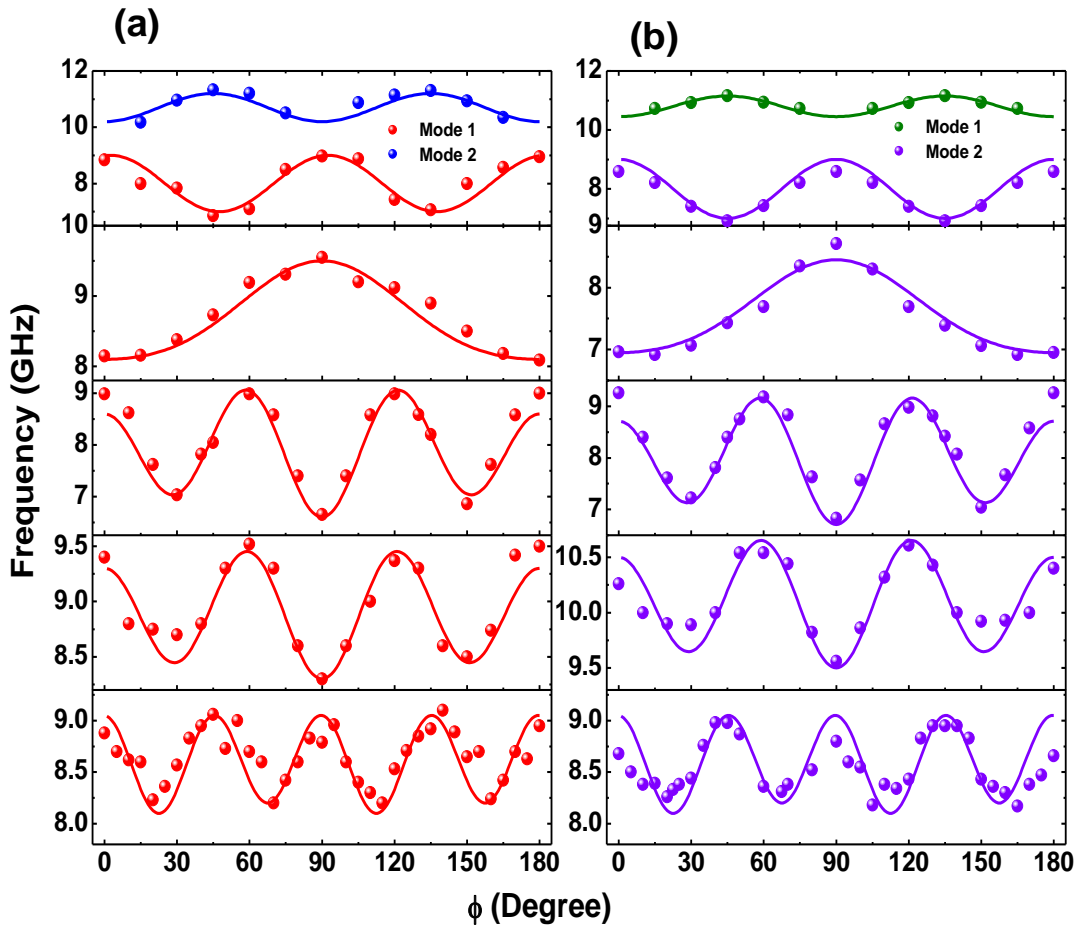


Fig. 7.2 (a) Experimental and (b) simulated spin wave frequencies (symbols) as a function of the azimuthal angle ϕ of the in-plane bias magnetic field at $H = 1.3$ kOe. The solid curves show the theoretical fits.

SEM image of the rectangular lattice. A clear difference is observed in the SW spectra both with the variation of the lattice arrangement and ϕ . The solid curves correspond to theoretical fits to harmonic functions with anisotropies having different symmetries (Fig. 7.2 (a) and (b)). For the square lattice a single uniform collective mode splits into two modes as ϕ changes (Fig. 7.1(c)) and a clear four-fold anisotropy is observed for both the branches. The rectangular lattice shows two modes for all ϕ values (Fig. 7.1(c)) and the lower frequency mode (asterisk marked) shows a combination of two-fold (88%) and four-fold (12%) anisotropies (Fig. 7.2(a)) from the theoretical fit. For hexagonal lattice the

highest intensity peak (asterisk marked) shows a combination of two-fold (77%) and four-fold (23%) anisotropies with the variation in ϕ , while the other modes for this lattice do not show any clear anisotropy with the variation in ϕ . For honeycomb lattice the situation is quite different. A broad band of modes for $\phi = 0^\circ$ transforms to a single mode with a small splitting at $\phi = 30^\circ$. As ϕ increases further new modes start to appear and at $\phi = 45^\circ$ two modes with a small splitting are observed while for $60^\circ \leq \phi \leq 90^\circ$ again broad band of modes appear. This phenomenon is repeated with a period of 90° . The frequency of the asterisk marked mode first decreases as ϕ deviates from 0° . At $\phi = 30^\circ$ the frequency attains a minimum value and

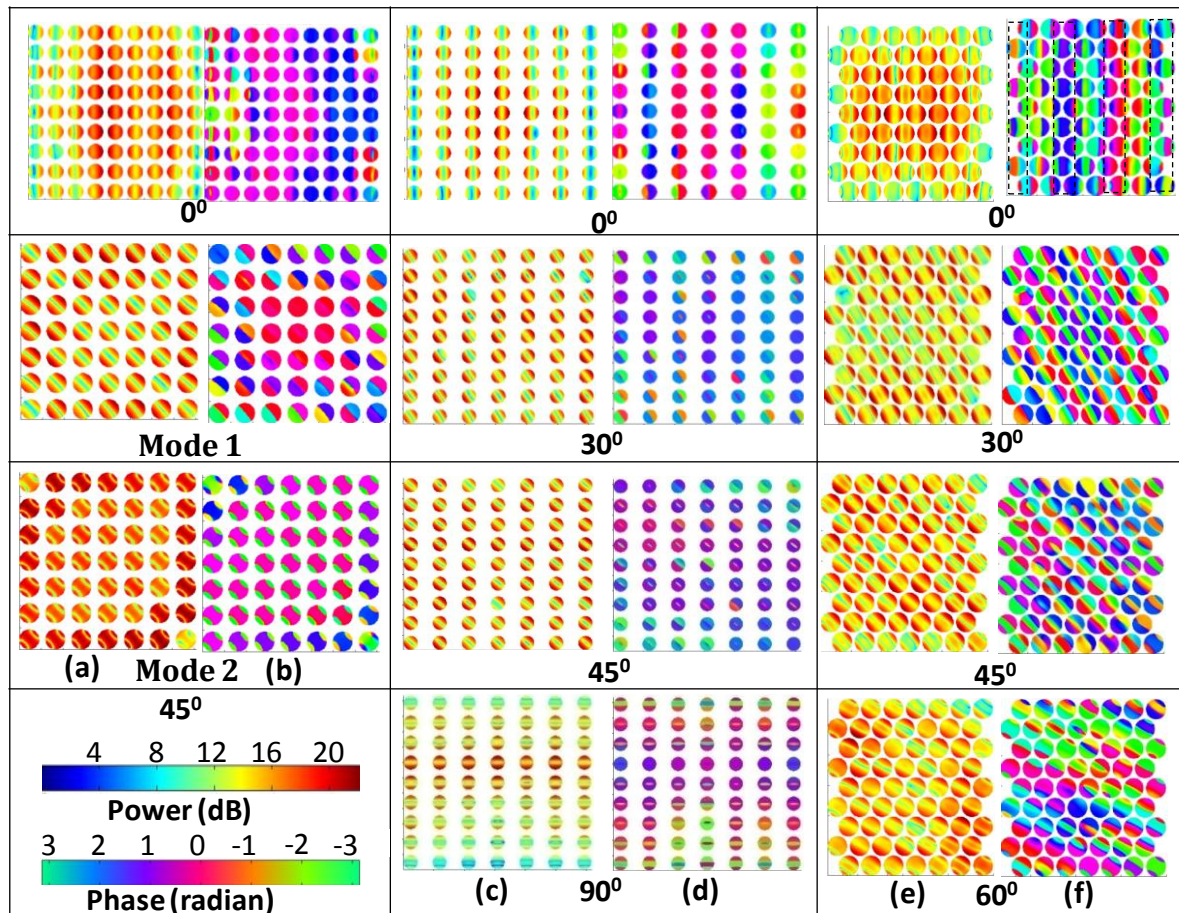


Fig. 7.3 The power ((a), (c) and (e)) and phase ((b), (d) and (f)) maps of the asterisk (*) marked modes for the square ((a), (b)), rectangular ((c), (d)) and hexagonal ((e), (f)) lattices for selected values of ϕ at $H = 1.3$ kOe. The color maps for power and phase distributions are shown at the bottom of the left panel of figure.

it increases again as the ϕ changes from 30° and a maxima is obtained at $\phi = 60^\circ$. This phenomenon is repeated and at $\phi = 30^\circ, 90^\circ$ and 150° minima are observed whereas at $\phi = 0^\circ, 60^\circ, 120^\circ$ and 180° maxima is observed as shown in Fig. 7.2 (a). Theoretical fitting of the variation of this mode frequency with ϕ shows a combination of six-fold (83%) and four-fold (17%) anisotropies. For octagonal lattice, three modes (Fig. 7.1(c)) are observed at $\phi = 0^\circ$ and the number of modes remained the same for all values of ϕ except for variation in their relative intensities. The asterisk marked mode corresponding to $f = 8.84$ GHz shows a combination of eight-fold (90%) and four-fold (10%) anisotropies as shown in Fig. 7.2(a).

To understand the origin of these anisotropies, we have performed micromagnetic simulations at $T = 0$ K using the OOMMF software [161] on $1100 \times 1100 \times 20$ nm³ volume consisting of circular dots arranged in different lattice symmetries. The sample geometries for the simulation are derived from the SEM image of the samples. The simulated array volumes are considered smaller than the experimental samples due to computational resources. However, they are larger than the excitation and probe volumes used in the experiment and are expected to capture the experimental observations well. The samples are discretized into rectangular prism-like cells with dimensions $2 \times 2 \times 20$ nm³. Discretization of circular nanodots by rectangular prism like cells introduces some artificial edge roughness but this is negligible compared to the dimensions of the nanodots and does not affect the dynamics significantly. The lateral cell size is well below the exchange length of Py (5.3 nm). The parameters used for the simulation are $\gamma = 18.5$ MHz/Oe, exchange stiffness constant, $A = 1.3 \times 10^{-6}$ erg/cm, magnetocrystalline anisotropy constant $K = 0$ and saturation magnetization $M_s = 860$ emu/cc. The external bias field H is applied according to the experimental configuration and a pulsed field of rise time of 50 ps and peak amplitude of 30 Oe is applied perpendicular to the sample plane. The optical excitation used in the experiment is simulated as a pulsed magnetic field, which is a valid approximation as within few picoseconds of the optical excitation the energy from the spin and electron systems are transferred to the lattice, which effectively launches a pulsed magnetic field within the system and triggers the spin wave dynamics as studied here.

The dynamic simulations were acquired for 1.5 ns at the time steps of 5 ps. The experimental results are qualitatively reproduced by the simulations. In Fig. 7.2(b), the

simulated mode frequencies for different lattices are plotted as a function of ϕ . The simulations reproduced the major experimentally observed features. Theoretical fits to the simulated results reveal the presence of two-fold, six-fold, six-fold and eight-fold anisotropy, superposed with a four-fold anisotropy for rectangular, hexagonal, honeycomb and octagonal lattice, respectively and a clear four-fold anisotropy is present for square lattice only. The fits are reasonable for both experimental and simulated data, and the deviations are possibly due to the edge roughness and irregularities in the samples, which modify the anisotropy arising due to the symmetry of the stray magnetic field in this lattice. There are primarily three contributions to the configurational anisotropy – 1) the shape of the array boundary 2) the lattice symmetry and 3) the shape of the individual dot. The first contribution arises due to the strongly collective magnetization dynamics, the second contribution originates from inter-dot the magnetostatic stray fields and the ensuing change in the internal fields of the constituent nanodots while the third contribution is not applicable in our case as the dot shapes are circular. Here, first two contributions are present for all the lattices.

7.4.1 Simulated Angular Variation of the Mode Profiles of the Collective Modes for Nanodot Lattice with Varying Lattice Symmetry:

We have further simulated the angular variations of mode profile of the studied modes for samples with different lattice symmetry. The power and phase map [162] of the modes for square, rectangular, hexagonal, honeycomb and octagonal lattices at different ϕ values are shown in Figs. 7.3 and 7.4. For square lattice the anisotropic mode (Fig. 7.3(a, b)) at $\phi = 0^\circ$ corresponds to the edge mode of the individual nanodots precessing coherently over the central part of the lattice, while the amplitude of precession dies out substantially near the vertical edges of the lattice. With the variation of ϕ the edge modes in the dots rotates and

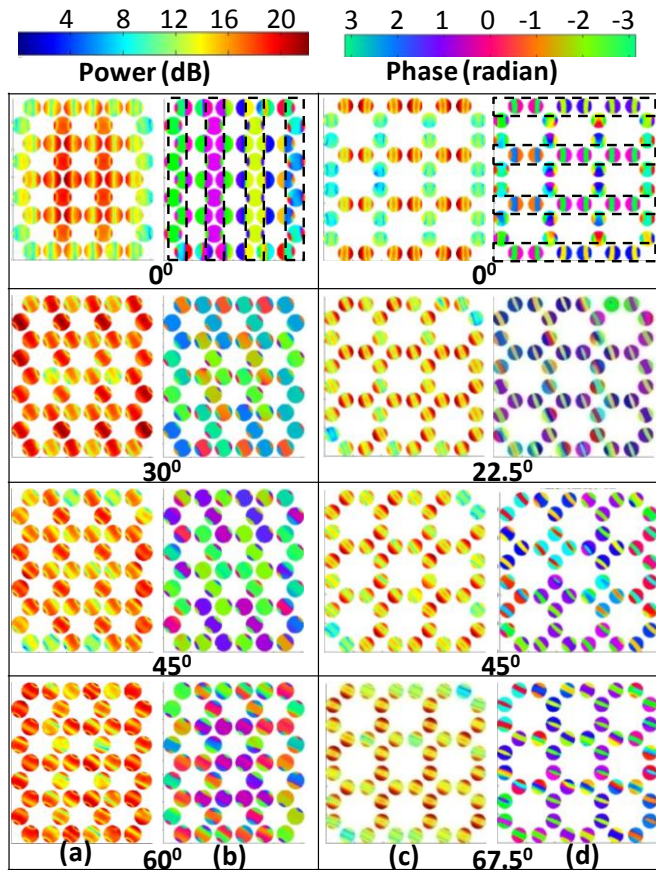


Fig. 7.4 The power ((a) and (c)) and phase ((b) and (d)) maps of the asterisk (*) marked modes for the honeycomb ((a), (b)) and octagonal ((c), (d)) lattices for selected values of ϕ at $H = 1.3$ kOe. The color maps for power and phase distributions are shown at the top of the figure.

at $\phi = 45^\circ$ edge mode of individual element (mode 2) and center mode (mode 1) of individual nanodots precessing coherently over whole array appear. In case of square lattice due to the strong magnetostatic interaction the boundary effect is superposed with the lattice symmetry effect. As a result, in case of square lattice a clear four-fold anisotropy is observed. For the rectangular lattice (Fig. 7.3(a, b)), the anisotropic mode at $\phi = 0^\circ$ corresponds to the edge mode of the individual nanodots distributed uniformly over the entire lattice barring the vertical edges. With the variation of ϕ the edge modes in the dots and their distribution in the array rotate following the bias field. Clearly the stronger interaction between the edge modes of the dots along the vertical direction (smaller lattice

constant) gives the stronger two-fold anisotropy while the square boundary of the array gives the weaker four-fold anisotropy due to the collective dynamics of the array. For hexagonal lattice, at $\phi = 0^\circ$ the anisotropic mode (Fig. 7.3(e, f)) corresponds to the edge mode of the individual dots, which forms a Backward volume (BV) like mode of the whole lattice. As the angle deviates from $\phi = 0^\circ$ the overall power of asterisk marked mode decreases and attains a minimum at $\phi = 30^\circ$. For further increase in ϕ the power increase again and attains a maximum at $\phi = 60^\circ$. This phenomena is repeated and we observe maxima at $\phi = 0^\circ, 60^\circ, 120^\circ$ and 180° and minima at $\phi = 30^\circ, 90^\circ$ and 150° . This periodic variation of power of asterisk marked mode with ϕ is a manifestation of the variation of the stray magnetic field in the lattice, and it gets reflected in the six-fold variation in the frequency of this mode. The honeycomb lattice shows a number of modes at $\phi = 0^\circ$ but the only anisotropic mode correspond to vertical stripe-like regions, where the half circles (full circle) are alternatively precessing in-phase and out-of-phase with each other (dotted boxes in Fig. 7.4(a, b)) forming a collective BV like mode of the array. As ϕ increases from 0° the collective BV like mode breaks down giving rise to a complicated mode profile. In addition, the distribution of the power of the mode at the central part of the array varies, first decreasing as ϕ increases from 0° to 30° and then increasing as ϕ increases further to 60° . For the octagonal lattice the anisotropic mode corresponds to the BV like modes of the nanodots collectively precessing in phase within the regions shown by the dotted boxes (Fig. 7.4(c, d)) at $\phi = 0^\circ$. As ϕ increases the collective modes of the arrays break down. In addition, the power map shows that the BV like mode of the constituent dots converts to edge mode of the dots at 22.5° , reappears at 45° and turns into edge modes again at 67.5° and repeat in this fashion. Since the edge mode has lower frequencies than the BV like mode the mode frequency varies with that period.

7.4.2 Angular Variation of Simulated Magnetostatic Field Distributions for Different Lattice Symmetry:

Although the spin wave mode profiles give some indication about the origin of the observed configurational anisotropy, we have further studied the variation of magnetostatic field distribution in the arrays with the bias field angle ϕ for rectangular,

honeycomb and octagonal lattice. The magnetostatic field consists of dipolar and higher orders multipolar fields as well as localized fields in some cases. Figure 7.5 shows the contour plots of the above field for different lattices at $\phi = 30^\circ, 45^\circ$ and 90° , while the

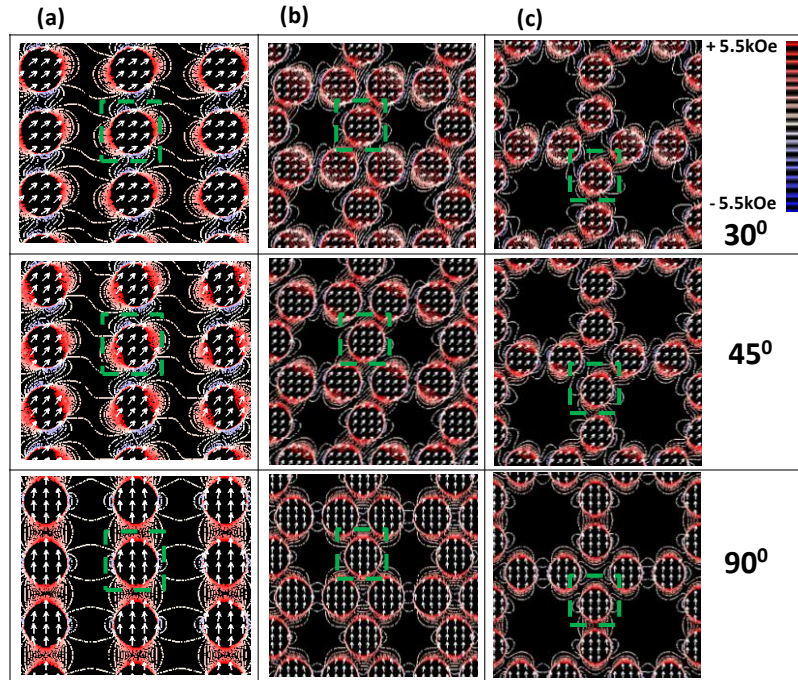


Fig. 7.5 Contour maps of simulated magnetostatic field distributions (x -component) are shown for (a) rectangular, (b) honeycomb and (c) octagonal lattice for selected values of ϕ at $H = 1.3$ kOe. The schematics of the applied bias field directions are also shown for all values of ϕ . The color map for the magnetostatic field is shown at the right panel of the figure.

arrows represent the magnetization inside the dots and the schematic shows the direction of the applied bias field. The stray fields as well as the internal fields change considerably with the variation of ϕ leading towards the variation in the observed mode structures as

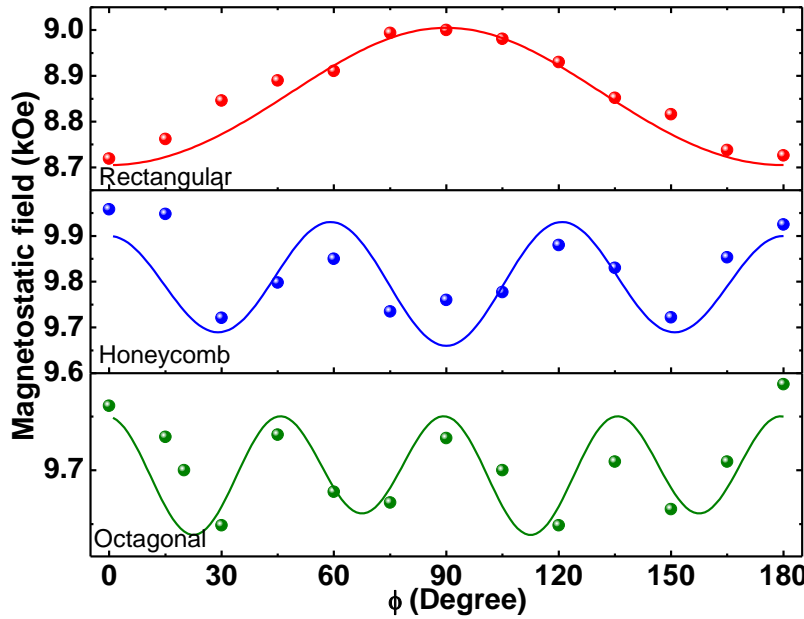


Fig. 7.6 Variation of the simulated average magnetostatic field as a function of ϕ at $H = 1.3$ kOe from samples with different lattice symmetry. The symbols show simulated data, while the solid curves show the theoretical fits.

well as the mode frequencies. We have further estimated the variation of the average magnetic field acting on a single dot from the array shown by the dotted boxes in Fig. 7.5 with ϕ and found a similar anisotropy in the magnetic field itself as shown in Fig. 7.6. Theoretical fitting with the data in Fig. 7.6 revealed two-fold, six-fold and eight-fold anisotropy superposed with a weak four-fold anisotropy for the rectangular, honeycomb and octagonal lattice, respectively. This variation is a result of the magnetic environment of the dots in different lattices and its ensuing variation with the angle of the bias field, and is manifested as the configurational anisotropy in the samples.

7.5 Conclusions:

In conclusion, we have investigated the configurational anisotropy in the precessional magnetization dynamics in two dimensional ferromagnetic nanodot lattices with different lattice symmetries. The azimuthal angle of the bias magnetic field is varied between 0° and 180° and the spin wave spectrum showed a drastic variation in number of peaks and peak positions with the angle. The dominant precessional mode showed two-fold, six-fold, six-fold and eight-fold anisotropy superposed with a weak four-fold anisotropy for rectangular, hexagonal, honeycomb and octagonal lattice, respectively whereas for square lattice only

four-fold is observed. For square lattice, the four-fold anisotropy originates due to the square boundary of the array due to the strong collective magnetization dynamics as well as the square lattice symmetry of the array due to the extrinsic configurational anisotropy arising from the inter-dot magnetostatic interaction. For rectangular, hexagonal, honeycomb and octagonal lattices the four-fold anisotropy originates due to the square boundaries of the arrays again due to the strong collective magnetization dynamics, whereas two-fold, six-fold and eight-fold anisotropies arise due to the extrinsic configurational anisotropy from the variation of the magnetostatic field distribution within the arrays with the lattice symmetry and bias field angle. Micromagnetic simulations reproduced the observations qualitatively and the simulated mode profiles identified the specific modes showing anisotropy. While the angular variation of the simulated mode profiles give sufficient indications towards the possible reasons of the observed anisotropy, analyses of the simulated magnetostatic field distribution pinpointed the exact reason as the variation of the stray fields inside the arrays and the internal fields inside the nanodots for the observed anisotropy. The observed tunability of anisotropy of spin wave frequency and mode structure with lattice symmetry is important for their anisotropic propagation in two-dimensional magnonic crystals.

8. Tunable Magnetic Anisotropy in Two-Dimensional Arrays of Ni₈₀Fe₂₀ Elements

8.1 Introduction:

Arrays of nanomagnets have huge potential in present and future technologies such as magnetic storage [1], memory [4], logic devices [5, 8] and spin torque nano-oscillators [11]. Periodic arrays of magnetostatically coupled nanomagnets can also act as magnonic crystal (MC) [23, 36-37] where spin waves are the transmission waves. MCs form magnonic minibands consisting of allowed and forbidden frequencies. The spin waves in MCs can be tuned by changing various physical and geometrical parameters such as material [39], shape [40-41], size, lattice spacing [38], lattice symmetry [43], and strength and orientation of the external bias field [43, 98]. The magnetization at the edges of a confined magnetic element deviates from the external field direction to minimize the magnetic energies. These regions are known as the demagnetized regions and they affect both the magnetization reversal and spin waves in confined magnetic elements. As a result the direction of the average magnetization changes within the plane of the element with the variation of the azimuthal angle of the external bias field. This leads to the configurational magnetic anisotropy [96, 186] in the static [126] and dynamic [96] magnetic properties of these systems. The influence of magnetostatic coupling on the spin configuration and magnetization reversal mechanism of a linear chain of Ni₈₀Fe₂₀ (Permalloy/Py) ellipse has been reported [237] but there is no report on the effect of such arrangements of magnetic elements on their magnetization dynamics. Here, we present the ultrafast magnetization dynamics of arrays of Py elliptical elements arranged along their long axis (LA) or short axis (SA) and show from dynamic measurements that a two-fold configurational anisotropy of these elements can be efficiently tuned by changing the arrangement of the elements.

8.2 Experimental Details:

Elliptical Py elements with thickness, length and width of 25 nm, 1 μm and 450 nm, respectively dispersed in three different lattice arrangements were fabricated using self aligned shadow deposition technique [105]. The detail about this technique is described in section 3.2.5 in chapter 3. In sample 1 (S1) the edge-to-edge separation of the elements along X (s_x) and Y (s_y) directions are 600 nm whereas for sample 2 (S2) $s_x = 600 \text{ nm}$, $s_y = 70 \text{ nm}$ and for sample 3 (S3) $s_x = 70 \text{ nm}$, $s_y = 600 \text{ nm}$. Figure 8.1 (a) shows the SEM images of S1-S3.

The ultrafast magnetization dynamics of the samples are measured by using an all-optical time-resolved magneto-optical Kerr effect microscope as described in details in section 3.4.2 of chapter 3. The second harmonic ($\lambda = 400 \text{ nm}$, pulse width = 100 fs) of a mode locked Ti-Sapphire laser (Tsunami, Spectra physics) is used to pump the samples whereas the time delayed fundamental ($\lambda = 800 \text{ nm}$, pulse width = 80 fs) is used to probe the magnetization dynamics. Both the pump and probe beams are made collinear and are focused by using a microscope objective to spot sizes of 1 μm and 800 nm, respectively on a single permalloy element in three different arrays. The inter-element magnetostatic interaction is different for three different arrays and magnetization dynamics of a single permalloy element is measured in presence of varying magnetostatic environments. An external magnetic field (H) is applied at a small angle ($\sim 10^\circ$) to the sample plane. In the experimental setup, we effectively vary the azimuthal angle (ϕ) (Fig. 8.1 (a)) of the bias field H between 0° and 180° at intervals of 15° by rotating the sample using a high precession rotary stage while keeping the microscope objective and the magnetic field constant. The pump and the probe beams are made to incident on the same element in the array after changing ϕ every time.

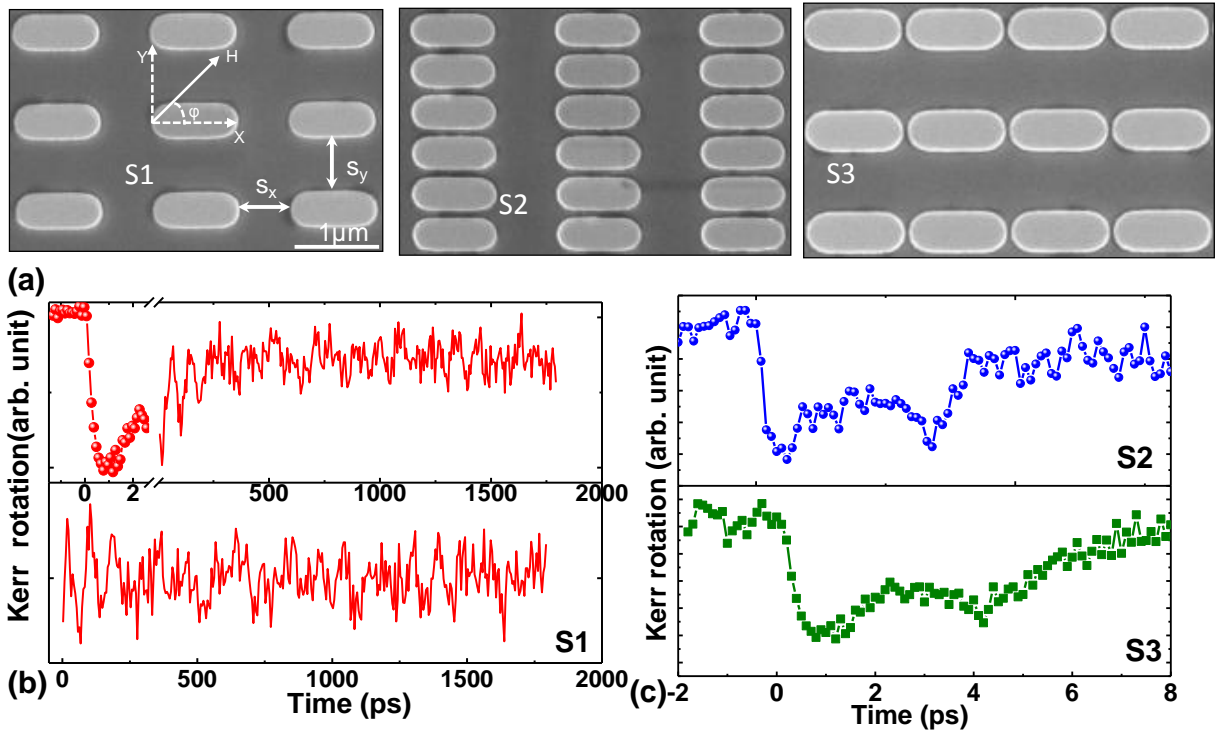


Fig. 8.1 (a) The scanning electron micrographs of two-dimensional arrays of Py elements (S1, S2 and S3). The schematic of the experimental geometry is shown on the SEM image of S1. (b) Typical experimental time-resolved Kerr rotation data for S1 at $H = 1.5$ kOe at $\phi = 0^\circ$ revealing ultrafast demagnetization, fast and slow relaxations and precession of magnetization is shown in the top panel. Background subtracted time-resolved Kerr rotation for S1 is shown in the bottom panel. (c) The Kerr rotation data showing ultrafast demagnetization and fast remagnetization are shown for S2 and S3 at $H = 1.5$ kOe at $\phi = 0^\circ$.

8.3 Results and Discussions:

Figure 8.1(b) represents a typical time-resolved Kerr rotation data for S2 when $H = 1.5$ kOe is applied parallel to the SA of a Py element ($\phi = 0^\circ$). The data shows that the demagnetization occurs within 500 fs with a bi-exponential decay with decay constants of 3.5 ps and 136 ps, respectively corresponding to spin lattice interaction and transfer of electron and lattice energy to the substrate and the surroundings [143]. The precessional dynamics appears as an oscillatory signal on top of the slowly decaying time-resolved Kerr rotation. The background subtracted Kerr rotation data is shown in the bottom panel of Fig.

8.1(b). A fast Fourier transformation (FFT) is performed to obtain the spin wave spectra for different samples at various ϕ values. In Fig 8.1(c) the ultrafast demagnetization is shown for S2 and S3. There is no significant variation of demagnetization time and fast relaxation time for different samples as these are primarily material properties. The slower relaxation time varies with sample as the geometry of the sample as well as their contacts with the substrate vary. However, no systematic variation is observed.

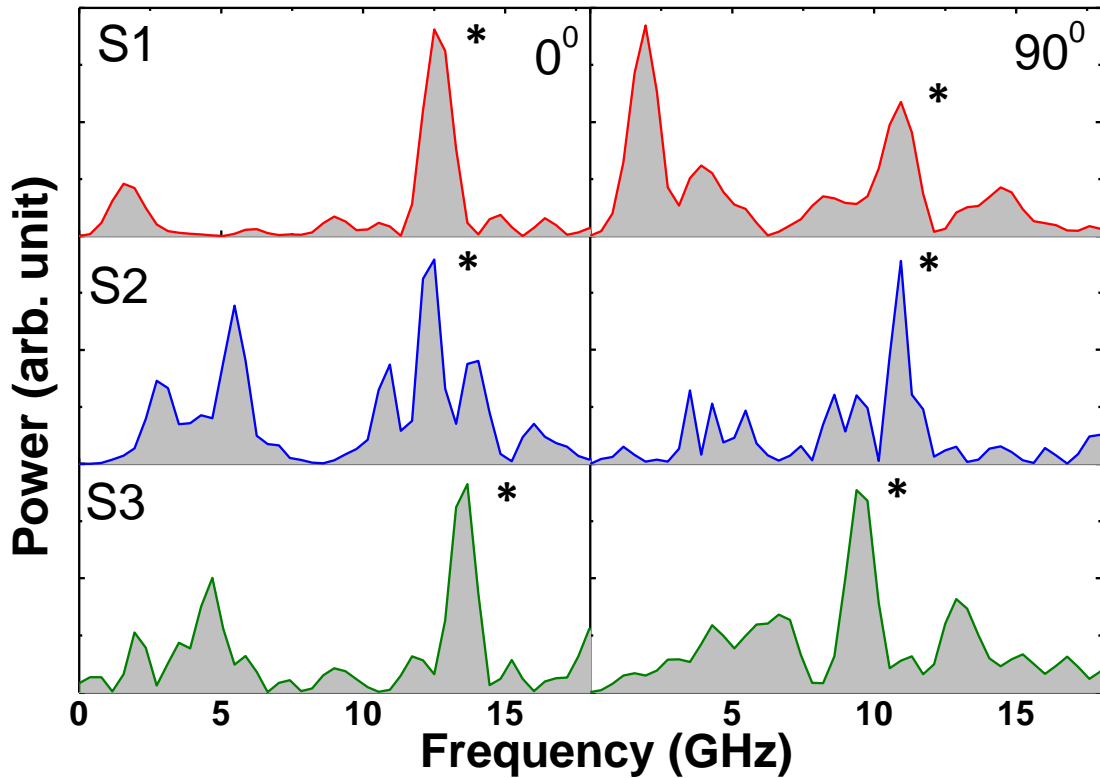


Fig. 8.2 The spin wave spectra obtained by FFT of the time-resolved Kerr rotation are shown for (a) $\phi = 0^\circ$ and (b) $\phi = 90^\circ$ at $H = 1.5$ kOe.

In Fig. 8.2(a) the corresponding spin wave spectra for $\phi = 0^\circ$ and 90° are shown. A clear difference is observed in the spin wave spectra when the bias field direction (ϕ) is varied for all three samples as well as when the lattice arrangement is varied at a fixed value of ϕ . At $\phi = 0^\circ$, a dominant mode at about 12.7 GHz and a lower frequency mode at about 1.9

GHz are observed. However, for S2 the higher frequency mode splits into three modes at about 13.9, 12.3 and 10.9 GHz and for S3 again a single dominant mode at 13.5 GHz is observed. A number of modes at the lower frequency end are also observed but here we concentrate mainly on the higher frequency mode marked by an asterisk in Fig. 8.3(a), which shows clear two-fold anisotropy. When the field direction is changed to 90° the higher frequency mode for S1 now occurs at about 11 GHz with a shoulder at 8.3 GHz, in addition to two broad bands at about 2 and 4 GHz. In S2 and S3, the most intense peak appears at 10.9 and 9.5 GHz along with closely spaced shoulders and other broad peaks. Here also the peaks under investigation are marked by asterisk. The variation of this peak frequency with the azimuthal angle is plotted in Fig. 8.3(a), which clearly shows a two-fold anisotropy. This variation in precessional frequency is fitted with a modified Kittel formula after introducing a two-fold anisotropy [145] and assuming zero magnetocrystalline anisotropy for permalloy as given below

$$f = \frac{\gamma}{2\pi} \sqrt{(H + \frac{2K_2}{M} \cos 2\phi)(H + \frac{2K_2}{M} \cos^2 \phi + 4\pi M)} \quad (8.1)$$

where $\gamma = 17.6$ MHz/Oe is the gyromagnetic ratio and $M = 820$ emu/cc is the effective magnetization of the sample. The effective anisotropy field can be written as $H_K = 2K_2/M$. The extracted anisotropy field (H_K) from the above fit is found to be significantly different for three different samples and are 320 Oe, 210 Oe, and 400 Oe, respectively for S1, S2 and S3.

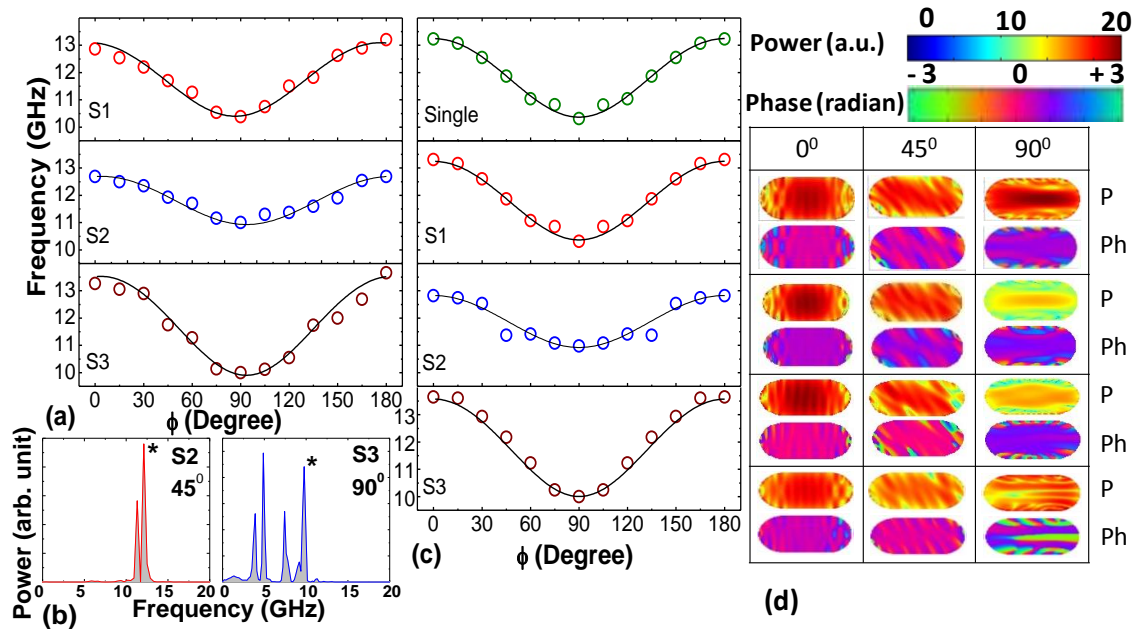


Fig. 8.3 (a) Experimental precessional frequencies (symbols) are plotted as a function of azimuthal angle of the bias field (ϕ) for S1, S2, and S3 at $H = 1.5$ kOe. (b) Simulated spin wave spectra from the central element of 3×3 arrays used in S2 ($\phi = 45^\circ$) and S3 ($\phi = 90^\circ$). (c) Simulated precessional frequencies (symbols) are plotted as a function of azimuthal angle of the bias field (ϕ) for a single permalloy element and the central element from three different arrays (S1, S2 and S3) at $H = 1.5$ kOe. The solid lines in (a) and (c) represent fits to Eqn. (8.1). (d) The power (P) and phase (Ph) maps of the corresponding mode (*) from the central element of S1, S2, and S3 at $\phi = 0^\circ, 45^\circ$, and 90° at $H = 1.5$ kOe.

We have performed micromagnetic simulation using OOMMF [161] software for arrays of 3×3 elements arranged like S1, S2 and S3. Further test simulations with larger arrays of 5×5 elements do not produce any significant difference in the precession frequencies. It has been shown that collective excitations with nonzero wave-vectors do not couple to spatially uniform excitation fields in arrays with boundary effects [238]. However, here, we are interested in uniform collective SW modes and hence simulations on arrays of 3×3 elements serve our purpose. The sample geometries for the simulation are derived from the SEM image of the samples. The samples are discretized into rectangular prism-like cells with dimensions $4 \times 4 \times 25$ nm³. The parameters used for the simulation are $\gamma = 17.6$

MHz/Oe, exchange stiffness constant, $A = 1.3 \times 10^{-6}$ erg/cm, magnetocrystalline anisotropy constant $K = 0$ and saturation magnetization $M_s = 860$ emu/cc. The static and the dynamic simulations are performed by methods described in chapter 4. The external bias field is applied according to the experimental configuration and a pulsed field of rise time of 50 ps and peak amplitude of 30 Oe is applied perpendicular to the sample plane. Figure 8.3(b) shows the simulated spin wave spectra from the central element of the array of 3×3 elements for samples S2 ($\phi = 45^\circ$) and S3 ($\phi = 90^\circ$). While in the first case, two closely spaced modes are observed, and in the second case a number of modes over broad frequency range are observed and the peak under investigation is marked by an asterisk. We have first simulated the angular variation of precession frequency of a single permalloy element as shown in Fig. 8.3(c) alongwith a fit with the Kittel formula. The extracted value of H_K from simulation of a single element is 340 Oe. We have further simulated three different lattices, which qualitatively reproduced the experimentally observed modes. The value of H_K extracted from simulations of S1, S2, and S3 are 340 Oe, 225 Oe, 420 Oe, respectively, which are also in good quantitative agreements with the experimental values (average deviation of $\sim 5\%$). The value of H_K for S1 is identical to that of a single element indicating negligible interaction between the elements, while for S2 and S3 it got significantly modified from the single element value.

8.3.1 Simulated Mode Profile Calculation of the Resonant Mode:

We have further simulated the mode profile of the studied mode for a single Py element and for S1-S3 as shown in Fig. 8.3(d) [162]. At $\phi = 0^\circ$, the single element shows a centre mode extending over the major part of the ellipse barring the small edge regions. In the arrays this mode qualitatively remains the same. At $\phi = 45^\circ$, the mode is rotated by 45° w.r.t., the major axis of the ellipse and this mode remains similar in S1 and S3 but in S2 there is a clear standing wave formation with two nodal lines inside the element. At $\phi = 90^\circ$, the mode is rotated by 90° w.r.t., the major axis of the ellipse. This mode qualitatively remains same in S1 and S2 but in S3 the mode looks discrete with nodes appearing parallel to the major axis of the ellipse.

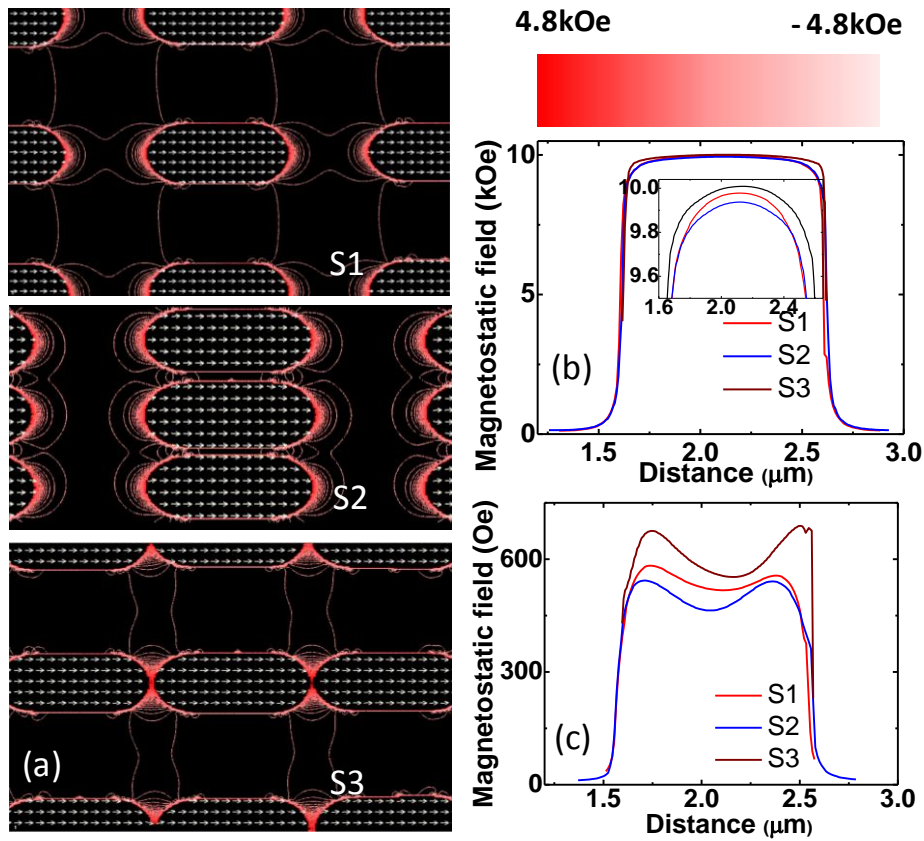


Fig. 8.4 (a) Contour maps of the simulated magnetostatic stray field distributions (X-component) for S1, S2 and S3 at $H = 1.5$ kOe at $\phi = 0^\circ$ are shown with the colour map. (b) The linescans of the simulated magnetostatic fields along X direction from S1, S2 and S3 at $H = 1.5$ kOe at $\phi = 0^\circ$. (c) The linescan of simulated magnetostatic fields along X direction from S1, S2 and S3 at $H = 1.5$ kOe at $\phi \approx 90^\circ$.

8.3.2 Simulated Magnetostatic Field Distribution:

To understand the variation in H_K in S1, S2 and S3 we have calculated their magnetostatic field distributions as shown in Fig. 8.4(a). The constituent elements have shape anisotropy due to their elongated shapes. In the arrays this anisotropy is modified due to the stray magnetic fields from the neighboring elements. Figure 8.4(a) clearly shows that at $\phi = 0^\circ$, the interaction between neighboring elements in S1 is negligible, while for S2 and S3 there are large interactions with the elements in the Y- and X- direction, respectively and negligible interaction with the elements in the perpendicular in-plane direction. We have

further calculated the linescans of the magnetostatic fields along the LA of the ellipse for $\phi = 0^\circ$ and 90° as shown in Figs. 8.4(b) and (c). At $\phi = 0^\circ$, all the spins are easily aligned along the external field direction as the shape anisotropy and the external field are parallel in this case. In this case the internal field distributions for three different samples are almost identical except for small deviations near the edge regions (Fig. 8.4(b)). However, at $\phi = 90^\circ$, the directions of the shape anisotropy and the external field are perpendicular to each other. In this case the linescans along LA represent the internal field only due to the combined effect of the shape anisotropy of the elements and the stray fields due to the lattice arrangements. From Fig. 8.4(c) it is observed that the internal field value is maximum for the S3, minimum for S2 and has an intermediate value for S1 similar to the values of H_K observed from experiment and simulation. This clearly shows that combined effects of the element shape and lattice arrangements of two-dimensional dot arrays can be efficiently used to tune its magnetic anisotropy.

8.4 Conclusions:

In conclusion, we have investigated the precessional magnetization dynamics in two dimensional arrays of elongated Py elements dispersed in three different lattice arrangements. The azimuthal angle of the bias magnetic field is varied between 0° and 180° and the dominant precessional mode shows a two-fold anisotropy. Micromagnetic simulations on arrays of 3×3 elements reproduce the spin wave spectra and the simulated anisotropy field values agree reasonably well with the experimental values. The anisotropy field showed a significant variation is with the lattice arrangement. Analysis shows that a competition between the shape anisotropy of the constituent elements and the inter-element magnetostatic field leads towards a variation in the net magnetic anisotropy and the corresponding frequency variation. Calculation of spin wave mode profile of the anisotropic mode shows that it is the extended centre mode of the ellipse, whose symmetry changes with the variation of the bias field orientation. Further calculation of magnetostatic field distribution confirms that the variation of the shape anisotropy and the magnetostatic field and their competition leads to the observed anisotropy. The observed tunability of magnetic anisotropy and precession frequency with lattice arrangements are important for anisotropic propagation of spin waves in two-dimensional magnonic crystal.

9. Time-Domain Study of Spin-Wave Dynamics in Two-Dimensional Arrays of Bi-Component Magnetic Structures

9.1 Introduction:

Magnonic crystals [36-37, 239] (MCs) are new types of artificial crystals formed by the periodic arrangements of magnetic nanostructures, where spin waves (magnons) are the transmission waves. Magnons with frequencies in the GHz to sub-THz regime have wavelengths in the micro- and nanometer scales, which make them potentially interesting for on-chip communication devices, including magnonic waveguides [26], filters, splitters, phase shifters [84], spin-wave emitters, interferometer [240] as well as for magnonic logic devices [241]. MCs form minibands consisting of allowed and forbidden spin-wave frequencies and corresponding magnonic bandgap. The bandgap can be tuned by changing various geometrical parameters such as shape, size, and arrangement of the nanostructures, lattice constant and lattice symmetry as well as by changing the constituent magnetic materials. Magnonic bandgap may be more efficiently tuned in a periodic composite nanostructure made of two different magnetic materials [217], popularly known as bi-component magnonic crystals (BMCs). Significant efforts have been made to fabricate one-dimensional (1D) [239, 242] and two-dimensional (2D) [24, 218, 221, 243-244] BMCs and to investigate their magnetization dynamics in last few years. The details of the existing literature on BMCs is described in chapter 5.

Very recently, magnetization switching and ferromagnetic resonance studies of binary Ni/Ni₈₀Fe₂₀ (Py/Permalloy) nanostructures fabricated by a novel self-aligned shadow deposition technique [105] have been reported. Here, we present the time-resolved magnetization dynamics of a similar binary nanostructure made of Py/Co arranged in two-dimensional arrays. As opposed to ref. 105, these samples have a clear gap (35 nm)

between the sub-elements of the bi-component unit ensuring that they are purely magnetostatically coupled. The dynamics were measured by applying bias field parallel to the long-axis (LA) and short-axis (SA) of the bi-component unit and the observed spectra are remarkably different for the bias-field applied along these two directions. Micromagnetic simulations revealed various collective modes of the 2D BMC, which are significantly different from those of the constituent Py and Co elements.

9.2 Experimental Details:

Py/Co binary structures with thickness of 25 nm, length and width of 1 μm and 450 nm and with a gap of 35 nm between the elliptical sub-elements of the bi-component unit, arranged in two different kinds of lattices were fabricated by a self-aligned shadow deposition technique. The details about self-aligned shadow deposition technique are described in section 3.2.5 of chapter 3. In sample 1 (S1) the separation between the nearest edges along both x (s_1) and y (s_2) directions are 600 nm whereas in sample 2 (S2) $s_1 = 140$ nm and $s_2 = 600$ nm. To create Py/Co binary structures, 25 nm Py and Co films were deposited in an electron beam deposition system with a base pressure of 4×10^{-8} Torr at deposition rates of 0.2 Å/s for both Py and Co films without breaking the vacuum. The sample holder was titled during deposition at an angle of $\sim +35^\circ$ and -35° respectively. A shadow area is formed on the left hand side of the pattern when the Py material is deposited from the left of the sample due to the thick resist sidewalls, while the shadow area appears on the right hand side of the patterns when Co material is deposited from the right of the sample. A lift-off process followed the deposition of the binary materials. The scanning electron micrographs of the samples are shown in Fig. 9.1(a), with a single bi-component unit magnified in the inset. The images showed the ellipses have pointed ends while the gap between the ellipses is reasonably uniform along their major axes. The ultrafast magnetization dynamics of the samples are measured by using an all-optical time-resolved magneto-optical Kerr effect microscope based upon two-color collinear pump-probe

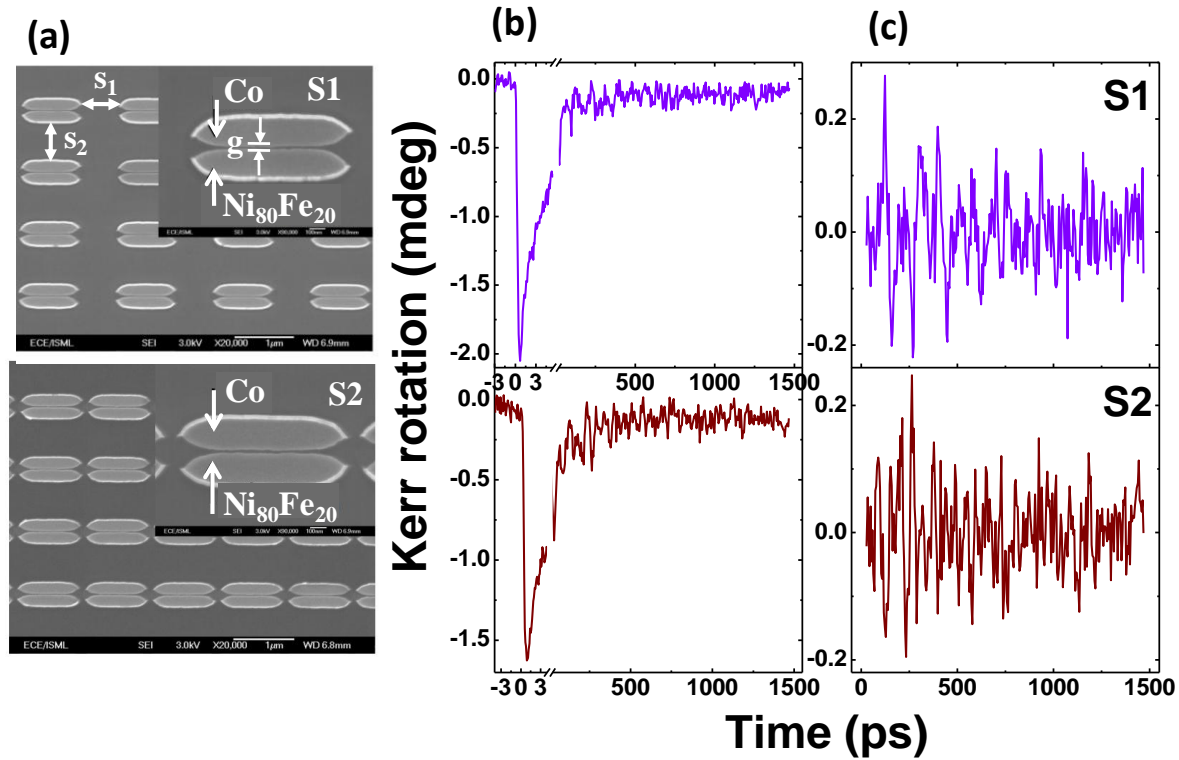


Fig. 9.1 (a) Scanning electron micrographs of two-dimensional lattices of bi-component structures (S1 and S2). The insets show magnified images of single bi-component units. (b) Typical experimental data of time-resolved Kerr rotation for S1 and S2 at $H = 1.65$ kOe applied along the long-axis (LA) of the bi-component unit. The time-resolved data reveal the ultrafast demagnetization, fast remagnetization and a slow remagnetization superposed with precession of magnetization. (c) The same data for S1 and S2 are shown after elimination of the demagnetization part and subtraction of a bi-exponential decay.

geometry and described in details in section 3.4.2. in chapter 3. The second harmonic ($\lambda = 400$ nm, pulse width ~ 100 fs) of a mode-locked Ti- Sapphire laser (Tsunami, Spectra Physics) is used to excite the magnetization dynamics in the sample whereas the time-delayed fundamental ($\lambda = 800$ nm, pulse width ~ 80 fs) is used to probe the dynamics by measuring the Kerr rotation as a function of the time-delay between the pump and probe beams. The pump and probe beams are focused by a single microscope objective in a

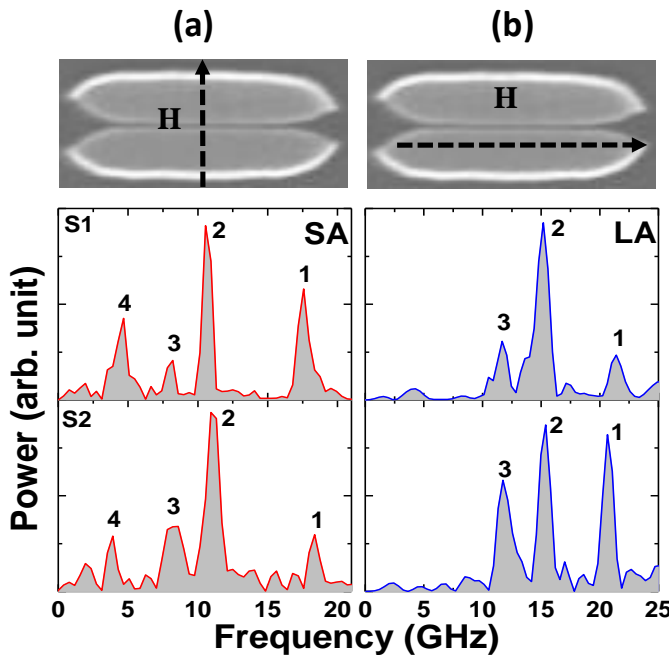


Fig. 9.2 Experimentally obtained SW spectra for S1 and S2 after a bias field $H = 1.65$ kOe is applied along (a) the short axis (SA) and (b) the long axis (LA) of the bi-component unit. The schematic of experimental geometry is shown on the SEM image of a single bi-component unit.

collinear geometry on a single bi-component unit, the dynamics of which is measured in presence of the magnetostatic fields from the neighboring elements. Due to imperfections introduced during fabrication, the bi-component units have small differences between them. We have performed measurements on a number of bi-component units (five units) at different locations in an array and found an average deviation of 5.5% in the frequencies of the different modes. An external bias field is applied at a small angle ($\sim 10^\circ$) to the sample plane, the in-plane component of which (H) is applied parallel to the LA or SA of the bi-component unit.

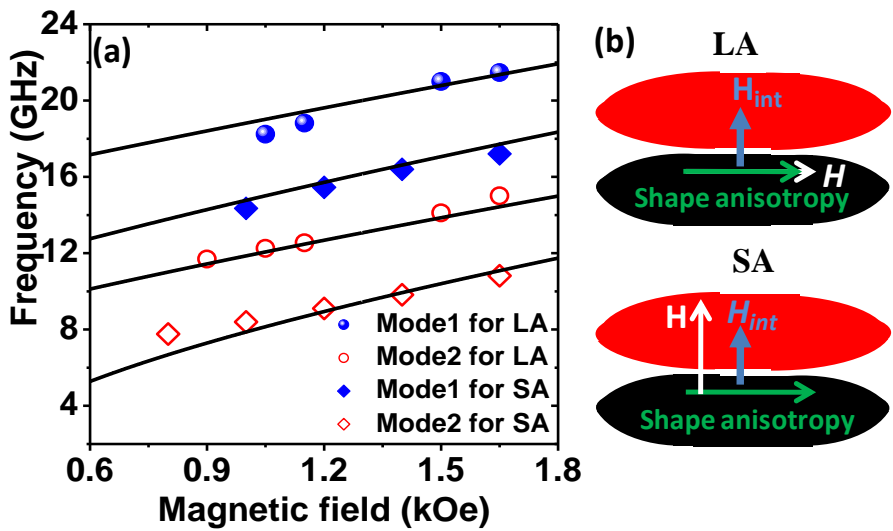


Fig. 9.3 (a) Variation of experimentally obtained mode frequencies (symbols) with bias magnetic field for S1. The bias field is applied along the LA and SA of the bi-component unit. The solid lines are fit to Eqn. 9.1. (b) Schematics of the external (H), and internal field (H_{int}) acting on the bi-component unit in LA and SA configurations are shown.

9.2 Results and Discussions:

Figure 9.1(b) presents a typical time-resolved Kerr rotation data showing the ultrafast demagnetization, fast remagnetization a slow remagnetization superposed with precession of magnetization for S1 and S2 when $H = 1.65$ kOe is applied parallel to the SA of the bi-component unit. The magnetization precession is observed on top of a slowly decaying magnetization and the time-resolved data after subtracting a bi-exponential background is shown in Fig. 9.1(c). The spin-wave spectra are obtained by performing fast Fourier transform (FFT) on the background subtracted time-resolved data and are shown in Fig. 9.2 (a, b) for S1 and S2 after the bias field is applied parallel to the SA and the LA of the bi-component unit. A clear difference in the spectra is observed for the bias field applied along these two directions, while very minor changes are observed in the spectra for the two different lattices (S1 and S2). Four well separated bands are observed for the SA spectra, while two well separated bands are observed for the LA spectra with a mode splitting for the lower frequency band giving rise to a 3rd peak. In addition, the frequencies of the modes increase significantly for the LA spectra as compared to the SA spectra. This is

probably because of the shape anisotropy along the long-axis of the ellipse although the detailed spin configurations would play important roles in determining both the frequencies and the nature of the spin-wave spectra. We have further studied the variation of the mode frequencies as a function of the bias magnetic field and Fig. 9.3(a) shows the variation of modes 1 and 2 for the sample S1 when the bias field is applied parallel to LA and SA of the bi-component unit. We have attempted to fit the bias-field dependence of the modes by modified Kittel's formula [144] for the uniform precession frequency.

$$f = \frac{\gamma}{2\pi} \sqrt{(H_1 + H_K + (N_z - N_x)4\pi M_s)(H_1 + H_K + (N_y - N_x)4\pi M_s)} \quad (9.1)$$

where $H_1 = H + H_{int}$ (H_{int} is an interaction field between the Co and Py elements), H_K is the uniaxial anisotropy, N_x , N_y , N_z are the demagnetization factors of the Co and Py elements of the bi-component structures and M_s is the saturation magnetization. The schematic of the external field (H) and internal field (H_{int}) acting in a bi-component unit is shown in Fig. 9.3(b) in LA and SA configurations. The solid lines in Fig. 9.3(a) shows the fit to Eq. (9.1) with $M_s = 860$ emu/cc, $H_K = 0$, $\gamma = 17.6$ MHz/Oe for Py and $M_s = 1400$ emu/cc, $H_k = 2$ kOe along [111] direction, $\gamma = 17.6$ MHz/Oe for Co. The values of N_x , N_y and N_z used in the fit were about 0.02, 0.08 and 0.9. H_{int} is found to be negligible for LA and about 400 Oe for SA due to significant inter-element interaction along that direction. The deviation in the fit is because Eqn. (9.1) is based upon macrospin approximation, which ignores the detailed microscopic spin configurations and the collective effects on the dynamics.

9.2.1 Micromagnetic Analysis of the Resonant Modes of BMCs:

We have performed micromagnetic simulations using OOMMF software [161] for 3×3 arrays of two different types of BMCs to reproduce our experimental data. It has been shown that finite arrays have modes, which are different from the modes of single elements as well as two-dimensional infinite arrays. However, in our case we have excited and probed a single bi-component unit, while placed in a large array and hence stray fields on that unit from the nearest neighbors are most important. We have done additional test simulations on arrays of 5×5 elements and the simulated spectra and mode profiles are nearly identical to that of a 3×3 array. The sample geometry for simulation was derived

from the SEM images and the samples were discretized into rectangular prism-like cells with dimensions $4 \times 4 \times 25$ nm³. The lateral dimensions of the cells are well below the exchange length of Co and Py. The magnetic parameters as obtained from the fit of the data in Fig. 9.3(a) are used in the simulation, while the exchange stiffness constants are used as $A = 1.3 \times 10^{-6}$ erg/cm for Py, and $A = 3.0 \times 10^{-6}$ erg/cm for Co.

The static and dynamic simulations were performed using methods as described in chapter 4. The dynamic simulations for single Py and Co ellipses, a single Py/Co bi-component unit and two different BMCs S1 and S2 were performed for systematic understanding of how formation of bi-component unit and further arrangement of that unit in two different BMCs affect the spin-waves in those systems.

Figure 9.4 shows the FFT spectra of the simulated time-domain magnetization for all the above simulated samples. The LA spectrum of the Py ellipse shows a dominant mode at around 16.5 GHz with a small shoulder at around 15.6 GHz, while the SA spectrum shows three well separated modes at 10.15, 5.5 and 2.7 GHz with the highest frequency mode occurring at a much lower frequency than that for the LA. The LA spectrum of the Co ellipse shows two modes with similar nature as that for Py with frequencies at around 24.4 and 22.7 GHz, while the SA spectrum shows a dominant mode at around 18.75 GHz with two small amplitude and closely spaced modes at 13.3 and 12.9 GHz. The mode frequencies for the SA spectrum are again significantly reduced as compared to the LA spectrum due to the shape anisotropy of the elongated ellipse. However, the SA and LA spectra for a single bi-component unit are drastically different from the constituent elements. For the LA a very small amplitude mode appears close to the Co mode and a large amplitude mode appears close to the Py mode. However, the four modes observed in the SA spectrum are completely different in nature and in peak frequency values as compared to the modes of the constituent elements. The modes are further modified in the two BMCs. In the LA spectra for S1 and S2 the higher frequency modes become larger in amplitude than a single bi-component unit, while the lower frequency mode splits into two modes.

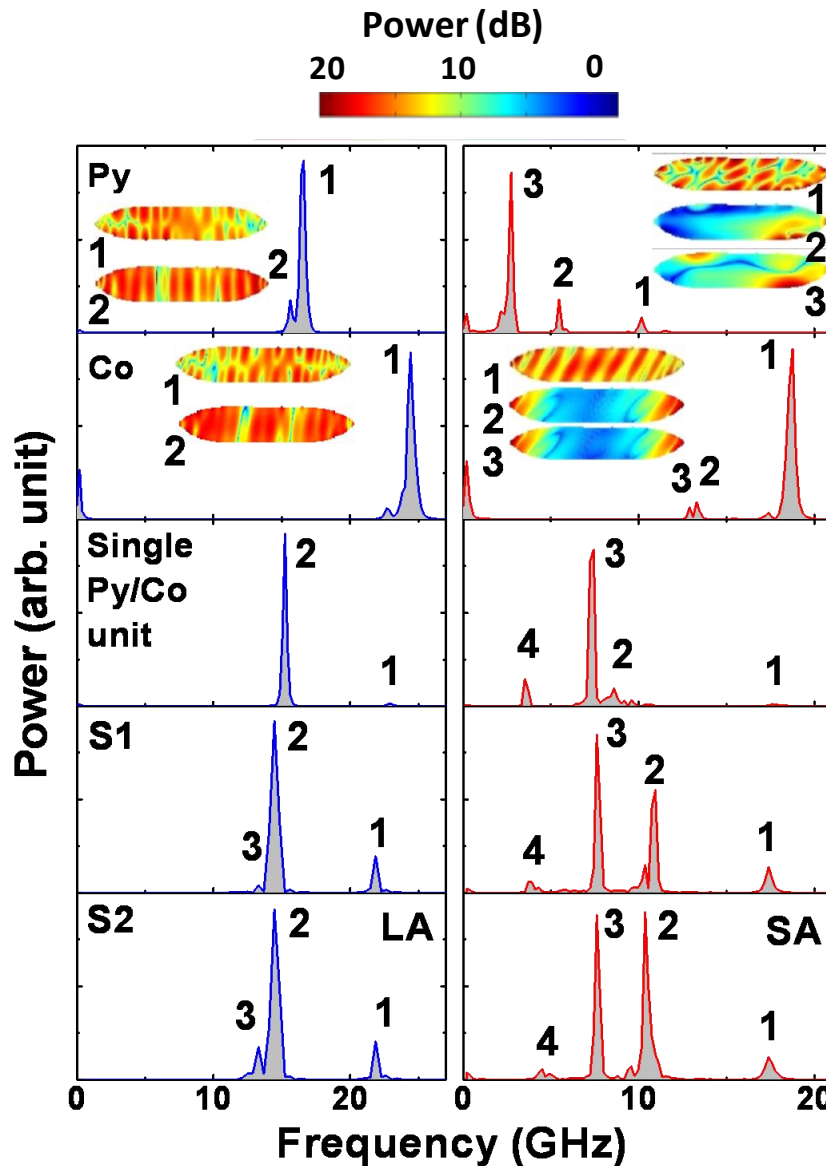


Fig. 9.4 Simulated spin-wave spectra from a single Py ellipse, single Co ellipse, single Py/Co bi-component unit and two-dimensional lattices of bi-component structures (S1 and S2) after application of a bias field along the long-axis (LA) and the short-axis (SA) of the ellipse. The mode numbers are assigned to each spectrum. The mode profiles (power) are shown for the single Py and Co ellipses at the inset of the corresponding spectrum. The colormap for power profile is shown at the top of the figure.

The frequencies of all modes are red-shifted in the BMCs. In the SA spectra of S1 and S2 all modes are blue-shifted compared to the single bi-component unit and modes 1 and 2 grew in amplitude, while mode 1 is reduced in amplitude. The simulations reproduced all the experimental modes qualitatively.

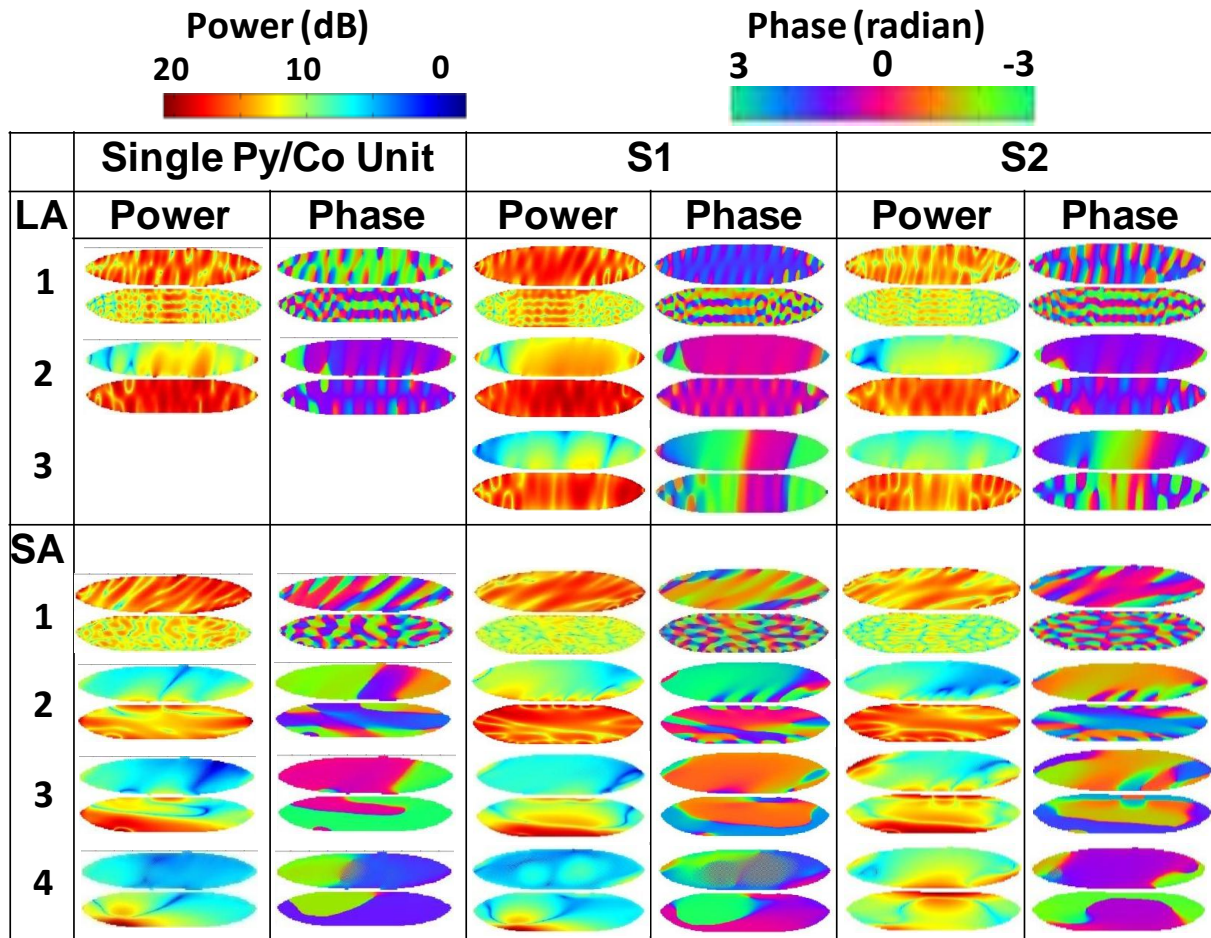


Fig. 9.5 Simulated mode profiles (power and phase) for a single bi-component unit and the central bi-component unit from 3×3 lattices of S1 and S2. The colormaps for power and phase are shown at the top of the image.

9.2.2 Simulated Mode Profiles of the Resonant Modes:

For further understanding, we numerically simulated the mode profiles for the single elements, single bi-component unit and for the two BMCs using a home build code [162]. The mode profiles (power) for the modes of the individual Py and Co ellipses are shown at

the inset of Fig. 9.4 with the colormap shown at the top of the figure. When the bias field is along LA, mode 1 for Py is a mixed backward volume magnetostatic (BWVMS) and Damon-Eshbach (DE) mode, while mode 2 is purely BWVMS mode forming standing wave within the element. When the bias field is along SA, mode 1 for Py is a mixed BWVMS-DE mode, while modes 2 and 3 are two localized modes. For the Co element with the bias field along LA, the modes are identical to those for the Py element. However, for bias field along the SA, mode 1 is BWVMS mode with its axis rotated from the central axis of the ellipse while modes 2 and 3 are edge modes. For a single bi-component unit with bias field along LA, mode 1 has majority of power (Fig. 9.5) on the Co ellipse with an out-of-phase small amplitude precession of the Py ellipse (optical mode). In mode 2 Py element has most power, while the Co element is precessing at small amplitude in-phase with the Py element (acoustic mode). When the bias field is along the SA, mode 1 has most power on the Co element with a negligible power on the Py element and a clear phase relationship between the Py and Co elements are not found. Modes 2, 3 and 4 have most power on the Py element with small power on the Co element. The power on the Py element gets increasingly more localized towards the lower edge of the ellipse with increase in mode number. In addition, in mode 2 Co and Py elements are primarily out-of-phase to each other (optical mode), while for modes 3 and 4, the Py and Co elements precess in phase with each other (acoustic modes).

For the BMCs (S1 and S2) modes 1 and 2, for bias field applied along LA, are essentially same as the corresponding modes for a single bi-component unit with the difference that in S2 the spatial profiles (Fig. 9.5) of these modes are more discrete on Co and Py elements, respectively due to the larger interaction between the neighboring elements. However, mode 3 in both cases form a collective BWVMS mode with the phase oscillating along the long-axis of the ellipse through both Co and Py elements. When the bias field is along the SA, the power and phase distributions of all four modes are significantly different than those of a single bi-component unit as well as between two different lattice arrangements (S1 and S2). Consequently, the frequencies and mode shapes are also different.

9.3 Conclusions:

In conclusion, we have investigated the ultrafast magnetization dynamics in two-dimensional BMCs made of Co and Py elliptical elements grown by a self-aligned shadow deposition technique. The frequency spectra change significantly depending upon the direction of the external bias field. When the field is applied parallel to the long-axis direction of the bi-component unit two bands of frequencies with a mode splitting of the lower frequency band are observed. On the other hand when the bias field is applied parallel to the short axis, four clear bands are observed. The measured spin-wave spectra are reproduced by micromagnetic simulations and their frequencies and power and phase profiles are compared with modes from individual Co and Py elements and a single bi-component unit. The frequencies and spatial profiles of the modes of the individual elements are modified significantly in the bi-component unit and further in the two-dimensional BMCs and additional modes also appeared. In addition to the fundamental understanding of the collective magnetization dynamics of arrays of bi-component structures, this opens up opportunities for engineering magnonic bands in bi-component magnonic crystals.

10. All-Optical Investigation of Tunable Magnetization Dynamics in Ni₈₀Fe₂₀ Nanostripes

10.1 Introduction:

Ordered arrays of magnetic nanostripes/nanowires have attracted considerable attention of the scientific community due to their intriguing physical properties as well as potential applications in microwave devices [170, 245], data storage and domain wall logic [246]. It is considered as waveguides [26, 83, 164] for SWs which is an important component of integrated magnonic circuits [52]. For unpatterened stripe dispersion curves for propagating dipole-exchange SWs are observed without any forbidden band. In contrary, allowed and forbidden bands are observed for stripes with periodically modulated width [247] and stripes with antidots [248] which make them as one of the most promising candidates for one dimensional magnonic crystals (1D-MCs). Their large surface-to-volume ratio, inhomogeneous demagnetizing fields due to lateral confinement significantly influence their static and dynamic magnetic properties and hence, give rise to rich and complicated SW spectra in ferromagnetic stripes. The SWs in a ferromagnetic stripe can also be tuned through sample geometry [247-249], propagation direction [250] and applied magnetic field [167, 177, 251]. In addition, ferromagnetic nanostripes/nanowires are important candidates for Racetrack memory [252] devices mediated by controlled domain wall movement by current [253-254] or magnetic field [255]. In this regard the interaction of the domains with the intrinsic spin waves in such confined nanostructures would play an important role in the functionality of these devices. Hence, understanding of the SW dynamics in ferromagnetic nanostripes/nanowires is an important problem but have not yet been studied in details.

Due to these interesting possibilities, the magnetization dynamics of micron and sub micron wide longitudinally and transversely magnetized stripes have been studied by using Brillouin light scattering (BLS) experiment [181, 249-250, 256], ferromagnetic resonance (FMR) experiment [177, 242] and time-resolved scanning Kerr microscopy (TRSKM) [171]. Interesting SW physics such as quantization [91], interference [168-169], filtering [170], and self-focusing of SWs [82] are observed in ferromagnetic stripes. The lateral quantization of the surface SWs due to the formation of lateral standing waves in a periodic array of micron sized stripes is already reported. However, there are only few reports [171, 257-258] of picosecond magnetization dynamics of ferromagnetic stripes with micrometer sized width by using TRSKM. They observed the localized SW modes in backward volume (BV) and Damon-Eshbach (DE) geometries. However, picosecond magnetization dynamics of magnetic stripes with deep nanoscale dimensions have not been reported before. The possibility of tuning magnetization dynamics by varying the width of the stripe as well as the bias magnetic field orientation may lead towards interesting anisotropic magnetic properties suitable for applications in magnetic storage, memory, logic and communication devices. However, this has not been studied yet due to the difficulties in fabricating good quality high aspect ratio nanostripes with sub-100 nm width and the required thorough and non-trivial characterization methods.

In this present work we have overcome these difficulties and fabricated high quality arrays of Ni₈₀Fe₂₀ (Py) nanostripes with width down to 50 nm and length 5 μm and measured their time-resolved magnetization dynamics by varying the orientation of the bias magnetic field and the width of the stripe (from 50 to 200 nm). A remarkable variation in the spin wave quantization properties is observed with the variation of stripe width as well as the bias field orientation, which is modeled by using micromagnetic simulations. Finally, simulation of magnetostatic field distribution clearly shows that the 50 nm wide stripes are magnetically isolated in the array leading towards the measurement and understanding of magnetization dynamics of a single magnetic nanostripe with 50 nm width for the first time.

10.2 Experimental Details:

$5 \times 10 \mu\text{m}^2$ arrays of 30 nm thick (t) and 5 μm long (L) Py nanostripes of width (w) 200 nm (S1), 100 nm (S2) and 50 nm (S3) were fabricated by a combination of electron beam lithography and electron beam evaporation technique which is described in chapter 3. The edge to edge separation (s) of the stripes is fixed at 300 nm for all three samples to avoid strong dipolar interaction between the nanostripes. The scanning electron microscope (SEM) images of the nanostripes of different width are shown in Fig. 10.1(a). The SEM images show that the stripes are reasonably well prepared with slight deviations in the width of nanostripes from the nominal dimensions.

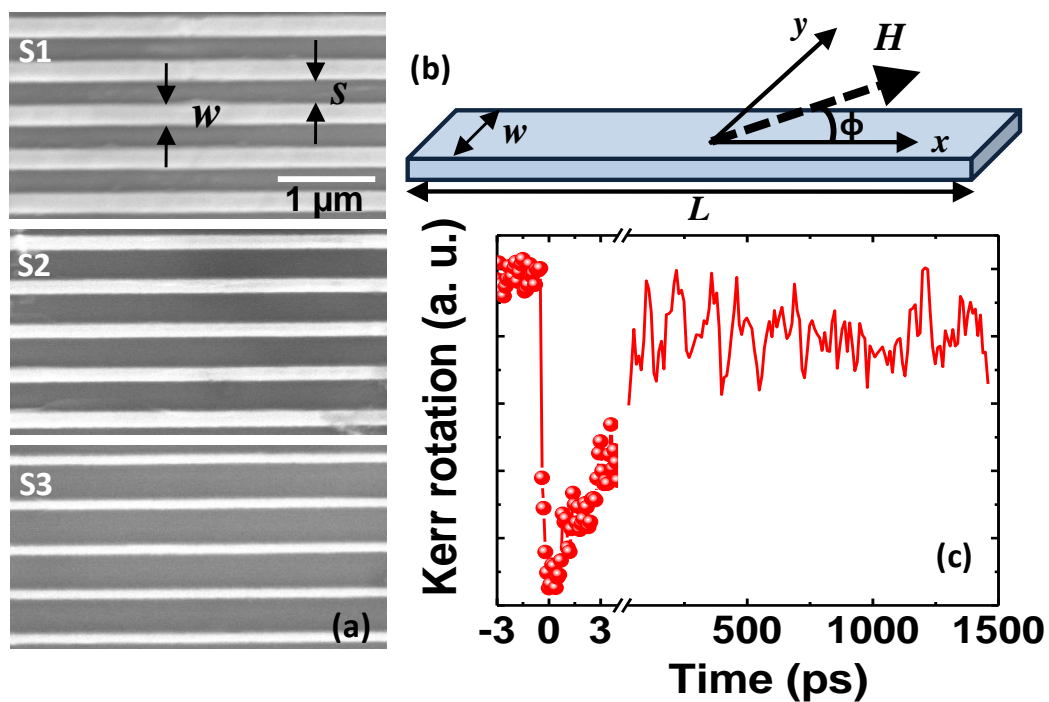


Fig. 10.1 (a) Scanning electron micrographs of Py nanostripes with different stripe widths (S1, S2 and S3) are shown. (b) The schematic of the experimental configuration. Here, $\phi = 0^\circ$ corresponds to backward volume (BV) geometry and $\phi = 90^\circ$ corresponds to Damon-Eshbach (DE) geometry. (c) Typical experimental time-resolved Kerr rotation data from S3 ($w = 50 \text{ nm}$) for $H = 1 \text{ kOe}$ applied at $\phi = 0^\circ$. The data reveals three different temporal regimes namely, the ultrafast demagnetization, fast and slow relaxations, and precession of magnetization.

The ultrafast magnetization dynamics of the samples are measured by using an all-optical time-resolved magneto-optical Kerr microscope based upon two-color collinear pump-probe geometry. The second harmonic of a mode-locked Ti-sapphire laser is used to excite the magnetization dynamics in the samples whereas the time-delayed fundamental is used to probe the dynamics by measuring the Kerr rotation as a function of the time-delay between the pump and probe beams. The pump and probe beams are focused by using a single microscope objective (MO) at the center of the array of the nanostripes. The pump beam excites the dynamics within a spot size of about 1 μm and the time delayed probe beam with spot size 800 nm, placed at the center of the pump beam detect the magnetization dynamics by measuring the Kerr rotation as a function of the time delay between the pump and the probe beams. The details of the experimental set up are described in chapter 3. About 2 to 3 nanostripes are probed during the measurements of three different samples. A bias field $H = 1 \text{ kOe}$ is applied to the sample, the direction of which was tilted slightly out of the plane of the sample to have a finite demagnetizing field along the direction of the pump pulse. The pump pulse rapidly modifies the out-of-plane demagnetizing field and thereby induces precessional magnetization dynamics within the dots. The azimuthal angle (ϕ) of the bias field H is varied between 0° and 90° at intervals of 15° by rotating the sample using a high precession rotary stage while keeping the microscope objective and the magnetic field constant. The schematic of the experimental geometry is shown in Fig. 10.1(b). The pump and the probe beams are made to incident on the same nanostripes in the array after changing ϕ every time.

10.2.1 Variation of Precessional Dynamics with the Width of the Stripe and the Orientation of External Bias Magnetic Field:

Figure 10.1(c) shows a typical time-resolved Kerr rotation data from the nanostripe with 50 nm width at $H = 1 \text{ kOe}$ applied at $\phi = 0^\circ$. The data shows an ultrafast demagnetization within 500 fs of the zero delay and subsequent bi-exponential remagnetization with time constants of 3.3 ps and 84 ps. The faster relaxation occurs because the hot electrons and the spins exchange energy with the lattice via electron–phonon interaction whereas the

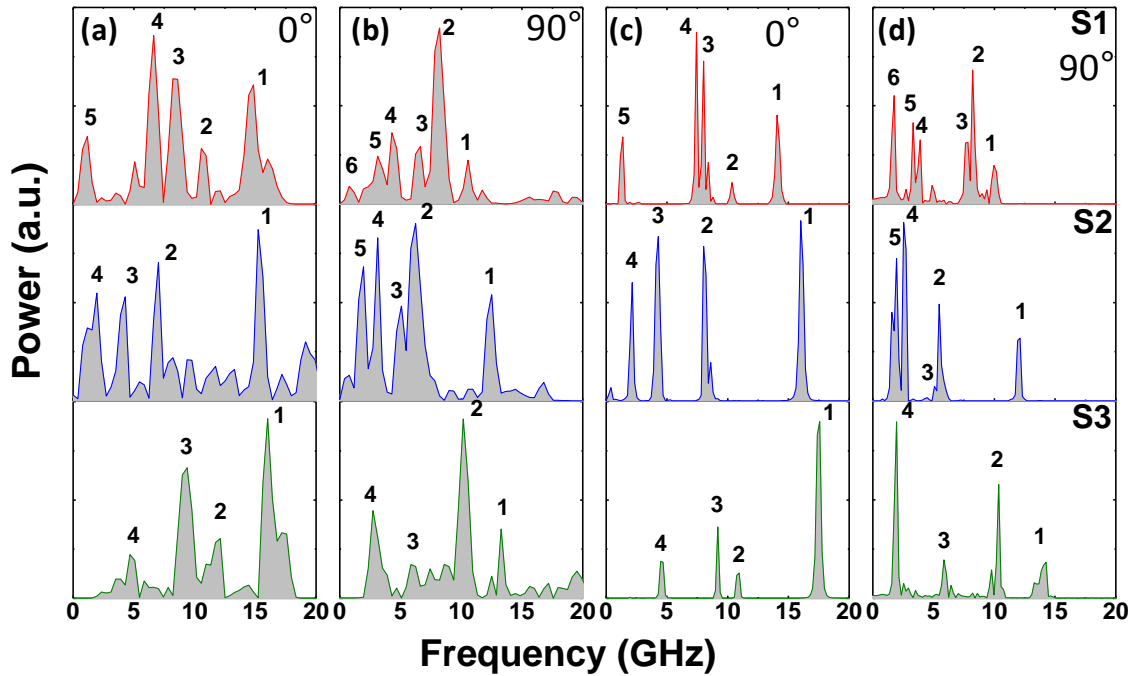


Fig. 10.2 Experimental SW spectra at (a) $\phi = 0^\circ$, (b) $\phi = 90^\circ$ and simulated SW spectra at (c) $\phi = 0^\circ$, (d) $\phi = 90^\circ$ are shown for S1, S2 and S3 at $H = 1.0$ kOe.

slower relaxation corresponds to the transfer of energy to the substrate and the surrounding [143]. The precessional dynamics appears as an oscillatory signal on top of the slowly decaying time-resolved Kerr rotation. A fast Fourier transformation (FFT) is performed to obtain the SW spectra for different samples at various ϕ values. Figures 10.2(a) and (b) show experimental SW spectra of S1, S2 and S3 for bias field $H = 1$ kOe applied at $\phi = 0^\circ$ and 90° , respectively. A clear variation in the SW spectra is observed for different samples and also with the orientation of the bias field. In all cases rich SW spectra with a number of modes are observed. While for $\phi = 0^\circ$, the modes span upto about 17 GHz, the bandwidth is little less (about 14 GHz) for $\phi = 90^\circ$. At $\phi = 0^\circ$ five modes are observed in S1, whereas the number of modes reduces to four for S2 and S3. The frequencies of all modes increase with the decrease of the width of the stripe (increase in aspect ratio L/w) and it attains a maximum value in S3 having an aspect ratio of 100.

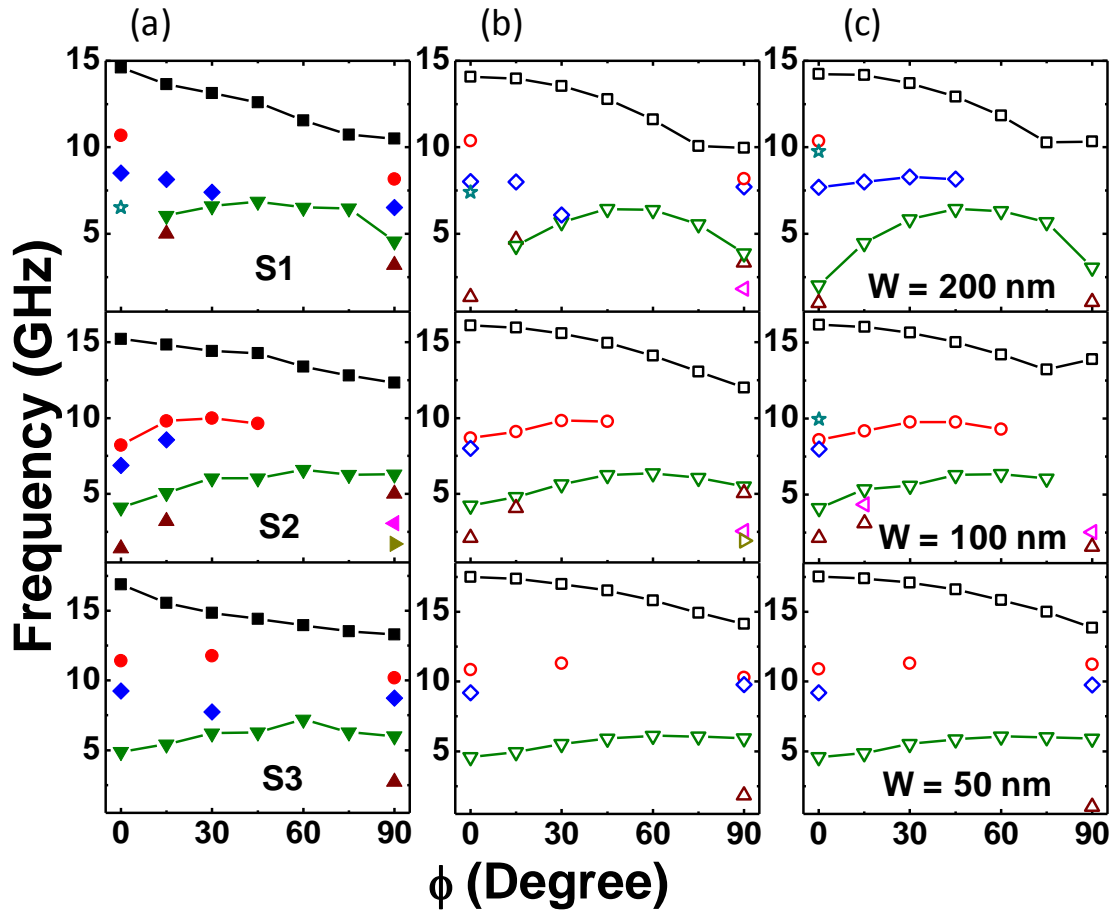


Fig. 10.3 (a) Experimental (filled symbols) and (b) simulated SW frequencies (open symbols) as a function of the azimuthal angle ϕ of the in-plane bias magnetic field at $H = 1$ kOe for S1, S2 and S3. (c) Simulated SW frequencies (symbols) as a function of the azimuthal angle ϕ of the in-plane bias magnetic field at $H = 1$ kOe for single nanostripes of widths $w = 200$ nm, 100 nm and 50 nm. The solid lines are only guide to the eyes.

This is apparently due to the increase in the shape anisotropy with the increase in aspect ratio. In contrary, at $\phi = 90^\circ$ six modes are observed for S1 and the number of modes gradually reduces to five and four for S2 and S3, respectively. In addition, the frequencies of all modes for all three samples are decreased significantly for $\phi = 90^\circ$ as opposed to those for $\phi = 0^\circ$. This is due to the reduction in the effective magnetic field along the bias field direction for $\phi = 90^\circ$. However, the detailed spin configuration of the magnetic ground

states for different samples at different orientations of the bias magnetic field would play crucial role in determining the details of the SW spectra.

Subsequently, we measured the magnetization dynamics as a function of ϕ at a fixed strength of $H = 1$ kOe. The variation of all the experimentally observed peak frequencies with ϕ is plotted in Fig. 10.3(a). It is observed from Fig. 10.3(a) that a number of modes at $\phi = 0^\circ$ for all samples converge into two modes at around $\phi = 60^\circ$ and again diverge to the same number of modes at $\phi = 90^\circ$. All the SW modes show anisotropic behavior but it is difficult to fit the variation of the precessional frequency by using modified Kittel formula for reason that will be discussed later in this chapter.

Micromagnetic simulations were performed considering arrays consisting of three stripes using OOMMF [161] software to reproduce the experimental results. The samples were discretized into rectangular prism-like cells with dimensions $5 \times 5 \times 30$ nm³. The lateral cell size is below the exchange length (5.3 nm) of Py. The absence of discretization along the stripe thickness is justified as we did not observe any perpendicular standing spin waves in these stripes. The parameters used for the simulation are $\gamma = 17.6$ MHz/Oe, exchange stiffness constant, $A = 1.3 \times 10^{-6}$ erg/cm, magnetocrystalline anisotropy constant $K = 0$ and saturation magnetization $M_s = 860$ emu/cc. The external bias field is applied according to the experimental configuration and a pulsed field of rise time of 50 ps and peak amplitude of 30 Oe is applied perpendicular to the sample plane. Figures 10.2(c, d) show the FFT power spectra of the simulated time-domain magnetization for all three samples at $\phi = 0^\circ$ and 90° , respectively. The simulated results qualitatively reproduced the experimental observations. The relative intensities and the precise positions of the peaks in the frequency domains are not always quantitatively reproduced because of lack of inclusion of the precise edge roughness and other defects in the simulated samples as observed experimentally. In addition, the optical excitation is replaced by pulsed magnetic field in the simulation. Figure 10.3(b) shows the variation of the simulated precessional frequency for different samples with the azimuthal angle (ϕ) of the bias field. The important features like the rich and broad SW spectrum, the number of SW modes at different azimuthal angles (ϕ), are well reproduced using micromagnetic simulations.

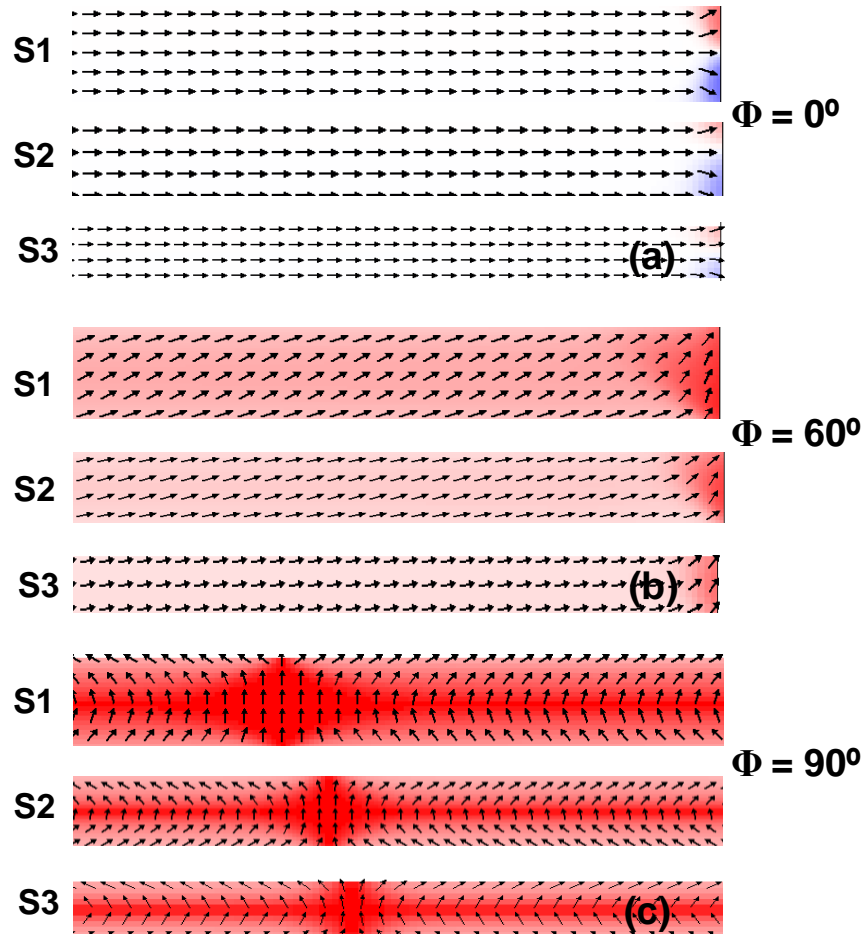


Fig. 10.4 Simulated static magnetic configurations for S1, S2 and S3 are shown for $H = 1$ kOe applied at (a) $\phi = 0^\circ$, (b) $\phi = 60^\circ$ and (c) $\phi = 90^\circ$. The region close to right edge of the stripe is shown in (a) and (b) whereas the center of the stripe is shown in (c). The y-component of magnetization vector is represented by blue-white-red color map.

We have also simulated the magnetization dynamics of single nanostripes of different widths to understand the intrinsic modes of the single stripes and how they got affected by the other stripes when placed in an array. Figure 10.3(c) shows the variation of the simulated mode frequencies with the azimuthal angle (ϕ) of the bias field for single stripes of different widths. For the wider stripes (S1 and S2) there is a sharp difference in the number of modes between single stripe and arrays of stripes whereas it remains identical for the narrowest stripe S3. This indicates that while S1 and S2 are significantly influenced by the inter-stripe interaction, the nanostripes in S3 are nearly magnetically isolated.

Figures 10.4(a, b, c) show the static magnetic configurations of the central stripe from the simulated arrays corresponding to S1, S2 and S3 for $\phi = 0^\circ$, 60° and 90° . For each stripe the static magnetic image from the centre to the right edge of the stripe is shown for convenience. At $\phi = 0^\circ$ all three stripes show uniform magnetization parallel to the bias field with a small flower like state near the stripe ends. At $\phi = 60^\circ$ all three stripes show leaf like state. However, only for S1 the magnetization is nearly parallel to the bias field and it started to deviate towards the long axis of the stripe with decreasing stripe width and the deviation is maximum for S3. At $\phi = 90^\circ$, a completely different magnetic state is observed in all three samples where two domains with clock-wise and anticlock-wise C-states separated by a transverse domain wall is observed. In addition, for S1 and S2, the spins near the axis of the stripes are parallel to the bias field while the spins towards the two edges systematically deviate from the bias field direction. This allows us to divide the stripes (waveguides) in two sub-waveguides. However, this is not possible for S3 as all spins are deviated from the bias field in this case.

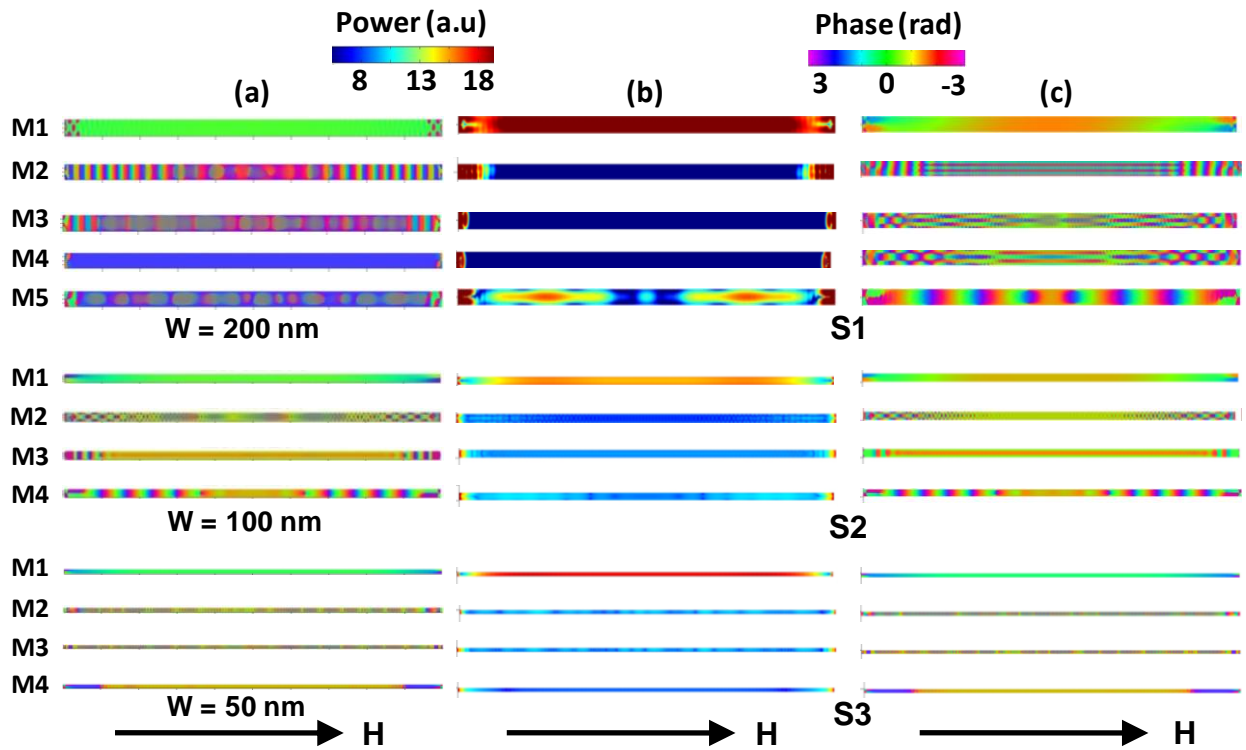


Fig. 10.5 (a) The phase profiles of all SW modes for single stripes of three different widths for $H = 1$ kOe applied at $\phi = 0^\circ$. The (b) power and (c) phase profiles of all simulated SW

modes for S1, S2 and S3 for $H = 1$ kOe applied at $\phi = 0^\circ$. The color maps for power and phase distributions are shown at the top of the figure. The direction of external bias magnetic field (H) is shown at the bottom of the figure.

10.2.2 Micromagnetic Simulations of the SW Mode Profiles for Single Nanostripes and Array of Nanostripes:

For further understanding, we numerically calculated the SW mode profiles of single stripes and arrays of stripes using a home build code [162]. Figure 10.5(a) shows the phase maps of SW mode profile of single stripes of width 200, 100 and 50 nm at $\phi = 0^\circ$. It is clear from Fig. 10.5(a) that at $\phi = 0^\circ$, the 200 nm and 50 nm wide single stripes show standing SWs in backward volume (BV) geometry, whereas for the stripe with intermediate width ($w = 100$ nm), standing SWs with a combination of Damon-Eshbach (DE) and BV geometry are observed. However, the modes are significantly modified for the wider stripes ($w = 200$ nm and 100 nm) when they are arranged in an array (S1 and S2). In Figs. 10. 5(b and c) the power and phase profiles of the resonant modes for S1, S2 and S3 are shown. From Fig. 10. 5(b, c) it is observed that mode 1 (M1) for S1 and S2 correspond to the uniform precessional mode at the centre of the stripe (centre mode). However, M2, M3, M4 for S1 and M2, M3 for S2 are quantized modes with combination of DE and BV geometries. While the standing SWs of BV (mode quantization number: n) geometry are primarily confined near the stripe edges, the DE-like modes (mode quantization number: m) are located near the centre of the stripe. The quantization numbers m of the DE modes for M2, M3 and M4 for S1 are 5, 3 and 3, respectively whereas for M2 and M3 in S2, $m = 3$ for both modes. The quantization number n for the BV-like standing SW modes could not be determined due to the lack of resolution of this mode for most parts of the stripe. In contrary to the other modes, M5 for S1 and M4 for S2 are both BV-like standing SW modes with quantization number (n) 15 and 29, respectively. On the other hand, the mode structure in S3 is completely different than S1 and S2. Further for this sample the modes are identical to those of a single stripe of same width. Here, M1 is the centre mode whereas M2, M3 and M4 are all BV-like standing SW modes but the mode numbers could not be counted due to the lack of spatial resolution.

The phase profile of single nanostripes with three different widths at $\phi = 90^\circ$ are shown in Fig. 10.6(a). For wider stripes ($w = 200$ and 100 nm) three modes each are observed in single stripes, while for the arrays of those the number of modes changed to 6 (S1) and 5(S2). Further, for the stripe with $w = 200$ nm, only mode 1 retained its identity in the array while the other two modes disappeared in the array. In contrary, for the stripe with $w = 100$ nm all three modes retained their identities in the array. The demagnetized region right on the long axis of the stripe divided the stripe into two sub-stripes and modes in the lower sub-stripe are mirror images of those in the upper sub-stripe. In addition, the quantization axes of the standing SW modes deviate substantially from the long axis of the stripe creating arrow-like standing SW modes (Modes M1 to M4 for S1 and modes M1 to M3 for S3). M1, M2, M3, M4 for S1and M1, M2, M3 for S2 are arrow-like standing SW modes with quantization number (n) 69, 45, 41, 5 for S1 and 121, 29, 25 for S2, respectively.

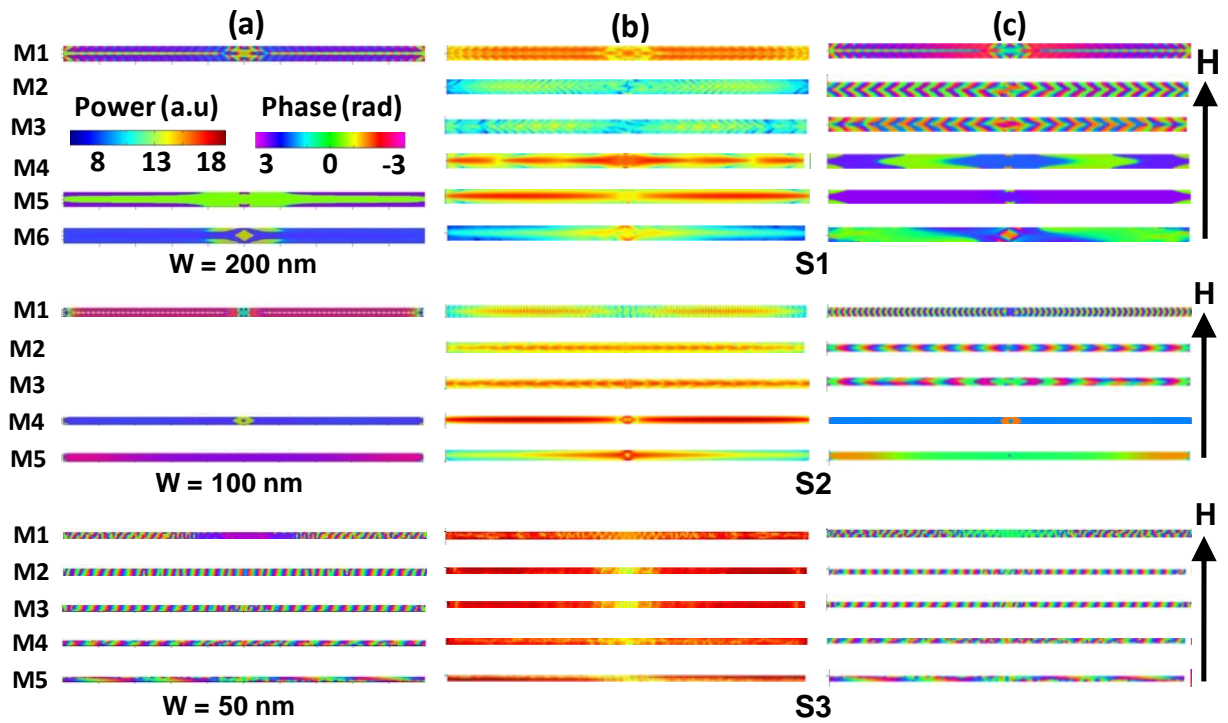


Fig. 10.6 (a) The phase profile of all SW modes for single stripes of different widths for $H = 1$ kOe applied at $\phi = 90^\circ$ are shown. The (b) power and (c) phase profiles of all SW modes for S1, S2 and S3 for $H = 1$ kOe applied at $\phi = 90^\circ$ are shown. The color maps for power and

phase distributions are shown in (a). The direction of external bias magnetic field (H) is shown at the right of the figure.

M5 for S1 and M4 for S2 correspond to uniform (centre) modes, while M6 for S1 and M5 for S2 are DE-like standing SW modes with $n = 3$. As for $\phi = 90^\circ$, in S3 the modes are again identical to the modes observed for the single stripe. Here, all modes correspond to DE-like standing SW modes with their quantization axes deviated from the direction of the long-axis of the stripe. While the mode quantization number n could not be counted for M1 due to lack of resolution, the values of n are observed as 61, 57, 37 and 11 for M2, M3, M4 and M5, respectively. From the simulated mode profiles, it is observed that for all three samples standing SW is formed either in BV-like geometry or in DE-like (arrow-like) geometry with different quantization numbers depending upon the orientation of bias magnetic field (ϕ). As a result it is not appropriate to model the anisotropy of the spin wave frequency with the orientation of the bias magnetic field using a modified Kittel formula because it is only valid for uniform precessional mode (Kittel mode).

10.2.3 Simulated Magnetostatic Field Distributions for Arrays of Nanostripes:

To understand the collective behavior of the magnetization dynamics, we have simulated the magnetostatic field distributions in the arrays of nanostripes. For all three samples at $\phi = 0^\circ$, the spins are fully aligned parallel to the boundaries of the stripes leaving no free magnetic charges at the stripe boundaries. As a result the inter-stripe interaction will be negligible (not shown here) if we calculate linescans of magentostatic field along the red dashed line as shown in Fig. 10.7(a). However, at $\phi = 90^\circ$, the spins deviate from being parallel to the long boundaries of the stripes creating some free magnetic charges at those boundaries and consequently finite amounts of inter-stripe interaction fields. From Fig. 10.7(b) it is observed that the inter-stripe interaction is maximum (261 Oe) for S1 and minimum (52 Oe) for S3 and has an intermediate (118 Oe) value for S2. We have further calculated the linescans of the magnetostatic fields along the length of the central stripes (green dashed line) from the three arrays for $\phi = 0^\circ$ and $\phi \sim 90^\circ$ as shown in Fig. 10.7(c, d). At $\phi = 0^\circ$, the internal field is

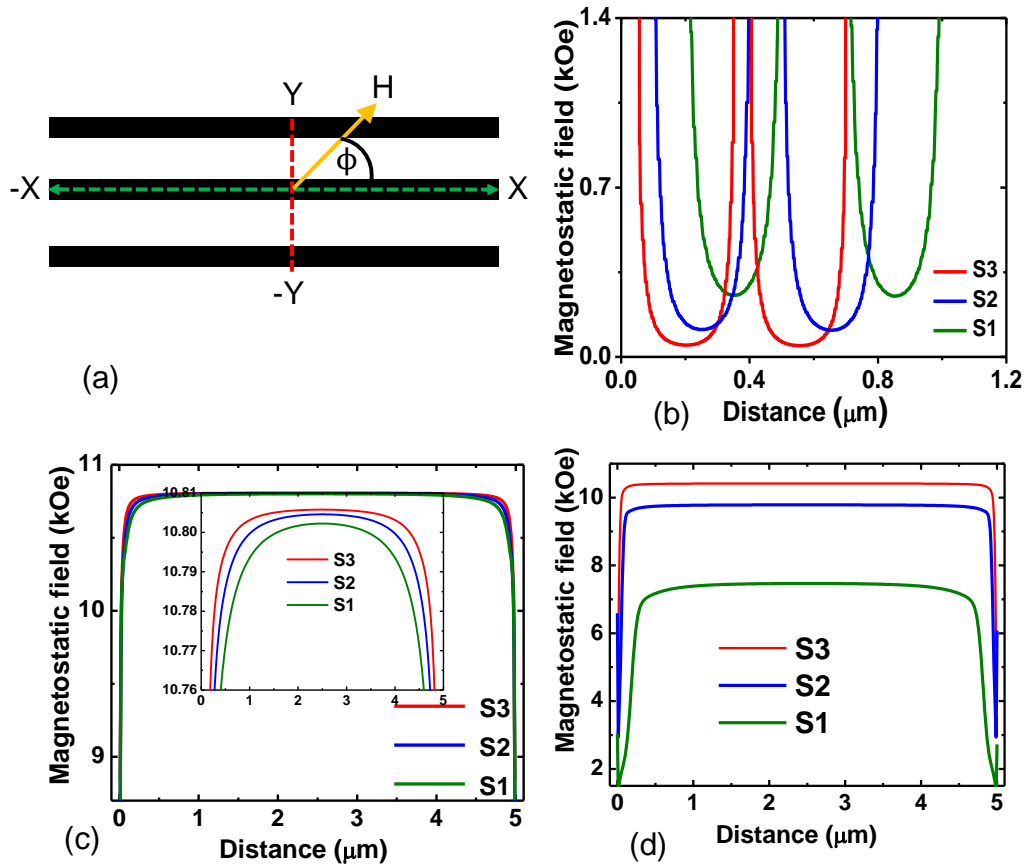


Fig. 10.7 (a) The schematic of the linescan of the simulated magentostatic field and the geometry of the applied magnetic field for the array of stripes are shown. (b) The linescans of the simulated magnetostatic fields along Y (red dotted line) direction from S1, S2 and S3 for $H = 1$ kOe applied at $\phi \approx 90^\circ$ are shown. The linescans of the simulated magnetostatic fields along X direction (green dotted line) from S1, S2 and S3 for $H = 1$ kOe applied at (c) $\phi = 0^\circ$ and (d) $\phi \approx 90^\circ$ are shown.

uniform at about 10.8 kOe for 80% of the stripe length barring the edge regions, where the field curves off from the flat line with highest curvature for S1, which decreases with increasing aspect ratio. The inset clearly shows a small difference in the internal field between three samples. At $\phi \sim 90^\circ$, the spin configurations for three different stripes are very different leading to a large difference in the internal field, spin wave frequencies and mode structures as well. Figure 10.7(d) confirms that the shape anisotropy is maximum for

S3 and minimum for S1 and the shape anisotropy of the stripe increases as the aspect ratio of the stripe increases.

10.3 Conclusions:

In conclusion, we have investigated the ultrafast magnetization dynamics of Ni₈₀Fe₂₀ nanostripes of three different widths by varying the orientation of the external bias magnetic field using an all optical time-resolved magneto-optical Kerr microscopy. For the narrowest stripe with 50 nm width the inter-stripe interaction becomes negligible enabling us to detect the dynamics of a single 50 nm wide stripe. We have observed a significant difference in the spin wave frequencies and nature of modes with the variation of the width of the stripe as well as by varying the bias field orientation. When the bias field is applied along the length of the stripes the wider stripes ($w = 200$ and 100 nm) showed uniform mode, a combination of BV- and DE-like standing spin wave modes and pure BV-like standing spin wave mode. However the 50 nm wide stripe showed only uniform mode and pure BV-like standing spin waves. As the bias field is rotated towards the stripe width the 200 and 100 nm wide stripes showed arrow-like standing spin waves, while for the 50 nm wide stripe only DE-like standing spin waves with quantization axis deviated from the stripe axis are observed. Simulated magnetostatic field distribution gives further evidence for the variation of the spin waves with stripe width and bias field orientation and confirmed a single stripe like behavior for the 50 nm wide stripe. The width dependent quantization of SWs in magnetic stripes opens up opportunities in engineering of domain-wall, spintronic and magnonic devices.

11. Giant Amplification and Fan-Out Operation in Asymmetric Magnetic Vortex Transistor

11.1 Introduction:

In magnetic thin films, magnetostatic interactions usually force the magnetization to lie parallel to the plane of the film. When it is further constrained to an area of about a square micrometer or less, the magnetic moments will form rotationally symmetric patterns that follow flux closure configuration. Magnetic platelets of micron or submicron size characterized by an in-plane flux closure configuration are known as magnetic vortices. Due to the closed flux lines, the dipolar energy is minimized and the structure is quite stable. However, at the centre of the disk, magnetization can not remain flat, because the short-range exchange interaction favors a parallel alignment of neighboring magnetic moments. The exchange energy forces the magnetization to stay out-of-plane in a very small area of only a few exchange lengths in diameter and thus creates the vortex core with a distinct polarization p , either up ($p = +1$) or down ($p = -1$) [97, 190-191]. The excitation spectrum of the magnetization involves the gyroscopic motion of the vortex core in several MHz to ~ 1 GHz range. The sense of the gyration (clockwise or counterclockwise) is determined by the vortex core polarization.

Magnetic vortices can be brought to gyration by the application of the magnetic fields and spin polarized currents [210-212, 259-262]. Recently, dynamic vortex core reversal was obtained by application of pulsed magnetic fields [197, 263-264], alternating magnetic fields [32] or spin-polarized currents [199, 203]. These findings opened up the possibility of using magnetic vortices as memory bits and for further spintronics applications. Wide investigations of the physics behind this reversal mechanism have also been started.

Due to the coupling of the external magnetic fields and spin polarized currents with the magnetic moments of the vortex core, the vortex core starts to move from the equilibrium position. In addition to this, the moving vortex core experiences another internal force arising from the demagnetizing field of the vortex flux closure pattern and this internal force acts along the perpendicular direction to the vortex core velocity. This creates the gyroscopic motion of the vortex core. For large amplitude excitation, non linear vortex core gyration occurs due to nonlinear increment of internal force and vortex core switching occurs along with the creation and annihilation of new vortex and antivortex pair [205, 265]. For small amplitude excitation, the internal force increment is linear and the vortex core motion remains in the linear regime [266].

The vortex core gyration is qualitatively described by the Landau-Lifshitz Gilbert equation. In the linear regime, the vortex core equation of motion can be obtained from Thiele's equation [266]. During the motion of the vortex core, the demagnetization field at the vortex core points antiparallel to the enlarged domain generated due to the displaced vortex and the time derivative of magnetization vector at the vortex core points into the disk centre or into the opposite direction. A variation in chirality naturally changes the direction of the demagnetization field and therefore it does not affect the vortex core gyration direction. Therefore, the vortex core gyration direction is solely controlled by the core polarization. Since the vortex core motion is governed by the demagnetization field, the demagnetization energy determines the vortex core potential. In the linear regime, parabolic potential can be assumed and vortex core can be described under a harmonic oscillator model [208]. Therefore, magnetostatically coupled vortex gyration in the linear regime can be considered as the coupled forced oscillator. Consequently, one expects mutual energy transfer between the gyrating vortices in the linear regime and a constant phase relation exists between the gyrating vortices [27, 213].

The mutual transfer of energy between uniformly excited magnetostatically coupled vortices due to the gyroscopic motion is extremely important for devices for microwave communication [200]. Dynamical property of coupled vortices in two nanodisks has been investigated analytically, numerically and experimentally [81, 211-212, 215]. The magnetostatic interaction between two closely spaced vortices is found to play an

important role in determining the dynamics of vortices. The rigid vortex model has been employed to calculate the magnetostatic interaction between the coupled vortices [211]. The eigenfrequencies of circular vortex core motion is found to depend on polarizations of the vortices. The chiralities of the vortices do not influence the eigenfrequencies. It is found that the time-averaged magnetostatic interaction energy varies as the minus sixth power of the separating distance. Therefore, the dynamical system of coupled vortices can be compared with a diatomic molecule with the Van der Waals bonding induced by the dipolar interaction. Magnetic charges on the side surfaces of the off-centered nearby vortices induce the magnetic dipole-dipole interaction. The splitting of gyration mode of coupled vortex system into higher and lower frequency modes via dipolar interaction has been demonstrated experimentally [200]. The main mode splitting is due to a chirality sensitive phase difference in gyrations of the coupled vortices, whereas the magnitude of the splitting is determined by their polarity configuration. It has been shown that the coupled pair of vortices behaves similar to a diatomic molecule with bonding and antibonding states. Selective excitation of coupled gyration modes has been performed by spin transfer torque [267]. The excited modes depend on combination of chiralities and polarities of the coupled vortex. For coupled gyration, the variation in resonance frequency is asymmetric with respect to the external magnetic field for same polarization and opposite chirality, implying a transition from stronger to weaker magnetostatic coupling depending upon the magnetic field direction. On the other hand, for the coupled vortices with the same polarizations and same chirality, the variation in resonance frequency is asymmetric with respect to the external magnetic field implying that the strength of the magnetostatic interaction is not modified. A controlled propagation of locally excited magnetic vortex dynamics through a linear array of magnetostatically coupled nanomagnetic discs has been studied by controlling the polarization, chirality and shape of the discs [27, 213]. The propagation of vortex core gyration is based upon the magnetostatic interaction between the nanodiscs, mediated by the magnetic side charges, generated by the gyrating vortices. It has been found that the magnitude and sign of the side charges and their separation depend strongly on the magnetic ground states of the vortices, including the core polarization and the chirality. The transmission of peak amplitude and velocity of propagation of the excitation along the linear array has been optimized for identical core

polarization and chirality of the nanodiscs with geometric asymmetry. Stimulated vortex gyration based energy transfer between spatially separated dipolar coupled magnetic vortices has been obtained by state-of-the-art time resolved soft X-ray microscopy technique [212]. In this case, a complete energy transfer and all of the collective normal modes have been observed. This novel method provides the advantage of tunable energy transfer rate, low power input signal, negligible energy loss in case of negligible intrinsic damping. Analytical and numerical calculations of the vortex gyration transfer rate and energy attenuation coefficients indicates that the transfer rate is characterized by the relative polarization configuration, saturation magnetization, the aspect ratio of the magnetic disks and core to core distance [215]. On the other hand, the energy attenuation is governed by the intrinsic damping constant as well as the values of saturation magnetization, thickness and radius of the single disks. Experimental demonstration of logic operations based on magnetic vortex state networks was also achieved via the vortex gyration mediated signal transfer mechanism [214].

However, in the case of stimulated vortex gyration, generally, the propagated signal amplitude in the neighbouring vortex is smaller in amplitude if one excites the first vortex in its resonant frequency [27, 213]. It has also been observed that the signal transfer is maximum when the core polarizations of the vortices are opposite [212]. However, to increase the efficiency of the microwave communication devices based on magnetostatically coupled vortices one needs to increase the amplitude of the response and constantly maintain the amplitude. For higher amplitude input, the vortex motion enters into nonlinear regime, vortex core switching occurs via the creation and annihilation new vortices and antivortices. Therefore, in this case it is not possible to increase and maintain a larger amplitude output and a constant phase relation between gyroscopic motions of the both vortices. On the other hand, if the applied signal is of very small amplitude and the frequency is that of the resonance frequency of that vortex, the amplitude of the response gradually increases indicating that the core switching may occur at some point, which is not desirable for microwave communication devices. One alternative is to use a very small amplitude off-resonant signal (within 5 % of the resonance frequency) to get around this problem [200].

It has been recently shown that in a pair of magnetostatically coupled vortices if a signal is applied to only one of them the other one shows a greater core gyration *i.e.*, amplification, when the core polarities are opposite [81]. Antivortex solitons moving through the strayfield is proposed to be responsible for this gain of transferred energy to the unexcited vortex. Later, a three vortex sequence was proposed where the left vortex (emitter) is locally excited and the output gain on the extreme right vortex (collector) can be switched from an ON to OFF state by controlling the core polarity of the middle vortex (base). This system has been proposed to work as magnetic vortex transistor (MVT) similar to an electronic bipolar junction transistor. However, the maximum gain obtained in ref. 41 is about 15 dB. With the miniaturization of devices and complexity of the circuits it is imperative to obtain larger gain and to obtain a fan-out operation, which was not obtained in the earlier works. The gain, which is defined as the difference between the energy spectral densities at the output and input, is expected to depend upon a number of parameters such as the distance between the three vortices, excitation frequency, aspect ratio of the magnetic disks and symmetry of the arrangement of three vortices. At the same time, the failure towards fan-out operation was due to the fact that the antivortex solitons do not split easily leading towards the asymmetry in different branches of symmetrical network. Lack of topologically stable antivortices may forbid any preferential energy transfer to the two branches. Keeping this in mind one may introduce additional asymmetry in the arrangement of the fan-out circuit for a successful fan-out operation. Here we showed a large increase in the gain of the MVT by tailoring the inter-disk separation and the arrangement asymmetry. The absorption of antivortex solitons at the neighbouring vortex and absence of a feedback loop is found to be responsible for this high gain. Furthermore, the output from this asymmetric magnetic vortex transistor is fed into the input of another two asymmetric magnetic vortex transistor to perform a successful fan-out operation and significantly large and nearly equal gains are observed at both the outputs.

11.2 Methods:

Magnetic vortex dynamics was simulated using finite difference method based Landau-Lifshitz-Gilbert (LLG) ordinary differential equation solver called Object Oriented

Micromagnetic Framework (OOMMF). At first a magnetic ground state was obtained with the required polarity and chirality. This was accomplished by using a Gaussian pulsed field

$$H_t = H_0 \exp(-t'^2) \quad (11.1),$$

where $\mu_0 H_0 = 1$ T and normalized time t' can be expressed as

$$t' = (t - t_0) / \sqrt{2\sigma} \quad (11.2)$$

and σ is the standard deviation of the Gaussian pulse in time whose full width at half maxima is 30 ps. To control the core polarity we have applied a field $H_z = \pm H_t / 10$, along z direction, close to the centre of the circular disk, where the sign of the field determines the core polarity. X and Y components of the applied Gaussian field to produce the desired chirality are

$$H_x = \mp H_t \sin(\theta) \quad (11.3)$$

$$H_y = \pm H_t \cos(\theta) \quad (11.4)$$

where $\theta = \tan^{-1}(y/x)$ and the upper or lower sign was chosen for the CCW and CW chirality. This pulse signal dies down quickly during the simulation. The simulation was run for 40 ns under a high damping (Gilbert damping constant $\alpha = 0.95$ was used here) to obtain the ground state. The other material parameters used here are saturation magnetization $M_s = 0.8 \times 10^6$ A/m, exchange stiffness constant $A = 13 \times 10^{-12}$ J/m and a zero magneto-crystalline anisotropy. During the vortex dynamics simulation we have used the value of damping as $\alpha = 0.008$, which is a realistic value of damping for Ni₈₀Fe₂₀ (Permalloy or Py). The dynamic simulation was run for 40 ns and the average magnetization was observed in every 10 ps. The cell size used during simulation was 5 nm × 5 nm × 40 nm.

At first, the dynamics of single vortex was studied by using a broadband excitation signal and the natural frequency of the single vortex was obtained. The signal had only x component H_x^S which contained power up to $f_{cut} = 45$ GHz and dependent upon time as given by

$$H_x^s = H_x^0 \frac{\sin(2\pi f_{cut}(t - t_0))}{2\pi f_{cut}(t - t_0)} \quad (11.5)$$

Here, $\mu_0 H_0 = 0.05$ T and $t_0 = 200$ ps.

After obtaining the data from OOMMF, we analyze the results by investigating the time evolution of x component of magnetization, $\langle m_x \rangle$ for each vortex, and its corresponding energy spectral density (ESD). We normalize the magnetization by dividing x component of magnetization M_x by M_s . Subsequently, we perform the Fourier transform to obtain the required ESD. This is plotted in decibel scale as $w_H \times 20\log_{10}|m_x|$, where a window scaling factor of $w_H = 2$ is used for the Hanning window. The Hanning window is used to avoid spectral leakage. These ESDs were calculated after running the dynamics for 40 ns so that any transient vortex core dynamics is suppressed and steady state dynamics becomes prominent in the spectrum. The strayfield was also obtained from OOMMF during the dynamics. The strayfield plots and the supplementary movies were created using MATLAB. The contour colour scale is based on the sum of squares of x and y components of the stray field.

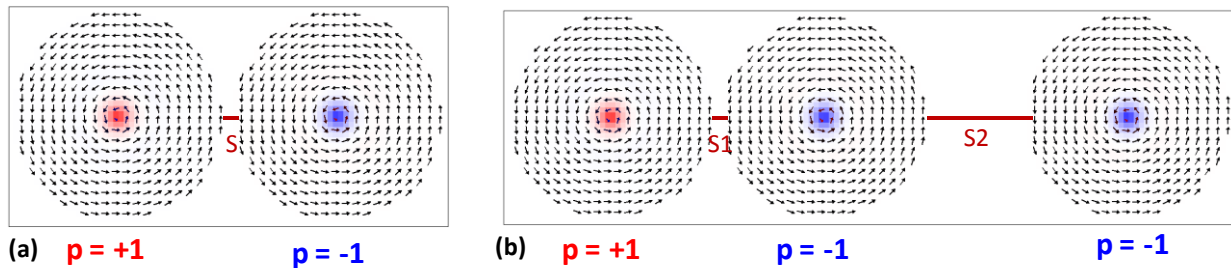


Fig. 11.1 The ground state spin configurations of Py disks of diameter (d) 200 nm and thickness (t) 40 nm arranged in coupled (a) two vortex system with inter disk separation (S) 10 nm and (b) three vortex system with the separation between left and centre vortex ($S1$) of 10 nm and the separation between centre and right vortex ($S2$) of 100 nm.

11.3 Results:

A circular disk of 200 nm diameter (d) and 40 nm thickness (t) made up of Ni₈₀Fe₂₀ (permalloy or Py) is used to form a stable magnetic vortex. The coupled vortex system is

formed by placing another Py disk of same dimension next to the first disk and similarly three vortex system is formed by placing three such magnetic disks in a row. Figures 11.1(a) and (b) show coupled two vortex and three vortex systems with core polarities (1, -1) and (1, -1, -1), respectively. Spatially averaged x -component of magnetization $\langle m_x \rangle$ is considered as an indicator of core displacement away from its equilibrium position. The square of the amplitude of Fourier transform of $\langle m_x \rangle$ is considered as the energy spectral density (ESD), which shows the peak power corresponding to maximum core displacement.

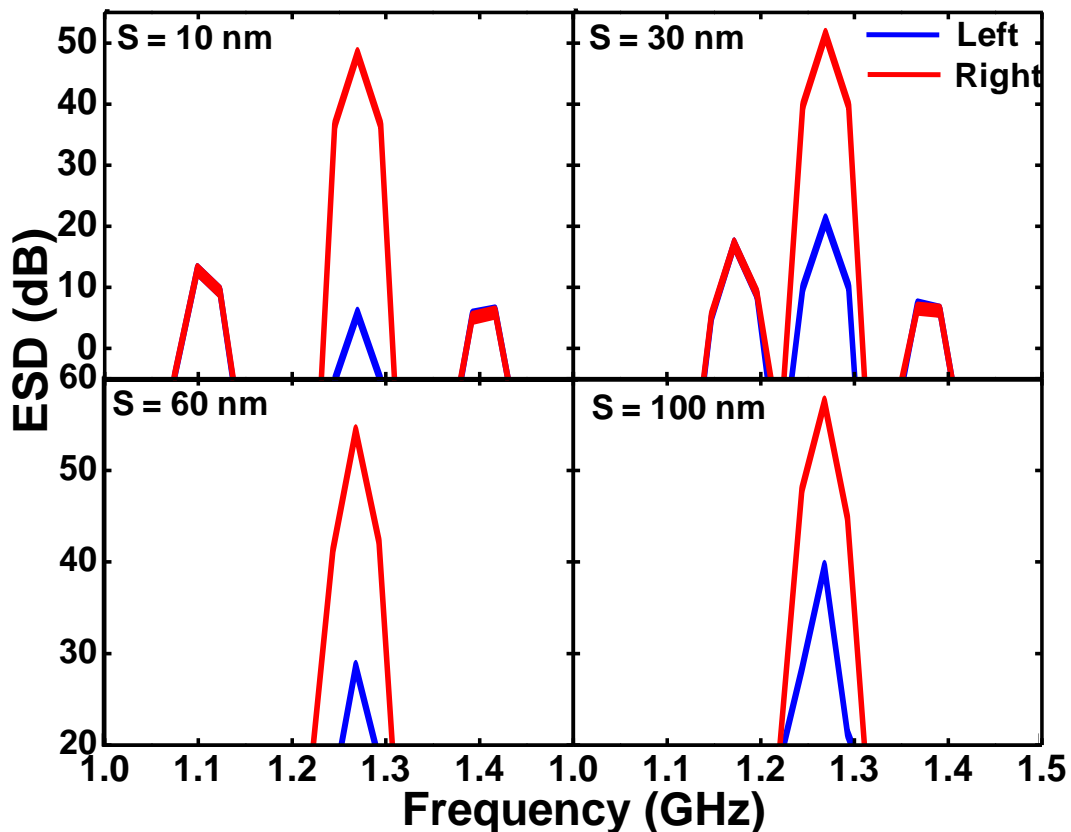


Fig. 11.2 Energy spectral densities (ESDs) for coupled two vortex systems with varying inter-disk separation (S) for a signal amplitude of 1.5 mT rotating CCW at $f_0 = 1.27$ GHz.

11.3.1 Coupled Pair of Magnetic Vortices:

Before optimizing the MVT gain and other related MVT operations, we investigated the energy transfer gain in a coupled two vortex system as a function of inter-disk separation. Figure 11.2 shows the ESDs for the left and right vortex for the coupled two vortex systems with four different inter-disk separations. Here, only the left vortex is excited with a local field. For higher separations (60 and 100 nm) a single gyration mode is observed, while for lower separation three coupled modes are observed. The central peak corresponding to highest ESD is always considered for calculating the energy transfer gain. The gain (B) is

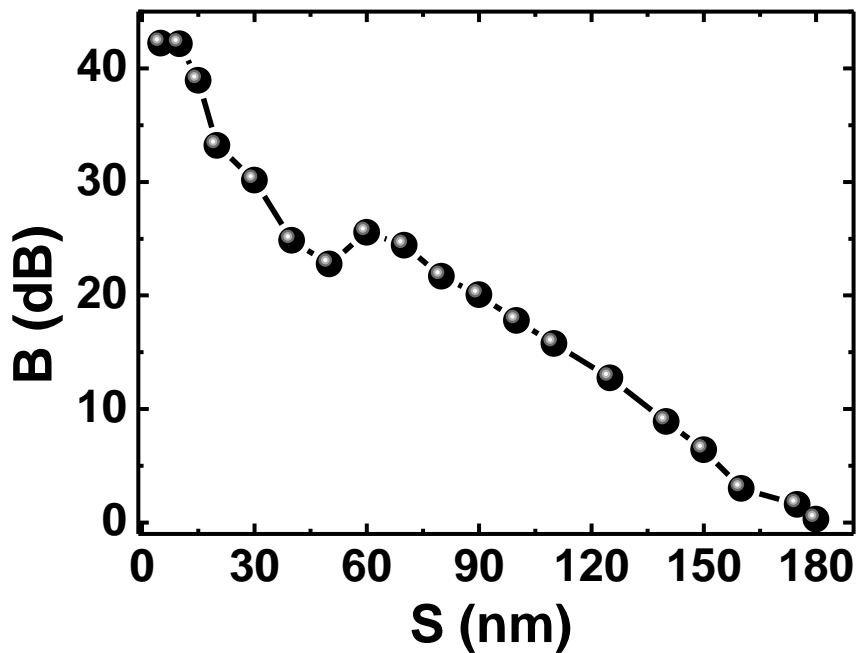


Fig. 11.3 Variation of gain (B) with inter-disk separation (S) is plotted for coupled two vortex systems.

calculated as the difference between maximum value of energy spectral density of right vortex and the left vortex. For all four separations large gain is observed. The gain (B) is systematically plotted as a function of inter-disk separation (S) in Fig. 11.3. Here, B shows almost a linear increase with the decrease in S and reaches a value of about 25.55 dB at $S =$

60 nm. For $S < 60$ nm B suddenly decreases to 22.77 dB followed by another steeper increase down to $S = 10$ nm, where it reaches a maximum value of 42.15 dB. Below that, B shows a saturation and does not increase any further. To understand this non-monotonic

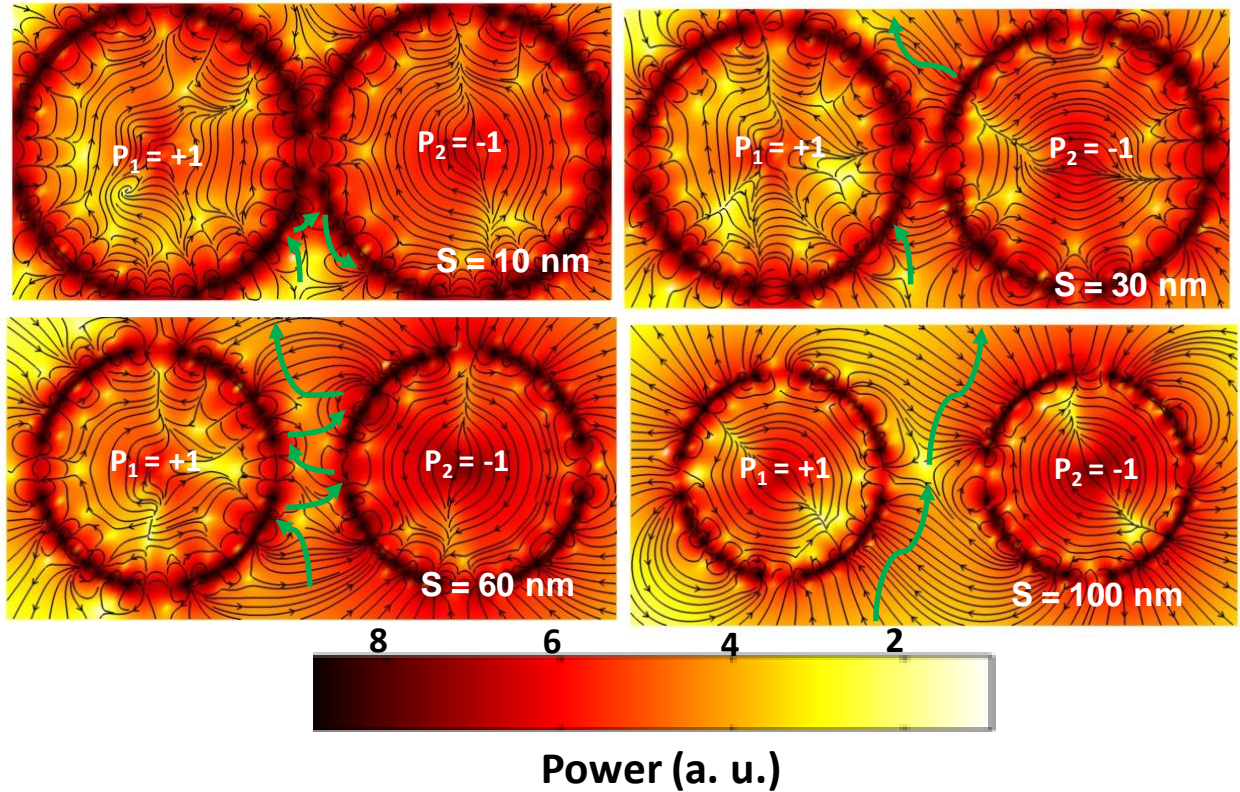


Fig. 11.4 Strayfield distributions for coupled two vortex systems with four different interdisk separations (S) are shown. The green arrows represent the paths of the antivortex solitons. The dimensions of the disk shown in different panels are not in scale.

increase in B with S we have studied the temporal evolution of the stray field. Figure 11.4 shows the snapshot of the simulated stray fields for four different samples at specific instants of time of the dynamics. The supplementary movie 1 - 4 show the dynamics in detail. Earlier work showed that the energy transfer from left to right vortex is mediated by stray field antivortices, which travels from the left disk and collides with the right disk. It is also inferred in ref. 81 from the only case studied ($S = 50$ nm) that an amplification occurs when no feedback loop of strayfield antivortex trajectory is present between the two disks. The feedback loop causes an energy rebalancing and hinders amplification. However, a

detailed study of variation of inter-disk separation as presented here shows that amplification may occur even in the presence of a feedback loop and even when the strayfield antivortex do not directly collide with the right vortex. For $S = 100$ nm, the antivortex generates after the onset of the dynamics and passes through the gap between the two disks without a single collision with either of the disks and the energy is transferred only due to the variation of the flux lines with time, which leads to a gain of 17.80 dB. With the reduction of S collision of antivortex starts to occur with both disks leading to an increase in gain in the energy transfer albeit with a feedback, which hinders a very large value of the gain. The feedback mechanism weakens with further reduction in S , causing a continuous increase in gain value. However, for S close to 60 nm a special situation occurs where a strayfield antivortex is present even in the ground state before the onset of the dynamics and the energy transfer process occurs immediately after the onset of the dynamics causing the feedback mechanism to weaken further. However, when S deviates significantly from 60 nm this antivortex disappear from the ground state and the transfer of energy starts after the creation of a stray field antivortex following the onset of gyration in the left vortex. As S reduces further, the feedback mechanism and the ensuing energy rebalancing disappears and one way transfer of energy from the left to right disk causes energy build up in the right vortex and a giant amplification occurs. This continues to increases with the reduction of S due to the faster transfer of energy. Finally a saturation at 42.15 dB occurs at $S \leq 10$ nm, when a very high dipolar interaction energy between the nearest edge regions of the disk forbids the antivortex to enter that zone and it transfers energy only in the lower half of the disk.

11.3.2 Magnetic Vortex Transistor (MVT):

For the MVT operation, we begin with a three vortex sequence with polarizations 1, -1 and -1, which worked successfully in ref. 81. Here, we vary the distance between the left and middle vortex (S_1) and the middle and right vortex (S_2) to optimize the gain (difference between the ESD in the right vortex and left vortex). In symmetric MVT, the distances S_1 and S_2 are same and maximum gain achieved was 14.8 dB for $S_1 = S_2 = 50$ nm[81]. Based on simulations by systematic variation of the values of S_1 and S_2 we show here that

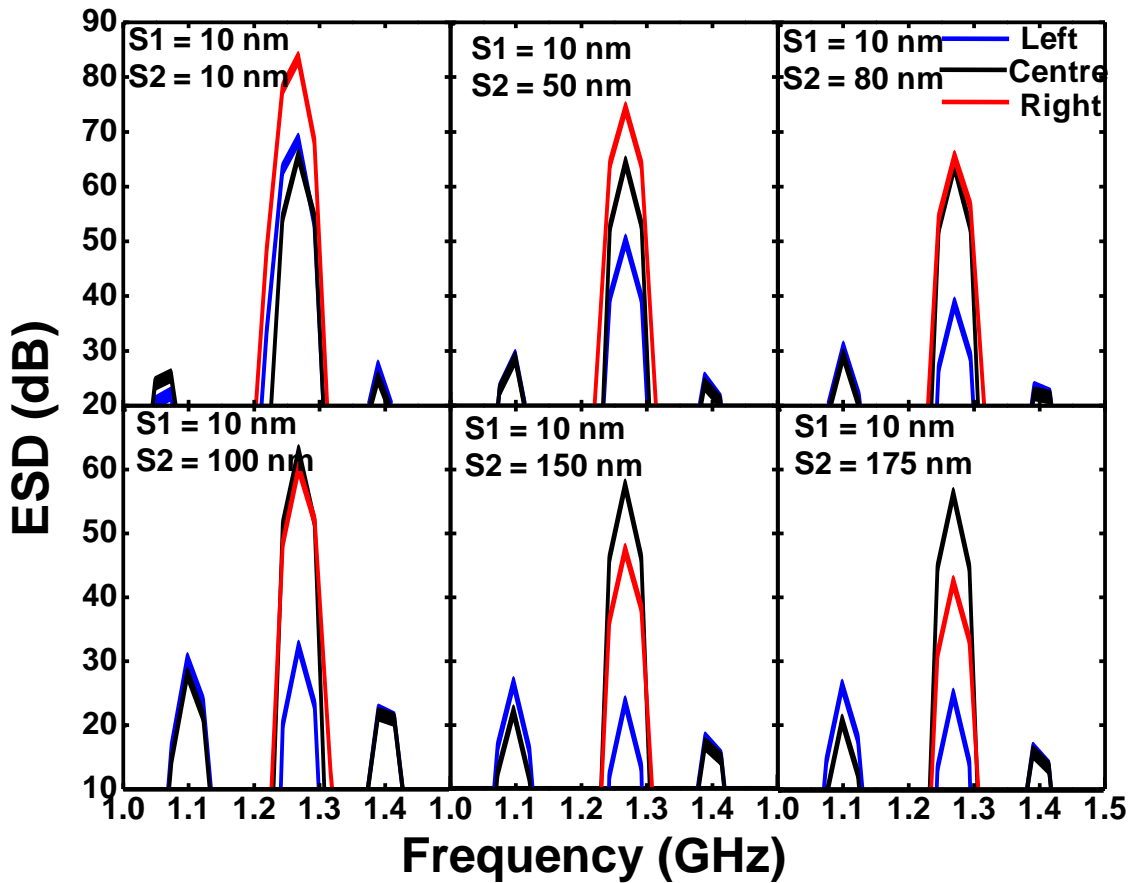


Fig. 11.5 Energy spectral densities (ESDs) for asymmetric magnetic vortex transistor (AMVT) with varying S_2 . A 1.5 mT signal rotating CCW at $f_0 = 1.27$ GHz is applied to the left vortex.

introduction of asymmetry in the arrangements of the three vortices lead to a giant gain in MVT and the gain can be maintained in complex circuits along branches. The asymmetry is introduced by making the separation between the central vortex and right vortex (S_2) larger than that between the left vortex and middle vortex (S_1). The optimum value is obtained by fixing $S_1 = 10$ nm, which provides maximum gain for coupled two vortices. Figure 11.5 shows the ESDs of MVTs for $S_1 = 10$ nm and for S_2 varying between 10 nm and 175 nm and in Fig. 11.6(a) gain (B) is plotted as a function of S_2 . It is observed that the gain

increases with the increase in $S2$, and a maximum of 28.28 dB is observed at $S2 = 100$ nm, beyond which it decreases with further increase of the $S2$. This two-fold increase in the

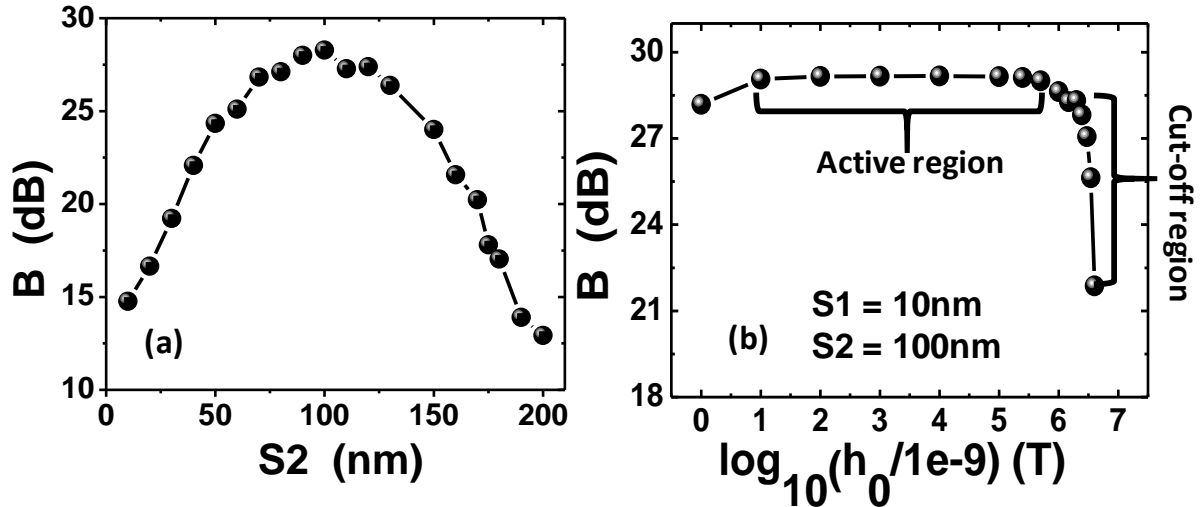


Fig. 11.6(a) Variation of gain (B) with $S2$ is plotted for AMVT. (b) Gain B , versus logarithm of signal amplitude h_0 is plotted for AMVT with $S1 = 10$ nm and $S2 = 100$ nm.

gain in an asymmetric magnetic vortex transistor (AMVT) is remarkable and can lead to applications magnetoelectronic circuits requiring signal amplification. To understand this giant amplification we again investigated the temporal evolution of the magnetic stray field as presented in Fig. 11.7 while greater details of the dynamics can be found in the supplementary movies 5-10. We observe that the mechanism of transfer of energy from the left vortex to the center vortex for all cases are same as the coupled two vortex systems with $S1 = 10$ nm. However, the mechanism of transfer of energy from the center vortex to the right vortex varies with $S2$. Consequently, the final gain of the vortex transistor is dominated by the strayfield dynamics between the center vortex and third vortex. At $S1 = S2 = 10$ nm, the antivortices created between the center vortex and right vortex are very small in size and therefore, very little energy is transferred from the center vortex to right vortex leading to a smaller gain of 14.76 dB. As $S2$ increases, larger antivortices are created and they move along nearly elliptical paths through the stray field between the center vortex and right vortex. The length of the major axis of the elliptical path appears to

determine the amount of transfer of energy. The variation of the length of the major axis of the elliptical path with S_2 presented in Fig. 11.8 shows that it increases with increase in S_2 and reaches a maximum at $S_2 = 100$ nm beyond which it drops. This variation is consistent with the variation of gain and hence we believe they are strongly correlated.

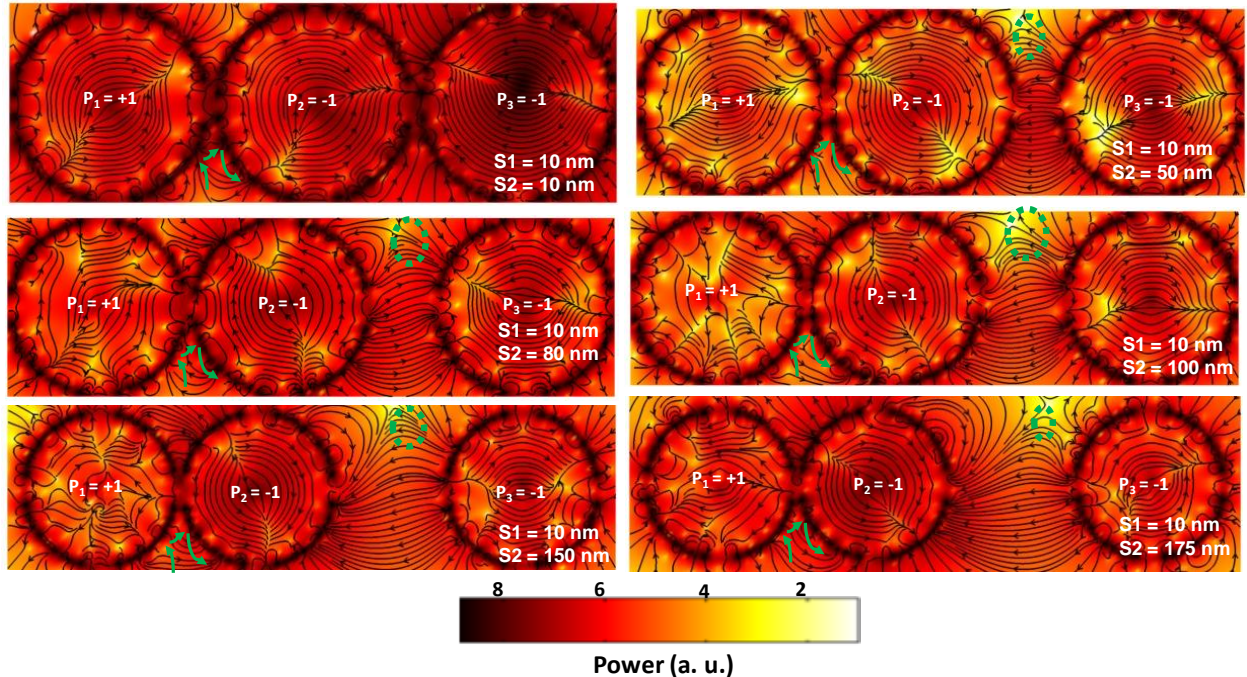


Fig. 11.7 Strayfield distributions for three vortex sequences with varying inter-disk separations S_1 and S_2 are shown. The green dotted lines represent the paths of the antivortex solitons. The dimensions of the disk shown in different panels are not in scale.

We further investigated the variation of gain of the optimized AMVT structure ($S_1 = 10$ nm and $S_2 = 100$ nm) with the input signal amplitude h_0 . Figure 11.6(b) shows a plot of variation of gain with logarithm of signal amplitude h_0 . Here, left vortex's core reversed for $h_0 = 5$ mT and therefore, we limit ourselves to 4 mT. For lower values of h_0 , the gain remains nearly constant at $B_{active} = 28.28$ dB. This is considered as the active region of the magnetic vortex transistor and B_{active} resembles the small-signal gain of an electronic bipolar junction transistor. At 4 mT the left vortex core switches, and gain suddenly drops and this can be considered as the cutoff region. Unlike the symmetric MVT the non-linear

distortion of gain from B_{active} at higher signal strength (before cut-off occurs) is not observed in the AMVT.

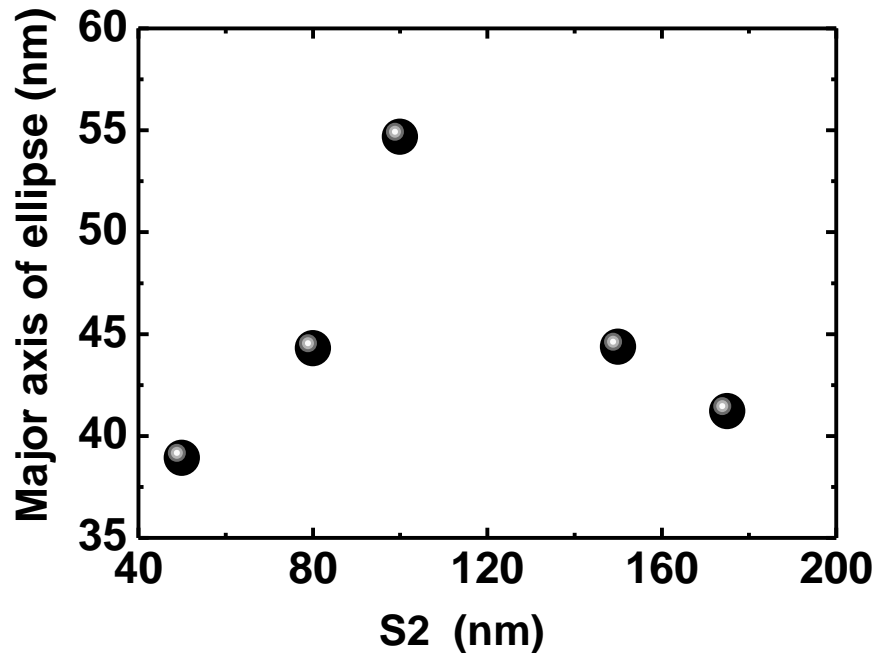


Fig. 11.8 Variation of the length of the major axis of the ellipse with S2 for AMVT are plotted.

11.3.3 Fan-Out:

The symmetric MVT did not show a fan-out operation as the antivortex soliton does not split easily leading towards an asymmetry in energy transfer in the two arms of the fan-out circuit. Here, we investigate the possibility of fan-out using AMVT. The optimized AMVT with the horizontal distance between the left and central vortex (S_{x1}) as 10 nm and that between the central and right vortex (S_{x2}) as 100 nm is used as a unit here. We placed two AMVTs vertically above and below the original AMVT while keeping the left vortex of the upper and lower branches and right vortex of the original AMVT in the same line and vary the vertical distances of the upper (S_{y1}) and lower (S_{y2}) AMVTs with the input AMVT to tune the gains at the two outputs. The ESDs and strayfield profiles for fan-out circuits with

different values of S_{y1} and S_{y2} are shown in Fig. 11.9. The detailed temporal evolution of the magnetic strayfield are provided in supplementary movies 11-13.

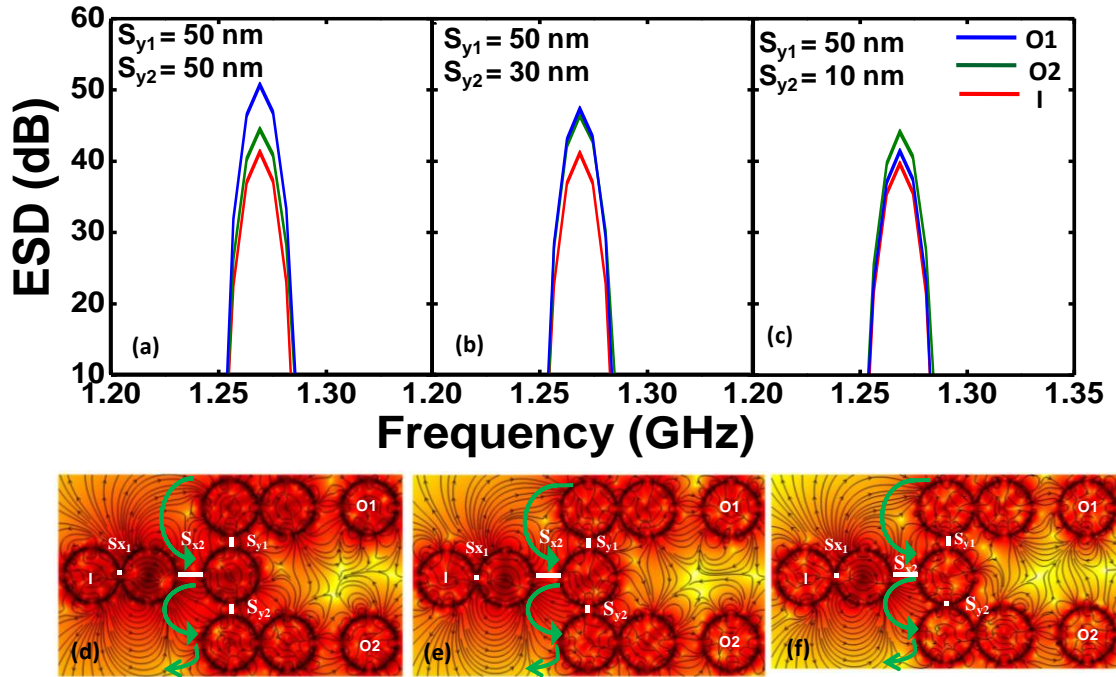


Fig. 11.9 (a) - (c) ESDs for fan-out operation are plotted. (d) - (f) Strayfield distributions in an AMVT network are shown. Signal is given only to the left vortex ('I') in the middle row and gain is measured at upper and lower right vortices which are marked as 'O1' and 'O2' respectively. The green lines represent the paths of the antivortex solitons.

At first we started with a symmetric fan-out circuit by setting $S_{y1} = S_{y2} = 50 \text{ nm}$. Gain is observed in both the outputs (O1 and O2) but gain in the upper branch is much higher than the gain in the lower branch ($B_{O1} - B_{O2} = 6.33 \text{ dB}$). To remove this asymmetry in gain we have introduced a second level of asymmetry in the fan-out circuit. A systematic variation of S_{y1} and S_{y2} shows that for $S_{y1} = 50 \text{ nm}$ and $S_{y2} = 30 \text{ nm}$ the ESDs at O1 and O2 are nearly same and subsequently the gains are also the same, $B_{O1} = B_{O2} = 5.4 \text{ dB}$. When S_{y2} is further decreased, the gain in O2 becomes higher than O1. Figure 11.9(c) shows that $B_{O2} - B_{O1} = 2.77 \text{ dB}$.

To understand this behaviour, we have studied the strayfield dynamics (Fig. 11.9(d)-(f)) of the fan-out circuits in details. An antivortex soliton is observed to be moving from the left

vortex of the upper AMVT to left vortex of the lower AMVT via the right vortex of the original AMVT. The size and speed of this antivortex soliton and interaction time with right vortex of the original AMVT is determined by the amount of asymmetry in the structure. For the first case shown here ($S_{y1} = S_{y2} = 50$ nm), four antivortices are observed close to the middle and right vortices of the upper and lower AMVTs (Fig. 11.9(d)). Among these four antivortices, two are situated between the right vortices of the upper and lower AMVTs. The larger antivortex is stationary at the halfway between the right vortices of the upper and lower AMVT branches and the smaller one moves towards the right vortex of the upper AMVT branch. As a result, the upper AMVT (O2) shows higher gain for symmetric fan-out circuit.

In the case of successful fan-out ($S_{y1} = 50$ nm, $S_{y2} = 30$ nm), the energy transfer mechanism is different from that in the symmetric case. Here we observe three antivortices close to the middle and right vortex of the upper and lower branches (Fig. 11.9(e)). Two of them first combine and then again split into two antivortices. These two antivortices move towards the right vortex of upper and lower AMVT branches and transfer energy equally. In the third case ($S_{y1} = 50$ nm, $S_{y2} = 10$ nm), in addition to the above mentioned antivortices, there are very small antivortices near the right vortex of the lower branch, causing the energy transfer to be significantly higher in the lower branch as compared to the previous two cases (Fig. 11.9(f)).

In addition to the distribution of energy to the two outputs in a fan-out circuit, we also observe an interesting trend in the sum of energy transferred to the two outputs and its relation to the stray field antivortex dynamics. When $S_{y1} = S_{y2}$, the antivortex soliton is quite large and it moves very quickly between the two branches (interaction time ≈ 0.55 ns). As a result, the sum of the output gains is large ($O1 + O2 = 12.71$ dB). As we break the symmetry by lifting up the lower branch slightly towards the input AMVT, the sum of the gains decreases to 11.67 dB. In this case, the size of the antivortex soliton moving from the left vortex of the upper AMVT branch to left vortex of the lower AMVT branch via the right vortex of the input AMVT decreases slightly as compared to that of the symmetric fan-out circuit. The interaction time of about 0.51 ns is nearly same as that for the symmetric case and the sum of gain is also similar. As we increase the asymmetry further ($S_{y2} = 10$ nm), the

size of the antivortex decreases further and it moves very slowly between the left vortex of the upper and lower branches of the circuit via the right vortex of input AMVT (interaction time ≈ 1.02 ns). As a result the sum of the gains at two output branches decreases significantly ($O_1 + O_2 = 6.31$ dB).

11.4 Discussions:

We have numerically explored the dependence of signal amplification of vortex core gyration in coupled vortex pair on the inter-disk separation with the goal of increasing the gain of a magnetic vortex transistor (MVT). We observe a non-monotonic increase in the amplification in the energy transfer with separation in the two-vortex case. An almost linear increase in the amplification occurs with the decrease in separation from higher separation down to 60 nm where the amplification suddenly drops followed by another steeper increase with further decrease in separation. The amplification saturates at a giant value of 42.15 dB for the inter-disk separation of 10 nm. This amplification of energy transfer is extended to a MVT consisting of a three vortex sequence with a particular combination of polarity of the three vortices (1, -1, -1). We found that a symmetric arrangement of the three vortex sequence does not give the maximum gain of the transistor but an asymmetric arrangement is necessary. In this case, we found that a particular combination of separation i.e., 10 nm between the left and middle disk and 100 nm between the middle and the right disk give the maximum gain of 28.28 dB, which is a factor of two improvement as compared to previously reported value. This remarkable observation can be interpreted in terms of the temporal evolution of stray magnetic field and antivortex packets moving through the strayfield is held responsible for the above observation. We postulated some mechanisms based upon the motion of antivortex solitons and this can successfully explain our numerical results in great detail.

Further we have numerically explored the fan-out operations using the asymmetric magnetic vortex transistor (AMVT). Total gain and distribution of gain among the two branches were observed to be dependent upon the vertical separation between the input AMVT and the branches. The mechanisms of movement of antivortex solitons moving through the dynamic strayfield were explored. With the advent of nano-electronic devices

we hope that our findings will promote the design of complex circuits entirely based on magnetic vortices and is big leap towards all-magnetic computation.

12. Summary and Future Perspectives

12.1 Summary:

In this thesis, we have investigated the collective magnetization dynamics of magnetic nanostructures at various length scales and time scales. We have studied the extrinsic and intrinsic configurational magnetic anisotropy of magnetic nanostructures at various length scales (100 nm to 5 μm) over a broad time scale (femtosecond to nanosecond). The samples are mainly fabricated by using a combination of electron beam lithography and electron beam evaporation technique. In few cases self aligned shadow deposition technique is used for sample fabrication. The initial characterization of the samples is done by using Scanning Electron microscopy (SEM) and Energy dispersive X-ray (EDX) spectroscopy techniques. The thickness and the surface roughness of the sample are measured by using Atomic Force microscopy (AFM) technique. The quasistatic magnetization reversal is studied using focused magneto-optical Kerr effect microscopy (MOKE). The ultrafast magnetization dynamics is measured using a home-built TR-MOKE microscope with collinear pump-probe geometry. The experimental results are analyzed and interpreted with the help of micromagnetic simulation (OOMMF, LLG Micromagnetics) and macrospin formalism.

First we have investigated tunable magnetization dynamics in two-dimensional magnonic crystals (MCs) in the form of arrays of Py circular nanodots) with variable lattice symmetry namely square, rectangular, hexagonal, honeycomb and octagonal lattices. The SW spectra show significant dependence on the lattice symmetry. The square lattice shows a single uniform precessional mode, which is the coherent precession of the edge mode of all the dots in the lattice. The rectangular lattice shows two modes, which are coherent precession of the edge and centre modes of the dots over the entire lattice. The hexagonal lattice shows three clear modes, which correspond to the uniform collective mode, a backward volume (BV) like mode and a bowtie like mode of the whole lattice. The honeycomb lattice

shows broad and rich SW spectrum, which includes various localized and extended modes including Damon-Eshbach (DE) like mode of the lattice. For octagonal lattice three modes are observed, which are uniform, DE like, and localized modes of the lattice. As can be seen from simulated magnetostatic field distribution for Bravais lattices (square, rectangular and hexagonal), dipolar contribution to the stray field is dominant. However, for the honeycomb and octagonal lattices the stray field is even more complicated primarily due to the broken translational symmetry. This causes unequal distributions of stray fields within the lattices and the occurrence of higher order multipolar contributions to the stray fields. It has been found that the symmetry of the lattice plays a major role in determining the magnetic stray field configuration which eventually affects the SW spectra. In addition to this, the variation of the stray field with the azimuthal angle of the bias magnetic field leads towards an extrinsic configurational magnetic anisotropy in these lattices.

To investigate the magnetization dynamics at a different length scale we studied elongated Py ellipse with length 1 μm and width 450 nm dispersed in three different lattice geometries (S1, S2 and S3). The dominant precessional mode shows a two-fold anisotropy. We have also observed that the anisotropy field is maximum (minimum) when the elements are closely packed along their LA (SA) and take an intermediate value when they are well separated. Analysis shows that a competition between the shape anisotropy of the constituent elements and the inter-element magnetostatic field leads towards a variation in the net magnetic anisotropy and the corresponding frequency variation. Calculation of mode profiles of the anisotropic mode shows that it is the extended centre mode of the ellipse, whose symmetry changes with the variation of the bias field orientation.

Next we investigated the SW spectra 25 nm thick Py and Co bi-component units of length and width of 1 μm and 450 nm, respectively and with a gap of 35 nm between the elliptical sub-elements of the bi-component unit ensuring that they are purely magnetostatically coupled. The frequency spectra change significantly depending upon the direction of the external bias magnetic field with respect to the LA of the sample while very minor changes are observed between the spectra for the two different lattices (S1 and S2). Four well separated bands are observed for the SA spectra, while only two well separated bands are observed for the LA spectra with a mode splitting for the lower frequency band giving rise

to a 3rd peak. From micromagnetic simulation it is observed that the frequencies and the spatial profiles of the modes of individual elements are modified significantly in the bi-component unit as opposed to the individual constituents and further in the two-dimensional arrays due to the inter-element interaction. In addition to this occurrence of both optical and acoustic modes are also observed for these BMCs.

Next we move to an even longer length scale and studied Py nanostripes with 5 μm length and width varying between 50 nm and 200 nm. We demonstrated a manipulation of the SW spectra in these systems by changing the bias field orientation (ϕ) both by experiment and simulation results. A rich SW spectra is observed for all three samples for both $\phi = 0^\circ$ and 90° , which make them a potential candidate for nanoscale microwave filter. Numerical calculations of SW mode profiles show that at $\phi = 0^\circ$ a mixed Damon-Eshbach (DE) and Backward Volume (BV) mode is observed which forms a standing SW with the quantization axis along the width of the stripe whereas at $\phi = 90^\circ$, pure DE like standing SW is observed with quantization parallel to the length of the stripe.

Finally, we numerically studied the gyroscopic motion of magnetic vortex cores in physically separated by magnetostatically coupled Py nanodisks. Such system was previously used to show a magnetic vortex based transistor operation. In this thesis we have optimized the gain of two and three vortex systems by controlling the separation between the vortices and by introducing some asymmetry in their arrangements. A magnetic disk of 200 nm diameter and 40 nm thickness made up of Py is used to form a magnetic vortex. For the coupled vortex systems, only the leftmost disk is excited with a magnetic field (Gaussian pulsed field with FWHM 30 ps and $\mu_0 H_0 = 1 \text{ T}$) and the transfer of the energy to the following disks on its right side are measured. The gain is defined as the difference of the energy spectral density (ESD) which is the square of the amplitude of Fourier transform of $\langle m_x \rangle(t)$ (with respect to t) of two vortices. For the two vortex system, the gain is found to be maximum (42.15 dB) for a separation of 10 nm below which the gain does not increase any further. Investigation of the temporal evolution of the stray field shows that steady packets of antivortices are generated in the stray field which travels towards the second vortex through the stray field. These antivortices are absorbed at the second vortex causing a transfer of energy between the two vortices. The three vortex

system (vortex transistor) showed the maximum gain (28.28 dB) for a specific combination of distances between the first two vortices and between the second and third vortex and it can efficiently work as a vortex transistor. The mechanism of transfer of energy from the first vortex to the second vortex is same as the two vortex system. But the energy from the second vortex to the third vortex is occurred due to the generation strayfield antivortices which rotate in an nearly elliptical path. The length of the major axis of this elliptical path increases as separation between second and third vortex increases. We also managed to successfully demonstrate a fan out operation of such transistors by carefully selecting their arrangements.

12.2 Future Perspectives:

Now-a-days nanofabrication is the core of modern technological progress. The principal challenge is to fabricate high quality samples with nanometer precision and with a very narrow distribution of shapes, sizes and distances. The currently used tools and techniques for nanofabrication will soon reach its limit and for efficient and cost effective production of large scale nanostructured devices one has to search for alternative techniques. In such situation “bottom-up” technologies might take an important role to synthesize monodisperse nanocrystals of uniform shapes and sizes.

The collective magnetization dynamics of magnetic nanodot arrays is a multidimensional problem. As we discussed in chapters 6 and 7 that the lattice symmetry is an attractive option by which the interdot magnetostatic interaction of highly complex nature can be introduced and the interdot magnetostatic interaction in the lattices plays an important role in determining the collective magnonic modes of the lattices. The periodicity of the lattice determines the Brillouin zone and the allowed wave vectors for magnonic modes. It is very interesting and challenging to measure the wave vector dispersion of the collective modes of arrays of nanodots arranged in different lattice symmetry by using Brillouin light scattering (BLS) technique.

The ever increasing demand of miniaturization and speed of devices offers challenges in controlling spin dynamics in ferromagnetic nanostructures by tailoring material parameter. For a bi-component magnonic crystal (BMCs) as two different magnetic

materials are in direct contact with each other, the dynamical dipole coupling is maximized due to the exchange coupling at the boundary. As a result, SWs are subject to scattering at the interfaces between the two materials and can easily transmit through the boundary. Therefore SWs can propagate across its entire structure with considerable group velocities. It is very interesting to study the SW dynamics of BMCs arranged in different lattice symmetry by using various technique.

The interdot magnetostatic interaction in ordered arrays of nanodots also get affected by the shape of the elements because the profile of the stray magnetic field depends on the shapes of the boundary of the elements as well as the internal magnetic field and one may tailor the stray magnetic field to any complicated nature beyond the dipolar and higher order multipolar terms. If we vary the lattice symmetry as well as the shape of the dot, the stray magnetic field configuration will be very complex in nature allowing to tune the magnonic spectra will far more rigor. As a result, the ultrafast magnetization dynamics of ferromagnetic nanodots with different dot shapes arranged in different lattice symmetry will be an interesting topic to study. Following that study of magnonic quasicrystals in the form of nanodots arranged in quasiperiodic arrangements will be a very interesting area of research.

Recently a three vortex system has been proposed to work as vortex transistor, where the vortex at one end is excited and the gyration amplitude at the vortex situated at the other end is observed to be higher (gain) than the gyration amplitude at the vortex which has been excited directly. We have attempted to optimize the gain of such two and three vortex system by controlling the separation between the vortices and by introducing some asymmetry in this arrangement by using micromagnetic simulation. It will be challenging to measure experimentally the gain of two and three vortex systems by using various electrical and x-ray based imaging techniques. The leftmost disk (disk-1) may be excited by applying a pulsed/monochromatic current induced Oersted field or a spin-polarized current/spin current while the transferred excitation (gain) can be detected by electrical measurement using spin torque diode effect or by inductive measurement using a second antenna and a vector network analyzer. In a different scale this can also be measured by x-ray microscopy. Finally, the TR-MOKE microscope can be extended to measure the

magnetization dynamics at different temperature, especially at lower temperature down to 1 K and at high magnetic field upto 8 T using a Helium cryostat and a superconducting magnet. This may reveal various new physics including magnon-phonon interaction and mechanisms of damping behavior. In addition new materials including manganites, multiferroics and diluted magnetic semiconductors with Curie temperature close to or below room temperature can be studied.

In summary, magnetization dynamics of different types of magnetic nanostructures over a broad range of time-scale are investigated by using different techniques which have both fundamental interests as well as applications in different spin based technologies.

References

1. T. Thomson *et al.*, *Phys. Rev. Lett.* **96**, 257204 (2006).
2. O. Hellwig *et al.*, *Appl. Phys. Lett.* **90**, 162516 (2007).
3. J. Åkerman, *Science* **308**, 508 (2005).
4. S. Tehrani *et al.*, *J. Appl. Phys.* **85**, 5822 (1999).
5. D. B. Carlton *et al.*, *Nano Lett.* **8**, 4173 (2008).
6. A. Imre *et al.*, *Science* **311**, 205 (2006).
7. J. Ding *et al.*, *Appl. Phys. Lett.* **100**, 073114 (2012).
8. D. A. Allwood *et al.*, *Science* **309**, 1688 (2005).
9. S. H. Chung *et al.*, *Appl. Phys. Lett.* **85**, 2971 (2004).
10. M. Arruebo *et al.*, *Nano Today* **2**, 22 (2007).
11. S. Kaka *et al.*, *Nature* **437**, 389 (2005).
12. M. Krawczyk and H. PuszkarSKI, *Phys. Rev. B* **77**, 054437 (2008).
13. A. V. Chumak *et al.*, *Appl. Phys. Lett.* **93**, 022508 (2008).
14. B. D. Terris and T. Thomson, *J. Phys. D: Appl. Phys.* **38**, R199 (2005).
15. A. Moser *et al.*, *J. Phys. D: Appl. Phys.* **35**, R157 (2002).
16. S. H. Charap *et al.*, *IEEE Trans. Magn.* **33**, 978 (1997).
17. D. Weller and A. Moser, *IEEE Trans. Magn.* **35**, 4423 (1999).
18. S.-i. Iwasaki, *J. Magn. Magn. Mater.* **235**, 227 (2001).
19. S. N. Piramanayagam, *J. Appl. Phys.* **102**, 011301 (2007).

References

20. C. A. Ross, *Annu. Rev. Mater. Res.* **31**, 203 (2001).
21. G. F. Hughes, *IEEE Trans. Magn.* **36**, 521 (2000).
22. B. D. Terris *et al.*, *Microsyst. Technol.* **13**, 189 (2007).
23. S. A. Nikitov *et al.*, *J. Magn. Magn. Mater.* **236**, 320 (2001).
24. G. Gubbiotti *et al.*, *Appl. Phys. Lett.* **100**, 162407 (2012).
25. A. B. Ustinov *et al.*, *Appl. Phys. Lett.* **96**, 142513 (2010).
26. J. W. Kłos *et al.*, *Sci. Rep.* **3**, 2444 (2013).
27. S. Barman *et al.*, *J. Phys. D: Appl. Phys.* **43**, 335001 (2010).
28. K. Y. Guslienko *et al.*, *Phys. Rev. B* **65**, 024414 (2001).
29. K. Y. Guslienko *et al.*, *Phys. Rev. Lett.* **100**, 027203 (2008).
30. T. Shinjo *et al.*, *Science* **289**, 930 (2000).
31. R. Antos *et al.*, *J. Phys. Soc. Japan* **77**, 031004 (2008).
32. B. Van Waeyenberge *et al.*, *Nature* **444**, 461 (2006).
33. R. P. Cowburn, *Nat Mater* **6**, 255 (2007).
34. R. P. Cowburn, *J. Magn. Magn. Mater.* **242–245**, 505 (2002).
35. V. V. Kruglyak *et al.*, *J. Phys. D: Appl. Phys.* **43**, 264001 (2010).
36. S. Neusser and D. Grundler, *Adv. Mater.* **21**, 2927 (2009).
37. B. Lenk *et al.*, *Phys. Rep.* **507**, 107 (2011).
38. R. Mandal *et al.*, *ACS Nano* **6**, 3397 (2012).
39. S. Saha *et al.*, *Appl. Phys. Lett.* **102**, 242409 (2013).
40. B. K. Mahato *et al.*, *Appl. Phys. Lett.* **105**, 012406 (2014).

References

41. B. K. Mahato *et al.*, *Appl. Phys. Lett.* **102**, 192402 (2013).
42. B. Rana *et al.*, *Appl. Phys. Express.* **4**, 113003 (2011).
43. S. Saha *et al.*, *Adv. Funct. Mater.* **23**, 2378 (2013).
44. S. Saha *et al.*, *Appl. Phys. Lett.* **103**, 242416 (2013).
45. S. Saha *et al.*, *RSC Adv.* **5**, 34027 (2015).
46. M. Jamali *et al.*, *Sci. Rep.* **3**, (2013).
47. K. S. Lee and S. K. Kim, *J. Appl. Phys.* **104**, 053909 (2008).
48. A. Khitun *et al.*, *J. Phys. D: Appl. Phys.* **43**, 264005 (2010).
49. M. P. Kostylev *et al.*, *Appl. Phys. Lett.* **87**, 153501 (2005).
50. T. Schneider *et al.*, *Appl. Phys. Lett.* **92**, 022505 (2008).
51. A. V. Chumak *et al.*, *Nat Commun* **5**, (2014).
52. S.Urazhdin *et al.*, *Nat Nano* **9**, 509 (2014).
53. V. E. Demidov *et al.*, *Nat Mater* **9**, 984 (2010).
54. M. Tsoi *et al.*, *Nature* **406**, 46 (2000).
55. S. Urazhdin *et al.*, *Phys. Rev. Lett.* **91**, 146803 (2003).
56. M. R. Freeman and B. C. Choi, *Science* **294**, 1484 (2001).
57. S. Petit *et al.*, *Phys. Rev. Lett.* **98**, 077203 (2007).
58. J. Podbielski *et al.*, *Phys. Rev. Lett.* **99**, 207202 (2007).
59. M. J. Hurben and C. E. Patton, *J. Magn. Magn. Mate.* **139**, 263 (1995).
60. R. W. Damon and J. R. Eshbach, *J. Phys. Chem. Solids* **19**, 308 (1961).
61. K. Vogt *et al.*, *Nat Commun* **5**, (2014).

References

62. A. A. Serga *et al.*, *J. Phys. D: Appl. Phys.* **43**, 264002 (2010).
63. T. Sebastian *et al.*, *Phys. Rev. Lett.* **110**, 067201 (2013).
64. T. Sebastian *et al.*, *Appl. Phys. Lett.* **100**, 112402 (2012).
65. J. Fassbender *et al.*, *Phys. Rev. B* **73**, 184410 (2006).
66. J. A. King *et al.*, *Appl. Phys. Lett.* **104**, 242410 (2014).
67. V. Dasgupta *et al.*, *J. Appl. Phys.* **99**, 08G312 (2006).
68. J. E. Hirsch, *Phys. Rev. Lett.* **83**, 1834 (1999).
69. Y. K. Kato *et al.*, *Science* **306**, 1910 (2004).
70. A. Ganguly *et al.*, *Appl. Phys. Lett.* **104**, 072405 (2014).
71. A. Ganguly *et al.*, *Appl. Phys. Lett.* **105**, 112409 (2014).
72. B. F. Miao *et al.*, *Phys. Rev. Lett.* **111**, 066602 (2013).
73. O. Mosendz *et al.*, *Phys. Rev. Lett.* **104**, 046601 (2010).
74. E. Saitoh *et al.*, *Appl. Phys. Lett.* **88**, 182509 (2006).
75. K. Uchida *et al.*, *Nature* **455**, 778 (2008).
76. K. Uchida *et al.*, *Nat Mater* **9**, 894 (2010).
77. S. O. Valenzuela and M. Tinkham, *Nature* **442**, 176 (2006).
78. S. Datta and B. Das, *Appl. Phys. Lett.* **56**, 665 (1990).
79. G. E. W. Bauer *et al.*, *Appl. Phys. Lett.* **82**, 3928 (2003).
80. T. Chiba *et al.*, *Appl. Phys. Lett.* **102**, 192412 (2013).
81. D. Kumar *et al.*, *Sci. Rep.* **4**, (2014).
82. V. E. Demidov *et al.*, *Phys. Rev. B* **77**, 064406 (2008).

References

83. S.-K. Kim *et al.*, *Appl. Phys. Lett.* **95**, 082507 (2009).
84. Y. Au *et al.*, *Appl. Phys. Lett.* **100**, 172408 (2012).
85. F. Goedsche, *Phys. Status Solidi B* **39**, K29 (1970).
86. J. Gouzerh *et al.*, *J. Magn. Magn. Mater.* **101**, 189 (1991).
87. Y. I. Gorobets and S. A. Reshetnyak, *Tech. Phys.* **43**, 188 (1998).
88. V. K. Dugaev *et al.*, *Phys. Rev. B* **72**, 024456 (2005).
89. S. K. Choi *et al.*, *Appl. Phys. Lett.* **89**, 062501 (2006).
90. K. Perzlmaier *et al.*, *Phys. Rev. B* **77**, 054425 (2008).
91. C. Mathieu *et al.*, *Phys. Rev. Lett.* **81**, 3968 (1998).
92. M. Bauer *et al.*, *Phys. Rev. B* **56**, R8483 (1997).
93. V. Vlaminck and M. Bailleul, *Science* **322**, 410 (2008).
94. S. O. Demokritov *et al.*, *Phys. Rev. Lett.* **93**, 047201 (2004).
95. A. Kozhanov *et al.*, *J. Appl. Phys.* **105**, 07D311 (2009).
96. A. Barman *et al.*, *Appl. Phys. Lett.* **82**, 3065 (2003).
97. R. P. Cowburn *et al.*, *Phys. Rev. Lett.* **83**, 1042 (1999).
98. V. V. Kruglyak *et al.*, *Phys. Rev. B* **75**, 024407 (2007).
99. J. Aizenberg *et al.*, *Appl. Phys. Lett.* **71**, 3773 (1997).
100. P. B. Fischer and S. Y. Chou, *Appl. Phys. Lett.* **62**, 2989 (1993).
101. F. Rousseaux *et al.*, *J. Vac. Sci. Technol. B* **13**, 2787 (1995).
102. E. F. Wassermann *et al.*, *J. Appl. Phys.* **83**, 1753 (1998).
103. N. Singh *et al.*, *Nanotechnology* **15**, 1539 (2004).

References

104. J. Moritz *et al.*, *IEEE Trans. Magn.* **38**, 1731 (2002).
105. J. Ding and A. O. Adeyeye, *Adv. Funct. Mater.* **23**, 1684 (2013).
106. T. Devolder *et al.*, *Appl. Phys. Lett.* **74**, 3383 (1999).
107. S. Pal *et al.*, *Solid State Commun.* **151**, 1994 (2011).
108. H. Masuda *et al.*, *Appl. Phys. Lett.* **71**, 2770 (1997).
109. W. D. Williams and N. Giordano, *Phys. Rev. B* **33**, 8146 (1986).
110. L. Folks *et al.*, *Appl. Phys. Lett.* **76**, 909 (2000).
111. C. Banerjee *et al.*, *J. Appl. Phys.* **116**, 163912 (2014).
112. B. E. Argyle and J. G. McCord, *J. Appl. Phys.* **87**, 6487 (2000).
113. W. H. Rippard and R. A. Buhrman, *Appl. Phys. Lett.* **75**, 1001 (1999).
114. G. N. Kakazei *et al.*, *J. Appl. Phys.* **93**, 8418 (2003).
115. S. Kasai *et al.*, *Appl. Phys. Lett.* **104**, 092408 (2014).
116. S. O. Demokritov *et al.*, *Phys. Rep.* **348**, 441 (2001).
117. S. O. Demokritov and V. E. Demidov, *IEEE Trans. Magn.* **44**, 6 (2008).
118. T. J. Silva *et al.*, *J. Appl. Phys.* **85**, 7849 (1999).
119. A. Barman *et al.*, *J. Appl. Phys.* **95**, 6998 (2004).
120. A. Barman *et al.*, *Appl. Phys. Lett.* **90**, 202504 (2007).
121. A. Barman *et al.*, *Rev. Sci. Instrum.* **79**, 123905 (2008).
122. C. Kittel, *Introduction to Solid State Physics*, Seventh edition, Wiley India, New Delhi, India. (2009).
123. A. H. Morrish, *The Physical Principles of Magnetism*. (IEEE Press, New York, United States, 2001).

References

124. A. Aharoni, *Introduction to the Theory of Ferromagnetism, Second Edition.* (Oxford University Press, New York, United State, 2000).
125. P. Bruno, *Physical Origins and Theoretical Models of Magnetic Anisotropy.* (Jürich, 1993).
126. R. Cowburn *et al.*, *Phys. Rev. Lett.* **81**, 5414 (1998).
127. W. H. Meiklejohn and C. P. Bean, *Phys. Rev. B* **102**, 1413 (1956).
128. J. Nogués and I. K. Schuller, *J. Magn. Magn. Mater.* **192**, 203 (1999).
129. M. D. Kaufmann, *Magnetization Dynamics in All-optical Pump-Probe Experiments: Spin - wave Modes and Spin - current Damping.* (Ph.D Thesis, George - August University, Gottingen, Germany, 2006).
130. A. T. J. Miltat and G. Albuquerque, *Spin Dynamics in Confined Magnetic structures - I.* (Springer, Berlin, Heidelberg, 2002).
131. E. Beaurepaire *et al.*, *Phys. Rev. Lett.* **76**, 4250 (1996).
132. M. van Kampen *et al.*, *Phys. Rev. Lett.* **88**, 227201 (2002).
133. J.-Y. Bigot *et al.*, *Nat Phys* **5**, 515 (2009).
134. B. Koopmans *et al.*, *Phys. Rev. Lett.* **95**, 267207 (2005).
135. E. Beaurepaire *et al.*, *Appl. Phys. Lett.* **84**, 3465 (2004).
136. M. Battiato *et al.*, *Phys. Rev. Lett.* **105**, 027203 (2010).
137. A. Eschenlohr *et al.*, *Nat Mater* **12**, 332 (2013).
138. G. P. Zhang *et al.*, *Nat Phys* **5**, 499 (2009).
139. B. Koopmans *et al.*, *Nat Mater* **9**, 259 (2010).
140. G. P. Zhang and W. Hübner, *Phys. Rev. Lett.* **85**, 3025 (2000).

References

141. M. Krauß *et al.*, *Phys. Rev. B* **80**, 180407 (2009).
142. A. Laraoui *et al.*, *Eur. Phys. J. D* **43**, 251 (2007).
143. A. Laraoui *et al.*, *J. Appl. Phys.* **101**, 09C105 (2007).
144. C. Kittel, *Phys. Rev.* **73**, 155 (1948).
145. O. Kohmoto, *J. Magn. Magn. Mater.* **262**, 280 (2003).
146. J. h. B. Hillebrands, *Handbook of Magnetism and Advanced Magnetic Materials*. (John Wiley & Sons Ltd., 2007).
147. C. Herring and C. Kittel, *Phys. Rev. B* **81**, 869 (1951).
148. J. Kerr, *Philos. Mag. Series 5* **3**, 321 (1877).
149. Z. Q. Qiu and S. D. Bader, *Rev. Sci. Instrum.* **71**, 1243 (2000).
150. A. O. Adeyeye and N. Singh, *J. Phys. D: Appl. Phys.* **41**, 153001 (2008).
151. B. Rana and A. Barman, *SPIN* **03**, 1330001 (2013).
152. Y. Martin and H. K. Wickramasinghe, *Appl. Phys. Lett.* **50**, 1455 (1987).
153. M. R. Freeman *et al.*, *IEEE Trans. Magn.* **27**, 4840 (1991).
154. M. R. Freeman *et al.*, *Appl. Phys. Lett.* **60**, 2555 (1992).
155. W. K. Hiebert *et al.*, *Phys. Rev. Lett.* **79**, 1134 (1997).
156. A. Barman *et al.*, *Nano Lett.* **6**, 2939 (2006).
157. T. Schrefl, *J. Magn. Magn. Mater.* **207**, 45 (1999).
158. T. Schrefl, *J. Magn. Magn. Mater.* **207**, 66 (1999).
159. S.-K. Kim, *J. Phys. D: Appl. Phys.* **43**, 264004 (2010).
160. T. F. H. Fangohr, M. Franchin, G. Bordignon, J. Generowicz, A. knittel, M. Walter, M. Albert, *NMAG User Manual Documentation, Release 0.2.1.* (2012).

References

161. M. Donahue and D. G. Porter, *OOMMF User's guide, Version 1.0.*, (NIST Interagency Report No. 6376, National Institute of Standard and Technology, Gaithersburg, MD, URL: <http://math.nist.gov/oommf>, 1999).
162. D. Kumar *et al.*, *J. Phys. D: Appl. Phys.* **45**, 015001 (2012).
163. E. Yablonovitch and T. J. Gmitter, *Phys. Rev. Lett.* **63**, 1950 (1989).
164. J. W. Kłos *et al.*, *Phys. Rev. B* **86**, 184433 (2012).
165. G. Gubbiotti *et al.*, *J. Phys. D: Appl. Phys.* **43**, 264003 (2010).
166. S. Pal *et al.*, *Appl. Phys. Lett.* **98**, 082501 (2011).
167. J. Topp *et al.*, *Phys. Rev. B* **78**, 024431 (2008).
168. R. Hertel *et al.*, *Phys. Rev. Lett.* **93**, 257202 (2004).
169. J. Podbielski *et al.*, *Phys. Rev. Lett.* **96**, 167207 (2006).
170. S. Choi *et al.*, *Phys. Rev. Lett.* **98**, 087205 (2007).
171. J. P. Park *et al.*, *Phys. Rev. Lett.* **89**, 277201 (2002).
172. Z. K. Wang *et al.*, *Nano Lett.* **6**, 1083 (2006).
173. V. V. Kruglyak *et al.*, *Phys. Rev. Lett.* **104**, 027201 (2010).
174. R. Zivieri *et al.*, *Phys. Rev. B* **83**, 054431 (2011).
175. G. Gubbiotti *et al.*, *J. Appl. Phys.* **99**, 08C701 (2006).
176. S. Tacchi *et al.*, *Phys. Rev. B* **82**, 024401 (2010).
177. J. Ding *et al.*, *Phys. Rev. Lett.* **107**, 047205 (2011).
178. P. S. Keatley *et al.*, *Phys. Rev. B* **78**, 214412 (2008).
179. A. Barman *et al.*, *Appl. Phys. Lett.* **81**, 1468 (2002).
180. A. Barman and S. Barman, *Phys. Rev. B* **79**, 144415 (2009).

References

181. J. Jorzick *et al.*, *Phys. Rev. Lett.* **88**, 047204 (2002).
182. S. Jung *et al.*, *Phys. Rev. B* **66**, 132401 (2002).
183. V. V. Kruglyak *et al.*, *J. Appl. Phys.* **99**, 08F306 (2006).
184. B. Rana *et al.*, *ACS Nano* **5**, 9559 (2011).
185. G. N. Kakazei *et al.*, *Phys. Rev. B* **74**, 060406 (2006).
186. B. Rana *et al.*, *J. Appl. Phys.* **111**, 07D503 (2012).
187. S. M. Weekes *et al.*, *J. Appl. Phys.* **99**, 08B102 (2006).
188. E. K. Semenova *et al.*, *Phys. Rev. B* **87**, 174432 (2013).
189. R. Mandal *et al.*, *Appl. Phys. Lett.* **103**, 262410 (2013).
190. A. Wachowiak *et al.*, *Science* **298**, 577 (2002).
191. T. Shinjo *et al.*, *Science* **289**, 930 (2000).
192. S. D. Bader, *Rev. Mod. Phys.* **78**, (2006).
193. K. Shigeto *et al.*, *Appl. Phys. Lett.* **80**, 4190 (2002).
194. S. D. Bader, *Rev. Mod. Phys.* **78**, 1 (2006).
195. G. Srajer *et al.*, *J. Magn. Magn. Mater.* **307**, 1 (2006).
196. Q. F. Xiao *et al.*, *Appl. Phys. Lett.* **89**, 262507 (2006).
197. R. Hertel *et al.*, *Phys. Rev. Lett.* **98**, 117201 (2007).
198. M. Curcic *et al.*, *Phys. Rev. Lett.* **101**, 197204 (2008).
199. K. Yamada *et al.*, *Nat Mater* **6**, 270 (2007).
200. S. Sugimoto *et al.*, *Phys. Rev. Lett.* **106**, 197203 (2011).
201. A. Vansteenkiste *et al.*, *Nat Phys* **5**, 332 (2009).

References

202. J. P. Park *et al.*, *Phys. Rev. B* **67**, 020403 (2003).
203. S. Kasai *et al.*, *Phys. Rev. Lett.* **97**, 107204 (2006).
204. M. Kammerer *et al.*, *Nat Commun* **2**, 279 (2011).
205. B. L. Mesler *et al.*, *J. Appl. Phys.* **111**, 07D311 (2012).
206. K.-S. Lee and S.-K. Kim, *Appl. Phys. Lett.* **91**, 132511 (2007).
207. T. L. Gilbert, *IEEE Trans. Magn.* **40**, 3443 (2004).
208. B. Krüger *et al.*, *Phys. Rev. B* **76**, 224426 (2007).
209. B. Krüger *et al.*, *J. Appl. Phys.* **103**, 07A501 (2008).
210. A. Vogel *et al.*, *Phys. Rev. Lett.* **106**, 137201 (2011).
211. J. Shibata *et al.*, *Phys. Rev. B* **67**, 224404 (2003).
212. H. Jung *et al.*, *Sci. Rep.* **1**, (2011).
213. S. Barman *et al.*, *IEEE Trans. Magn.* **46**, 1342 (2010).
214. H. Jung *et al.*, *ACS Nano* **6**, 3712 (2012).
215. J.-H. Kim *et al.*, *Appl. Phys. Lett.* **101**, 092403 (2012).
216. A. Haldar and A. O. Adeyeye, *Appl. Phys. Lett.* **106**, 032404 (2015).
217. J. O. Vasseur *et al.*, *Phys. Rev. B* **54**, 1043 (1996).
218. G. Duerr *et al.*, *Appl. Phys. Lett.* **99**, 202502 (2011).
219. M. Krawczyk *et al.*, *J. Phys. D: Appl. Phys.* **46**, 495003 (2013).
220. X. M. Liu *et al.*, *Appl. Phys. Lett.* **100**, 242411 (2012).
221. S. Tacchi *et al.*, *Phys. Rev. Lett.* **109**, 137202 (2012).
222. F. S. Ma *et al.*, *Appl. Phys. Lett.* **98**, 153107 (2011).

References

223. N. I. Polushkin *et al.*, *Appl. Phys. Lett.* **101**, 132408 (2012).
224. C. C. Wang *et al.*, *Nanotechnology* **17**, 1629 (2006).
225. S. Tacchi *et al.*, *IEEE Trans. Magn.* **46**, 1440 (2010).
226. A. V. Chumak *et al.*, *Nat. Commun.* **1**, 141 (2010).
227. Z. Zeng *et al.*, *ACS Nano* **6**, 6115 (2012).
228. G. M. Müller *et al.*, *New J. Phys.* **10**, 123004 (2008).
229. L. Giovannini *et al.*, *Phys. Rev. B* **75**, 024416 (2007).
230. R. Zivieri and R. L. Stamps, *Phys. Rev. B* **73**, 144422 (2006).
231. L. Thevenard *et al.*, *J. Appl. Phys.* **106**, 063902 (2009).
232. J. M. Shaw *et al.*, *Phys. Rev. B* **79**, 184404 (2009).
233. H. Nembach *et al.*, *Phys. Rev. B* **83**, 094427 (2011).
234. V. E. Demidov *et al.*, *Appl. Phys. Lett.* **99**, 082507 (2011).
235. M. E. Zoorob *et al.*, *Nature* **404**, 740 (2000).
236. N. Wang *et al.*, *Phys. Rev. Lett.* **59**, 1010 (1987).
237. S. Jain *et al.*, *Nanotechnology* **21**, 285702 (2010).
238. O. Dmytriiev *et al.*, *Phys. Rev. B* **87**, 174422 (2013).
239. Z. K. Wang *et al.*, *Appl. Phys. Lett.* **94**, 083112 (2009).
240. O. Rousseau *et al.*, *Sci. Rep.* **5**, (2015).
241. D. Bhowmik *et al.*, *Nat Nano* **9**, 59 (2014).
242. K. L. Livesey *et al.*, *Phys. Rev. B* **87**, 064424 (2013).
243. A. O. Adeyeye *et al.*, *IEEE Trans. Magn.* **47**, 1639 (2011).

References

244. H. Yu *et al.*, *Nat Commun* **4**, (2013).
245. S. Zhang *et al.*, *Appl. Phys. Lett.* **70**, 2756 (1997).
246. X. Zhu *et al.*, *Appl. Phys. Lett.* **87**, 062503 (2005).
247. K.-S. Lee *et al.*, *Phys. Rev. Lett.* **102**, 127202 (2009).
248. D. Kumar *et al.*, *J. Appl. Phys.* **114**, 023910 (2013).
249. G. Gubbiotti *et al.*, *Phys. Rev. B* **72**, 224413 (2005).
250. M. P. Kostylev *et al.*, *Phys. Rev. B* **76**, 054422 (2007).
251. C. Schoeppner *et al.*, *J. Appl. Phys.* **116**, 033913 (2014).
252. S. Parkin and S.-H. Yang, *Nat Nano* **10**, 195 (2015).
253. I. M. Miron *et al.*, *Nat Mater* **10**, 419 (2011).
254. S.-H. Yang *et al.*, *Nat Nano* **10**, 221 (2015).
255. G. S. D. Beach *et al.*, *Nat Mater* **4**, 741 (2005).
256. M. Kostylev *et al.*, *Appl. Phys. Lett.* **92**, 132504 (2008).
257. O. Dmytriiev *et al.*, *Phys. Rev. B* **87**, 174429 (2013).
258. V. V. Kruglyak *et al.*, *Phys. Rev. B* **77**, 172407 (2008).
259. J. Shibata and Y. Otani, *Phys. Rev. B* **70**, 012404 (2004).
260. K. Y. Guslienko, *Appl. Phys. Lett.* **89**, 022510 (2006).
261. K.-S. Lee and S.-K. Kim, *Phys. Rev. B* **78**, 014405 (2008).
262. M. Bolte *et al.*, *Phys. Rev. Lett.* **100**, 176601 (2008).
263. M. Weigand *et al.*, *Phys. Rev. Lett.* **102**, 077201 (2009).
264. Q. F. Xiao *et al.*, *J. Appl. Phys.* **102**, 103904 (2007).

References

265. K.-S. Lee *et al.*, *Phys. Rev. B* **76**, 174410 (2007).
266. A. A. Thiele, *Phys. Rev. Lett.* **30**, 230 (1973).
267. S. Sugimoto *et al.*, *IEEE Trans. Magn.* **47**, 2951 (2011).